# INVESTIGATIONS OF A PRECAST BRIDGE DECK SYSTEM

By

MOSTAFA FARHAT GHASHGESH

Bachelor of Science in Civil Engineering
Al-Fateh University
Tripoli, Libya
1996

Master of Science in Civil Engineering
Al-Fateh University
Tripoli, Libya
2002

Submitted to the Faculty of the
Graduate College of the
Oklahoma State University
in partial fulfillment of
the requirements for
the Degree of
DOCTOR OF PHILOSOPHY
July, 2012

# INVESTIGATIONS OF A PRECAST BRIDGE DECK SYSTEM

Dissertation Approved:

**Dr. M. Tyler Ley**

Dissertation Adviser

**Dr. Bruce W. Russell**

**Dr. Robert N. Emerson**

**Dr. J. Keith Good**

Outside Committee Member

**Dr. Sheryl A. Tucker**

Dean of the Graduate College

# TABLE OF CONTENTS

Chapter Page

# LIST OF FIGURES

Figure Page

Figure Page

Figure Page

Figure Page

# LIST OF TABLES

Table Page

# CHAPTER I

# I. INTRODUCTION

Development of a precast bridge construction system grants an efficient and economical design concept that can be executed for new bridge construction and the rehabilitation of existing bridges. Recently, there has been increased interest in constructing bridges that last longer, are less expensive, and take less time to construct(1). The concept increases the cost-effectiveness of bridges by providing satisfactory durability, and uses rapid construction techniques to minimize construction time and disruptions to the traveling public(2). With precast construction the individual components are manufactured off-site where increased quality is usually achieved. Further, because much of the work is completed away from the bridge site, user interferences are minimized since the amount of labor intensive on-site work is reduced, leading to reduced onsite construction time(2). In brief, the benefits of precast components in bridge construction enhance the philosophy of "get in, get out, and stay out".(2)

Precast elements can be utilized for pedestrian, highway and railway bridges. They can be adapted to all types of structures having short, medium and long spans.(3) Precast products can be implemented to some or most of the components of a bridge's superstructure and/or substructure. The use of precast-prestressed concrete panels is popular in the construction of concrete bridge decks in certain US states. For composite decks consisting of precast panels and cast-in-place topping, partial-depth precast-prestressed concrete panels can serve as formwork for the cast-in-place concrete slabs and accelerate the construction of bridge decks in a cost-effective way(4). Traditionally these panels are reinforced with mild steel temperature reinforcement in the traffic direction along with low relaxation seven wire steel prestressing strands perpendicular to the traffic direction (along the span length of the panel)[4].

Recent studies[5,6] revealed that 22% of the bridges in Oklahoma are structurally deficient; that is the second highest percentage of any state after only Pennsylvania. More than 60% of the structurally deficient bridge ratings in Oklahoma are due to severe bridge deck deterioration. Because the bridges in Oklahoma and across the nation are in dire need of improvement and the associated costs are so overwhelming, the Federal Highway Administration (FHWA) has made it a priority to seek new methods to economically repair and construct bridges and other transportation infrastructure. What is needed is a bridge deck system that is durable, rapid to construct, and economical.

In response to this need, several recent attempts have been made to create a bridge deck system with *full depth* precast concrete pieces that are lifted into place with large cranes to serve as the bridge deck. These precast deck systems have been attempted in around 10 states, but have not been widely adopted for the following reasons:

(i) difficulty adjusting the precast pieces to meet construction tolerances;

(ii) inability to provide a smooth final riding surface without extensive grinding; and

(iii) expense due to specialized equipment or materials.

However, a new system is being investigated in this dissertation. The system utilizes individual precast panels that are one half of the final bridge deck thickness in the interior spans and a precast panel that has a full depth and partial depth section in the overhangs and the first interior span. Additionally, this system includes a welded rebar mats serving as top reinforcement in the interior bays. These panels serve as structural stay in place formwork, working surface, and support for the screed rail. A 4” topping of cast in place reinforced concrete is placed to tie the structural systems together and provide the final riding surface for the bridge deck.

Reinforced concrete structures are commonly designed to satisfy criteria of serviceability and safety. In order to ensure the serviceability requirement it is necessary to predict the cracking and the deflections of RC structures under service loads. In order to evaluate the margin of safety of RC structures against failure, an accurate estimation of the ultimate load is crucial and the prediction of the load-deformation behavior of the structure throughout the range of elastic and inelastic response is desirable.

Advanced analytical tools can be an essential aid in the assessment of the safety and the serviceability of a proposed design.(7) The safety and serviceability evaluation of structures demands the development of accurate and reliable methods and models for their analysis. The objective of such an analysis is the investigation of the behavior of the structure under all possible loading conditions, both, monotonic and cyclic, its time-dependent behavior, and, especially, its behavior under overloading.

Within the framework of developing advanced design and analysis methods for modern structures, the need for experimental research continues. Experiments provide a rigid basis for design equations, which are very useful in the preliminary design stages. Experimental research also supplies the basic information for finite element models, such as material properties. In addition, the results of finite element models have to be evaluated by comparing them with experiments of full-scale models of structural subassemblies or, even, entire structures. The development of reliable analytical models can, however, reduce the number of required test specimens for the solution of a given problem, recognizing that tests are time-consuming and costly and often do not simulate exactly the loading and support conditions of the actual structure. Many factors(7) can complicate the development of analytical models of the response of RC structures:

- Reinforced concrete is a composite material made up of concrete and steel, two materials with very different physical and mechanical behavior;
- Concrete exhibits nonlinear behavior even under low level loading due to nonlinear material behavior, environmental effects, cracking, biaxial stiffening and strain softening;
- Reinforcing steel and concrete interact in a complex way through bond-slip and aggregate interlock.

With the arrival of digital computers and powerful methods of analysis, such as the finite element method (FEM), many efforts to develop analytical solutions which would turn aside the need for experiments have been undertaken by investigators. The finite element method has thus become a powerful computational tool, which allows complex analyses of the nonlinear response of RC structures to be carried out in a routine fashion. With this method the importance and interaction of different nonlinear effects on the response of RC structures can be studied analytically.

Alternatively, the complex phenomena taking place inside a reinforced concrete member have led engineers in the past to rely heavily on empirical formulas and analysis methods for the design of concrete structures(4), which were firmly based on numerous experiments. These empirical formulae were presented in different forms of design codes and recommendations. Such provisions may take simplicity, low time and computational effort as profound advantages over computer-based analysis techniques represented in the FEM.

Another analysis method standing halfway between the simplified hand methods and FEM is the strut and tie method. Strut and tie modeling (STM) provides a valuable analysis and design tool for concrete structures(8), especially for regions where the plane sections assumption of beam theory does not apply. It is a rational approach to visualize the flow of forces at the strength limit state based on the variable-angle truss analogy, and a unified approach that considers all load effects simultaneously.

The present study is part of the continuing effort to understand the behavior of composite bridge decks and to satisfy concerns about their performance. Chapter two presents the first phase of the experimental study to explore the performance of the precast prestressed overhangs compared to the conventionally built ones. Chapter three provides the outlines and results of an experimental study of using pre-welded rebar mats as a replacement to the conventional tied reinforcement in the cast-in-place (CIP) portion of the bridge deck. Chapter four includes an analytical modeling of the problems tested experimentally. Self-written, non-linear FE code has been authored and used, with the experimental results used as references for comparison purposes and to judge on the modeling accuracy. chapter five provides a test of the failure load prediction accuracy of design codes and recommendations that are currently in practice. STM prediction accuracy is also investigated as well. Finally, chapter six wraps up all work done in this dissertation and presents conclusions for the main points extracted, and recommendations for future work.

This dissertation has been largely written in journal paper format. This was done to reduce the time required to publish each of the chapters as a journal paper. Because of this; background information is contained in each chapter. Also, this may explain why there will be some redundancy in the chapters.

# CHAPTER II

# II. DEVELOPMENT OF A PRECAST OVERHANG FOR BRIDGE DECK CONSTRUCTION

## 2.1- INTRODUCTION

In the United States and internationally, there is a need for renewal of transportation infrastructure. The American Society of Civil Engineers has estimated that $190 billion is needed over the next 20 years to eliminate deficiencies in US bridges.[(9)] It is in the best interest of society to find ways to provide durable bridge systems in an economic and rapid manner. Currently, the most costly and labor intensive element to construct on a bridge is the bridge deck. Improvements in bridge deck construction would help satisfy these needs.

In response to this need, several attempts have been made to create a concrete bridge deck system that is partially pre-assembled in a manufacturing facility (or precast) and then shipped to the construction site where construction can be completed. However these systems have not been widely adopted for the following reasons: (i) difficulty adjusting the pre-assembled pieces to meet construction tolerances, (ii) inability to provide a smooth final riding surface without extensive grinding, and (iii) expense due to specialized equipment or materials needed for construction.

After careful investigation of these challenges, a new precast bridge deck system was developed and implemented by TxDOT in Ft. Worth, Texas with the help of researchers at Oklahoma State University, Texas A&M University, and Austin Prestressed. This system has addressed each challenge by modifying the form of the precast deck panels so they contain a full depth and partial depth section. This system removes the need for all form work, provides a construction work platform, is adjustable to meet construction tolerances, and provides a support for all needed construction equipment. A 4” topping of cast-in-place reinforced concrete is then used to tie the pre-assembled pieces together and provide the final riding surface for the bridge deck.

This system has yielded drastic improvements in speed of construction, and improvements in economy are projected over modern methods of bridge deck construction in Texas. The TxDOT estimates significant savings in cost and over a week in construction time per bridge span.

This chapter describes the features of the system, laboratory testing, the construction of the system in Texas, and the planned improvements for the future.

### 2.1.1- Precast Bridge Deck Construction Techniques

One bridge element that was recognized in the 1970s that could greatly benefit from precast construction is the bridge deck. This element is repeatable and is quite costly to construct due to the labor required for formwork placement and removal, for placement of the needed reinforcement, for placement of the concrete, and for providing adequate curing. A typical conventional forming system is shown in Figure 1A.

#### *2.1.1.1- Partial Depth Bridge Decks*

In an effort to improve the economy and constructability of bridge decks several US DOTs began using partial depth prestressed precast panels as stay in place formwork. These panels were typically used in the interior portion of the span and were only half of the bridge deck depth. Next mild reinforcing steel was added above these panels and cast-in-place concrete was placed to finish the bridge[(10)]. While these partial depth stay-in-place forms yield definite benefits over conventional construction methods the cantilever portion of the bridge deck is currently conventionally formed by using overhang brackets that serve as both formwork and a work platform. This system is shown in Figure 1B.

The partial depth system was tried in several states and has had challenges due to slow speed of overhang construction, obtaining the correct elevation of the finished riding surface, and inadequate amount of support under the panel during construction which caused serviceability problems. However, there has been an extensive amount of research on this system by the Texas DOT[11,12,13,14,15]. This research found that this system if constructed correctly was able to provide an economical bridge deck system with a large amount of reserve capacity. Currently, several states use this system as a standard method of bridge construction because of the improvements in safety, economy and speed over conventionally formed bridge deck construction.

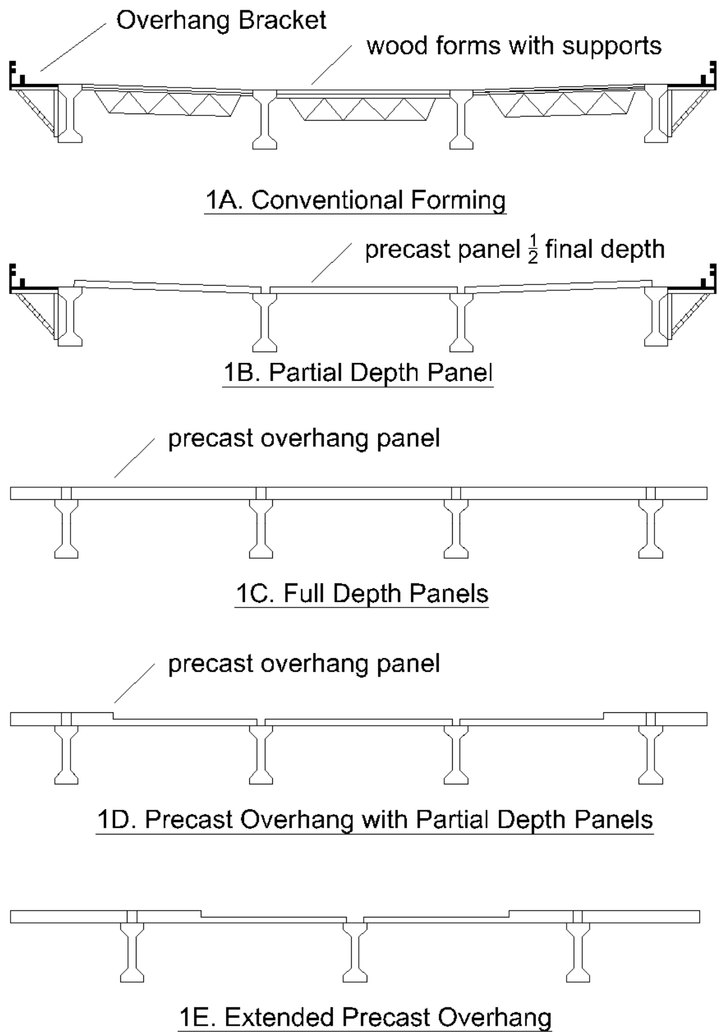


**Figure 1:** Display of various precast and cast in place bridge decks.

### *2.1.1.2- Full Depth Precast Bridge Decks*

Beginning in 1985 several state DOTs (Texas, Louisiana, New York, New Jersey, Vermont) started investigating the use of full depth precast bridge deck systems[16,17].

Typically, these bridge deck systems consist of thick concrete planks that run the entire width of the bridge deck that are placed on the beams below. An example of one of these systems is shown in Figure 1C. These concrete planks are heavy and are not easy to transport or place. Once these elements are in place, they are connected with reinforcing steel and some cast-in-place grout or concrete. Some systems are then post-tensioned in an attempt to minimize the amount of cracking in the bridge deck.

There was a flourish of recent research over this topic as several states continue to investigate these systems(17,18). One benefit that these systems have over the partial depth deck panel system is that they remove the need for the conventional forming used in the overhang construction. These systems typically use very little cast-in-place concrete or grout and require the use of several leveling bolts to obtain the correct geometry and riding surface of the bridge deck. While these grade bolts are very useful, they have proven to be challenging to provide adequate flexibility to meet the large number of different geometries required for a bridge deck. Furthermore, due to differential camber between prestressed concrete beams these systems have been found to only be useable on steel girders. This attribute has limited the use of these systems. It is often necessary to provide an asphalt wearing surface or grind the surface of the deck elements where the concrete planks interface to obtain the correct riding surface. An example of an unsatisfactory riding surface provided by one of these full depth panel sections can be found in Figure 2. While the full depth precast section has shown an improvement in speed of construction, it has also shown an increase in the cost of construction(18,19). This increase can be attributed to large shipping weights, increase in crane size, and additional wearing surface or grinding.

### 2.1.2- Development of the New System

While reviewing the benefits and challenges of the full depth and partial depth bridge decks, it was realized that some features of both systems could be combined in a hybrid system that is able to achieve significant improvements over the previous systems. An overview of this new hybrid system is shown in Figure 1D, and Figure 1E.

In this system, a new precast panel is used in the overhang that extends from the first interior girder to the tip of the cantilever. This precast panel is full depth from the cantilever tip until the compression zone of the exterior bay. The panel is then only partial depth until the first interior girder. Each proportion and size of the precast overhang panel was chosen for specific reasons. The full depth portion of the precast panel at the exterior of the bridge allows for the removal of the overhang forming brackets and also provides a construction work platform and area for the safety rail.

**Figure 2:** A wooden stick placed at the intersection of two full depth precast panels that have been adjusted using grade bolts. The difference in panel height is over ¼”.

Pockets in this full depth section are used to provide a connection between the precast panel and the exterior girder. Grout is used to fill the haunch area and concrete is used to fill the pockets. These grout pockets also provide a location for the screed rail to be attached to the bridge deck. These panels also have special inset areas in the full depth section to allow for a connection to be made between panels and for grade bolts to be used for altering panel geometry. In addition to this panel, a novel adjustable haunch gasket was developed to be used with this system. This haunch forming system is made with low density polyethylene foam that is glued to the top of the girder allowing it to compress or expand as the grade bolts are adjusted in the precast overhang panel. A detailed summary of the precast overhang element can be found in Figure 3 and Figure 4. For the interior bays, the partial depth precast panels are used. After the geometry of the precast overhang panel has been established with the grade bolts, the reinforcing steel in the interior span and between panels is placed and concrete is used in the partial depth section. Finally, the haunch of the exterior girder is grouted and then the pockets are filled with a low shrink concrete mixture. The traffic rail for the bridge is then completed, and the deck is finished.  A pictorial explanation of the construction process is shown in Figure 5 through Figure 14.

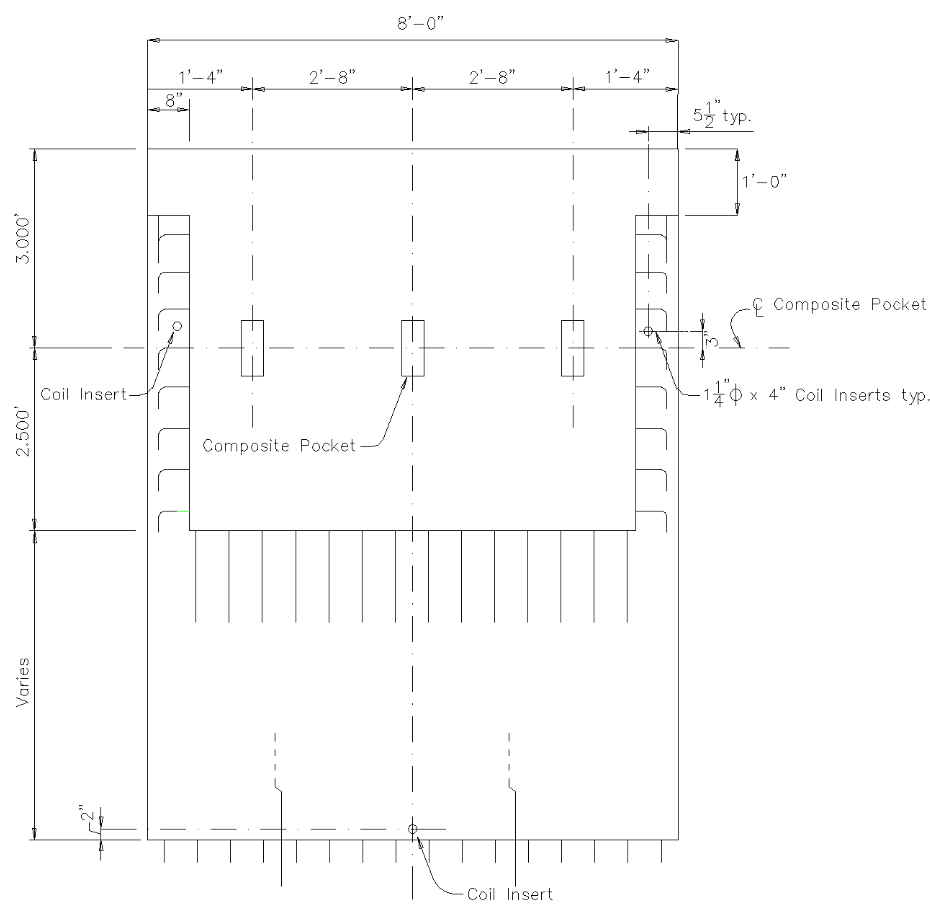


**Figure 3:** A plan view of the precast overhang panel showing dimensions.

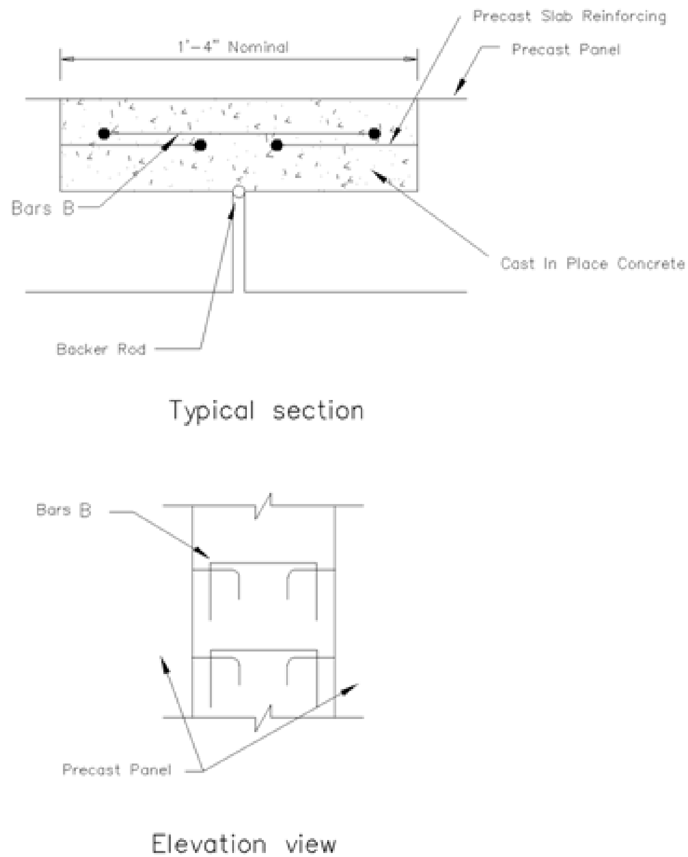


**Figure 4:** Connection details between the precast overhang panels.

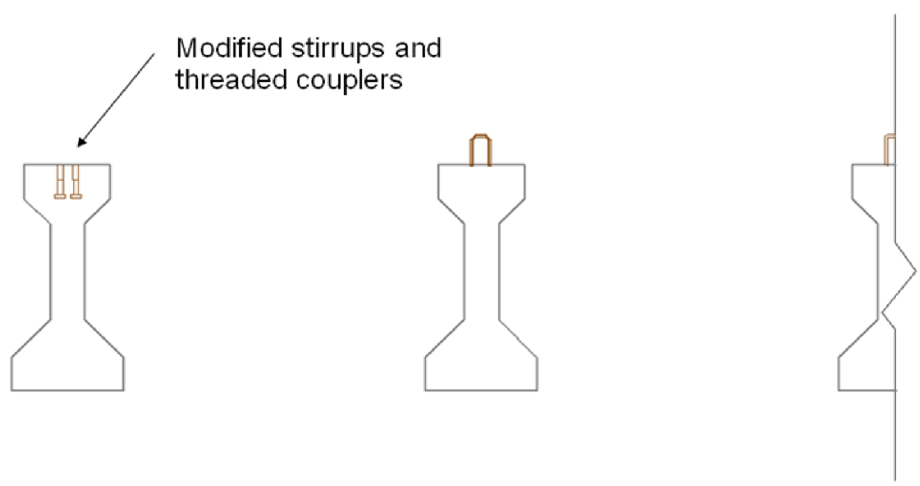


**Figure 5:** The beams are erected on the bents. A shear connector is used on the external beam for load transfer.

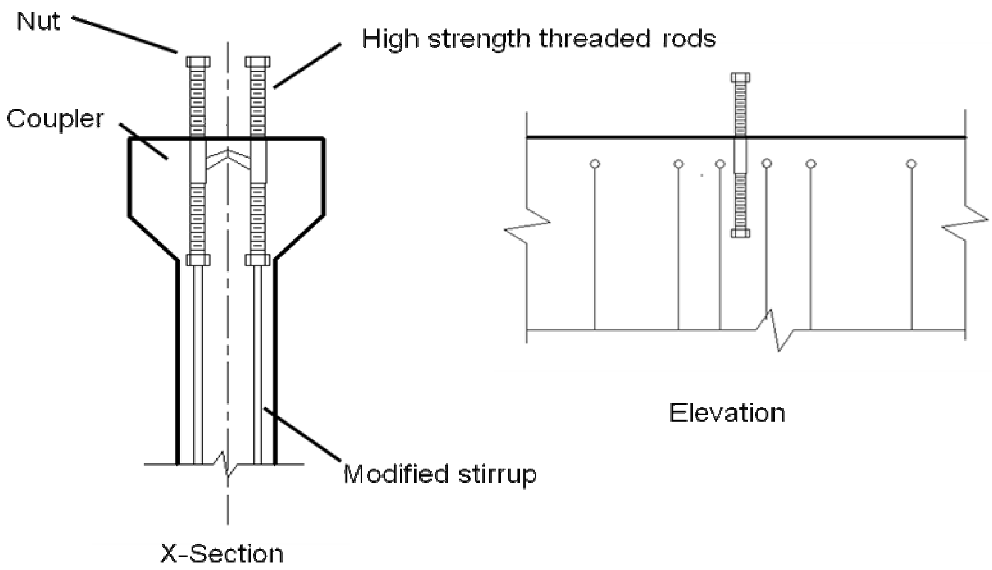


**Figure 6:** Structural details for the modification of the external beam.

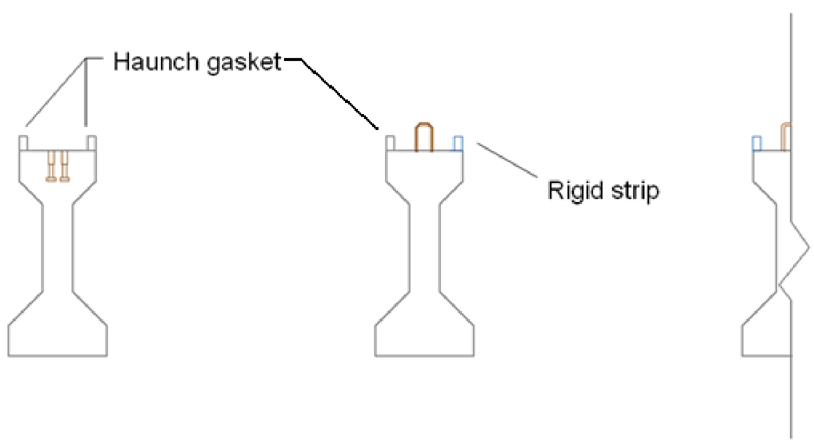


**Figure 7:** The haunch gasket is glued to the external girder and the outside face of the interior beam.

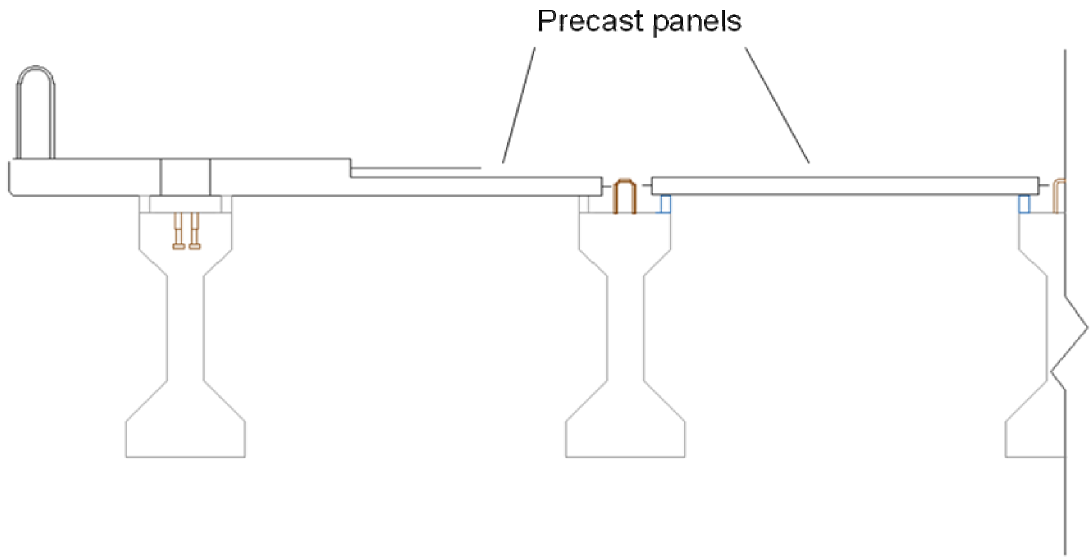


**Figure 8:** Precast panels are then placed. Precast overhang panels are used in the exterior bay and partial depth panels in the interior bays.

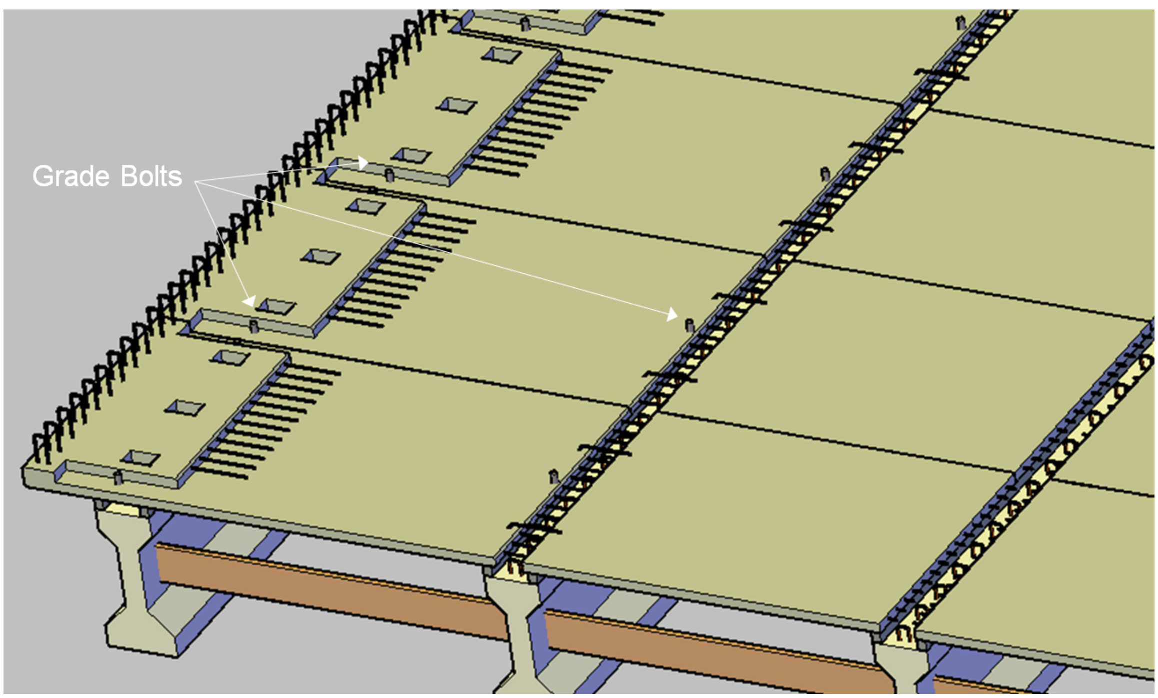


**Figure 9:** Grade bolts are adjusted in the overhang panels to the desired grade.

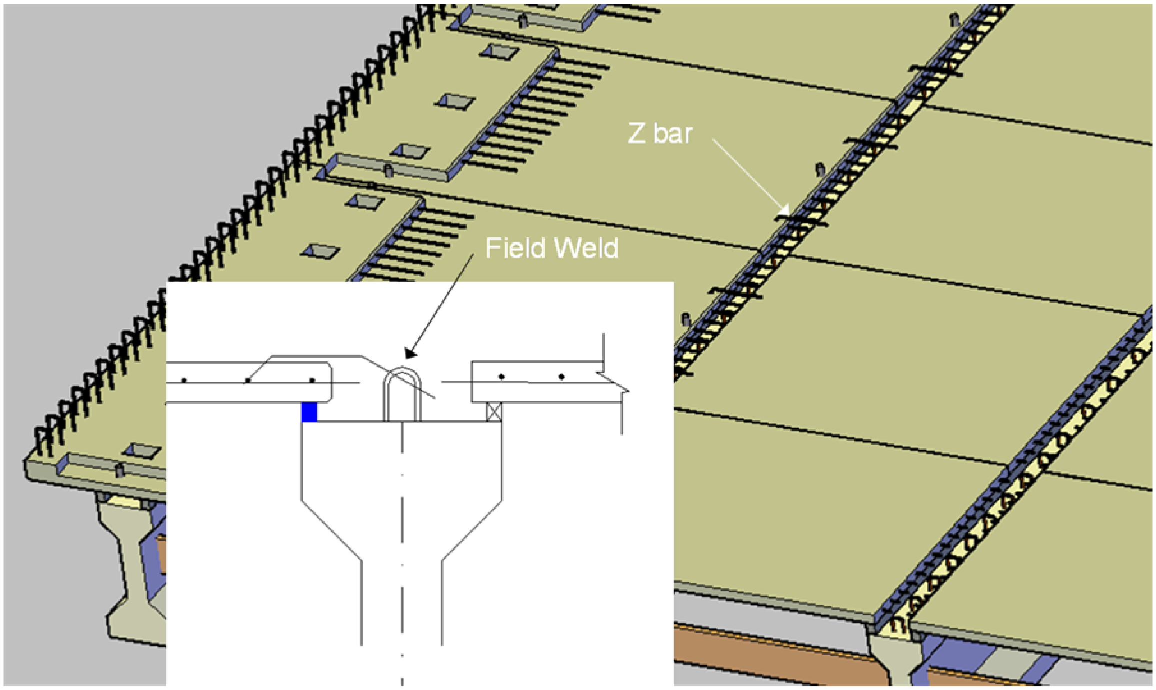


**Figure 10:** The external rebar is a failsafe bar that is bent down and welded to the stirrups of the first interior beam to prevent overturning.

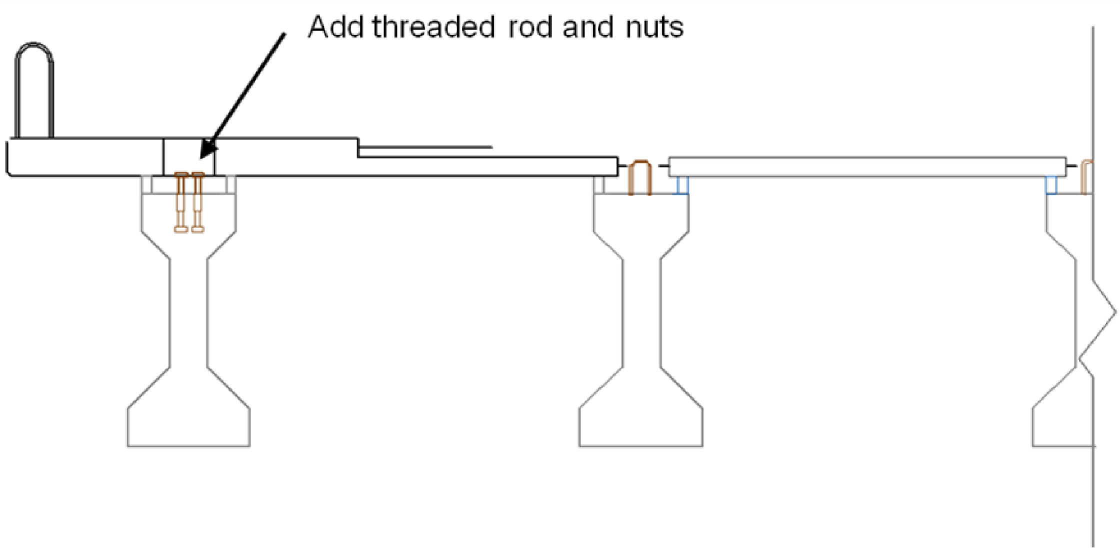


**Figure 11:** Threaded rods and nuts are added to the grout pocket of the external beam. This step could be carried out before the placement of the overhang panels.

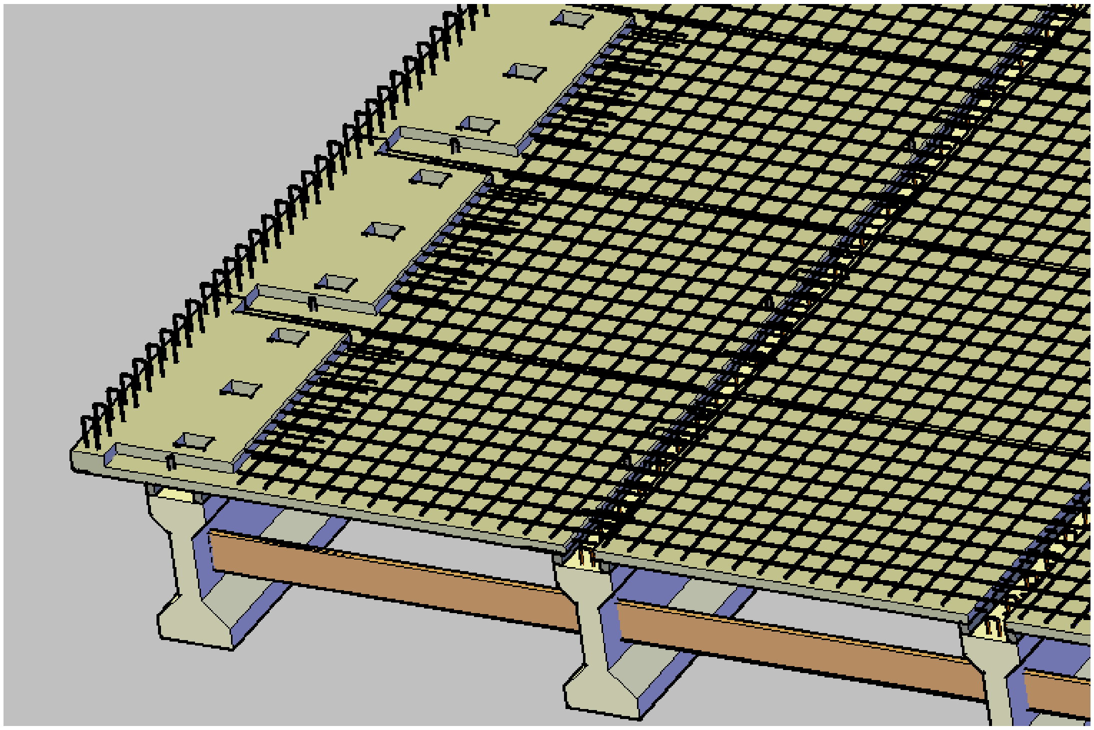

**Figure 12:** Rebar is placed above the partial depth portions of the deck.

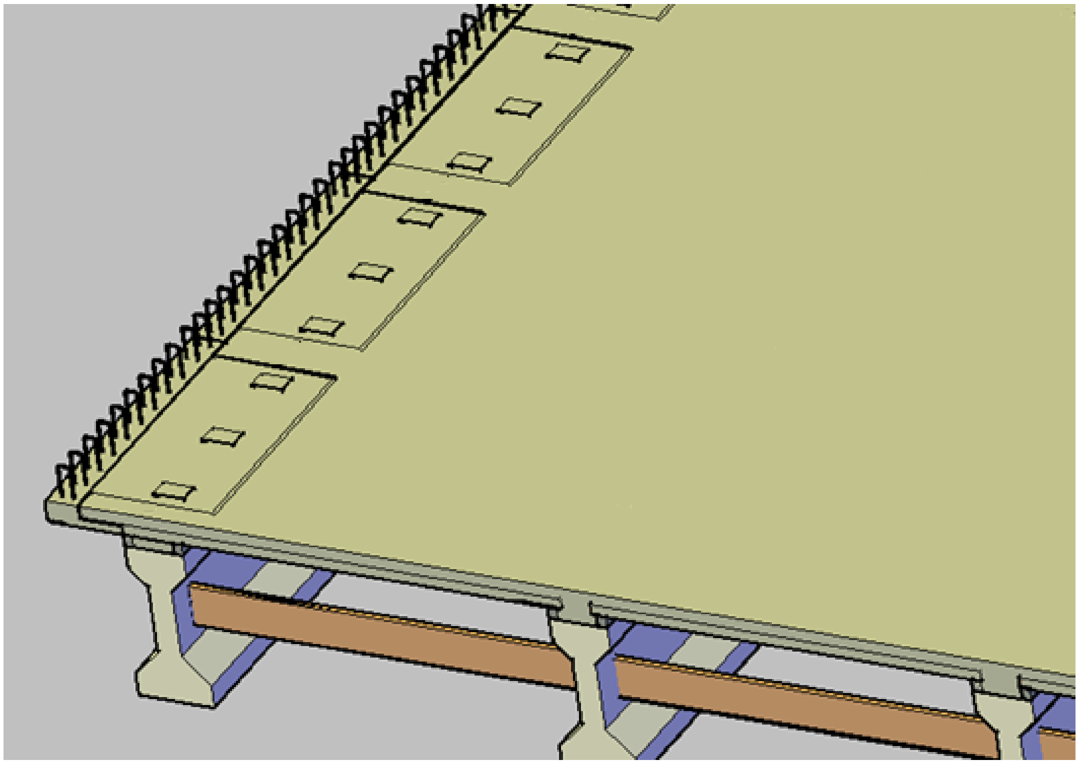

**Figure 13:** Concrete is placed to tie the precast system together. The haunch of the external girder is filled with grout, and then the composite pockets are filled with concrete.

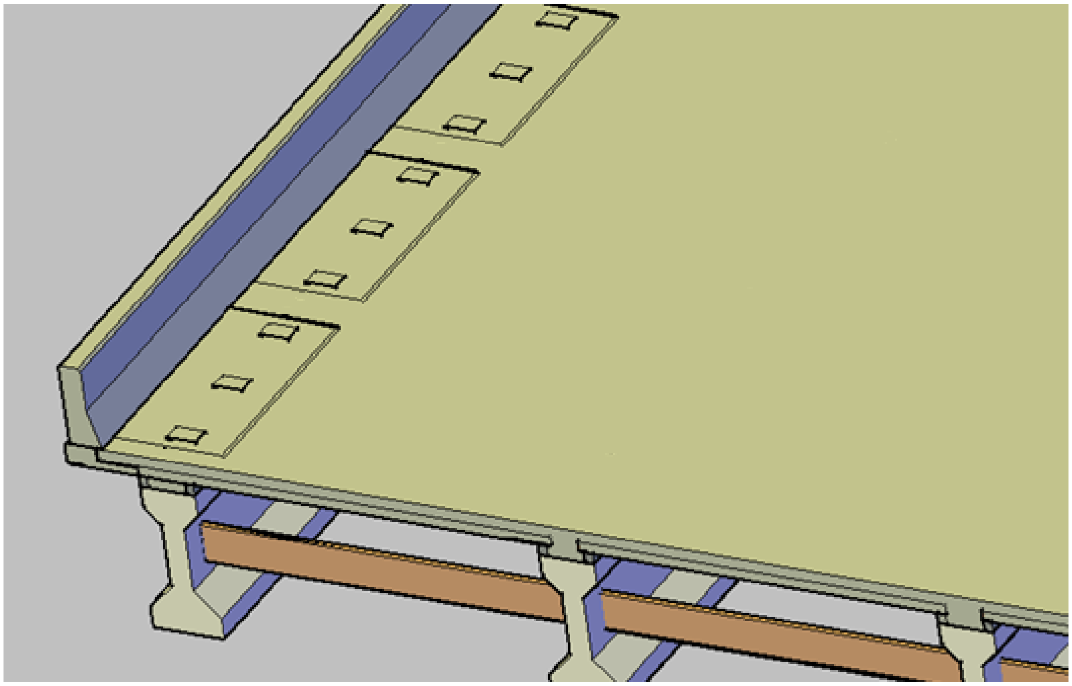

**Figure 14:** The concrete barrier is constructed by either slip forming or conventional forming.

### *2.1.2.1- System Attributes*

As stated previously, this bridge deck system was specifically designed to combine advantageous features from the partial depth bridge deck with the full depth bridge deck systems in such a manner as to address the challenges of both systems.

This system specifically adapted the full depth section of the bridge deck in the overhang portion as it eliminates the placement and removal of formwork for the overhang and the work platform that is required with the partial depth panel system. Furthermore, this full depth length was sized to create a significant work platform for the screed rail and the construction workers to hand finish the external areas of the bridge deck. The precast panel is designed to be continuous over the exterior girder and extends to the first interior girder to provide a stable support for the panel.

Incorporated into the precast overhang panels are threaded inserts for installation of the columns for the contractors hand rail/fall protection system. This allows fall protection to be installed concurrently with the overhang units. While almost any system can be accommodated, the inserts for the Rock Creek bridge were cast into the top slab approximately 3” in from the outside edge (inside the concrete traffic rail footprint). This location negates the need for any patching after the temporary hand rail is removed as the rail concrete covers the inserts.

Grade bolts were used in the precast overhang panel to obtain the desired riding surface, like they are used in full depth bridge deck construction techniques. However, the precast overhang system only requires three grade bolts at the exterior bay, as this is the only full depth portion of the bridge deck. By using a set of non-continuous precast panels, it allows the system to avoid the past challenges that other full depth precast members have seen where construction tolerances from differential beam deflection have caused the need for grinding or an overlay as shown in Figure 2.

One other benefit that may not be obvious is the simplification of the bridge deck construction. When the full depth portion of the precast panel is placed on the exterior beam, it is placing almost the entire dead load on the outside girder before the placement of the remaining cast-in-place concrete. The placement of this dead load on the external girder insures that the height of the bridge deck established by the grade bolts for the full depth section will be very close to the final height of the bridge deck. The reason for this is that no additional dead load deflection will occur. This allows the construction engineer to directly establish the roadway profile to match the desired elevation and ensure that all concrete cover requirements are met. Currently, there are numerous challenges to provide the correct ride and reinforcement cover with partial depth panel systems as one must accurately determine the deflection of the bridge deck from the placement of the fresh concrete. This is often challenging due to the complex construction geometry and differential beam deflection, especially in the cast of precast concrete girders. Again, because of the preloading of the external beam this is not a problem with this system and the desired bridge deck height can be directly established with the grade bolts.

## 2.2- TESTING METHODS

### 2.2.1- Specimens

The specimen layout can be seen in Figure 15. Each of the tested slabs was 8.25" thick and 8' x 18' or 8' x 22' planar dimensions. The slabs were supported on three girders spaced at 6' center to center with 3', 5', or 5'-8" overhangs. The testing setup was restrained at the center beam by using post-tensioned bars and load was applied in the cantilever as shown in Figure 15. The supporting girders were 1' wide and 1'-2" high and made of reinforced concrete. The 1' width was chosen to mimic a small but still reasonable flange width for a prestressed or steel support beam.

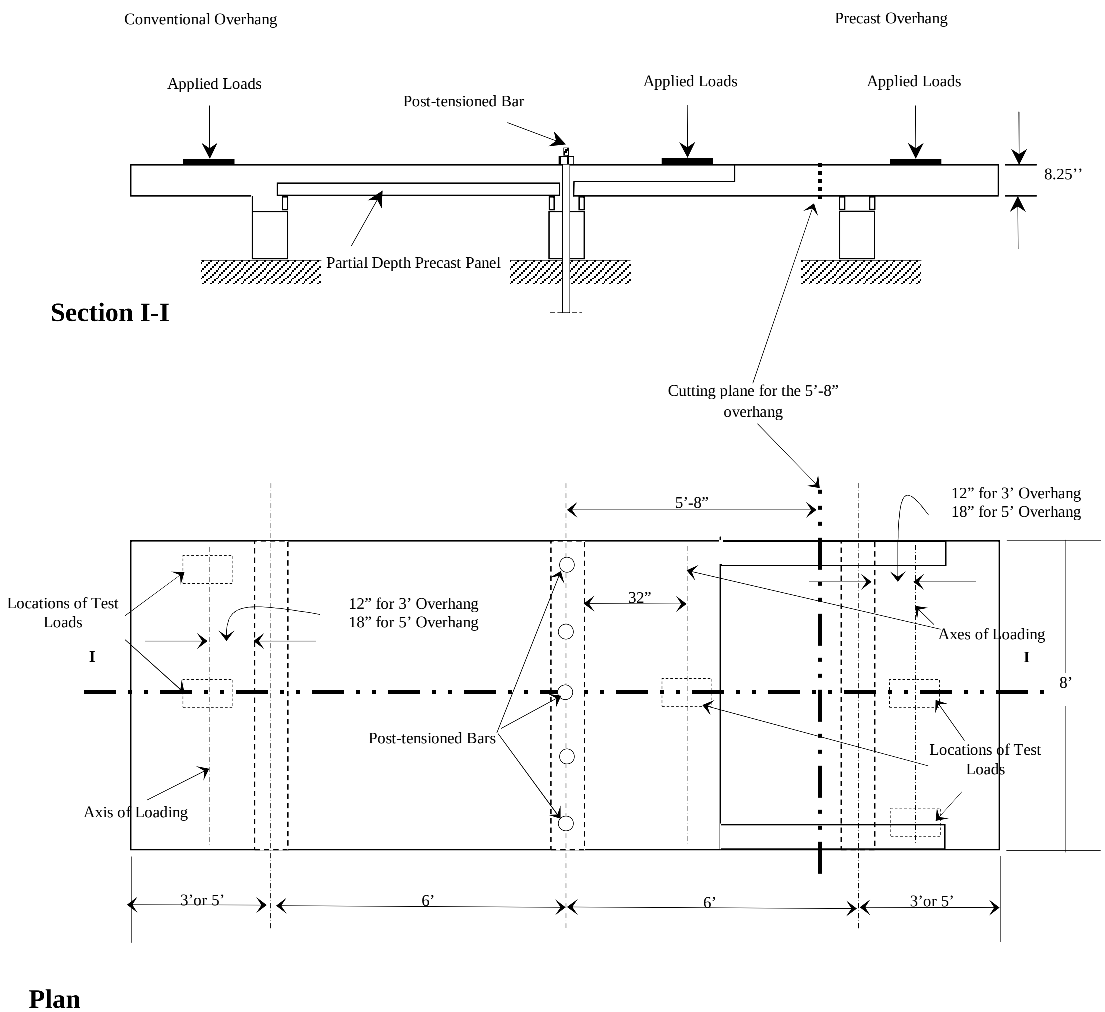


**Figure 15:** Test specimen: Typical Overall layout

The novel precast overhang system has prestressing strands in the transverse direction and mild steel in the longitudinal direction in the bottom layer and mild reinforcing steel in both directions in the top layer. This layout was chosen so that the existing forms for partial depth precast panels could be used to construct the bottom portion of the precast overhang panel. The opposing cantilever was made with cast-in-place (CIP) concrete and had mild steel in both the top and bottom layers. Reinforcement details can be found in Figures 16 and 17.

A 4” partial depth precast panel was used for the interior span that received a 4.25” topping of concrete with mild reinforcement in both directions. This specimen construction style allowed investigation of the performance of each side independently with a minimal behavioral interference; and hence gave the chance to compare the strength and stiffness of both structural systems by using a single specimen. By restricting the bridge decks to these sizes it forces all load transfer to be made in the 8’ width of the specimen. In addition this specimen construction style allows for the CIP concrete used for both specimens to be as similar as possible between the tested specimens as they were from the same concrete mixture and were placed at the same time.

The author recognizes this test protocol does not mimic the actual performance of a bridge deck; as the support beams on the ground are continuously supported. Furthermore, the center beam is restrained at the center. While the supports are different than actual practice, both systems are evaluated with equivalent support conditions; therefore the results from the testing are comparable. With this support condition the specimen response are conservative when compared to bridge decks in the field. This is because this test setup did not allow the beam supporting the cantilever to deflect and would therefore not allow load to be shed to other parts of the bridge. The 6’ beam spacing used in the testing was chosen because it is a reasonable beam spacing for prestressed bridge construction and it allowed the specimen to be tested with the facilities available. The results from this testing would not be expected to vary with the spacing of the interior beams but would vary with changes in the cantilever length as investigated in the testing.

Precast elements were created by Austin Prestressed of Austin, Texas. The cast-in-place concrete for the specimens were from a local ready mix company and the grout used to fill the haunch of the system was Sika 212™. The grout was mixed by the research team.

Typical reinforcing details used in this study are given in Figures 16 and 17. Reinforcing bars consisting of #5 bars at 6” spacing transversely and #4 bars at 9” longitudinally were used in the top mat of steel. A lap splice was used at the interface between the precast panel and the CIP concrete topping. The partial depth precast panel reinforcing was 3/8-in diameter, stress-relieved, Grade 270 prestressing strands at 6-in centers in the transverse direction and 0.22 $in^2$/ft of welded rebar mats in the longitudinal direction. The specified prestressing force during casting was 16.1 kips per strand. This prestressing force was 54% of the general ultimate tensile strength for the strand. This value matches the requirements by the Texas Department of Transportation in precast panel construction. The bottom layer of steel in the cast-in-place overhang consisted of #4 bars at 1’-6” centers for the majority of the specimens. One specimen was constructed with these bars at 6” centers. One would not expect that this change would have an impact on the results since this bar was in compression. During the construction of the precast overhang panels by Austin Prestressed the reinforcing bars in the top of the slab were inadvertently switched for the 3’ overhang corner testing. After the error was discovered it was decided to use this same reinforcing detail throughout the top layer of reinforcing in specimens 1 and 2. This change in height of approximately 0.5” is estimated based on flexural failure to reduce the ultimate strength of the specimen by approximately 10% and would be expected to reduce the cracking resistance of the specimen. This change is shown in Figure 18.

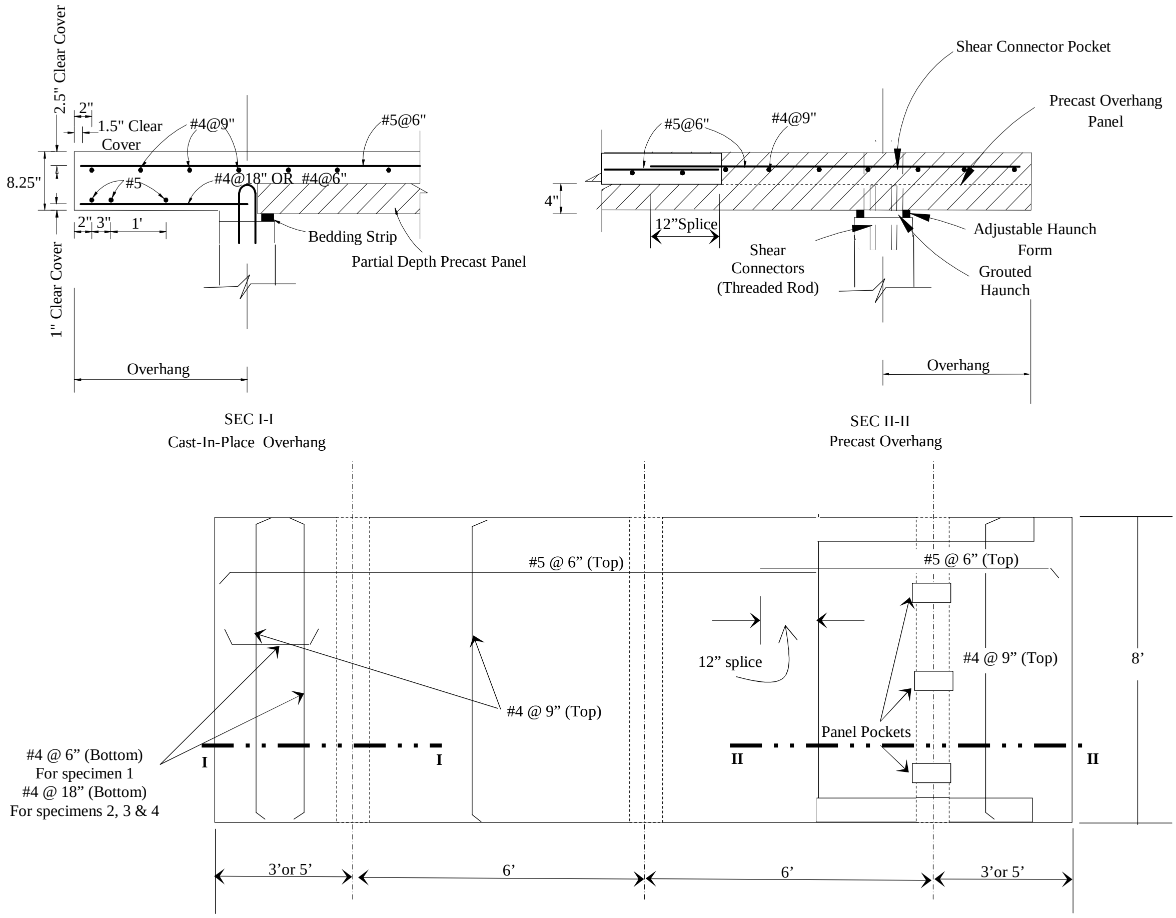


**Figure 16:** Bridge decks reinforcement details

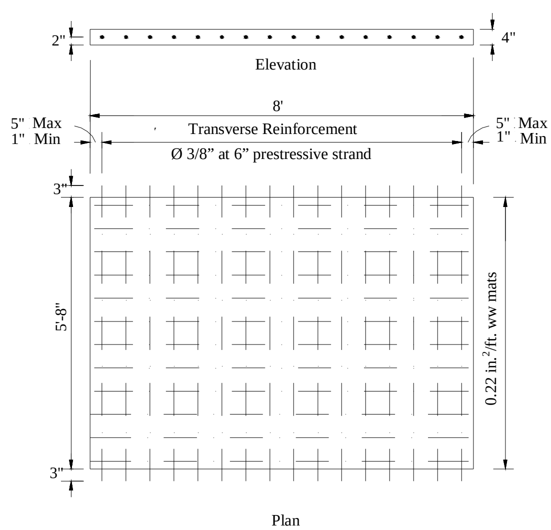


**Figure 17:** Precast panel reinforcement details

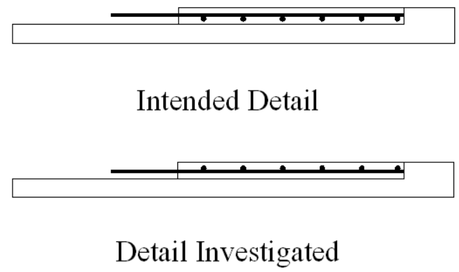


**Figure 18:** The intended detail and the detail actual used in the 3’ overhang specimens.

### 2.2.2- Test Set-up

The two cantilevers of each test specimen were tested by either loading at the specimen center or at the corner by applying concentrated loads with hydraulic rams as shown in Figure 19. On the final specimen after both cantilevers were tested, a cut was made just to the inside of the external beam, as shown in Figure 19.d, to create another cantilever to be tested. This cantilever was cut so that it had a span length of 5’-8”. This specimen was then tested. For each test a 10” x 20” steel plate was used to represent an AASHTO HL 93 tire patch. The edge of the tire patch was placed at 1’-2” away from the face of the cantilever.

These loading conditions were chosen to simulate an HL 93 truck traveling at the very edge of the guard rail at midspan and where the bridge deck terminates such as at the approach slab. For the cantilevers of 3’, 5’, and 5’-8” this lead to an eccentricity of 12”, 18” and 32” respectively. It should be mentioned that when loading the conventional side midspan loading of the 3’ overhang that the load area HL93 AASHTO tire patch was inadvertently rotated 90$^o$. The correct loading orientation was used for the remainder of the specimens. This modification should be conservative as the midpoint of the load is in the same point but the clear distance between the edge of the plate and the edge of the beam was increased by 5”.

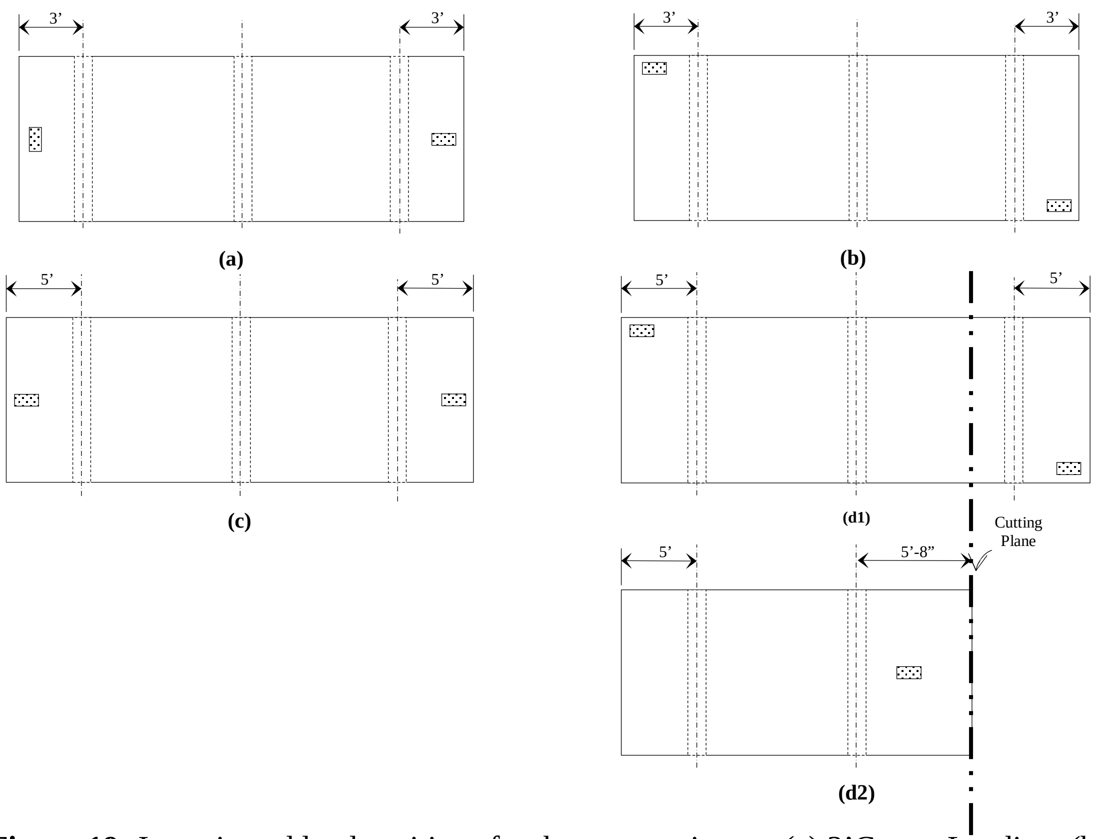


**Figure 19:** Investigated load positions for the test specimens: (a) 3'Center Loading, (b) 3'Corner Loading, (c) 5'Center Loading, (d1) 5'Corner Loading, (d2) 5'-8" Center Loading

### 2.2.3- Materials

The average compressive strength, modulus of elasticity and splitting tensile strength of the four specimens for concrete and grout mixtures are shown in Table 1. These tests were conducted according to ASTM C873/C873M-04e1, ASTM C469/C469-02e1, and ASTM C496/C496M-04e1 respectively. The average age of the cast-in-place concrete at the time of testing was 7 days. The properties of concrete were measured on 4" x 8" concrete cylinders.

The grout to fill the haunch is SikaGrout 212$^{TM}$ high performance grout. This material is used to fill the haunch on the precast overhang portion of the bridge. This requires the grout to be sufficiently fluid to flow through the haunch while maintaining dimensional stability and later attain sufficient strength. Obtaining both of these criteria can have conflicting effects. To evaluate these characteristics the flowability, segregation, bleeding, early age dimensional stability, fresh density, and strength were evaluated. Details of the grout investigation can be found in Trejo et al.[20]. After the grout had obtained initial set then a concrete mixture was used to fill the remaining space in the pocket.

The mechanical properties of the reinforcement bar measured for various diameters met TxDOT 440 and ASTM A 615/A615M-08a grade 60 requirements. Table 2 provides the average stress and strain magnitudes for the rebar samples tested. The minimum yield strength found to be 62 ksi, while the ultimate strength was 85 ksi. All bars had a well defined yield plateau.

**Table 1:** Summary of the average material properties of the mixtures used in Test Specimens.

| Specimen | Test | CIP | Precast Panel (Stage I) | Precast Panel (Stage II) | Grout | Pocket Concrete | Depth Panel |
|---|---|---|---|---|---|---|---|
| 3' Overhang Center Loading | Compression, psi | 6980 | 9100 | 7100 | 8140 | 4090 | 8480 |
| | Tension, psi | 660 | 729 | 620 | 544 | 524 | 693 |
| 3' Overhang Corner Loading | Compression, psi | 5370 | 9150 | 6860 | 6290 | 4880 | 8480 |
| | Tension, psi | 514 | 774 | 550 | 600 | 458 | 693 |
| 5' Overhang Center Loading | Compression, psi | 5730 | 9680 | 8740 | 6800 | 5370 | 8480 |
| | Tension, psi | 514 | 713 | 792 | 507 | --- | 693 |
| 5' Overhang Corner, and 5'-8" Center Loadings | Compression, psi | 3370 | 9310 | 9480 | --- | 4560 | 9910 |
| | Tension, psi | 220 | 600 | 600 | --- | 530 | 770 |

**Table 2:** Stress values for steel reinforcement

| Specimen | Yield Stress, ksi | Yield Strain | Ultimate Stress, ksi |
|---|---|---|---|
| #5 Samples | 70 | 0.00244 | 100 |
| Precast wire mesh[12] | 63 | 0.00215 | 69 |

### 2.2.4- Measurements

During loading continuous measurements of the applied loads were recorded at the hydraulic jack. Deflections of the slab with electronic linearly variable displacement transducers (LVDTs) with (0.0005 in) accuracy and surface strain readings were taken at selected load stages by using a rectangular grid of stainless steel targets spaced at about 8” that was measured by a portable DEMEC gauge with 4.4 microstrain accuracy. The DEMEC gauge has machined ends that match the machined holes in the stainless steel discs. These systems provided flexible and accurate methods to investigate the performance of the overhang systems.

### 2.2.5- Determination of Principal Strains

The maximum average principal strain ($\varepsilon_{\max}$) was found for each set of DEMECs. This was found by averaging the perpendicular strains at the sides of each grid squares in both the x and y direction. This is shown in Figure 20 as $\varepsilon_x$ and $\varepsilon_y$; where:

$$\varepsilon_x = \frac{\varepsilon_{x1} + \varepsilon_{x2}}{2} \text{ and } \varepsilon_y = \frac{\varepsilon_{y1} + \varepsilon_{y2}}{2} \quad \text{……………………..} \ (1)$$

therefore,

$$\varepsilon_{\max} = \sqrt{\varepsilon_x^{\,2} + \varepsilon_y^{\,2}} \quad \text{……………………………..………..} \ (2)$$

and the orientation of this maximum principal strain is,

$$\alpha = \tan^{-1}\left( \varepsilon_y / \varepsilon_x \right) \quad \text{………………………..…………..} \ (3)$$

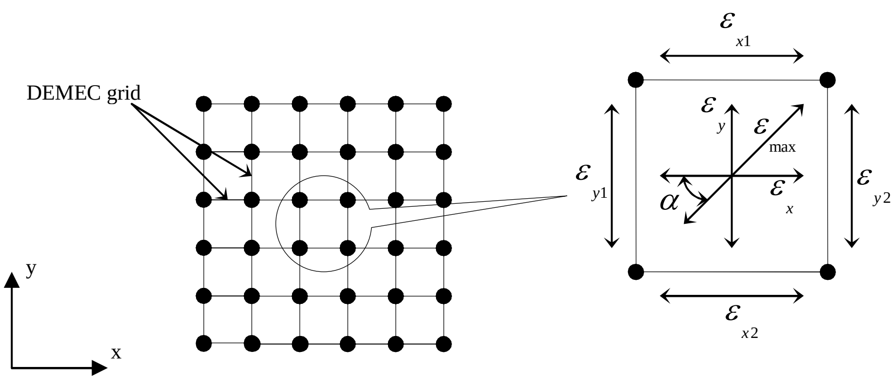


**Figure 20:** Determination of the principal strains

## 2.3- RESULTS

The load, deflection, crack location, and surface strain of each specimen were measured at each loading step. A summary of the measurements taken during testing as well as the surface strains is shown in Figure 21 through Figure 29. These graphs were displayed beginning with the cracking stage. Also, the top surface deflection, progression graphs, and the gauges locations have been accompanied to the former graphs.

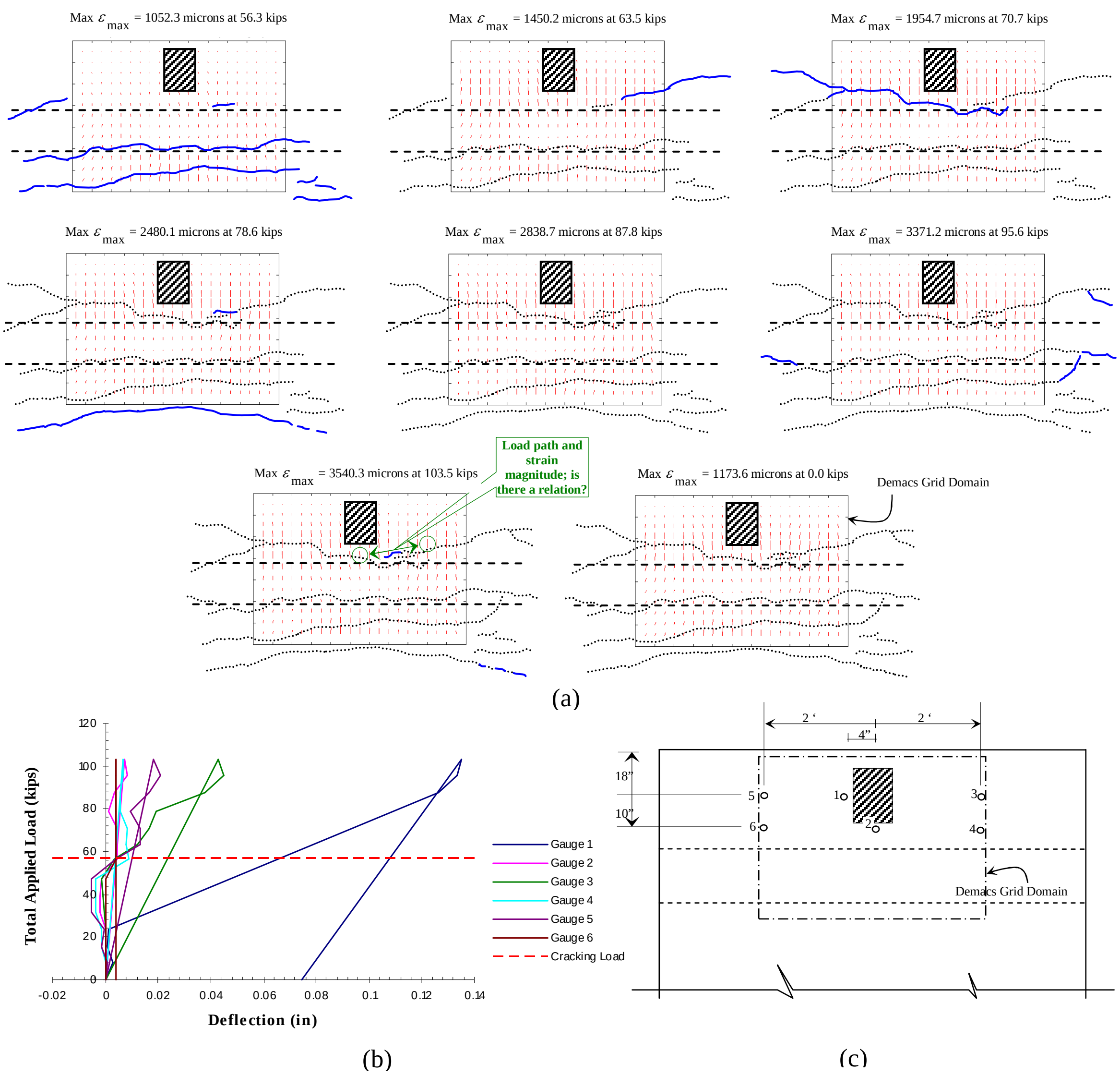


**Figure 21:** 3-ft. Overhang/ Conventional Side/ Center Loading.: a) Top surface cracks progression plots accompanied with maximum principal top surface strains, b) Deflection progress at different loading stages, c) Deflection gauges' locations

***Note:** Failure Load has not been reached*

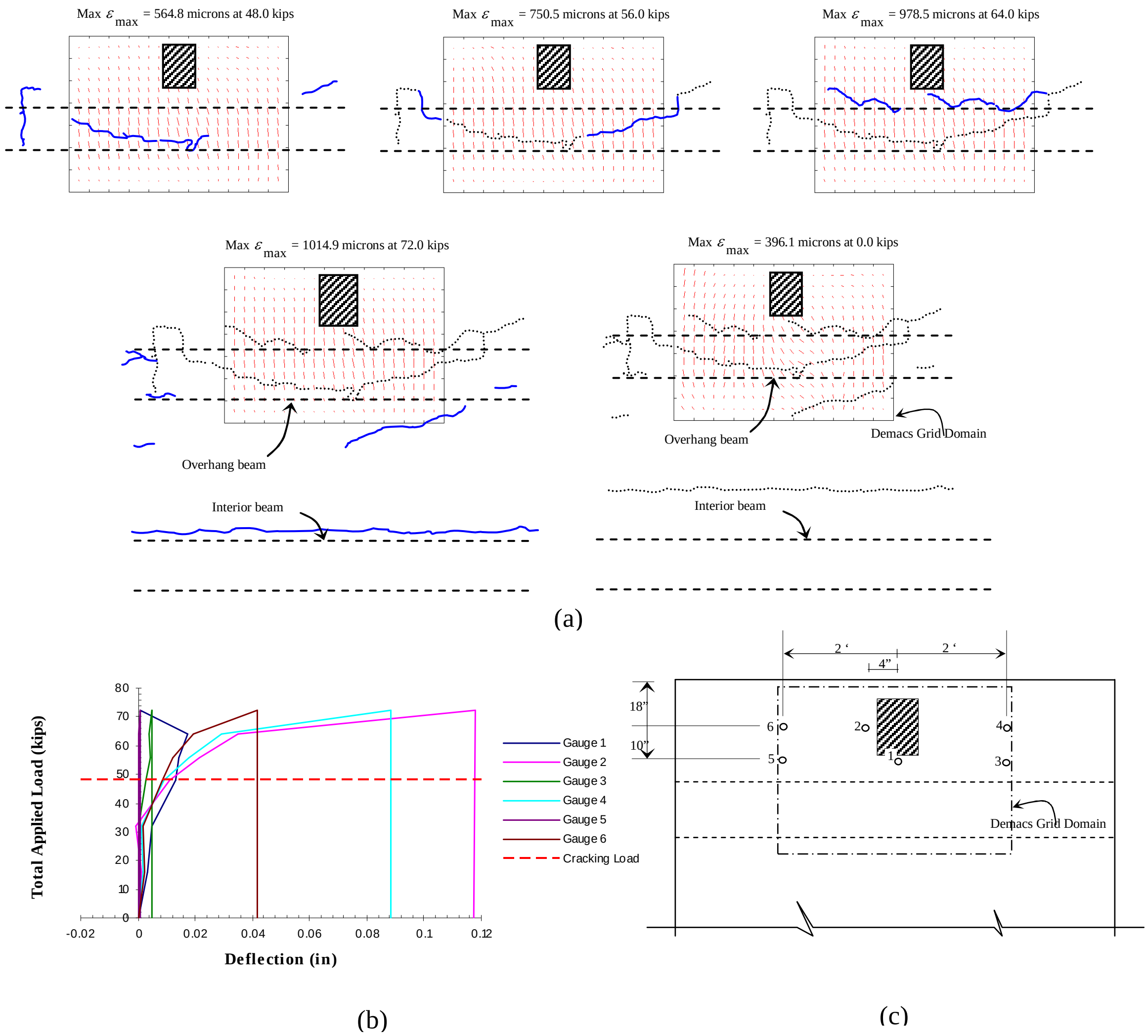


**Figure 22:** 3-ft. Overhang/ Precast Side/ Center Loading: a) Top surface cracks progression plots accompanied with maximum principal top surface strains, b) Deflection progress at different loading stages, c) Deflection gauges' locations

***Note:*** *Failure Load has not been reached*

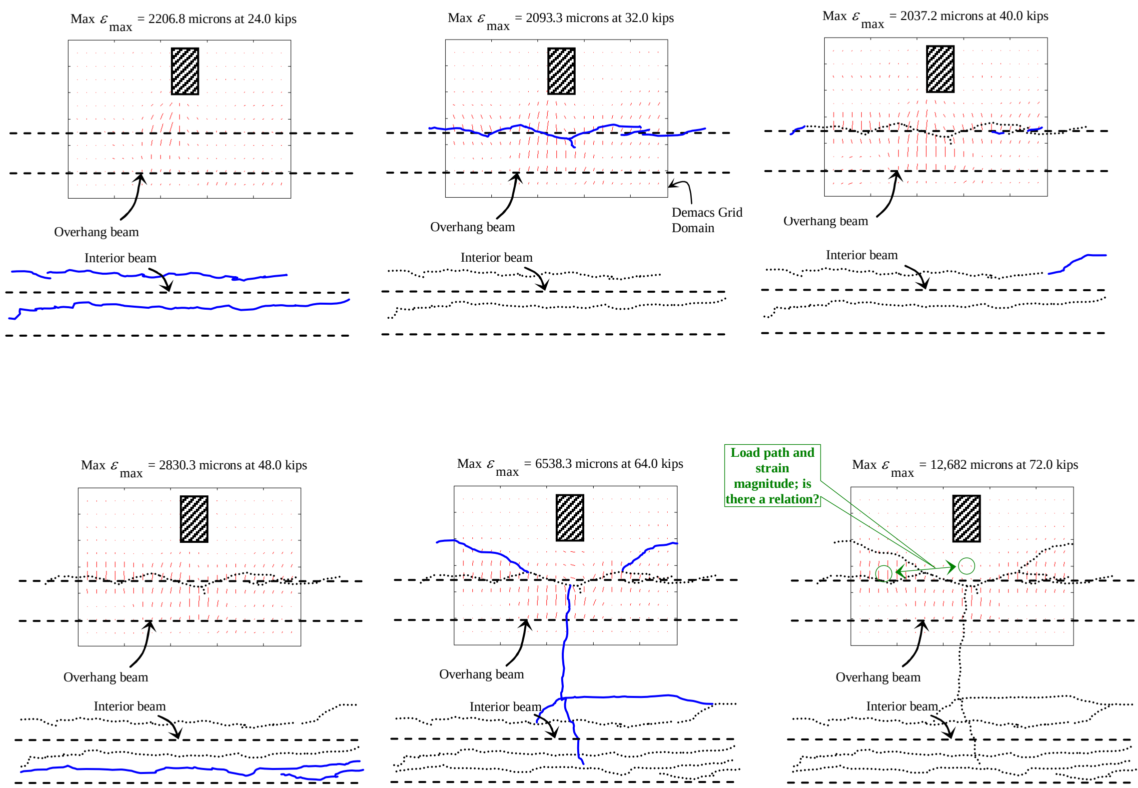


(a)

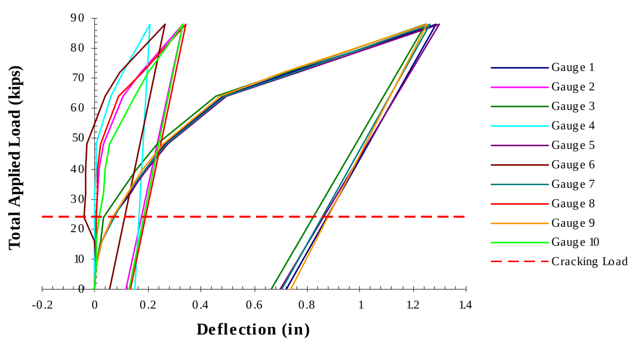


(b)

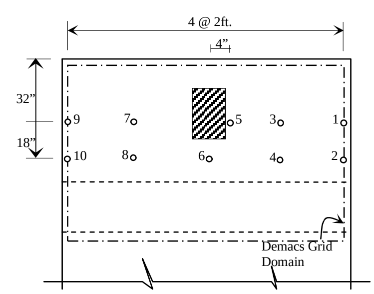


(c)

**Figure 23:** 5-ft. Overhang/ Conventional Side/ Center Loading: a) Top surface cracks progression plots accompanied with maximum principal top surface strains, b) Deflection progress at different loading stages, c) Deflection gauges' locations

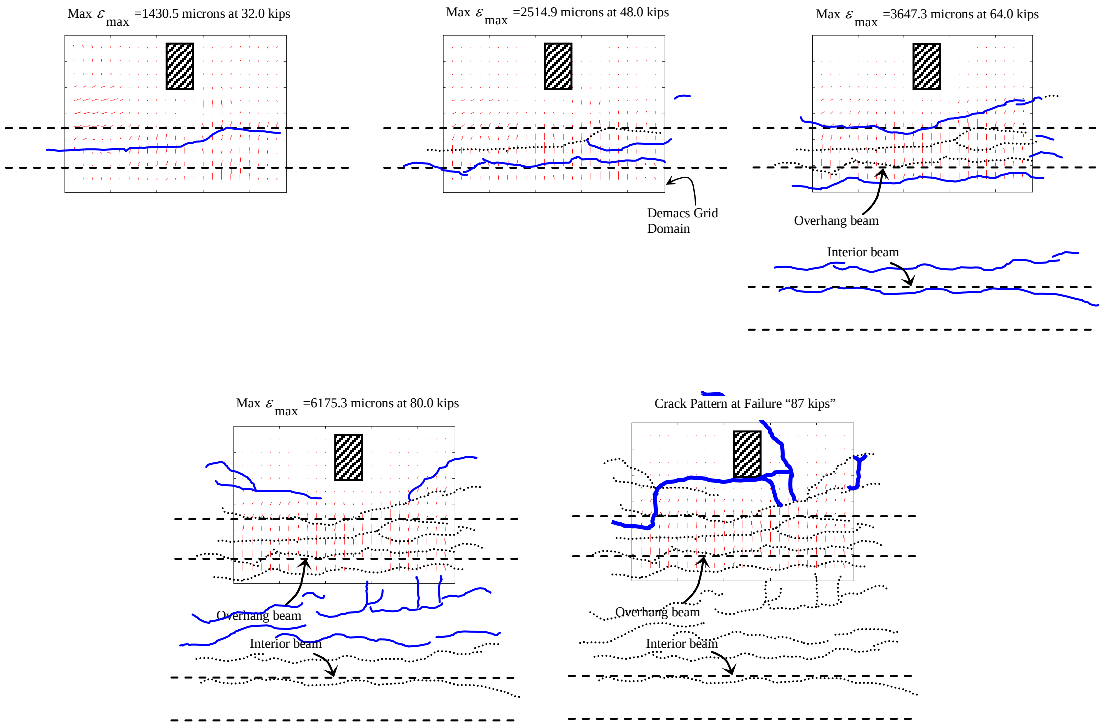


(a)

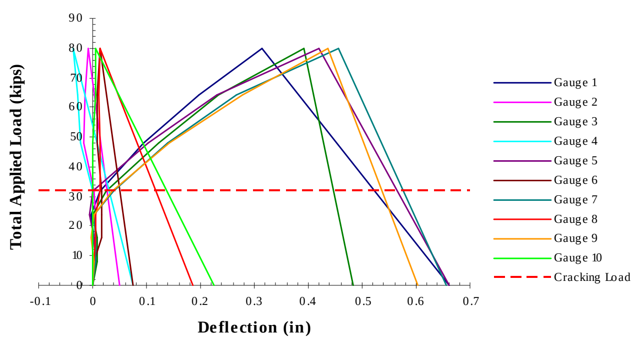


(b)

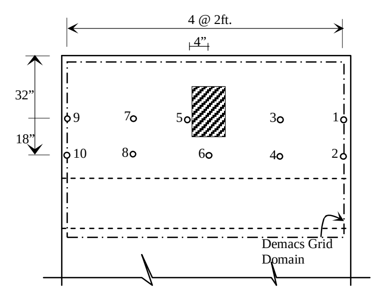


(c)

**Figure 24:** 5-ft. Overhang/ Precast Side/ Center Loading: a) Top surface cracks progression plots accompanied with maximum principal top surface strains, b) Deflection progress at different loading stages, c) Deflection gauges' locations

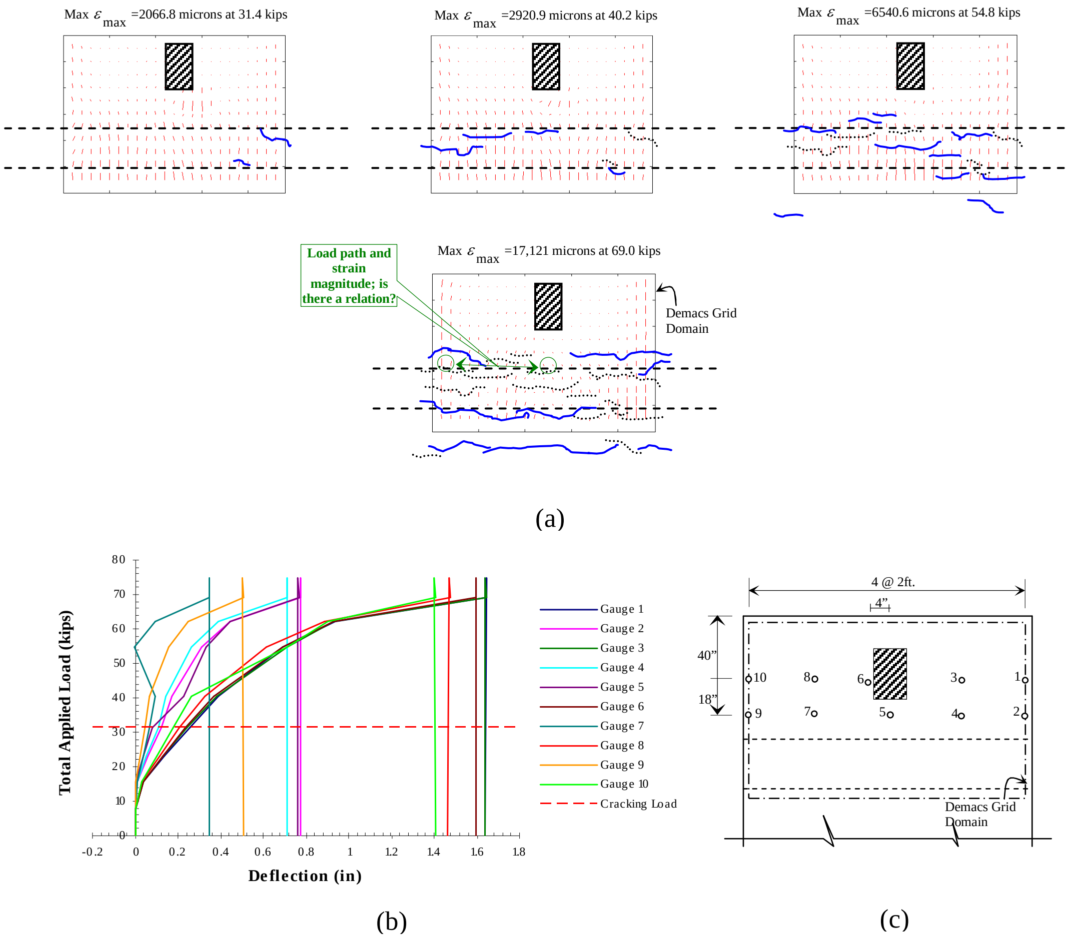


**Figure 25:** 5ft.-8in. Overhang/ Precast Side/ Center Loading: a) Top surface cracks progression plots accompanied with maximum principal top surface strains, b) Deflection progress at different loading stages, c) Deflection gauges' locations

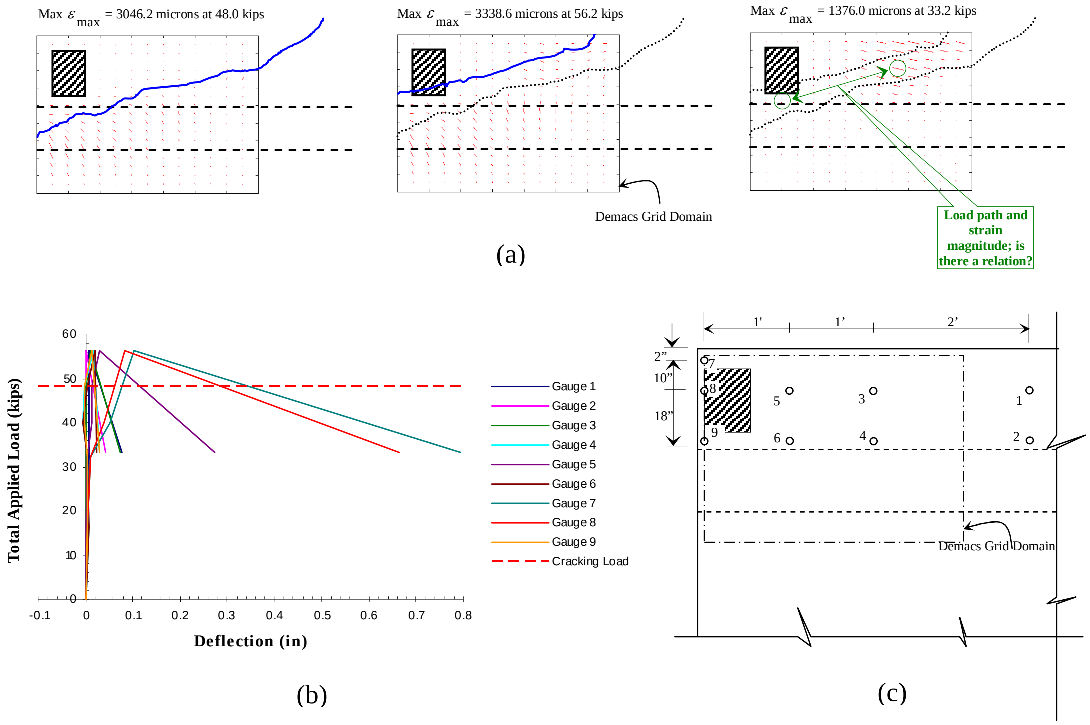


**Figure 26:** 3-ft. Overhang/ Conventional Side/ Corner Loading: a) Top surface cracks progression plots accompanied with maximum principal top surface strains, b) Deflection progress at different loading stages, c) Deflection gauges' locations

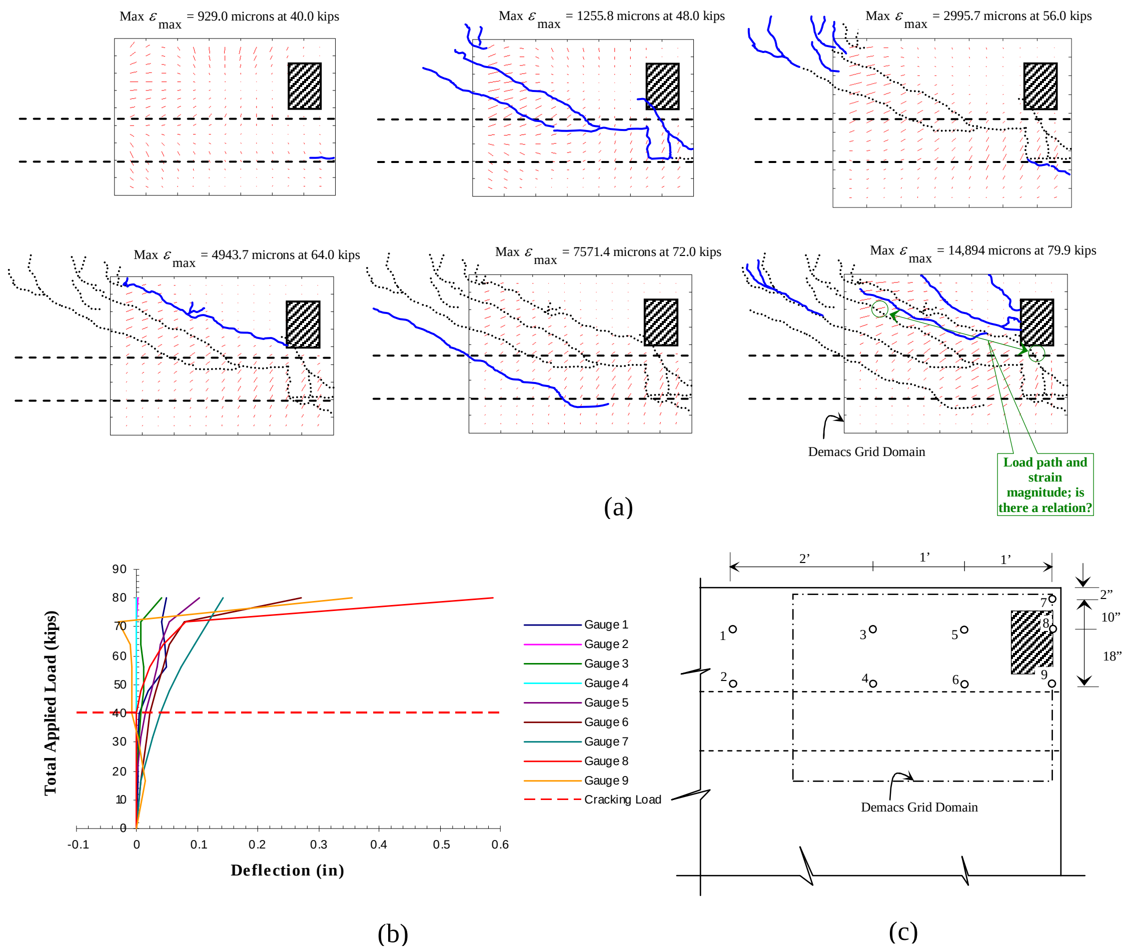


**Figure 27:** 3-ft. Overhang/ Precast Side/ Corner Loading: a) Top surface cracks progression plots accompanied with maximum principal top surface strains, b) Deflection progress at different loading stages, c) Deflection gauges' locations

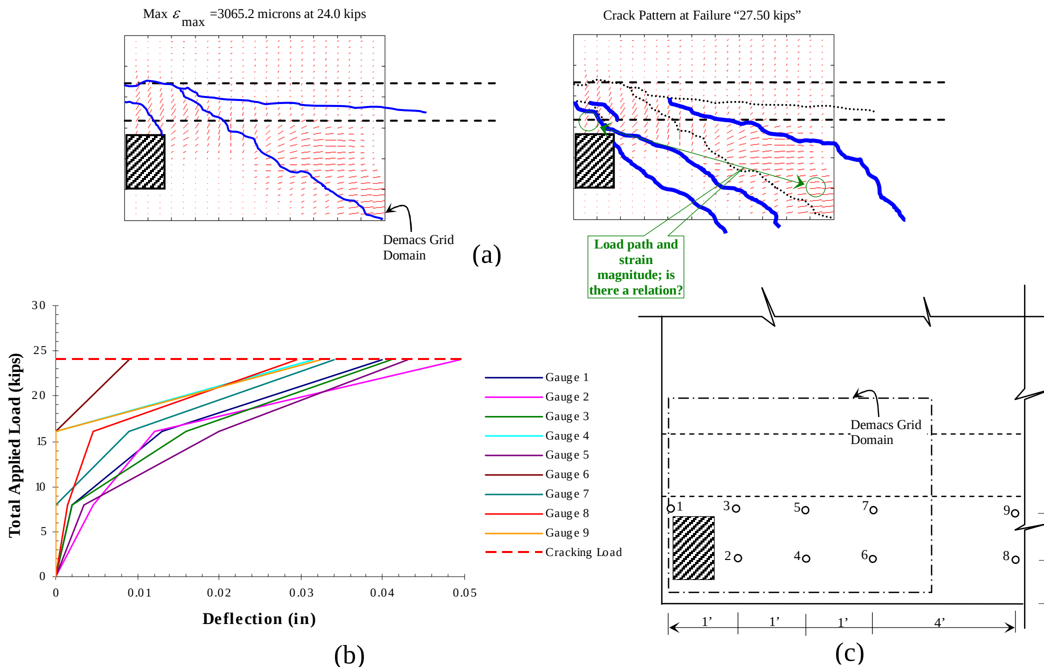


**Figure 28:** 5-ft. Overhang/ Conventional Side/ Corner Loading: a) Top surface cracks progression plots accompanied with maximum principal top surface strains, b) Deflection progress at different loading stages, c) Deflection gauges' locations

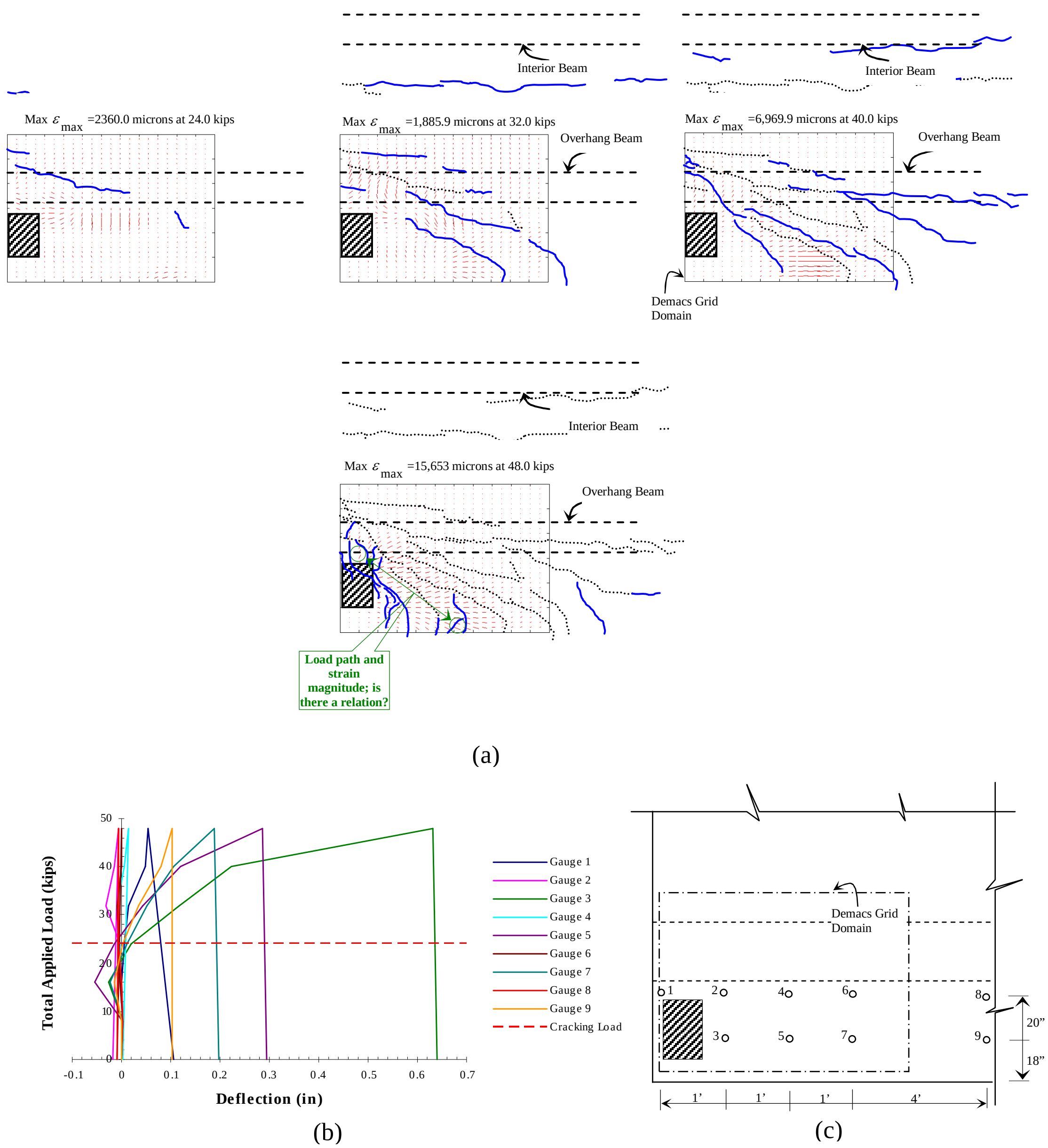


**Figure 29:** 5-ft. Overhang/ Precast Side/ Corner Loading: a) Top surface cracks progression plots accompanied with maximum principal top surface strains, b) Deflection progress at different loading stages, c) Deflection gauges’ locations

Comparisons of each overhang type, conventional and precast, for both overhang lengths, 3 ft. and 5 ft, have also been made via plotting the deflection progress at locations having maximum magnitudes. The same is applied for the top surface strains. Cracking loads have also been included as a reference. See Figures 30 and 31.

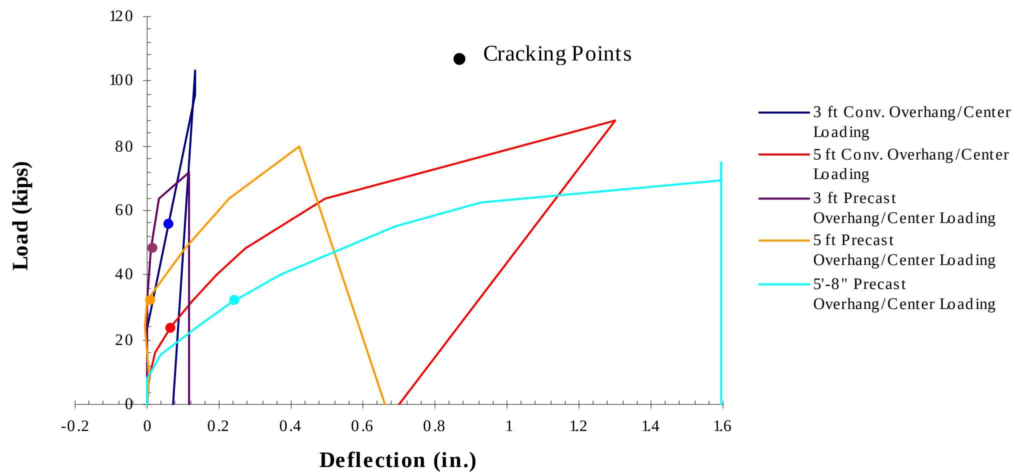


(a)

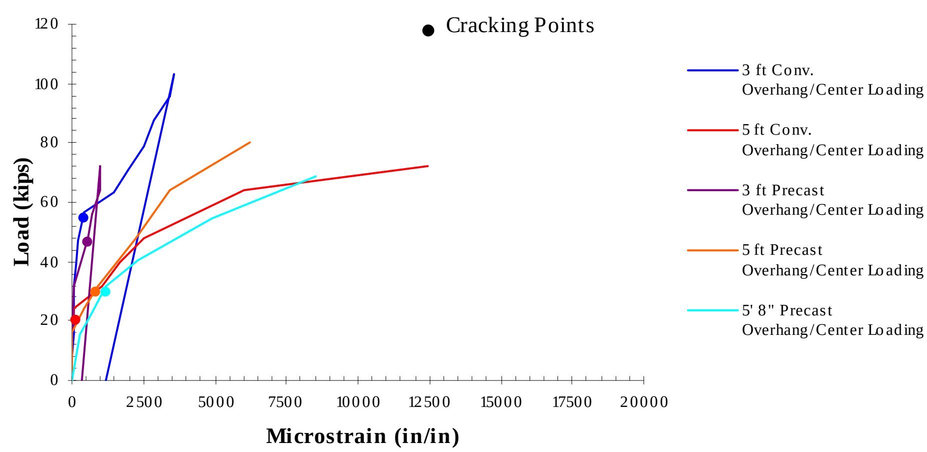


(b)

**Figure 30:** Center Loading: Comparison of a) Maximum Top Surface Deflections Progression, and b) Top Surface Strains for DEMECs Maximally influenced

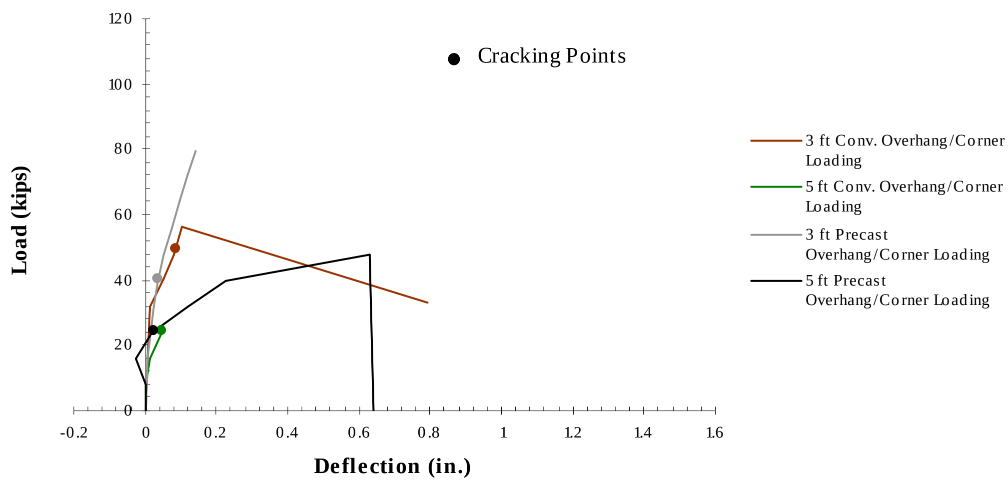


(a)

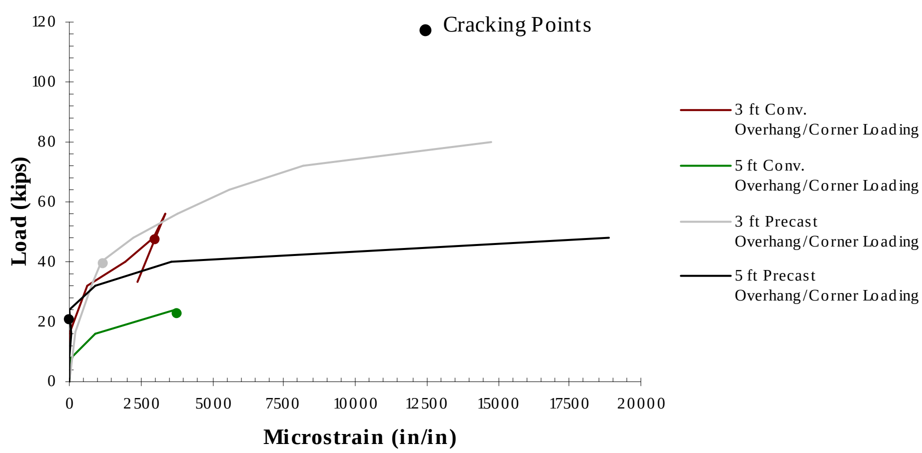


(b)

**Figure 31:** Corner Loading: Comparison of a) Maximum Top Surface Deflections Progression, and b) Top Surface Strains for DEMECs Maximally influenced

Considering the AASHTO's 16 kips design load as a reference, Table 3, Table 4, and Table 5 highlight the performance of all test specimens. Also, Figure 32 provides some sample photos for two of the test specimens after failure.

**Table 3:** AASHTO LRFD 2007 limit states for tested specimens.

| Check | Limit state | AASHTO LRFD 2007 Section |
|---|---|---|
| **Service limit state** | Deflection should be > L/1200 | 9.5.2 |
| **Fatigue and Fracture Limit state** | N.A | 9.5.3 |
| **Strength limit state** | First crack loading should be > 16 kips (service load) | 9.5.4 |

**Table 4:** Performance of Test Specimens (Loads and strains).

| **Specimen** | **Construction Type** | **Performance** | | | | | | | | **Remarks** |
|---|---|---|---|---|---|---|---|---|---|---|
| | | At Cracking | | | | At Failure | | | | |
| | | Load ((kips) | Ratio to AASHTO Design Load | Max. Defln. (in) | Max. Max. Surface Strain (x $10^{-6}$) (in/in) | Load, (kips) | Ratio to AASHTO Design Load | Max. Defln. (in) | Max. Max. Surface Strain (x $10^{-6}$) (in/in) | |
| **3' Overhang Center Loading** | *Conventional* | 56.3 | 3.5 | 0.093 | 1052.3 | 104 | 6.5 | 0.135 | 3540.3 | Failure loads have not been reached |
| | *Precast* | 48.0 | 3.0 | 0.011 | 564.8 | 72.0 | 4.5 | 0.118 | 1014.9 | |
| **5' Overhang Center Loading** | *Conventional* | 24.0 | 1.5 | 0.068 | 2206.8 | 72.0 | 4.5 | 1.300 | 12,682 | |
| | *Precast* | 32.0 | 2.0 | 0.001 | 1430.5 | 87.0 | 5.4 | 0.662 | 6175.3 | |
| **5'-8" Overhang Center Loading** | *Precast* | 31.4 | 2.0 | 0.235 | 2066.8 | 69.0 | 4.3 | 1.596 | 17,121 | |
| **3' Overhang Corner Loading** | *Conventional* | 48.0 | 3.0 | 0.078 | 3046.2 | 56.2 | 3.5 | 0.794 | 3338.6 | |
| | *Precast* | 40.0 | 2.5 | 0.038 | 929.0 | 79.9 | 5.0 | 0.143 | 14,894 | |
| **5' Overhang Corner Loading** | *Conventional* | 24.0 | 1.5 | 0.050 | 3065.2 | 27.5 | 1.7 | 0.050 | --- | |
| | *Precast* | 24.0 | 1.5 | 0.021 | 2360.0 | 48.0 | 3.0 | 0.641 | 15,653 | |

**Table 5:** Performance of Test Specimens (Deflections).

| **Specimen** | **Construction Type** | **Max. deflection at service load (in)** | **Max. deflection at max. applied load (in)** | **Deflection limit state at service load (in)** | **Remarks** |
|---|---|---|---|---|---|
| **3' Overhang Center Loading** | *Conventional* | 0.0925 | 0.1350 | 0.03 | |
| | *Precast* | 0.0110 | 0.118 | 0.03 | |
| **5' Overhang Center Loading** | *Conventional* | 0.0675 | 1.2995 | 0.05 | |
| | *Precast* | 0.0390 | 0.6565 | 0.05 | |
| **5'-8" Overhang Center Loading** | *Precast* | 0.2345 | 1.596 | 0.05 | |
| **3' Overhang Corner Loading** | *Conventional* | 0.078 | 0.7940 | 0.03 | |
| | *Precast* | 0.0375 | 0.1425 | 0.03 | |
| **5' Overhang Corner Loading** | *Conventional* | 0.0495 | 0.0495 | 0.05 | |
| | *Precast* | 0.0210 | 0.6300 | 0.05 | |

**Figure 32:** Sample photos for failures after testing.

## 2.4- DISCUSSION

All specimens that were loaded to failure developed a failure surface around the concentrated loads and failed in punching shear except the 5’-8” precast overhang and the 5’ conventional overhang with center loading which failed in flexure. The specimens that failed in punching shear failed in a brittle manner; however, all of the bridge decks failed at loads much higher than the design loads. It should be noted that the failure loads were not reached in the 3’ specimens with center loading because of the limitations of the rams. However the 3’ specimens provided a significant safety factor when compared to the design loads, a minimum of 2.5 for corner loading at cracking. In each of the specimens flexural cracks developed for all tests on the top surface at the external support beam, refer to Figure 21.a through Figure 29.a, (cracks along the longitudinal direction). Such cracks increased their widths during the test, reaching at failure values between 0.013” and 0.215”. The following observations can be made:

- When comparing the performance of each specimen to the 16 kip AASHTO design load satisfactory performances were obtained. A minimum factor of safety of 4.3 was obtained for center loading, and a minimum of 1.7 against failure for the corner loading.
- As shown in Table 4, the precast overhang system has a consistently higher ultimate strength than the conventional overhang specimens but similar cracking loads.
- Generally, losses of stiffness for the 5’ overhangs are faster than those of the ones that are 3’. This can be seen by looking at the maximum deflections in
- Figure 30.a and Figure 31.a. This is expected as the longer cantilevers have a lower amount of stiffness. For the corner loaded specimens this means that the increase in the cantilever length is more significant than the increase in load transfer area. The cracking of the two systems at the surface of the exterior beam was quite different. This performance can be seen in Figure 21 to Figure 29. In the conventional overhang system cracks were observed at the interface between the beam and deck, while the precast overhang system showed cracking at several locations over the top of the beam. This difference in behavior is likely

attributable to the presence of a continuous prestressed panel in for the precast overhang system.

- For a given load, the cracking of the precast overhang system was much more distributed than the conventional overhang system as shown in Figure 21 to Figure 29. This dispersion of cracks should lead to cracks that are smaller in size. Surface strain measurements shown in
- Figure **30**.b and Figure 31.b also reinforce this same observation as the maximum surface strains are lower for the precast systems when compared to the conventional overhangs. This made it possible to reduce surface strain by an average of 23% prior to failure stages. As a result, the expected average crack widths should also be 23% smaller therefore providing an increased durability of bridge decks for the same loading conditions.
- It was observed in the testing that the location of the maximum principal strains were not necessarily within the expected load path from the load point to the support beam. This can seen by observing the low levels of surface strains between the load point and the support beam in Figure 21.a, Figure 23.a, Figure 25.a, Figure 26.a, Figure 27.a, Figure 28.a, and Figure 29.a. This is due to the fact that surface strains are more related to, and directly affected by deformations rather than loads that were present in these instances. As might be observed, the only exceptions are the centrally loaded precast sides for the 3' and 5' overhangs. Presence of prestressing with the available load symmetry led to these two exceptions.
- In Figures 30 and 31, it can be observed that the CIP specimens showed the greatest increase in surface strain and deflection magnitudes when compared to their precast companions. This suggests that the precast system is stiffer and should exhibit less cracking for the same amount of exterior load. The deflection for both systems under the load cases tested were much lower than the AASHTO limit for serviceability, see Table 5.

This research investigated only static loading. Based on the significant reserve capacity of the specimens it would be expected for the system to show satisfactory fatigue performance based on service load levels. This is further supported by AASHTO LRFD 2007 section 9.5.3 which states it is not necessary to investigate the failure of concrete bridge decks under fatigue loading.

## 2.5- CONCLUSIONS

The research performed in this study evaluated the performance of the precast, prestressed full-depth bridge overhang system. Three overhang lengths were tested; 3', 5', and 5'-8" under center and corner loading. The findings are:

- All specimens provided significant safety factors when comparing the service loading specified to AASHTO to the cracking and ultimate loads. A minimum factor of safety of 1.5 for cracking, and 3.0 at ultimate were both obtained for the 5' overhang loaded at corner.
- A punching shear failure was observed in all specimens tested except for the 5' cast-in-place overhang and 5'-8" precast overhang with center loading which showed a flexural failure mode.
- The precast overhang specimens showed the ability to allow a much greater dispersion of cracks when compared to the cast-in-place overhangs. This was reflected in the reduction in surface strains by an average of 23% between the two systems when compared at the same loading conditions. This reduction in surface strain must lead to a similar reduction in crack sizes.

In conclusion the study recommends implementation of the 5' precast overhang system as it showed satisfactory performance from the center and corner loading under service and ultimate load states.

# CHAPTER III

# III. USE OF WELDED REBAR MATS FOR BRIDGE DECK CONSTRUCTION

## 3.1- INTRODUCTION

Past research indicates that concrete bridge decks that use flexural design methods show significant safety factors against failure. This was first noticed in testing by the Ontario Ministry of Transportation(21). This research pointed out that bridge decks of typical dimensions did not fail due to flexure, but instead showed a significant amount of load caring capacity after flexural yielding of the reinforcing steel and then failed suddenly due to punching shear. Similar load testing has been completed with bridge decks that use stay in place partial depth bridge panels, and capacities similar to bridge decks with mild reinforcing steel were observed(11,12,13,14). The arching action capacity is used in the AASHTO LRFD Design Manual (2007)(22) with the bridge deck direct design method, which has lead to a significant reduction in the amount of reinforcing steel in bridge decks.

Past research has shown that bridge decks are able to provide significant safety factors against failure; however, they continue to show serviceability problems in the field. These problems result from cracks in a bridge deck that expose the reinforcing steel and concrete to outside chemicals, which ultimately cause durability problems. These cracks are typically largest in the negative moment region over the beams as this area has the greatest tension on the bridge deck surface from typical loading. Because of this, it seems that the primary role of bridge deck reinforcing steel is to minimize the surface cracks and keep the cracks that do form as small as possible in order to promote a long service life.

Typically, the reinforcement for a bridge deck consists of tied reinforcing bars. While bridge decks with these bars have been used satisfactorily for years, the research team feels that the performance of these bridge decks could be improved if pre welded rebar mats were substituted for these bars. Some of these advantages include:

- Rebar mats can be pre-constructed by a machine and then shipped to the jobsite thus minimizing labor and increasing construction speed
- Mats with a similar density to current reinforcing designs can be used in the areas of high tension and lighter mats can be used in the temperature and shrinkage areas; this will allow for a reduction in the amount of required steel
- Since the mats are constructed with a machine, closely spaced reinforcing bars with smaller diameters could be used that would not be economical to place by hand
- Close bar spacing provides superior crack control over rebar of the same weight per foot that uses bars with a larger diameter and spacing
- This ability to improve crack control provides opportunities for a greater tolerance on the clear covers of bridge decks, which will result in improved constructability of the bridge deck

One primary challenge in constructing a bridge deck is to insure that a minimum amount of clear cover is uniformly provided over the reinforcing steel. It is common for construction crews to make significant adjustments to the reinforcing steel height during construction to insure that this specified amount of clear cover is provided at all locations. If a bridge deck was allowed to have a greater clear cover than what was specified then this would increase its constructability and lower the cost. One challenge with increasing the clear cover of the reinforcing steel is that the size of the surface cracking may increase. However, by using a rebar mat to economically use a tighter spacing of reinforcing bars, cracking can be controlled, which allows for an improvement in the constructability with an increased cover tolerance or an increase in the durability by using a similar clear cover.

## 3.2- EXPERIMENTAL METHODS

It was realized early in this research that it would be challenging to accurately simulate the long term performance of a bridge deck in the laboratory. Because of this it was decided that a standard test setup would be used to compare the performance of different structural systems to load applied by hydraulic jacks and examine their cracking and ultimate strength. While measuring the response of these structures to loading from external load does not replicate how a bridge deck will perform in the field, this loading can still be a useful method to compare the performance of two different reinforcing layouts as long as similar testing is completed on representative control specimens. If a specimen showed improved or equivalent performance in the testing program under external loading then it would be expected to show similar performance when implemented in the field.

In this project three control bridge decks were used for comparison purposes to the bridges that used rebar mats. These control bridge decks included:

- 8” partial precast bridge deck that uses a 4” precast panel and 4” of cast in place concrete with no steel in the cast in place concrete as shown in Figure 38, specimen A.
- 8” partial precast bridge deck that uses a 4” precast panel and 4” of cast in place concrete with #5 bars at 6” transversely and #4 bars at 9” longitudinally for the top layer of steel with 2” of clear cover with a 4” stay in place precast panel as shown in Figure 38, specimen B. (standard TxDOT design)
- 8” cast in place bridge deck with a top layer of #4 bars at 12” in both directions with 2” of clear cover and a bottom layer of reinforcing steel with #5 bars at 12” in both directions with 1” of clear cover as shown in Figure 38, specimen C. (standard AASHTO Direct Design Method)

These control specimens were chosen to provide a benchmark for the testing of two different styles of bridge deck design, and an extreme case of using no reinforcing steel in the top layer of the partial precast bridge deck. These control specimens allow for a direct comparison of the cracking, surface strains, and ultimate load with the test methods used and bridge decks that use pre-constructed rebar mats with different covers.

It is the goal of this project to use the rebar mats to develop a bridge deck system that either provides a reduction in cracking with similar covers or equivalent cracking at increased covers.

### 3.2.1- Test Setup

To investigate the performance of these systems the test setup shown in Figure 33 was used. Different deck thicknesses with different reinforcement arrangements were investigated as well, see Figure 38. This load setup uses a three support beam system with two large point loads symmetrically placed over the center beam. A spacing of 6' between the load points was used as this matched the transverse wheel spacing of an AASHTO HL 93 truck axle. The load areas used for the testing were 10" x 20" AASHTO tire patches. A beam spacing of 8' was used for the testing. This beam spacing was chosen as it was a reasonable spacing for a typical DOT bridge deck and could be tested with the available strong floor space. If a larger beam spacing was used then the ultimate loads in the testing may be decreased but the relative ultimate strengths and surface cracking of the different systems should still be similar. The width of the specimen was 8'. This was chosen as it was the dimension of a standard precast panel.

When constructing the load transfer area between the external beams and the bridge deck a construction detail was used where the precast panels were extended until about the beam centerline and then a plastic sheet was used between the panel and the concrete below. This was done to minimize the moment or horizontal load transfer between the bridge deck and the outside support beams. This simplifies the system to behave as if it is a two span structure that is continuous over the center support. The layout for the rebar mats used for the testing in this research is shown in

Figure 33.b, Figure 34, and Figure 35. As shown in Figure 34, a heavier rebar mat was used over the beams and a lighter mat was used in the areas between the beams. Figure 35 shows a finger splice detail that was used between the two mats. Figure 36 shows how the finger splices between four adjacent mats. This detail was chosen as it provides a full transfer of loads at the lap for the bars used. This detail also minimizes the amount of overlap of the rebar mats, improves the constructability, and economy of the system.

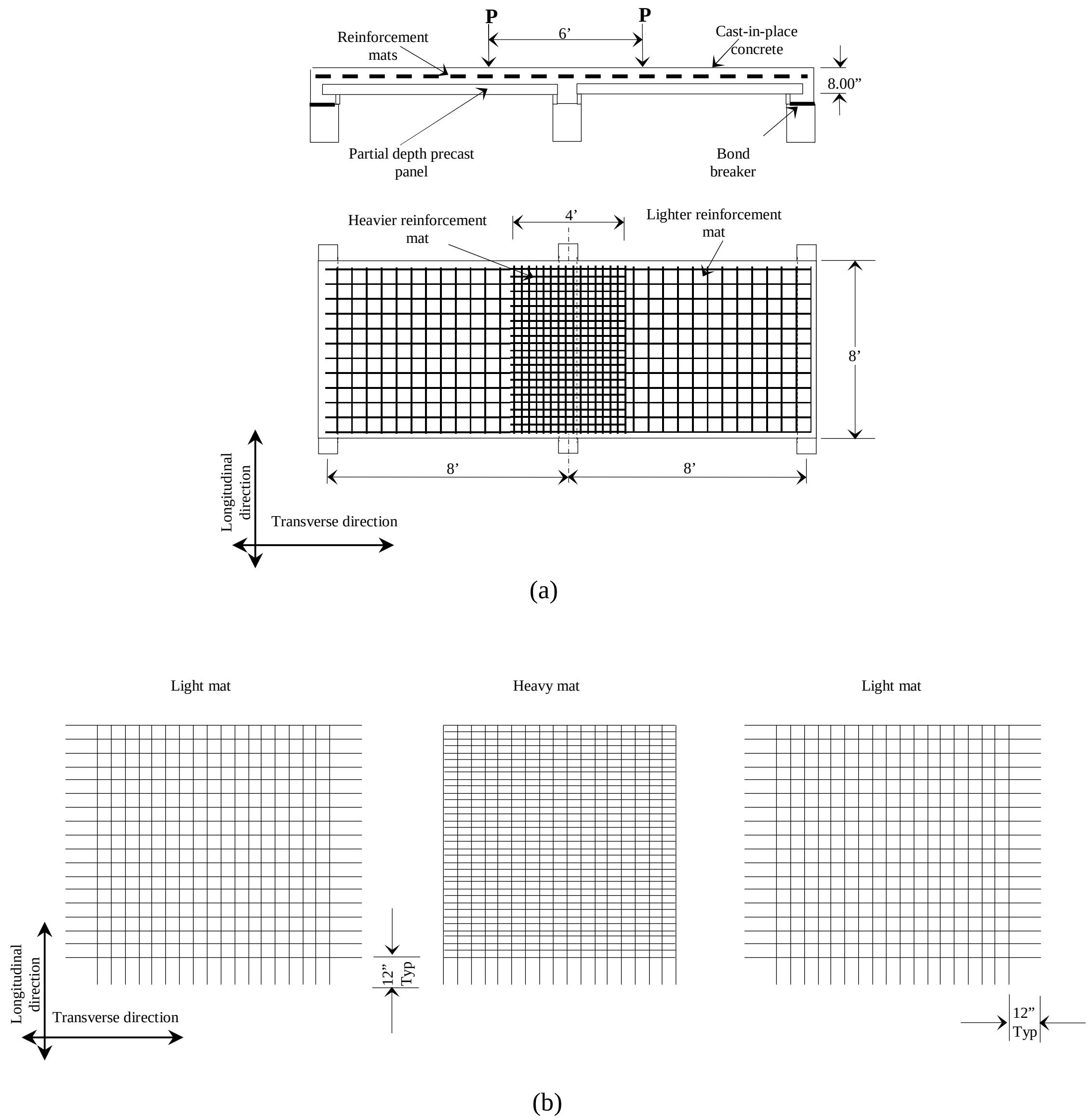


**Figure 33:** a) Loading Setup for Bridge Deck, b) Rebar mat overview showing the splice detail used in the testing.

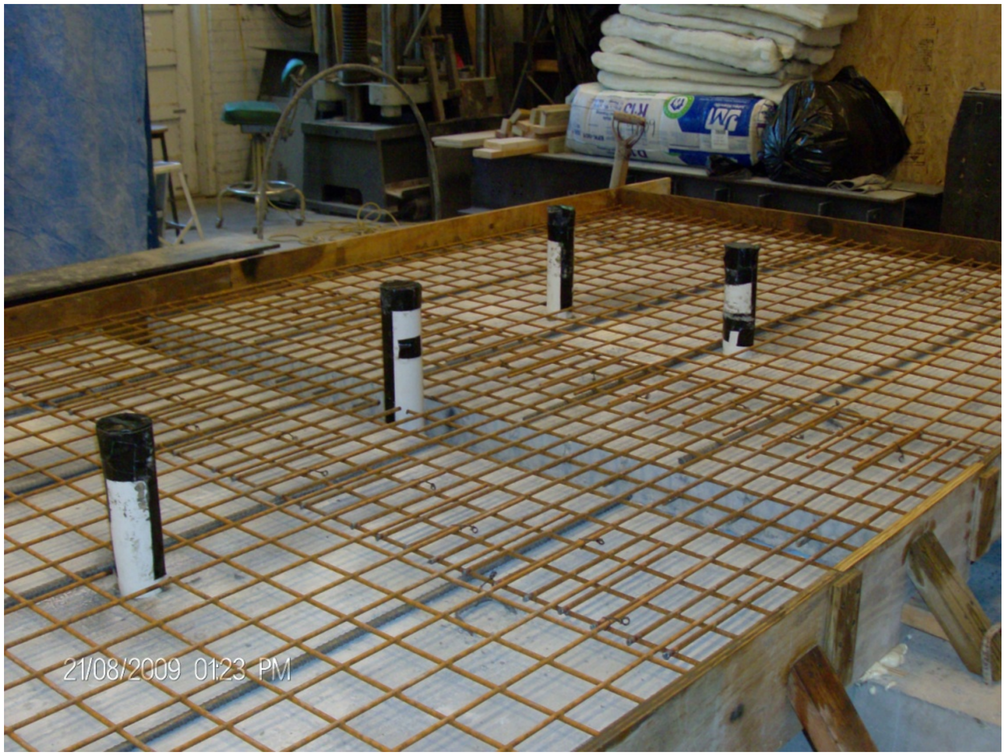


**Figure 34:** Rebar mat layout in specimen that used #5 bars as chairs. Note the heaver rebar mesh used over the interior beam.

The width of the rebar mat over the beam was chosen to be 25% of the adjacent span length plus the width of the beam. This was chosen based on a beam analysis of an HL 93 design truck that was systematically moved over the surface of the bridge deck while inspecting the locations of the inflection point. The controlling load case was a three beam bridge with a HL 93 truck centered in one span. The negative moment in the non loaded span was small enough at 25% of the span length that the design moment would be lower than the cracking moment and so only temperature and shrinkage steel could be used.

The lighter rebar mat that was used between the beams was chosen to satisfy the temperature and shrinkage steel requirements. Since this area would always be expected to be in compression or a low amount of tension under typical loading conditions, then temperature and shrinkage steel could be used. D8 bars at 4” in both directions provided an area of 0.24 $in^2$ per ft were used because they satisfied ACI and AASHTO specifications. This mat size was not modified during this testing. By using a lighter reinforcement mat in the areas between the beams, one can significantly reduce the amount of steel that is used in the top mat of the bridge deck compared to conventional bridge decks that carry the same reinforcing steel across the entire bridge.


**Figure 35:** A splice between the two rebar mats.

The designer should keep in mind that each mat should be designed to weigh around 150 lbs each and should not be wider than 8’ to insure easy shipping. This would allow them to be easily placed by two workers. Also, in order to insure that the mats are not incorrectly switched during the construction the designer should take the needed precautions and specify the mats to be dissimilar sizes. This should not be hard since the mats over the beams will be long and slender and the lighter reinforcement mats are closer to square.

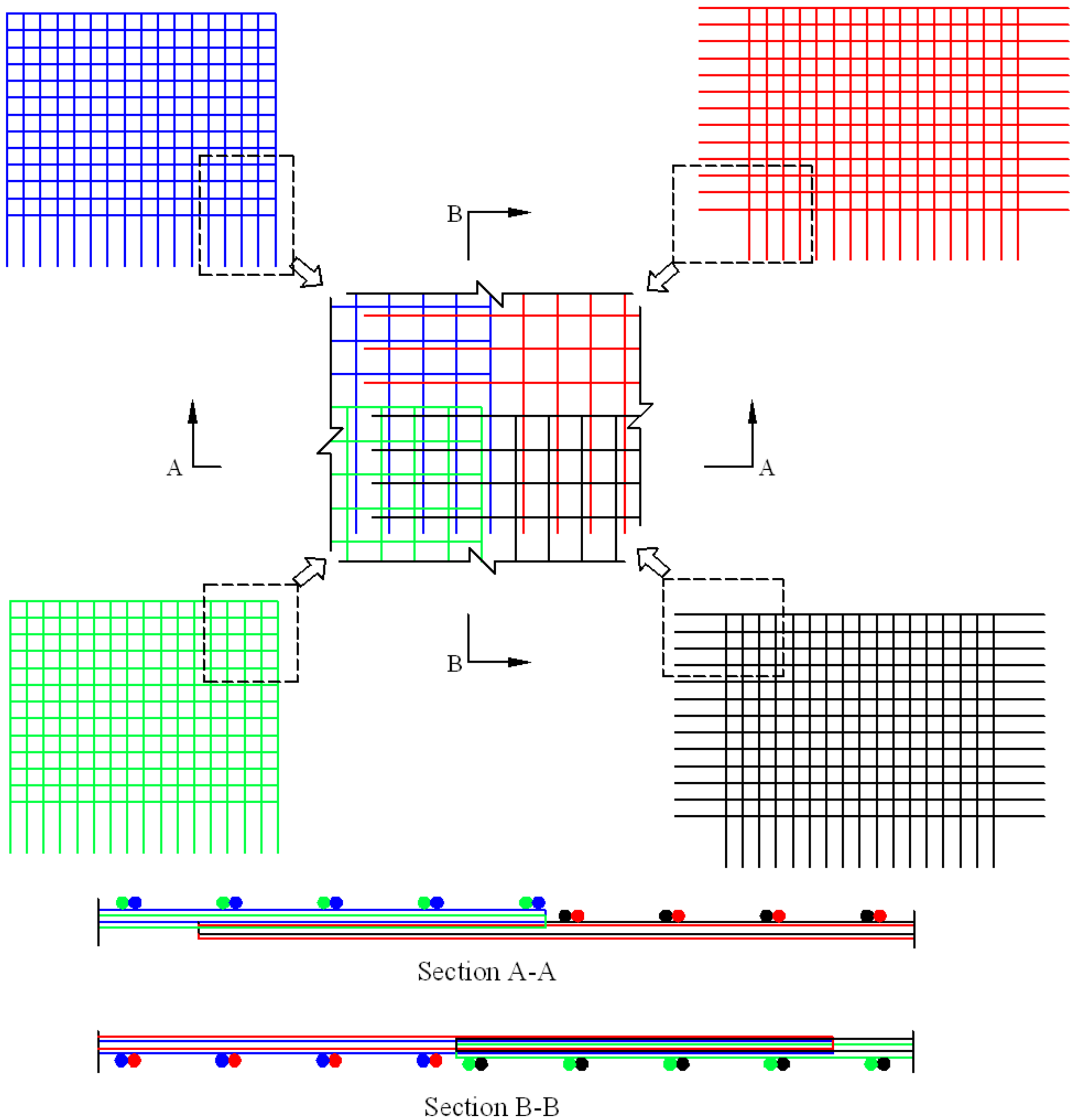


**Figure 36:** Details for a splice between four rebar mats[23]

The instrumentation used to evaluate the performance of the specimens included the measurement of the load, specimen deflection near the load application, crack mapping, and the measurement of the surface strains. These measurements were taken initially and then at discrete load points through the testing. Measurements were typically taken in loading increments of 8 kips per load point, or at a total load of 16 kips until initial cracking was observed. After that load increments of approximately 16 kips per point load, or 32 kips total, were used until failure. After each load step measurements were taken from the instrumentation.

The deflection of the specimen was measured by using six linearly variable displacement transducers (LVDTs) with (0.0005”) accuracy. These measurements were taken at the midspan and quarter points of the specimen. The surface strains of the specimens were measured by using stainless steel targets placed on an 8” rectangular grid and fixed to the surface with epoxy prior to loading. The movement of these targets with load in the longitudinal and transverse direction could be measured by using a portable demec stain gage that used special machined points that match a machined cone shaped void in the stainless steel discs. The accuracy of this system is 4.4 microstrain. This measurement technique has been used by a number of researchers to measure the surface strains of concrete specimens. A typical layout of the DEMEC points is shown in Figure 37. The crack maps for each specimen are shown in Appendix A. This measuring system allowed the research team to economically capture a significant amount of data that will help evaluate the performance of the different specimens.

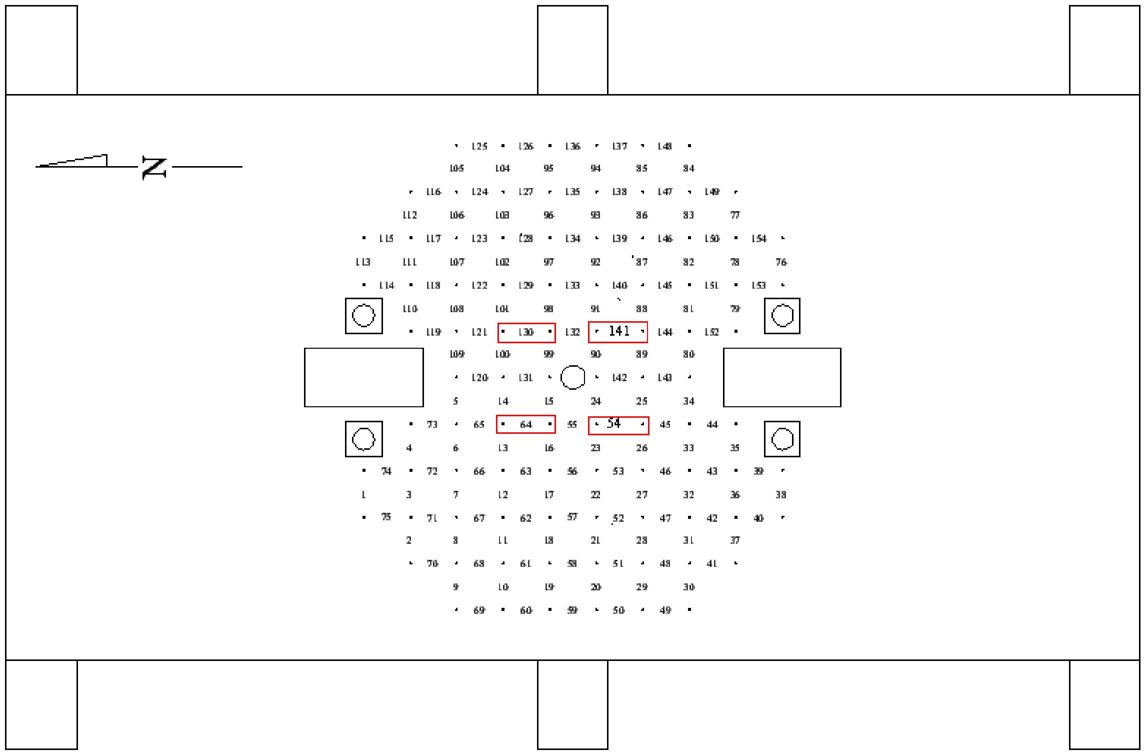

**Figure 37:** A typical demec gauge layout. The locations shown with a red box were the highest strains for the specimens investigated. The average readings from the side that failed were used to compare the performance of the different specimens.

Each specimen was constructed with a typical DOT bridge deck concrete with a 3” slump, 20% fly ash replacement, 0.42 w/cm, ¾” maximum nominal size aggregate, and 5% air content. Although the specified 28 day compressive strength of the concrete was 4,000 psi, the compression strength when evaluated at approximately 7 days for all of the specimens was around 5,500 psi. Based on the research team’s experience with past bridge deck mixtures this would be a typical value for the strength gain of these mixtures. A summary of the measured strengths is presented in Table 6.

All specimens were constructed by using 4” partial depth precast panels with a cast-in-place concrete topping except for specimen B which was entirely cast-in-place. All of the specimens were 8” in depth except for specimen G which was 9”. In specimen A no reinforcement was used in the cast-in-place section. In specimens D and E the density of the transverse reinforcement was varied. In specimens E, F, and G the same density of reinforcement was used at different clear covers. All of the specimen construction details are shown in Figure 38.

**Table 6:** A summary of the concrete specimen test results.

| Specimen | Test | CIP | Precast Panel (Stage II) |
|---|---|---|---|
| A | Compression, psi | 6490 | 10050 |
| | Tension, psi | 540 | 790 |
| B | Compression, psi | 5220 | 10540 |
| | Tension, psi | 410 | 760 |
| C | Compression, psi | 6240 | 10220 |
| | Tension, psi | 380 | 790 |
| D | Compression, psi | 5300 | 10130 |
| | Tension, psi | 430 | 510 |
| E | Compression, psi | 4500 | 10130 |
| | Tension, psi | 510 | 790 |
| F | Compression, psi | 4920 | 10380 |
| | Tension, psi | 380 | 790 |
| G | Compression, psi | 8850 | --- |
| | Tension, psi | 730 | --- |

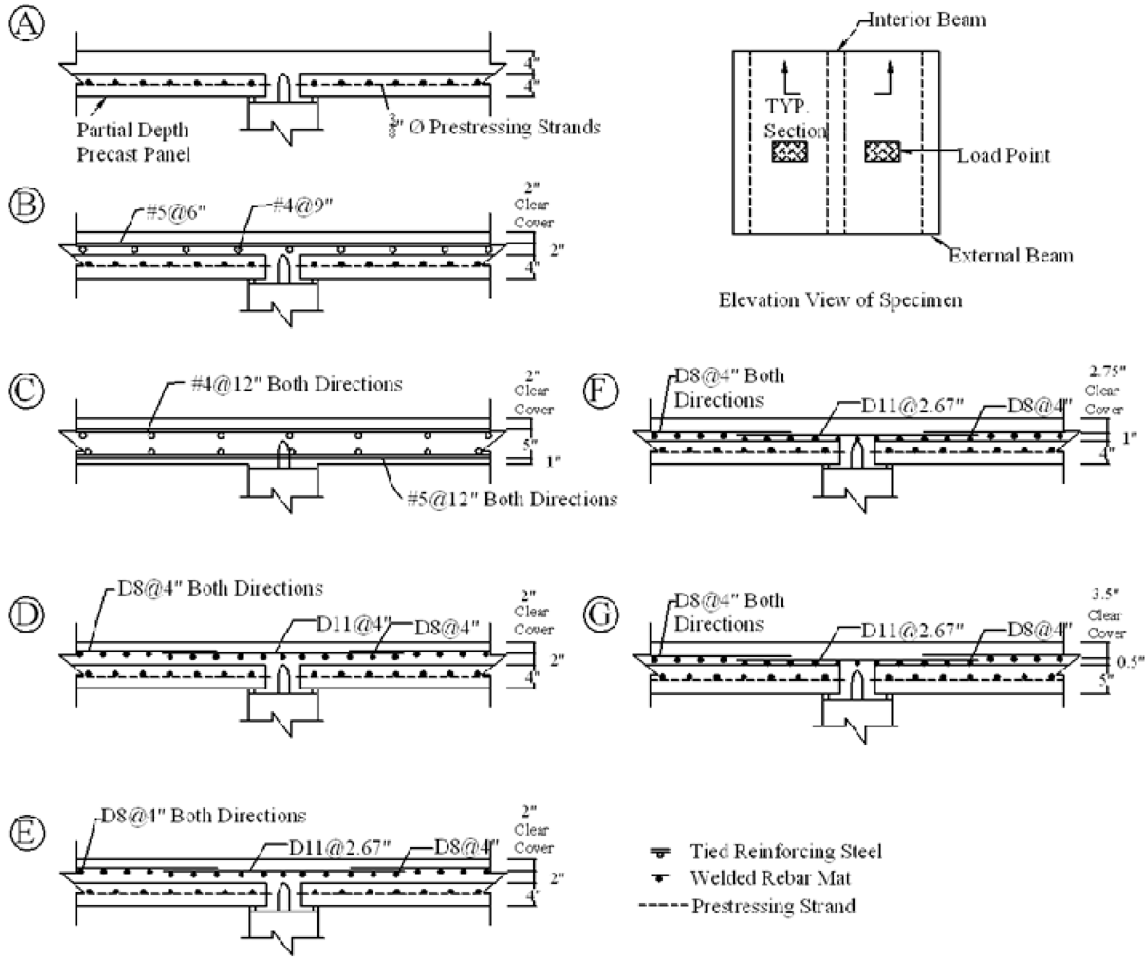


**Figure 38:** A graphical representation of the specimens tested.

## 3.3- RESULTS

An overview of the specimen details and results can be found in Table 7. The results given in Table 7 are for the total load placed on the specimen and so would need to be divided by two to determine the point load applied at each location. The cracking load corresponded to the load at which the first crack was visually observed. All of the specimens failed in either punching shear, a bond failure between the precast panel and the cast in place concrete, or a combination of the two. Some typical failures are shown in Figure 39, Figure 40, and Figure 41.

**Table 7:** A summary of the specimens tested.

| | Construction Type | | | | | Cracking | | Failure | | |
|---|---|---|---|---|---|---|---|---|---|---|
| Specimen Name | Negavite Moment Reinforcement at the Support Beam | | Partial Depth Precast Panel | Clear Cover | Depth | Load | Ratio to AASHTO Design | Load | Ratio to AASHTO Design | Load vs. Strain, Initial slope |
| | transverse | longitudinal | | (in) | (in) | (kips) | | (kips) | | (kips/(in/in)) |
| A | -- | -- | yes | N/A | 8 | 27 | 0.9 | 283 | 8.9 | 82200 |
| B | #5 @ 6" | #4 @ 12" | yes | 2 | 8 | 49 | 1.5 | 279 | 8.7 | 112000 |
| C | #4 @ 12" | #4 @ 12" | no | 2 | 8 | 79 | 2.5 | 212 | 6.6 | 219000 |
| D | D11 @ 4" | D8 @ 4" | yes | 2 | 8 | 36 | 1.1 | 287 | 9.0 | 103000 |
| E | D11 @ 2.67" | D8 @ 4" | yes | 2 | 8 | 49 | 1.5 | 204 | 6.4 | 145000 |
| F | D11 @ 2.67" | D8 @ 4" | yes | 2.75 | 8 | 49 | 1.5 | 215 | 6.7 | 124000 |
| G | D11 @ 2.67" | D8 @ 4" | yes | 3.5 | 9 | 51 | 1.6 | 314 | 9.8 | 92600 |

The load reported is the sum of both load points.
The AASHTO Design Load is 32 kips per axle.


**Figure 39:** A punching shear failure of specimen A.

**Figure 40:** A sliding failure between the precast concrete panel and the cast in place concrete topping for Specimen B (standard TxDOT bridge deck). Note that this failure occurred at 8.7 times the design load.

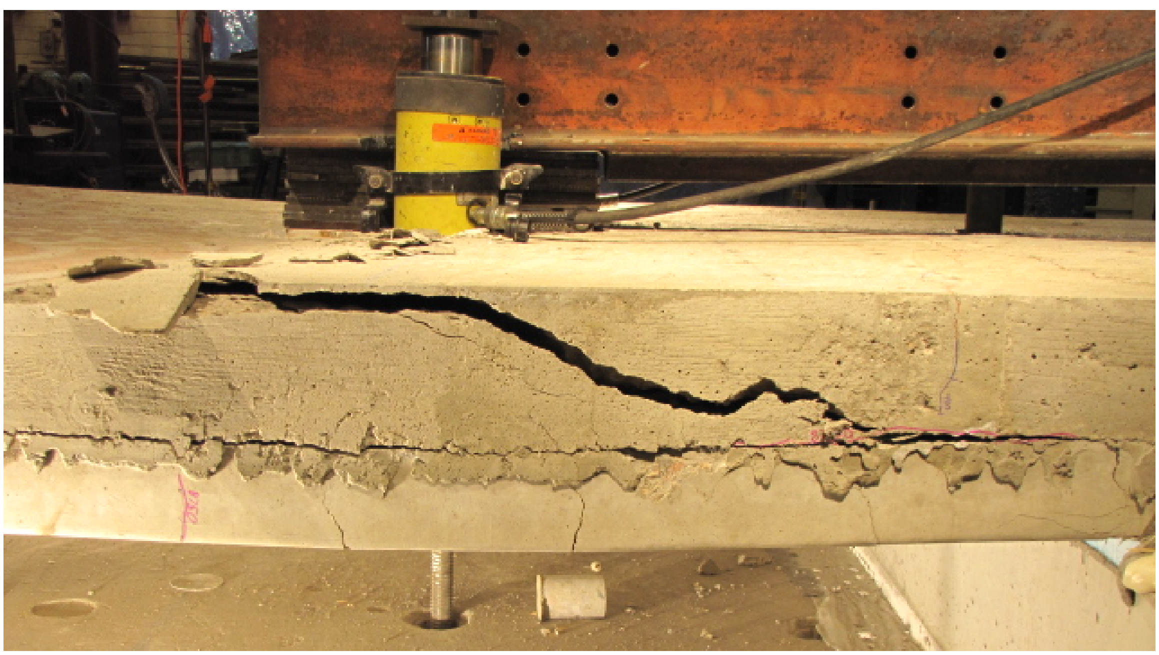

**Figure 41:** A combination punching shear and sliding failure of Specimen G.

One useful method of comparison between the specimens was to compare the magnitude of the maximum average surface strains on the failure side. This was always found to be at the edge of the interior beam and the bridge deck as shown in Figure 37. This point corresponded to the location of the largest crack during testing, as well as the largest moment.

The raw data from the average maximum surface strains from the failure side of the bridge deck can be seen in Figure 42. A smoothing technique was used so that an easier comparison of the data could be made. This was done by fitting a line to the two linear portions of the data. The typical procedure for this smoothing process is shown in Figure 43.  The results of the smoothing technique for all of the bridge deck specimens can be seen in Figure 44. A summary of the slopes of the initial load versus surface strain measurements is given in Table 7. Please note that the final surface strain readings correspond to the last surface strain reading before failure. Because the measurements were manually taken then the measurement of strain at failure was not possible. This limitation should not be a problem as the general behavior of the system has been characterized.

One should note that the location in the bilinear behavior was not at the point of first crack for the specimens. Since the values for the load at cracking for the specimen was determined visually it corresponds to the load when the first localized cracking occurred. These cracks had to be much larger and more distributed before the stiffness of the system was noticed to change.

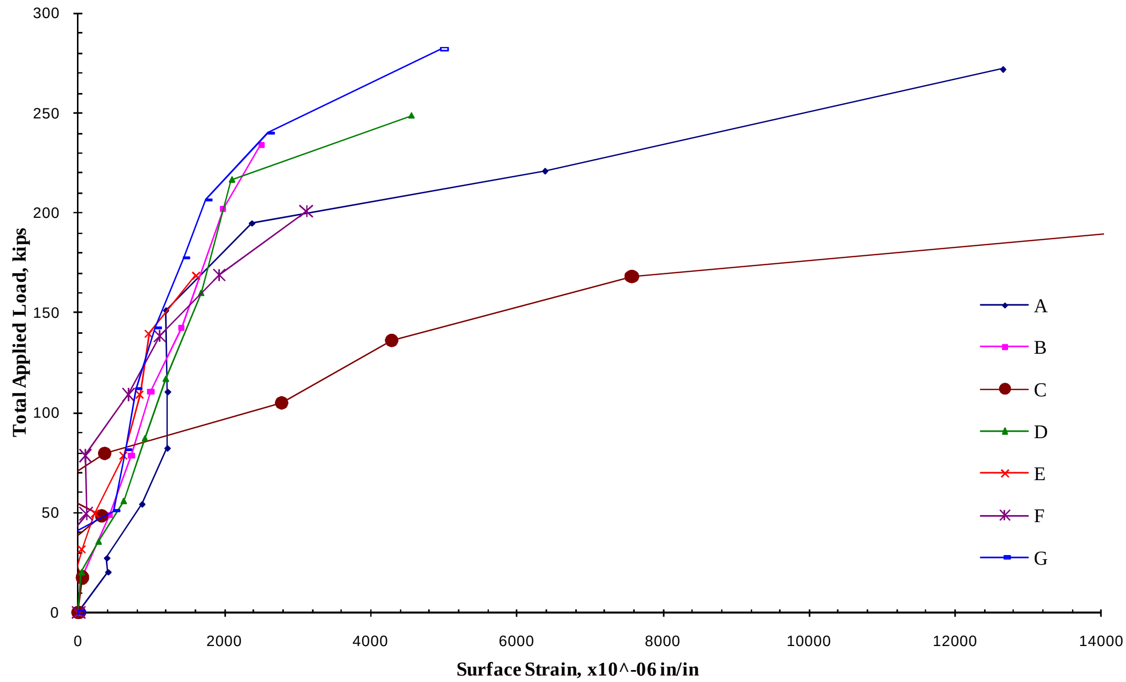


**Figure 42:** Raw data from the average maximum surface strains at the failure side of the bridge deck.

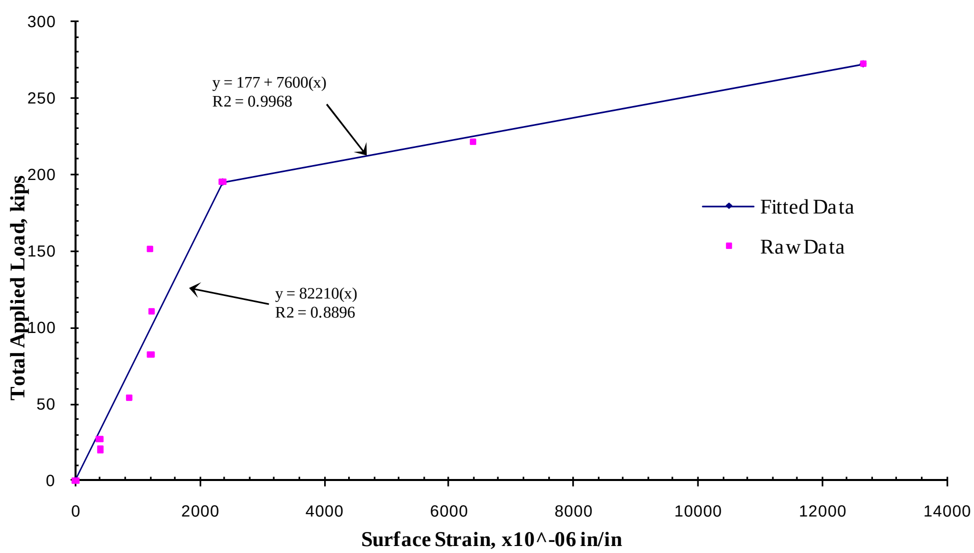


**Figure 43:** An example of the smoothing technique used for the data analysis in this dissertation.

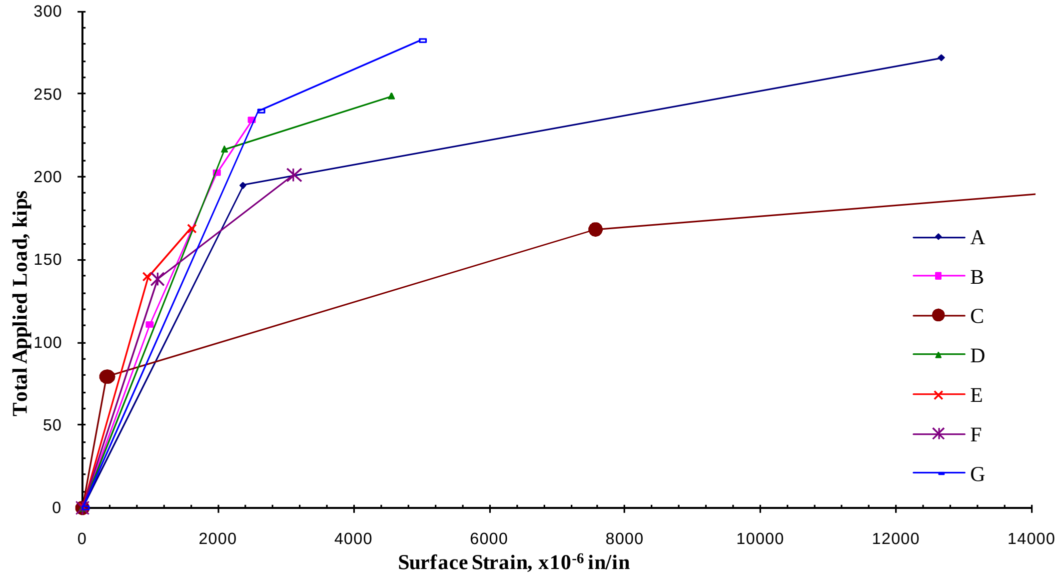


**Figure 44:** The smoothed results from the average maximum surface strains at the failure side of the bridge deck.

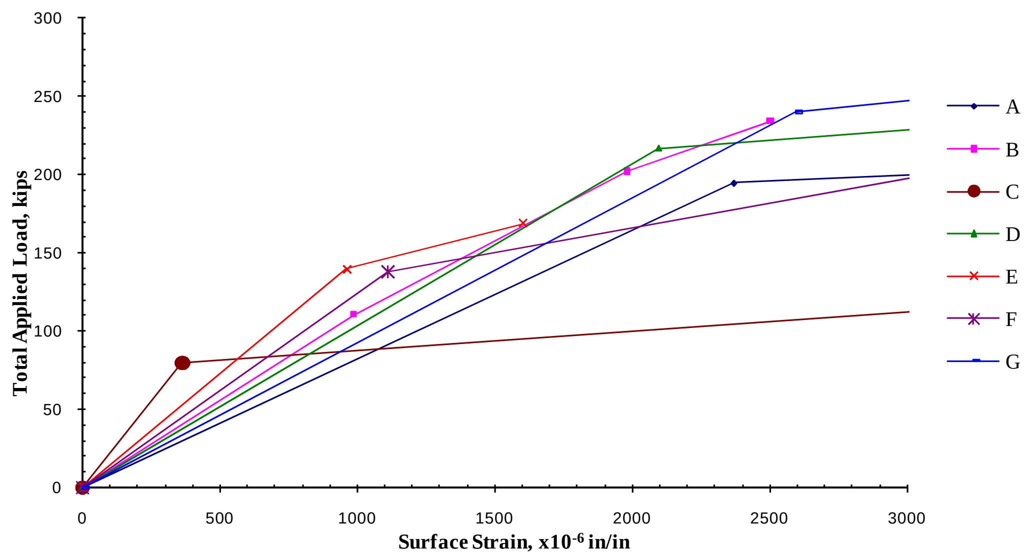


**Figure 45:** The smoothed results from the average maximum surface strains at the failure side of the bridge deck showing only the first 3000 microstrain for each specimen.

## 3.4- DISCUSSION

As can be seen in Table 7, every specimen tested showed a significant safety factor. The smallest ratio of the design load versus the actual load was 6.4 when compared to the HL 93, 16 kip point load or 32 kip axle load.

From the results one can see that all of the bridge decks tested provided satisfactory ultimate strength including the specimen that used no top reinforcing. Therefore, it appears that the steel provided in the top mat of a bridge deck is primarily used for resisting cracking.

Only two specimens showed a lower average maximum surface strain then the TxDOT bridge deck. Both specimens consisted of a rebar mat with D11 bars at 4” and D8 bars at 2.67” with 2” and 2.75” of clear cover. While the same rebar mat at 3.5” of clear cover showed a performance less than the TxDOT standard bridge deck this data is still useful as it can be used as a point of interpolation. From interpolation between the 2.75” and 3.5” specimen a clear cover of 3” with this mat would prove to show a cracking performance equal to a TxDOT standard bridge deck with 2” of clear cover. Therefore, if one wanted to use the rebar mats at an increased depth to optimize the construction tolerances then a mat with D11 bars at 2.67” transversely and D8 bars at 4” longitudinally could be placed at 3” of clear cover and an equivalent maximum surface strain or cracking performance should be expected between the bridge decks. If one used a bridge deck clear cover of 2” then by comparing the slopes of the average maximum surface strains the load at the failure side would be expected to be reduced by 30%. This reduction in maximum surface strain should also correlate to a reduction in crack sizes for the bridge deck by approximately 30%. While it is difficult to quantify, this reduction in crack size should correspond to the extension of service life of the bridge deck. If one used this rebar mat at either depth of clear cover, then for a 4 beam bridge with 8’ beam spacing the steel used would be reduced by 30%. By using rebar mats one would expect to significantly increase the speed of construction and reduce the amount of labor needed to construct a bridge deck. For bridge decks with larger beam spacing or with more beams, these improvements in economy and construction speed would be expected to increase.

It should be noted that while specimen C showed sufficient strength and outstanding surface strain performance up until the first cracking, the surface strain after first cracks were observed was not satisfactory. Of the specimens that contained reinforcing steel this specimen used the lowest amount and also performed the worst after first cracking. It is unfortunate that there was not enough funding in this project in order to investigate this behavior in more detail as this specimen had a much different load versus surface strain performance than the other specimens investigated. This behavior should be investigated with further research but is likely due to the presence of higher strength concrete in Specimen C and not using partial depth precast panels.

## 3.5- CONCLUSIONS

In this work welded rebar mats were used to replace tied reinforcing bars with partial depth panels to improve the economy, constructability, and construction speed of bridge decks. Bridge decks have been constructed and tested that have used tied reinforcing and welded rebar mats. The testing results suggest that:

- The specimen with no top reinforcing steel, Specimen A, showed ultimate strengths similar to the other specimens but high levels of surface strain. Therefore, it appears that the top mat of reinforcing steel is primarily responsible for keeping the surface cracks of a bridge deck small before failure.
- A rebar mat with D11 bars at 2.67" and D8 bars at 4" with 2" of clear cover provides a reduction in the average maximum surface strain by 30% when compared to the performance of a TxDOT standard bridge deck from first loading up until an axle load of 150 kips.
- A rebar mat with D11 bars at 2.67" and D8 bars at 4" with 3" of clear cover should provide the same average maximum surface strain as a typical TxDOT standard bridge deck.

The improved ability of the wire rebar mat to help the concrete bridge deck to resist the initial cracking could allow an owner a construction tolerance for the placement of the top mat of reinforcing. This would allow the contractor to place the rebar mats with a clear cover near 3" and any geometry changes in the mats of up to 1" upwards could be ignored. The tolerance on the grading of bridge deck steel would allow for significant improvements in constructability of bridge decks as grading of bridge decks would be greatly improved.

# CHAPTER IV

# IV. FINITE ELEMENT MODELING

## 4.1- INTRODUCTION

From the beginning of this research, it was considered important to develop analytical procedures that can quanitify the response of the tested bridge deck specimens. This attempt will significantly reduce the time and expense needed to build and test a full-sized bridge deck.

Depending on the structural characteristics, geometric configuration and support conditions, several analysis methods were available. The primary methods are; orthotropic plate theory, folded plate method, finite element method (FEM), finite strip method, grillage method and space frame method(24,25,26).

### 4.1.1 Methods

Finite element method was considered from the beginning for the analysis of these composite deck slabs because of its power and versatility. Because the bridge's deflections are small, geometrical nonlinearity is not expected to be significant (27). The main concern in such a problem is the material nonlinearity where the cracking and post-cracking behavior of the bridge decks is the approach to cover the complete life-span behavior. Nonlinear approximations in FEM are more difficult to formulate, and solving the resulting equations may cost 10 to 100 times as much as a linear approximation having the same number of degrees of freedom (d.o.f.)(28). Material nonlinearity was indirectly considered using the Sequential Linear Approach(29), also known as the Newton-Raphson method, or Newton Method, which is a powerful technique for solving equations numerically. A graphical example of this testing is shown in Figure 46. Each specimen is subjected to a given load. In each element, the maximum principal stress is compared to the maximum allowable tensile stress of concrete. Elements having maximum principal stresses greater than concrete tensile

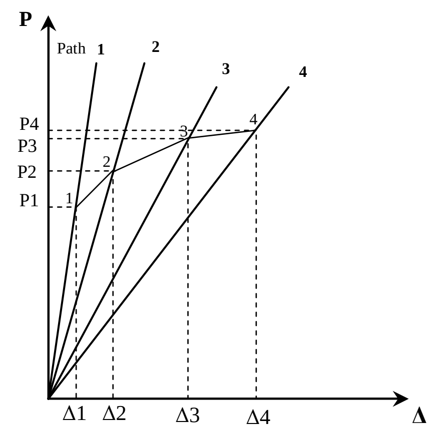


**Figure 46:** Schematic representation of sequential linear approach

strength are considered cracked. The cracking load and orientation of each cracked element is calculated, and its element stiffness matrix is reformed following the procedure for the smeared cracking model.

For crack representation, two methods are generally used; discrete crack models and smeared crack models. Due to the complexity and time-consuming manner of the discrete crack method it was not used. A discrete crack method is more useful for cases where dominant cracks control the behavior such as in the modeling of aggregate interlock and dowel failure.[(29)]

The smeared crack approach is the best choice when the overall load deflection behavior of the structure is desired[(27)]. The cracked concrete is assumed to remain continuous and the cracks are "smeared" as shown in Figure 47. An entire element is assumed to crack when the principal stress anywhere in that element exceeds the tensile capacity of concrete. Cracks are assumed to form perpendicular to the direction of the principal tensile stress as shown in Figure 47. After cracking, the stiffness of the entire element is set to zero in the direction perpendicular to the principal tensile plane. With the just stated condition, this cracking model has sometimes caused numerical difficulties in cases of low loads(30,31). A reduction shear factor; β, has then been introduced by others to address this issue (30,32,33). This reduction factor represents the remaining shear stiffness in the cracked plane due to aggregate interlock and dowel action. There are no clear suggestions for a suitable β factor. Some researchers suggested a magnitude of 0.50(27,34,35,36), while others(37) advised a range from 0.20 to 0.50, recommending the same time the 0.20 value. This last recommendation of β factor came after a series analyses were attempted in the mentioned study with various values for the reduction shear factor within this range, but convergence problems were encountered at low loads with β less than 0.20. The appropriate shear transfer coefficient was investigated for the models in this study to find the most appropriate value.

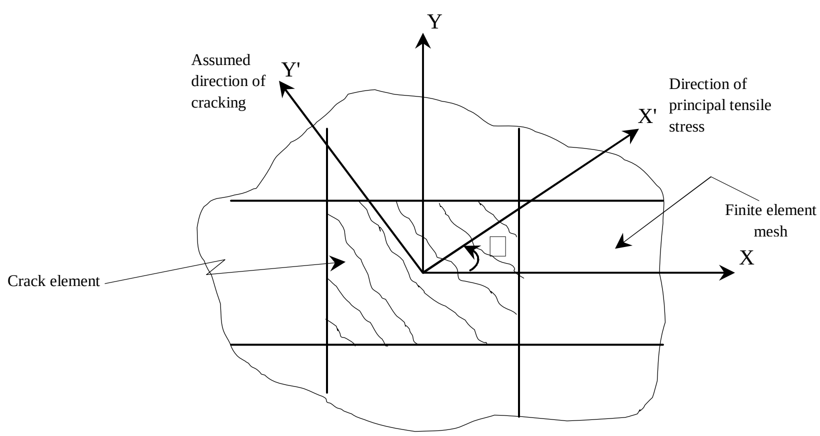


**Figure 47:** Schematic representation of smeared crack model

## 4.2- PROPOSED COMPUTER PROGRAM

A computer program was developed called "SAMO_01" in the MatLab programming language. This program was able to automatically generate the bridge deck mesh, apply the support restraints and use material nonlinearity through the Smeared Crack Model. Mild and prestressed reinforcement was also included in modelling. The program had the following four modules:

1. Mesh generation

2. Input check
3. Finite element analysis
4. Output plot

The eight-node hexahedron element, Figure 48a, was used to model the bridge deck geometry (concrete), while the line element, Figure 48b, was used to model all types of reinforcement. Small element sizes were used in order to overcome the issues where there could be no continuity between cracks in neighboring elements or same element[38,39,40]. This is shown graphically in Figure 49. Also, because of the requirement that the reinforcing had to be placed at the intersection of the nodes, this leads to the use of a fine mesh.

Because of concerns over execution time,a hexahedron element was used to model the concrete. Preliminary analysis showed that the eight node element provided satisfactory performance in regards to deflections, strain measurements, cracking, and failure loads. Additionally, when an actual crack or groups of cracks occur in concrete, the width of the crack band is many times larger than the maximum aggregate size[41]. As a result, the concrete element size should be two to three times greater than the maximum aggregate size to correctly and realistically model the actual cracks using the smeared cracking approach[41,42,43]. In this study, the maximum nominal aggregate size used in 3/4 in., and the minimum FE element size for the full-scale bridge decks was 1.30 in. x 1.30 in. x 1.30 in.

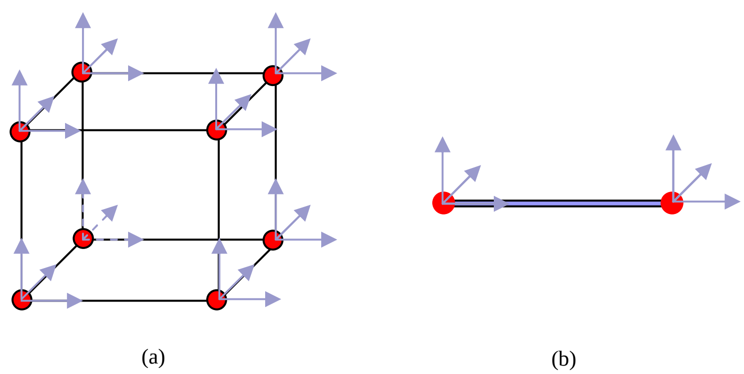


**Figure 48:** Elements used in SAMO_01 program: a) Eight-node hexahedron, b) Line

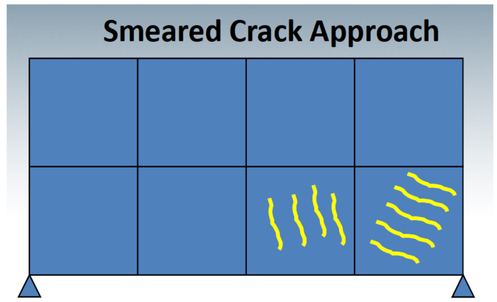


**Figure 49:** Discontinuity of cracks between elements

### 4.2.1- Mesh generation

This module is responsible of feeding the analysis module with all the required geometrical data related to both types of elements used, and their nodes as well. It develops the number of nodes and the number of elements that the deck media has been divided into. Also, it generates the nodal coordinates, the elements coding, and the numbers of connection nodes of the element with the other elements.

This module is versatile, time saving, and makes the developed software much more useful. The module can minimize the storage space required for the stiffness matrix through considering different node schemes, and hence allowing for the use of a much finer mesh, and more loading steps without significant increase in computation time.

### 4.2.2- Input check

This module "qualitatively" informs the user about the model that is going to be analyzed. Graphical displays are used to make easy, accurate, and quick checks of the input accuracy. The input data summarizes the deck media geometry and the mesh generation data.

### 4.2.3- Finite element analysis

This module begins by considering the media boundary conditions to the elements nodes, which are coded as zeroes and ones, where for each degree of freedom with zero denoting a free degree of freedom, while one denoting a fixed degree of freedom.

Next, the program computes and assembles the applied nodal forces in the structural loading vector, which unionize the self weight of elements and the effect of the applied loads. Afterwards, the program computes each element stiffness matrix and assembles them into the overall structural stiffness matrix, named “kdd”. In this matrix and after applying boundary conditions, each element address meets a free d.o.f..

This program utilizes a column oriented form of Gauss elimination technique called the active column solver; which exploits the differing heights above the diagonal exhibited by various columns. A summary of this technique is shown in Figure 50. This direct equation solver method was chosen because it provides solutions within a fixed number of steps. The number of steps can be calculated from knowledge of the size of the problem and the specific procedure elected. Simplicity to program and the constant array size required gives an advantage over the iterative methods; since the iterative methods are usually not competitive with direct methods except in specific cases[28]. The produced system of simultaneous linear algebraic equations are consequently solved, nodal unknowns are obtained; which are the three displacement components. From the obtained nodal displacement components, the normal and shearing strains $(\varepsilon_x, \varepsilon_y, \varepsilon_z, \gamma_{xy}, \gamma_{xz}, \gamma_{yz})$ and consequently stresses $(\sigma_x, \sigma_y, \sigma_z, \tau_{xy}, \tau_{xz}, \tau_{yz})$, also the principal stresses $(\sigma_{max}, \sigma_{min})$ and their orientation to be computed.

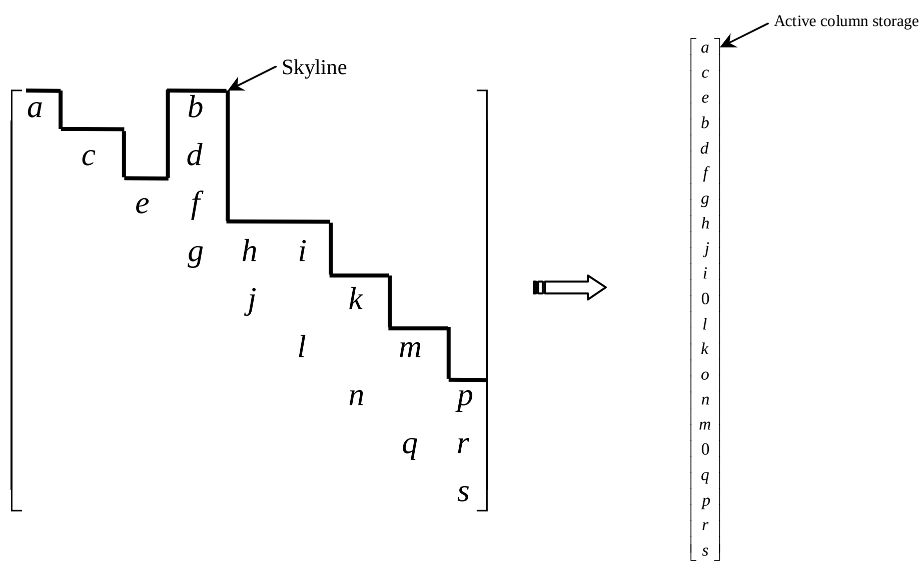


**Figure 50:** Example of active column storage for the global structural stiffness matrix after applying boundary conditions

### 4.2.4- Output plot

The goal of this module is to effectively display the resulting data. For every loading step, the program plots outputs related to;

1) Concrete crack progression.
2) Bridge deck deformed shape with the maximum deflection and corresponding node number and position displayed. This information is plotted over the original unloaded bridge deck position.
3) Maximum principal stresses on the exterior surface accompanied with their orientation.

Figure 51 provides a glimpse of the program output for one of the tests; 3ft overhang cip (corner loading).

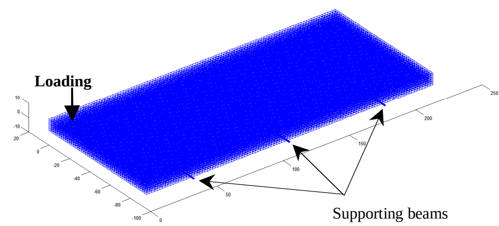


**(a)**

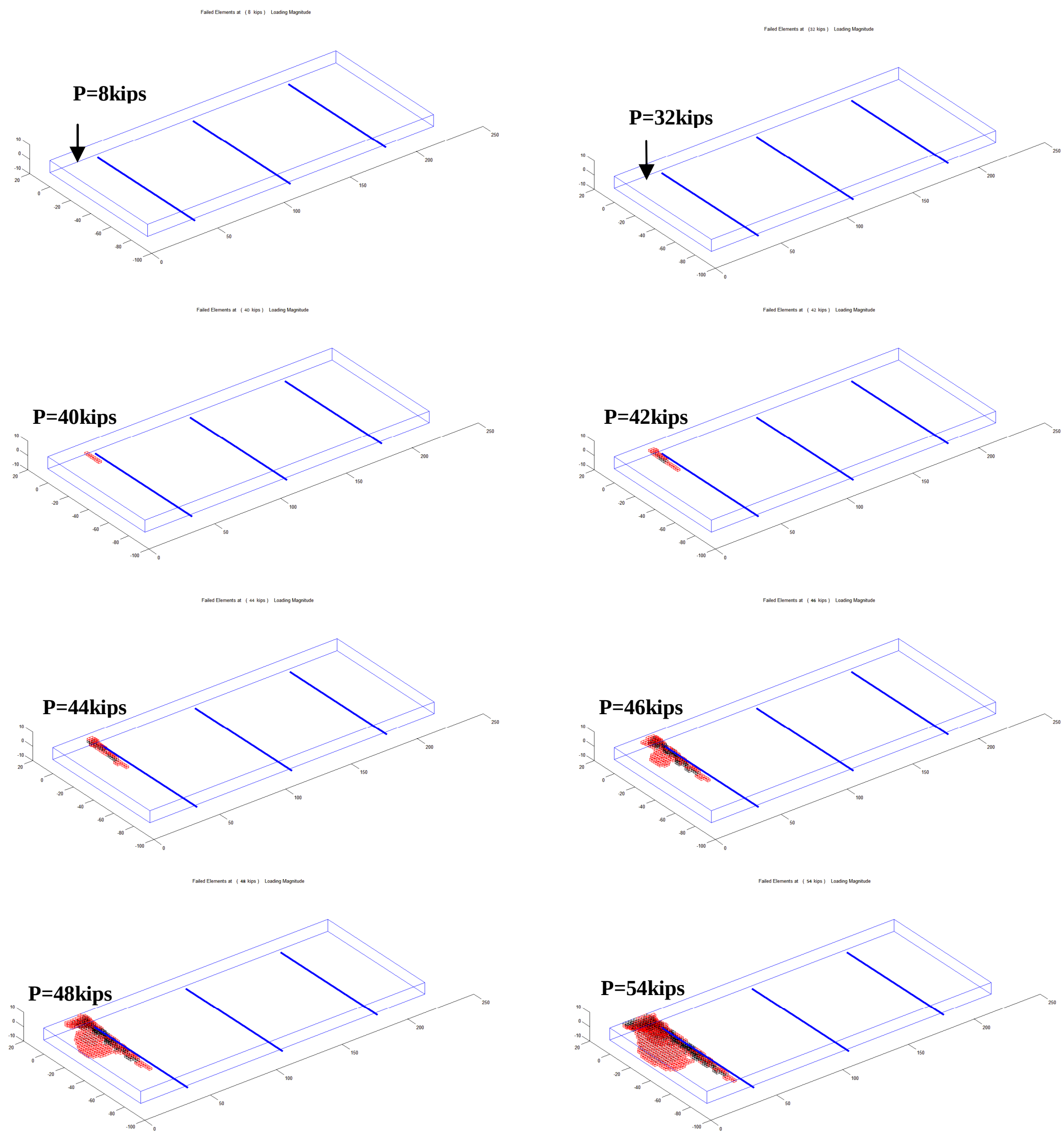


**(b)**

**Figure 51:** Sample of SAMO_01 program output: a) generated mesh, b) Crack progression, c) Deflected shape, d) Principal strains.

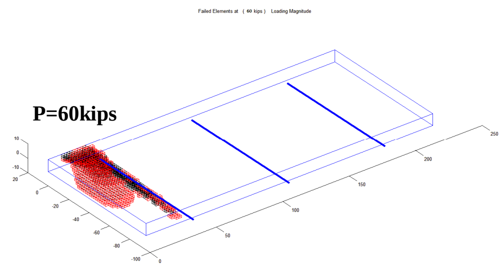


**(b)**

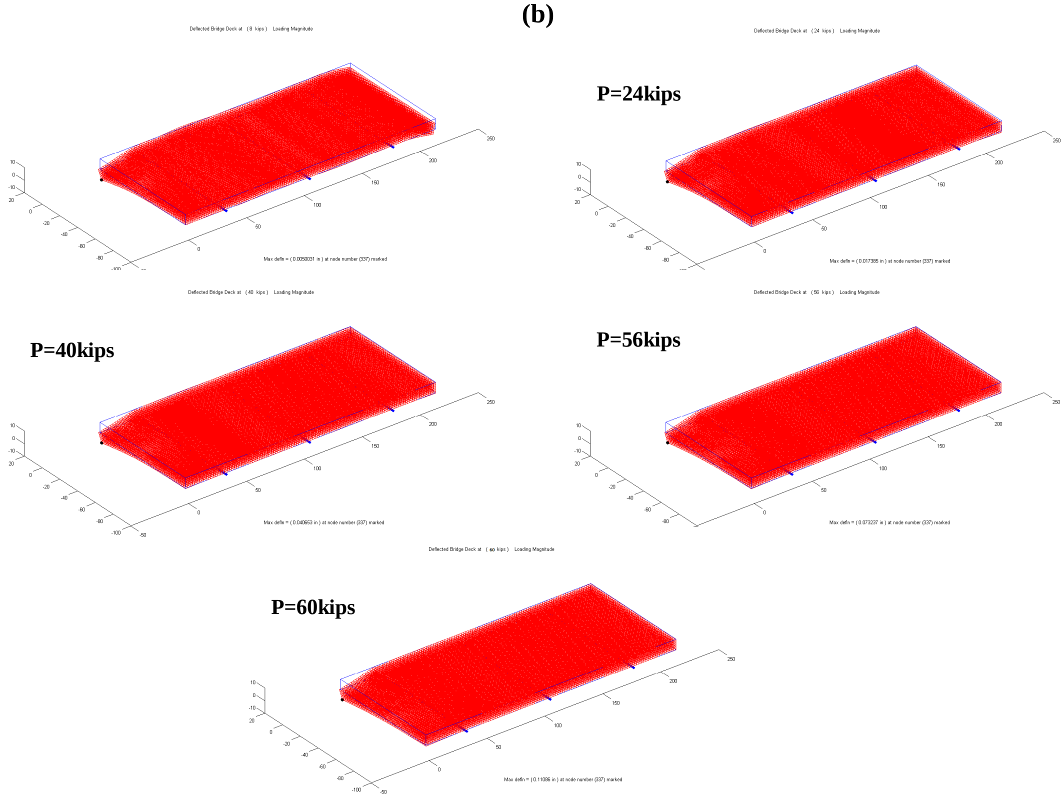


**(c)**

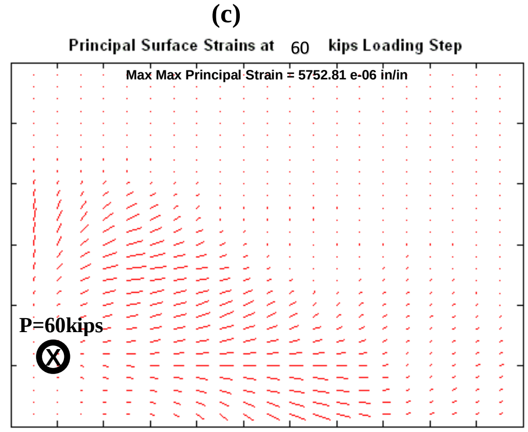


**(d)**

**Figure 51 (*cont.*):** Sample of SAMO_01 program output: a) generated mesh, b) Crack progression, c) Deflected shape, d) Principal strains

## 4.3- PROGRAM FLOW CHART

The program operational sequence may be declared briefly by the computer flow chart presented in Figure 52;

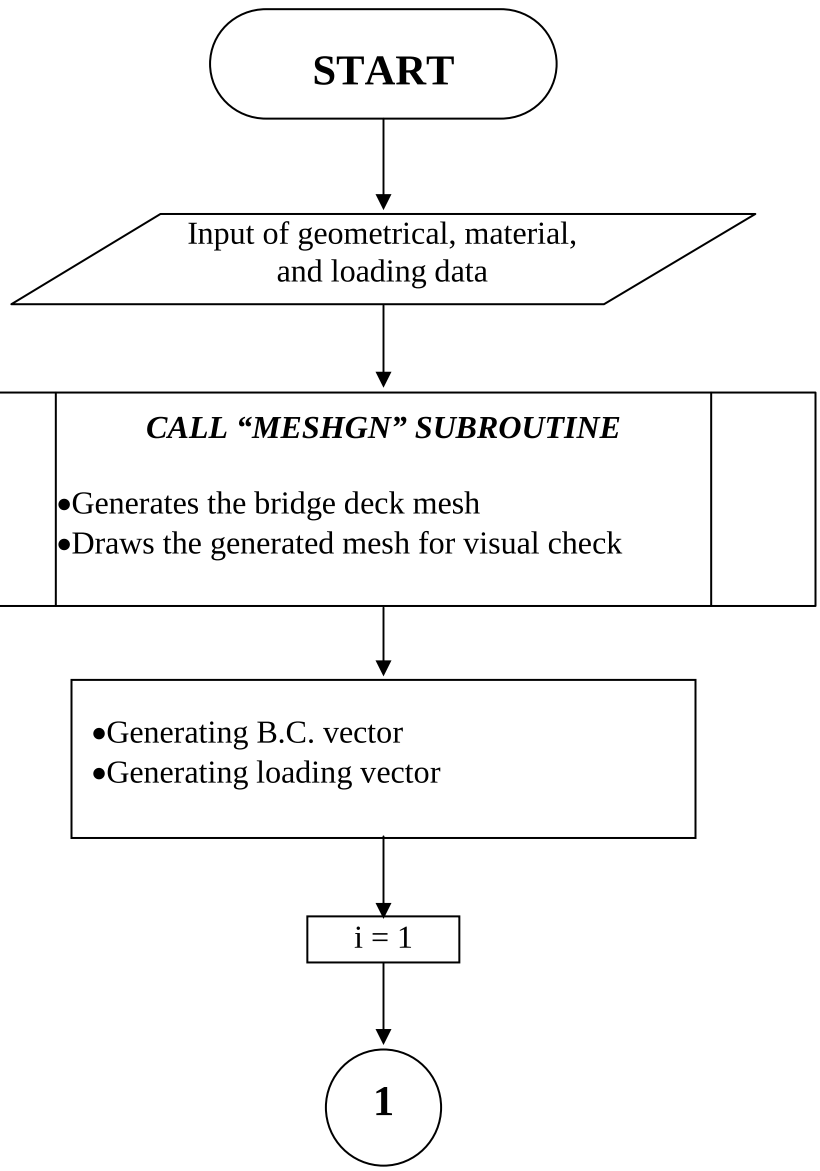


**Figure 52:** Program "SAMO_01" flow chart

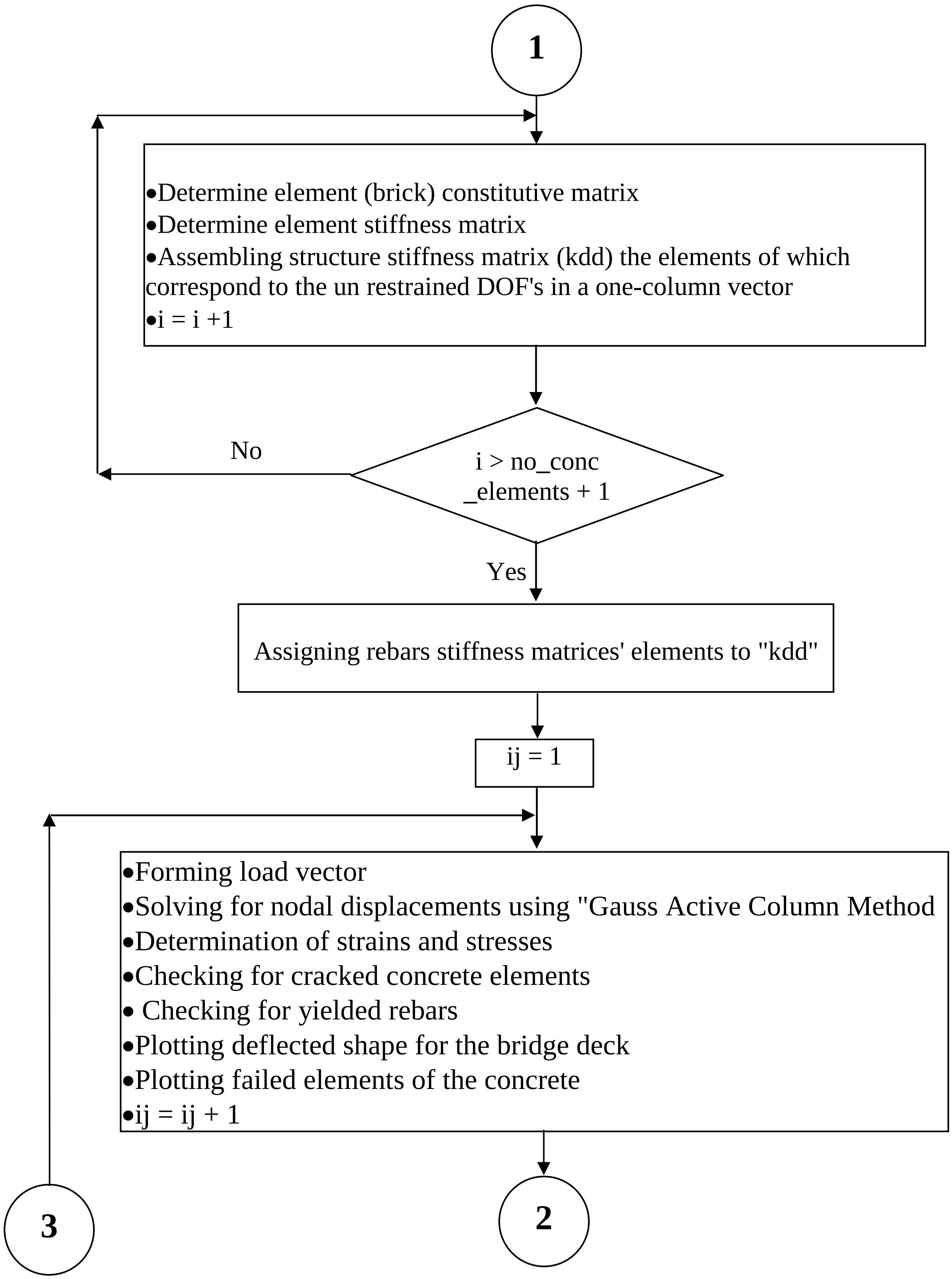


**Figure 52 (*cont.*):** Program "SAMO_01" flow chart

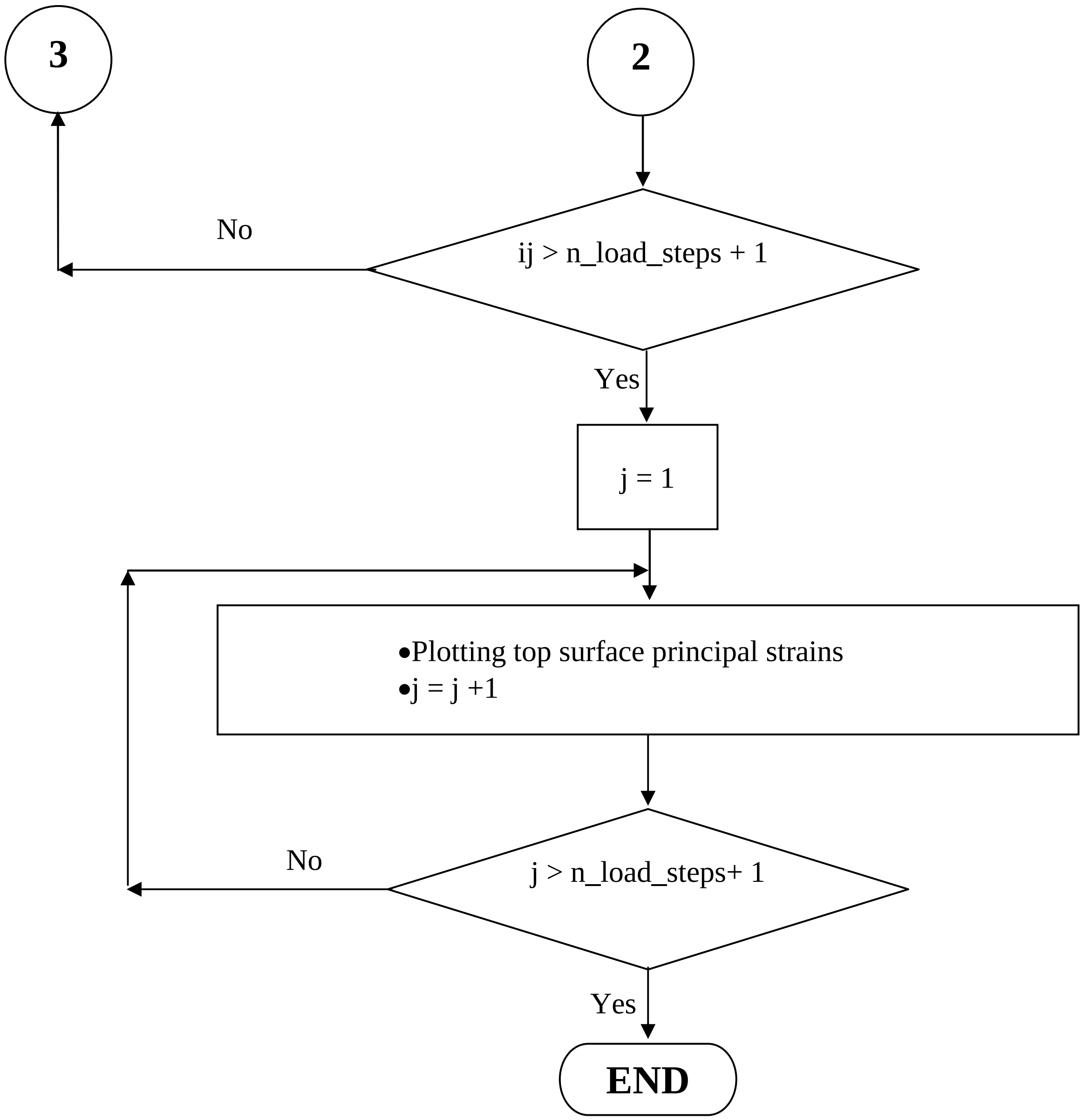


**Figure 52 (*cont.*):** Program "SAMO_01" flow chart

## 4.4- RESULTS

Since the finite element method is a numerical procedure utilized in solving complex engineering problems, important considerations pertaining to the accuracy of the results and the convergence of the numerical solution should be taken. For this reason, as a first step, the reliability and accuracy of the developed computer program has been measured using mesh and load conversion criteria before the execution of every test model to pick a reasonable mesh and loading divisions. Failure loads of full scale experimental tests have been used as benchmarks to pick the primary guess of ultimate (failure) load used in modeling. The program keeps adding load until a failure occurs. Failure (complete destruction) of the model is detected when solution instability occurs. This should correspond to where the deflections became excessive in the testing.

### 4.4.1- Tuning the finite element model

Because there is no clear recommended β value in the literature, the first efforts with the computer model was to compare the accuracy of the experimental results to the computer models with different β values. Because of lengthy run time required, three verification test specimens were investigated that had different failure modes. These include the corner loaded 3ft precast overhang, corner loaded 5ft cast-in-place overhang, and the centrally loaded 5ft precast overhang. Table 8 summarizes the effect of the mentioned factor using strain and deflection measurement data as a reference. Four β magnitudes were checked; 0.10, 0.20, 0.35, and 0.50. The percent difference of the sum of the total error between each β curve and the corresponding one from experiments was obtained to recognize the β that is best for the modeling of bridge decks. A summary of this analysis is shown in Table 8. All graphical representations studying this effect are presented in Appendix B; Figures B7, B8, B11, B12, B13, and B14.

Relying on these results, β magnitude of 0.20 has been adopted as the most reliable shear factor to model these experiments. This value was chosen as it provided the least percentage of absolute error sum.

### 4.4.2- Finite element solution versus experimental tests

While using $\beta = 0.20$, a complete comparison between FEM and the experiment is presented in this section and summarized in Table 9. The material properties from each test were used as inputs for each FEM analysis.

**Table 8:** Effect of the β factor

| | | % difference of the sum of absolute error from the experimental data | | | |
|---|---|---|---|---|---|
| | **β =** | **0.10** | **0.20** | **0.35** | **0.50** |
| **3ft_pre_corner** | | | | | |
| **DEMEC** | **35** | 26.00 | 8.30 | 19.86 | 25.27 |
| | **12** | 27.09 | 9.12 | 14.38 | 15.32 |
| | **15** | 29.97 | 8.32 | 10.65 | 9.64 |
| | **22** | 32.92 | 4.56 | 4.94 | 9.88 |
| | **37** | 23.58 | 10.72 | 15.54 | 30.00 |
| **defln. Gauge** | **1** | 3.61 | 14.44 | 33.08 | 42.11 |
| | **2** | 15.23 | 8.12 | 41.08 | 48.72 |
| | **3** | 29.92 | 11.06 | 7.69 | 9.22 |
| | **4** | 8.46 | 16.34 | 22.47 | 31.11 |
| | **5** | 18.56 | 13.18 | 15.19 | 17.08 |
| | **6** | 35.28 | 15.41 | 6.89 | 17.46 |
| | **7** | 30.27 | 13.16 | 14.16 | 23.70 |
| | **8** | 26.49 | 10.63 | 11.92 | 12.56 |
| | **9** | 26.76 | 15.07 | 15.33 | 16.31 |
| **5ft_cip_corner** | | | | | |
| **DEMEC** | **5** | 8.13 | 6.10 | 34.17 | 47.89 |
| | **1** | 26.14 | 8.13 | 14.47 | 24.67 |
| | **3** | 10.58 | 3.62 | 27.05 | 37.70 |
| | **6** | 13.37 | 4.61 | 23.09 | 32.12 |
| | **64** | 24.63 | 6.28 | 5.54 | 4.64 |
| | **66** | 13.48 | 4.11 | 16.34 | 29.87 |
| | **80** | 15.86 | 4.06 | 18.37 | 22.16 |
| **defln. Gauge** | **1** | 7.68 | 11.94 | 33.26 | 41.79 |
| | **2** | 9.42 | 10.60 | 38.38 | 47.71 |
| | **3** | 12.40 | 12.23 | 36.59 | 71.01 |
| | **4** | 18.97 | 16.94 | 33.88 | 47.43 |
| | **5** | 22.77 | 24.40 | 74.81 | 82.94 |
| | **6** | 21.42 | 17.47 | 16.35 | 18.04 |
| | **7** | 9.60 | 14.90 | 39.73 | 48.00 |
| | **8** | 9.73 | 18.58 | 38.93 | 53.09 |
| | **9** | 13.34 | 18.62 | 38.79 | 41.89 |
| **5ft_pre_center** | | | | | |
| **DEMEC** | **58** | 29.32 | 10.30 | 41.63 | 76.10 |
| | **3** | 22.10 | 8.51 | 13.26 | 20.63 |
| | **49** | 18.17 | 11.85 | 34.97 | 46.27 |
| | **66** | 13.20 | 9.90 | 19.48 | 37.24 |
| | **109** | 8.35 | 6.45 | 10.47 | 12.34 |
| **defln. Gauge** | **1&9** | 17.42 | 13.07 | 43.55 | 52.26 |
| | **2&10** | 34.12 | 29.84 | 31.27 | 33.74 |
| | **3&7** | 16.23 | 8.46 | 20.18 | 36.48 |
| | **4&8** | 27.30 | 25.73 | 26.08 | 28.11 |
| | **5** | 9.64 | 6.90 | 22.04 | 43.18 |
| | **6** | 53.88 | 30.76 | 26.22 | 25.81 |
| ***TOTAL AVERAGE* OF % DIFFERENCE OF THE SUM OF ABSOLUTE ERROR FROM THE EXPERIMENTAL DATA** | | | | | |
| **Strains** | | **20.2** | **7.4** | **19.1** | **28.3** |
| **Deflections** | | **19.9** | **15.7** | **28.7** | **37.1** |

**Table 9:** Absolute error % of FEM with β = 0.20 compared to experimental results

| | % difference (error) of the sum of absolute error from the experimental data | | | | | | | | | | | | | | | |
|---|---|---|---|---|---|---|---|---|---|---|---|---|---|---|---|---|
| | **DEMECs** | | | | | | | **Deflection gauges** | | | | | | | | |
| **3ft_cip_center** | **14** | **1&48** | **7&20** | **12** | **6** | **51** | | **1** | **2** | **3&5** | **4&6** | | | | | |
| | 14.29 | 3.71 | 5.33 | 4.52 | 2.07 | 1.49 | | 22.41 | 28.17 | 12.96 | 26.88 | | | | | |
| **3ft_cip_corner** | **13** | **26** | **20** | **22** | **35** | | | **1** | **2** | **3** | **4** | **5** | **6** | **7** | **8** | **9** |
| | 3.14 | 10.77 | 9.52 | 8.77 | 14.29 | | | 4.11 | 1.78 | 158 | 18.88 | 17.33 | 20.27 | 7.33 | 5.17 | 12.18 |
| **3ft_pre_center** | **41** | **29** | **36** | **37** | **42** | | | **1** | **2** | **3&5** | **4&6** | | | | | |
| | 10.33 | 7.63 | 14.27 | 6.67 | 9.52 | | | 26.32 | 63.61 | 18.87 | 42.65 | | | | | |
| **3ft_pre_corner** | **35** | **12** | **15** | **22** | **37** | | | **1** | **2** | **3** | **4** | **5** | **6** | **7** | **8** | **9** |
| | 8.30 | 9.12 | 8.32 | 4.56 | 10.72 | | | 14.44 | 8.12 | 11.06 | 16.34 | 13.18 | 15.41 | 13.16 | 10.63 | 15.07 |
| **5ft_cip_center** | **58** | **48&66** | **65** | **97** | | | | **1&9** | **2&10** | **3&7** | **4&8** | **5** | **6** | | | |
| | 8.42 | 9.78 | 17.18 | 24.53 | | | | 11.11 | 16.67 | 7.94 | 18.67 | 12.48 | 7.82 | | | |
| **5ft_cip_corner** | **5** | **1** | **3** | **6** | **64** | **66** | **80** | **1** | **2** | **3** | **4** | **5** | **6** | **7** | **8** | **9** |
| | 6.10 | 8.13 | 3.62 | 4.61 | 6.28 | 4.11 | 4.06 | 11.94 | 10.60 | 12.23 | 16.94 | 24.40 | 17.47 | 14.90 | 18.58 | 18.62 |
| **5ft_pre_center** | **58** | **3** | **49** | **66** | **109** | | | **1&9** | **2&10** | **3&7** | **4&8** | **5** | **6** | | | |
| | 10.30 | 8.51 | 11.85 | 9.90 | 6.45 | | | 13.07 | 29.84 | 8.46 | 25.73 | 6.90 | 30.76 | | | |
| **5ft 8in_center** | **98&106** | **84** | **101** | | | | | **1&10** | **2&9** | **3&8** | **4&7** | **5** | **6** | | | |
| | 17.76 | 14.27 | 22.72 | | | | | 14.29 | 10.18 | 14.44 | 12.79 | 16.45 | 11.58 | | | |
| **5ft_pre_corner** | **6** | **4** | **36** | **59** | **70** | | | **1** | **2** | **3** | **4** | **5** | **6** | **7** | **8** | **9** |
| | 9.57 | 6.72 | 11.12 | 6.91 | 14.51 | | | 4.17 | 210 | 9.62 | 77.31 | 17.51 | 22.81 | 12.71 | 21.44 | 16.16 |
| **Specimen_A** | **98&299** | **77** | **140** | **295** | **309** | | | **1&6** | **2&5** | **3&4** | | | | | | |
| | 11.36 | 14.21 | 12.33 | 21.19 | 7.31 | | | 14.74 | 10.45 | 7.32 | | | | | | |
| **Specimen_B** | **35&110** | **10** | **68** | **103** | **137** | | | **1&8** | **2&7** | **3&6** | **4&5** | | | | | |
| | 38.67 | 8.93 | 14.17 | 13.87 | 42.83 | | | 10.26 | 42.15 | 48.13 | 31.77 | | | | | |
| **Specimen_C** | **140&64** | **62** | **87** | **102** | **137** | | | **1&8** | **2&7** | **3&6** | **4&5** | | | | | |
| | 12.73 | 5.27 | 9.31 | 8.77 | 6.84 | | | 6.8 | 9.57 | 8.67 | 29.46 | | | | | |
| **Specimen_D** | **144&67** | **12** | **48** | **87** | **141** | | | **1&8** | **2&7** | **3&6** | **4&5** | | | | | |
| | 10.26 | 24.82 | 17.88 | 9.31 | 7.55 | | | 44.63 | 31.37 | 9.73 | 12.38 | | | | | |
| **Specimen_E** | **54&130** | **47** | **60** | **86** | **134** | | | **1&8** | **2&7** | **3&6** | **4&5** | | | | | |
| | 21.45 | 33.17 | 21.25 | 12.38 | 16.92 | | | 20.51 | 11.31 | 8.73 | 7.28 | | | | | |
| **Specimen_F** | **139,62&128** | **58** | **84** | **137** | | | | **1&8** | **2&7** | **3&6** | **4&5** | | | | | |
| | 14.67 | 41.17 | 34.12 | 6.78 | | | | 18.97 | 19.57 | 12.81 | 18.72 | | | | | |
| **Specimen_G** | **65&140** | **17** | **62** | **105** | **138** | | | **1&8** | **2&7** | **3&6** | **4&5** | | | | | |
| | 14.88 | 27.34 | 21.14 | 22.39 | 17.81 | | | 19.37 | 21.47 | 14.74 | 19.43 | | | | | |
| **Total Average** | **8.4% (Overhangs), 17.5%(Welded rebar specimens)** | | | | | | | **21.9% (Overhangs), 18.9%(Welded rebar specimens)** | | | | | | | | |
| **Std. Deviation** | **5.5% (Overhangs), 10.4%(Welded rebar specimens)** | | | | | | | **32.9% (Overhangs), 11.8%(Welded rebar specimens)** | | | | | | | | |

**Table 10:** Cracking and failure loads predicted by the FEM compared to the measured values

| Specimen | Matlab Code | | | | Experiments | | Actual Failure description |
|---|---|---|---|---|---|---|---|
| | Cracking Load, kips | Cracking Load, % Diff | Failure load, kips | Failure load, % Diff | Cracking Load, kips | Failure load, kips | |
| **3ft_cip_center** | 58.77 | 4.39 | 158.66 | --- | 56.30 | >103.50 | |
| **3ft_cip_corner** | 42.56 | -11.33 | 59.30 | 5.52 | 48.00 | 56.20 | Punching |
| **3ft_pre_center** | 41.12 | -14.33 | 167.03 | --- | 48.00 | >96.00 | |
| **3ft_pre_corner** | 43.17 | 7.93 | 84.71 | 5.89 | 40.00 | 80.00 | Comp. Strut failure + Punching |
| **5ft_cip_center** | 20.50 | -14.58 | 84.12 | -4.41 | 24.00 | 88.00 | |
| **5ft_cip_corner** | 20.18 | -15.92 | 33.70 | 22.55 | 24.00 | 27.50 | |
| **5ft_pre_center** | 25.60 | -20.00 | 89.74 | 3.15 | 32.00 | 87.00 | |
| **5ft 8in_center** | 32.80 | 4.46 | 72.10 | 4.49 | 31.40 | 69.00 | |
| **5ft_pre_corner** | 19.88 | -17.17 | 46.90 | -2.29 | 24.00 | 48.00 | |
| **Specimen_A** | 24.60 | -8.89 | 298.11 | 9.60 | 27.00 | 272.00 | Punching (south side) |
| **Specimen_B** | 47.80 | -2.45 | 305.71 | 9.57 | 49.00 | 279.00 | Punching (south side) |
| **Specimen_C** | 80.55 | 1.96 | 216.12 | 1.94 | 79.00 | 212.00 | Punching (south side) |
| **Specimen_D** | 39.40 | 9.44 | 323.12 | 12.59 | 36.00 | 287.00 | Punching @ cip only(south side) |
| **Specimen_E** | 47.76 | -2.53 | 228.54 | 12.03 | 49.00 | 204.00 | P/S panel flex. failure & Support failure (south side) |
| **Specimen_F** | 48.10 | -1.84 | 241.33 | 12.25 | 49.00 | 215.00 | Splitting & Punching at the south side |
| **Specimen_G** | 54.50 | 6.86 | 303.88 | -3.22 | 51.00 | 314.00 | Punching (north side) |

| **<u>ABSOLUTE</u> % DIFFERENCE (ERROR) FROM THE EXPERIMENTAL DATA** | | | | |
|---|---|---|---|---|
| **Total Average** | Overhangs | 12.2 | | 6.9 |
| | Welded rebar specimens | 4.9 | | 8.7 |
| **Std. Deviation** | Overhangs | 5.6 | | 7.0 |
| | Welded rebar specimens | 3.4 | | 4.4 |

These relative differences are shown for a specific number of DEMEC locations and deflection gauges. These strain measurements were chosen at positions either of high strain magnitudes or for ones through which loads are expected to transfer. Table 10 presents cracking and failure load magnitudes estimated by the proposed computer program. Relative differences to experimental data are shown as well. Additionally, the observed failure characters for some of the tests are provided.

### 4.4.3- Estimating the optimum β factor

Several unconsidered factors might affect the FE modeling. Bond between rebars and surrounding concrete, as well as microcracks initiate inside the concrete media at the aggregate-paste interface were not considered in the modeling. Microcrack initiation is because of the reduced strength of bond between aggregate and paste which makes concrete more inelastic. Thus, considering that the formerly adopted β=0.20 does not accommodate the just stated effects on concrete cracking, the idea of finding a better β perfectly models this behavior came to existence The former FE analyses done for all tests was based on the selected β=0.20 after the primary comparisons executed between the mentioned four β magnitudes, and partly on the recommendation(37) that suggested a minimum magnitude for β of 0.20. The goal of this section is an attempt to predict a better β for the FE modeling relying on all former analyses. Since most of the 0.20 β magnitude curves were above the experiments' curves and the 0.10 β curves were below. This urges to guessing that the optimum β is between 0.10 and 0.20 and should be much closer to 0.20 than 0.10; where an early solution instability was experienced. Neglecting any other factor affecting modeling except β, a rough (linear) interpolation using β = 0.50, 0.35, 0.20, and 0.10 were considered in the upcoming graphs. The areas between each β curve and the experiments' were calculated and presented in the following graphs; namely for the corner loaded 3ft precast overhang (Figure 53), corner loaded 5ft cast-in-place overhang (Figure 54), and the centrally loaded 5ft precast overhang (Figure 55). Another part of the decision of the optimum β was based on the area evaluation of the rest of graphs included in Appendix B; that is how much far was the “β=0.20” curve from the experiment's.

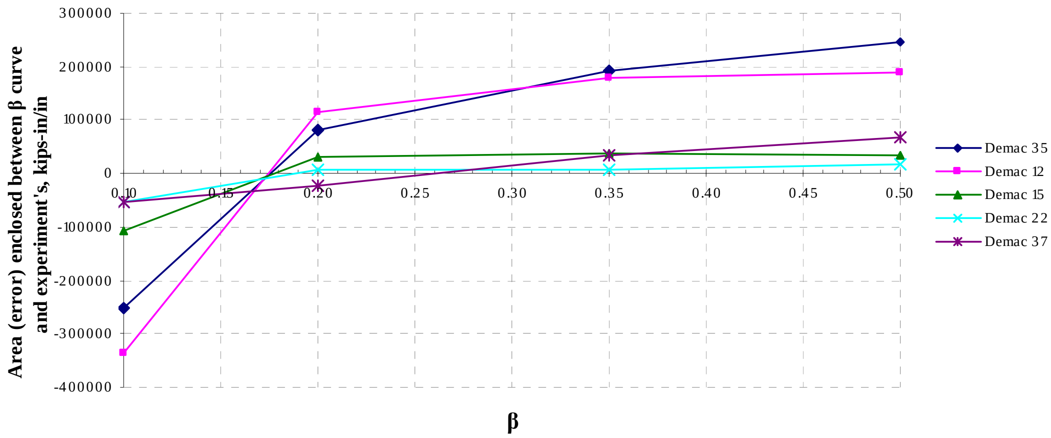


(a)

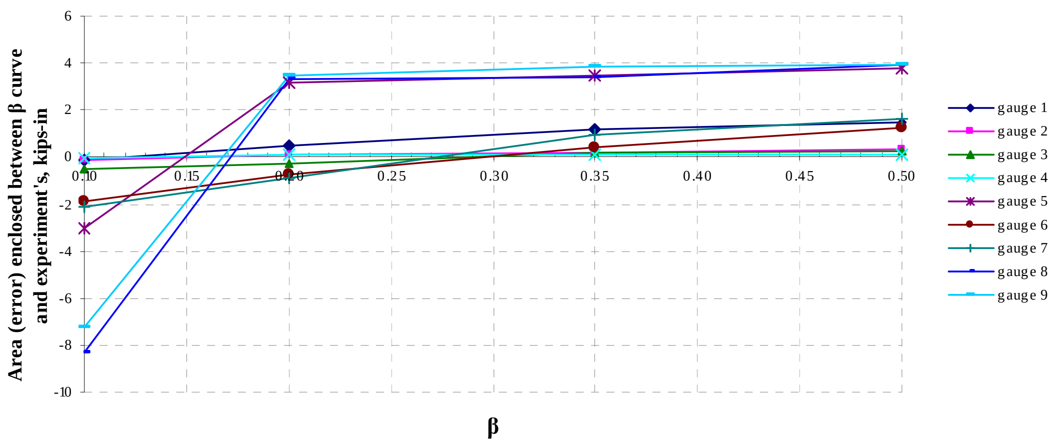


(b)

**Figure 53:** Effect of β on area enclosed between FE model and experiment curves for the 3ft_pre_corner test; a) strain, and b) deflection

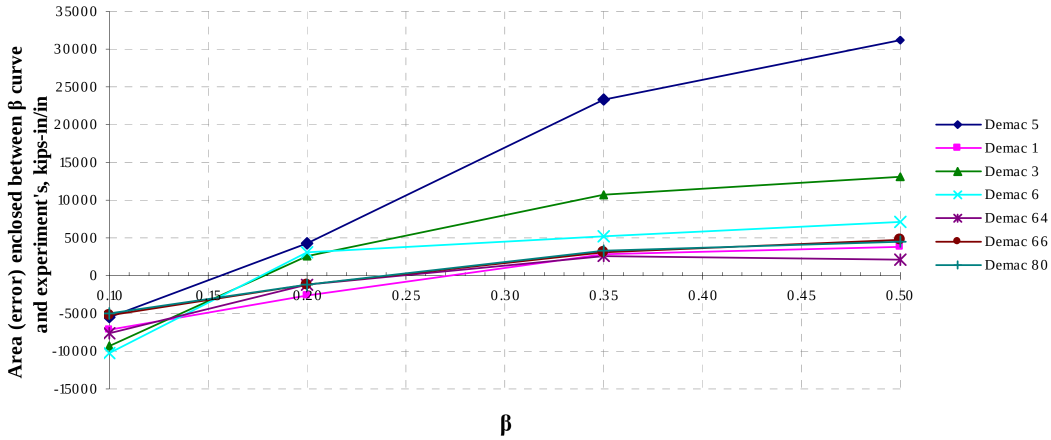


(a)

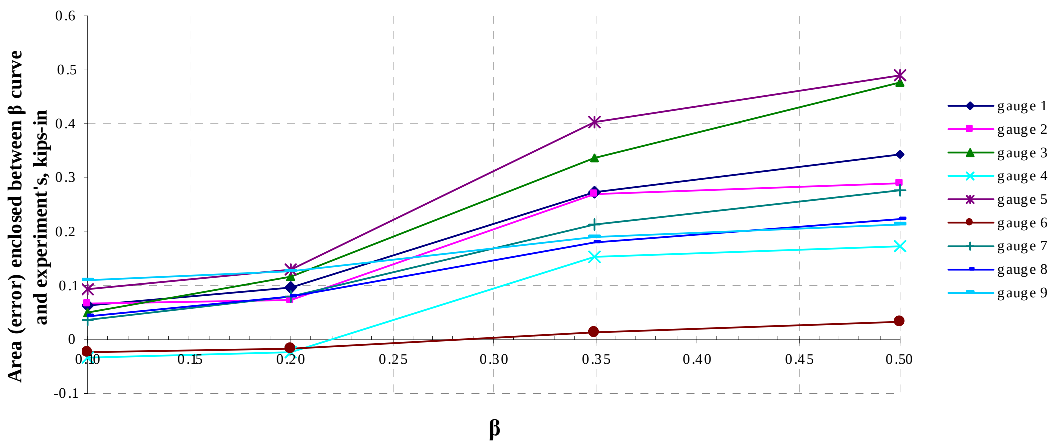


(b)

**Figure 54:** Effect of β on area enclosed between FE model and experiment curves for the 5ft_cip_corner test; a) strain, and b) deflection

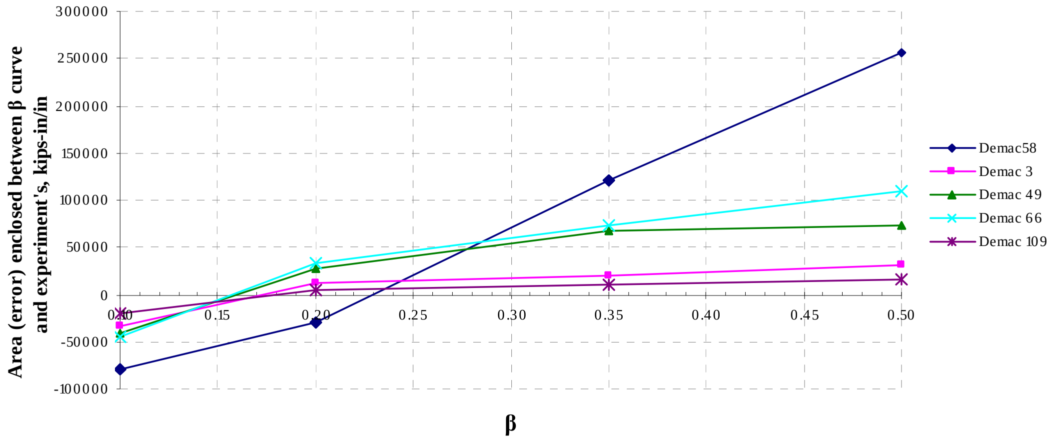


(a)

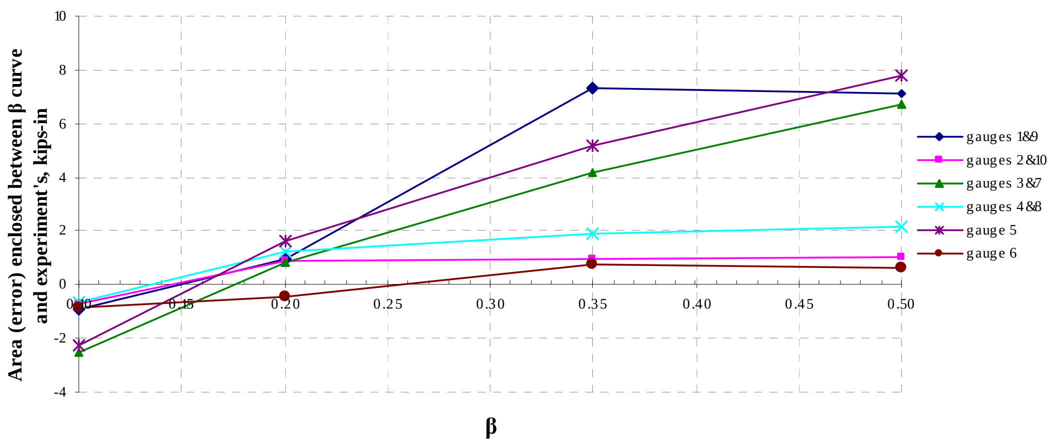


(b)

**Figure 55:** Effect of β on area enclosed between FE model and experiment curves for the 5ft_pre_center test; a) strain, and b) deflection

## 4.5- DISCUSSION

Upon recognition of Table 8 where the effect of the shear reduction factor has been summarized, and figures B7, B8, B11, B12, B13, and B14 for a graphical representation of these numbers, it is obvious that the percentage difference of the absolute error sum enclosed between the curves of the experimental data and the curves of the FEM plots for different β magnitudes has its minimum values for β = 0.20 when considering strain measurements. Regarding deflection data, the elected sum of the absolute error fluctuates between β curves of 0.10 and 0.20. Because of a greater trust in the strain measurements they were used to determine that β = 0.20. As soon as the most consistent β value that produced the nearest behavior to the experiments has been picked, remaining tests have been modeled using the proposed computer program. In brief detail of each test, hereinafter the bullet points observed by the aid of Table 9 and all Figures in Appendix B:

a) **3ft_cip_center;** Figures B.1 and B.2

- Very good surface strain agreement. The average Initial slope for the selected DEMECs is almost identical to experiments' and has the value of 238,000 kips/ (in/in). The average absolute error is 5.24%.
- Fair deflection gauges agreement except at gauge 1; where the FEM underestimates deflection at any given loading magnitude above 24 kips. The overall average error is 22.61%.

b) **3ft_cip_corner;** Figures B.3 and B.4

- Same trend for both surface strain plots, but near infinite initial slope was obtained from experiments until the 16 kips loading magnitude. Average initial slope of the FEM is 92,850 kips/ (in/in). This difference in initial slope may be referred *partly* (but not specifically) to the location at which some of the readings were taken using the FEM. For instance, this location was 1.61 in. off the measured one for DEMEC 13. The average error is 9.30%.
- Excellent deflection data agreement was obtained at all gauges with an average error of 11.43%.

**3ft_pre_center;** Figures B.5 and B.6

- 467,050 kips/ (in/in) average initial slope for the experimental strain versus 639,350 kips/ (in/in) for the strain predicted by the FEM. FEM overestimated the initial slope by 36% the magnitude of the actual one. Nevertheless, the Overall average error of 9.68% was obtained. It should be reassured that the given slopes are the initials, where at later loading stages, sometimes even before cracking, they decrease; this explains the contradiction seems between the difference in average slope and the overall error between the curves.

- Initial stiffness for the deflection measurement at the two gauges near the loading point (1 &2) are very different.
- Deflection readings of the last two loading values of gauge 1 were not expected. The difference may be due to localized gage malfunction. FEM underestimates deflection at any given loading magnitude for gauge 1, and above 40 kips at all other gauges.
- The overall average absolute difference in deflection readings is 37.86%.

c) **3ft_pre_corner;** Figures B.7 and B.8

- Identical initial slope was found for both surface strain plots of 89,600 kips/ (in/in). Generally, almost same trend for both plots is observed all over the plotting area with an average error percentage of 8.33%.
- Good deflection data agreement was obtained at all gauges except 6 and 8. At 6, the experimental plot was not as expected. One would expect that the data would be similar to measurement point 2 and 4. Less deflection at gage 5 would also be expected. While for gauge 8, the device seemed jammed; since the stiffness was infinite until 40kips then the results became reasonable. The overall average error, including the suspected gauges, is 10.21%.

d) **5ft_cip_center;** Figures B.9 and B.10

- Very good surface strain agreement for both plots. Initial slopes, except at DEMEC 65, almost identical and have an average value of 142,050 kips/ (in/in). These slopes decrease just after the cracking loads. The average error between the two curves is 14.98%.
- Initial stiffness is almost identical at all measured points. This initial agreement between plots is lower after cracking for the row of gauges next to the supporting beam, while this difference gets very large for the front row gauges; where the FEM significantly underestimates deflection especially near failure. The calculated average difference is 12.45%.

**e) 5ft_cip_corner;** Figures B.11 and B.12

- Approximately equal average initial slope of 101,000 kips/ (in/in) for both surface strain plots. This agreement diverges even before cracking loads at around 8 kips. The FEM underestimates strain prediction afterwards. The average error is found to be 3.54%.
- There was a small agreement between data especially for the initial stiffness. Gauges 4, 6, 7, and 9 seemed to not respond at initial loading stages; which may be referred to the very low corresponding deflection, although other gauges gave readings at similar deflection magnitudes. The former reason led to an unpredicted greater difference obtained at gauge 1 for a 0.20 β magnitude. The average error percentage is 15.73%.

**f) 5ft_pre_center;** Figures B.13 and B.14

- 135,750 kips/ (in/in) of average initial slope for the predicted strain by FEM versus infinite slope for the experimental strain. Otherwise, good agreement exists, and the FEM overestimates surface strain near failure. Average error was 4.71%.
- Relatively similar to the **5ft_cip_center,** initial stiffness is almost identical at all measured points. Also, this initial agreement between plots is lower after cracking for the row of gauges next to the supporting beam, while this difference gets very large for the front row gauges; where the FEM significantly underestimates deflection from cracking load to around 80% of the failure load. The average error percentage is 14.97%.

**g) 5ft 8in_center;** Figures B.15 and B.16

- Average initial slope of 50,750 kips/ (in/in) for the FEM versus 31,200 kips/(in/in) for the experiment. Generally, plots were a little far from each other with an average error of 18.25%. FEM underestimates surface strain over the entire range of the plot.
- Initial stiffness is almost identical at all measured points. Also, this initial agreement between plots is lower after cracking; where the FEM underestimates

deflection from around half the cracking load value to around 85% of the failure load. 13.29% average error was obtained.

**h) 5ft_pre_corner;** Figures B.17 and B.18

- Identical initial slope was found for both surface strain plots of infinite magnitude until cracking loads. Generally, almost same trend for both plots is observed all over the plotting area with an increasing difference. Average error is 9.77%.
- Good initial deflection data agreement was obtained at all gauges except the front row gauges; 3, 5, 7, 9. Near failure loads, agreement seems to be switched between gauges. Average error is 43.53%.

**i) Specimen A;** Figures B.19 and B.20

- Identical average initial slope for both surface strain plots of 228,570 kips/(in/in). Generally, almost same trend for both plots is observed all over the plotting area with an average error of 11.88%.
- Unexpected deflection curves were obtained from experiments for some gauges, where some of them seemed to have stopped responding. Overall, good deflection data agreement was obtained with an average error of 10.84%.

**j) Specimen B;** Figures B.21 and B.22

- An average of 400,000 kips/(in/in) in surface strain initial slope from the FEM versus 280,000 kips/(in/in) obtained by experiments. Weak correlation between these methods in the DEMECs within the load transfer path; where the error reached 59.67%, while it is better correlated in the other sample DEMECs. the overall average difference is 23.69%.
- Deflection gauges, except gauge 1, seemed to not properly work. At gauge 1, a very good agreement was found with an error of just 10.26%. The overall average error is 33.08%.

**k) Specimen C;** Figures B.23 and B.24

- Good agreement of surface strains between experiments and FEM. An average of 110,000 kips/(in/in) initial slope for the FEM versus 86,700 kips/(in/in) obtained by experiments. Average error obtained was 8.58%.
- Almost identical initial stiffness for deflection data with an average of 9,900 kips/in. The average error gets relatively larger as load reaches failure. Overall average error is 13.63%.

**l) Specimen D;** Figures B.25 and B.26

- Nearly matching average initial slope of surface strain plots is observed with a magnitude of 290,400 kips/(in/in) for the FEM versus 241,000 kips/(in/in). DEMECs 12 and 144 seemed off of this comparison. The overall average error equals 13.96%.
- General good correlation of deflection data is obtained with an average error of 24.53%. Some gauges seemed to malfunction as in the previous tests.

**m) Specimen E;** Figures B.27 and B.28

- Same general trend of strain measurements, but absolute error difference is relatively large with an average of 21.03%. An average difference of initial slope of 27.48% also took place.
- Generally, good agreement in deflection data is obtained with an average error of 11.96%. FEM deflections at gauges 2&7, and 3&6 has been compared to the averages of experimental data at the same locations. Average initial stiffness obtained using FEM is 52,200 kips/in versus 50,100 kips/in by the experiments.

**n) Specimen F;** Figures B.29 and B.30

- Similar general trend of strain measurements. Trend of DEMEC 139 versus DEMECs 128 & 62 (experimental data) look different despite of symmetry of their location, this may be referred to the failure of one side of the deck, while the other one does not have that tendency. Additionally, experimental strain at DEMECs 58 and 84 have sharp fluctuating tendency (zigzag behavior), but both have an overall trend to increase. Remarkably, the FE mode could not catch up with these sudden changes. Average absolute error equals 24.19%.

- Generally, good agreement in deflection data is obtained with an average error of 17.52%. Three of the four deflection gauges on the failed half gave readings too much off the predicted ones by the FEM, while the ones on the other half were very close.

**o) Specimen G;** Figures B.31 and B.32

- Good correlation does the FEM has to the experimental's average error percentage is 20.71%. Alike DEMECs of Specimen F, the FEM of the DEMECs on the failed side are much closer to the experimentals' than the other non failed half. Additionally, experimental strain at DEMECs 58 and 84 have sharp fluctuating tendency (zigzag behavior), but both have an overall trend to increase. Similarly, the FE mode could not catch up with the sudden changes in strain readings for some of the DEMECs (17&105).
- Generally, good agreement in deflection data with an average error of 18.75%. data from gauges 8 and 7 were discarded, while the averages for 3&6, and 4&5 were considered as a reference to which FEM data were compared.

### 4.5.1- General comments

In general, the FEM behavior matched the experimental data. The average strain difference is 8.44% and 17.53% for the overhang testing and the welded rebar mats specimens respectively. Deflection differences are almost identical for both tests with an average of 19.92%.

Sudden changes in experimental data (zigzag behavior) which resembles the actual occurrence of crack opening and closing, or in general, the change of strain magnitude/type (tension/compression), compared to a relatively very slow response to such changes in the FE modeling. Such a slow response, probably, may be enhanced by using higher order elements, a much finer mesh, or a smaller loading steps.

Considering cracking and failure loads provided in Table 10, loads predicted by the FEM excellently matched the ones experienced experimentally. The average cracking load difference is -4.62% with a standard deviation of 9.96, and was +6.4% with standard deviation of 7.37 for failure loads.

Recognizing Figure 53, Figure 54, and Figure 55; the predicted average β that gives an approximate zero difference between the FE modeling curves and the experiments' is "0.186". This approximation is based on the linear interpolation principle. By the aid of other figures presented in Appendix B, another projected value of "0.18" may be a good estimation for future study. It should be emphasized that this suggestion is completely independent of the other two previously stated factors affecting modeling; namely are the bond between reinforcing steel and concrete, and the effect of microcracks.

Although, the predicted cracking and failure loads, and overall behavior of the modeled specimens using the FEM were satisfactorily close to the actual ones, we notice some differences between the two. Causes of these odd drifts might be referred to measuring errors, temporary malfunction of some of the deflection gauges, graphs are point-based representations of the measured data taken at discrete load intervals connected afterwards by straight lines; possible need to use a higher order brick element to catch up with some of the missing modeled performance may improve this situation. Moreover, the finite element models show slightly more stiffness than the test data in both the linear and nonlinear ranges. The effects of bond slip (between the concrete and reinforcing steel) and microcracks occurring in the actual bridge decks were excluded in the finite element models, contributing to the higher stiffness of the finite element models.

## 4.6- CONCLUSIONS

The outlined non-linear finite element program can save significant time and cost to experimental testing. This program has proven successful at modeling the performance of concrete bridge decks with interior and overhang loading. Both, 8-node hexahedron and line element were used to model the tested specimens. The program is aided with mesh generation subroutine to facilitate the input process. Mesh and load convergence tests have been performed for each specimen to obtain the number of elements and number of loading steps optimum for later on comparisons. For these specimens it was found that a shear reduction factor β of 0.20 showed the best correlation with the experimental data.

The results obtained were close to the experimental data. An average difference of -4.62% was predicted for cracking loads, and 6.40% for failure loads for all tests. Additionally, a 12.46% average surface strain difference, and 19.92% difference for deflection. Total standard deviation is 18.89%. A higher-order brick element would be expected to provide more accurate solution, especially what regards to some discrepancies in behavior modeling represented in the slow response to catch up with actual behavior displayed in graphs. However, these elements would be more computationally expensive and their increase in accuracy should be investigated with future work to justify their use.

Although the obtained results were pleasing, it is foreseen by the author that a shear reduction factor β magnitude of 0.18 will provide the most optimum results.

# CHAPTER V

# V. SIMPLIFIED HAND METHODS

## 5.1- INTRODUCTION

The quest for a more efficient procedure to estimate a reliable and quick solution for the problems subject of study and to adequately predict their observed behaviors, this led to investigating some of the available analysis and design methods and codes. In the current chapter, ACI[44] and AASHTO LRFD[22] design provisions are investigated to determine their estimated bridge deck capacities. FIP[45] design recommendations, the suggested shear design equations by Muttoni and Ruiz[46,47] based on the critical shear crack principle, and Strut-and-Tie method (STM) have been used to reach the same goal as well.

Reinforced concrete slabs without shear reinforcement are commonly used in many structural systems, such as bridge deck slabs, flat slabs of buildings, parking garages, and cut-and-cover tunnels. Shear is usually the governing failure mode at ultimate of these slabs without shear reinforcement[47]. One-way shear is found for distributed loading and close to support lines, where parallel shear forces in the slab develop. On the contrary, two-way shear (punching shear) is associated to concentrated loading, since shear forces develop radially to introduce the load in the slab. Intermediate cases between one- and two-way shear, where shear forces in a slab develop neither parallel nor radially[48,49,50] are also found in practice.

Currently, codes of practice provide several approaches to check the one- and the two-way shear strength of flat slabs. Nevertheless, some codes either have conservative predictions, like ACI 318-08[44], or closer measures in others, sometimes overestimated, like the case with FIP recommendations[51]. These significant differences in ACI 318-08[44] are due to the fact that punching shear formulation accounts neither for the role of the reinforcement ratio nor for the size of the member[51]. The former findings were obtained by a series of experimental puching tests on slabs by Guandalini et al. 2009[51].

Based on the critical shear crack theory, Muttoni and Ruiz[46,47] derived their shear design equations. The amount of shear that can be transferred across the critical shear crack depends on the roughness of the crack, which in turn is a function of the maximum aggregate size[46]. Shear is initially resisted by three shear-carrying mechanisms: cantilever action, aggregate interlock, and dowel action. These mechanisms create a state of tensile stresses in the concrete that leads to the development of the critical shear crack. The development of the critical shear crack cancels the three previous shear-carrying mechanisms. A new one, the arching action, is activated. The parameters governing the arching action (and thus the shear strength) are then the location of the critical shear crack, its width, and the aggregate size.

To overcome some of the obstacles associated with simplified code provisions, strut and tie modeling (STM) can be used. These models are especially useful in predicting shear failure [52]. STM idealizes a series of trusses within the member to model the flow of forces. Consequently, this method has been validated and improved considerably in the form of full member or sectional design procedures. STM design provisions consist of rules for defining the dimensions and ultimate stress limits of struts and nodes as well as the requirements for the distribution and anchorage of reinforcement. The flexibility afforded by the method allows for the development of multiple solutions for the same problem. Consequently, sound engineering judgment and design experience are fundamental to achieve a safe and optimal solution.

In parallel with the increasing availability of experimental results and the development of limit analysis in plasticity theory, and discussions raised[53] on the adequacy of current strength factors for concrete struts, STM is listed as an alternate procedure in several sections of the previously mentioned codes (e.g. corbels, short shear walls), and currently required for shear strength design of deep beams. The mentioned discussions have been triggered by the significant discrepancies that exist between the proposed values in design codes and those predicted by STM; In some cases, the latter ones are substantially lower than those given in the ACI design code, especially for higher strength concrete(53).

## 5.2- FORMULATIONS OF DESIGN CODES

Hereinafter the formulations associated with the ACI 318-08(44), and AASHTO LRFD(22) design codes, and FIP Recommendations(45) grouped according to the internal force category:

### 5.2.1- Flexural capacity

$$M_n = A_s f_y \left( d - \frac{a}{2} \right) + A_s^{'} f_s^{'} \left( \frac{a}{2} - d' \right), \quad \frac{a}{2} > d' \qquad \text{.................. (1)}$$

Where:

$A_s$ = Total Area of tension reinforcement (in.$^2$).
$A_s^{'}$ = Area of rebars in compression zone (in.$^2$).
$f_y$ = Yield stress of tension reinforcement (psi).
$f_s^{'}$ = Level of stress of rebars in compression zone (psi).
d = Depth of tension reinforcement (in.).
$d^{'}$ = Depth of rebars in compression zone (in.).
a = Depth of compression block (Whitney's block) (in.).
= $\beta_1 c$
c = Distance from extreme compression fiber to the neutral axis of the cross section (in.).
$\beta_1 = 0.85 - .05(f_c^{'} - 4); \geq 0.65$
$\leq 0.85$ ................................ (ACI 318-08(44) and AASHTO LRFD(22))
$\beta_1 = 0.80$ ............................................................. (FIP 1996(45))
$M_n$= Nominal moment capacity of the cross section (lb-in.).

### 5.2.2- Shear capacity

a) One-way Shear

Since the bridge decks investigated did not have shear reinforcement, the nominal shear capacity, $V_n$, will be equal to the shear capacity of the concrete, $V_c$. For members subjected to shear and flexure only, ACI 318-08(44) provides the following formulae:

$$V_c = 2\sqrt{f_c^{'}} b_w d \qquad \text{.............................................. (2)}$$

$$V_c = 2\left(1+\frac{N_u}{2000A_g}\right)\sqrt{f_c^{'}}b_w d \quad \text{......................... (3)}$$

$$V_c = \left(0.6\sqrt{f_c^{'}}+700\frac{V_u d_p}{M_u}\right)b_w d \quad \text{....................... (4)}$$

Where:

$b_w$ = Width of the web of the cross section (in.).
$f_c^{'}$ = 28 day cylinder compressive strength (psi).
$N_u$ = Applied compressive force, +ve for compression (lb).
$A_g$ = Gross area of the section (in.$^2$), and $N_u/A_g$ in psi.
$d_p$ = Depth of prestressing strands (in.).
$V_u$ and $M_u$ = Ultimate shear and bending moments respectively, taken simultaneously at the critical section (lb) & (lb.in.).

Equations 2 and 3 are specifically applied for non-prestressed members, while equation 4 is applied to prestressed members.

In equation 4, Vc need not be taken less than $2\sqrt{f_c^{'}}b_w d$ nor greater than $5\sqrt{f_c^{'}}b_w d$. Additionally, $V_u d_p/M_u$ shall not be taken greater 1.0.

AASHTO LRFD(22) shear design equation for non-prestressed members is exactly eq.(2), while its provision for prestressed members (which is provided as a more detailed procedure in ACI 318-08(44) as well) is as follows:

$V_c$ is the lesser of $V_{ci}$ and $V_{cw}$, where;

$$V_{ci} = 0.02\sqrt{f_c'}b_v d_v + V_d + \frac{V_i M_{cre}}{M_{\max}} \geq 0.06\sqrt{f_c'}b_v d_v \quad \text{....................... (5)}$$

$$; \quad M_{cre} = S_c\left(f_r + f_{cpe} - \frac{M_{dnc}}{S_{nc}}\right)$$

$$V_{cw} = \left(0.06\sqrt{f_c'} + 0.30 f_{pc}\right)b_v d_v + V_p \quad \text{....................................... (6)}$$

$V_{ci}$ = nominal shear resistance provided by concrete when inclined cracking results from combined shear and moment (kip).
$V_{cw}$ = nominal shear resistance provided by concrete when inclined cracking results from excessive principal tensions in web (kip).
$V_d$ = shear force at section due to unfactored dead load and includes both DC and DW (kip).

$V_i$ = factored shear force at section due to externally applied loads occurring simultaneously with M,, (kip).
$M_{cre}$ = moment causing flexural cracking at section due to externally applied loads (kip-in).
$M_{max}$ = maximum factored moment at section due to externally applied loads (kip-in).
$f_{cpe}$ = compressive stress in concrete due to effective prestress forces only (after allowance for all prestress losses) at extreme fiber of section where tensile stress is caused by externally applied loads (ksi).
$M_{dnc}$ = total unfactored dead load moment acting on the monolithic or noncomposite section (kip- ft.).
$S_c$ = section modulus for the extreme fiber of the composite section where tensile stress is caused by externally applied loads (in.$^3$).
$S_{nc}$ = section modulus for the extreme fiber of the monolithic or noncomposite section where tensile stress is caused by externally applied loads (in$^3$)
$f_{pc}$ = compressive stress in concrete (after allowance for all prestresss losses) at centroid of cross section resisting externally applied loads or at junction of web and flange when the centroid lies within the flange (ksi). In a composite member, $f_{pc}$ is the resultant compressive stress at the centroid of the composite section, or at junction of web and flange, due to both prestresss and moments resisted by precast member acting alone.
$V_p$ = Vertical component of Prestress force (lb).

FIP[45] formulations for one-way shear is as follows:

$$V_{RD} = b_w\, d\;\; 0.12\;\; f_{ck}^{2/3}\; \beta_N \,/ \left(1 + 0.007\, d/\rho\right) \text{ ............................... (7)}$$

Where:

$V_{RD}$ = Nominal concrete shear capacity (N).
d = Effective depth (m).
$f_{ck}$ = Concrete compressive strength (MPa).
$\rho = A_s/(bd)$ = reinforcement ratio of transverse reinforcement.
$\beta_N = (1-(\sigma_N/400)\,(d/\rho))$ = factor of influence of axial forces or of prestress.
$\sigma_N = N/bd$ = axial stress (MPa); (+ve for tension)

Mutttoni and Ruiz[46,47] proposed the upcoming simplified design equation, which is giving slightly more conservative values than those obtained by using other design codes[46]; namely ACI 318-08[44], and AASHTO LRFD[22]. The following equation has been adopted by the Swiss code for structural concrete (SIA 262)[56]:

$$V_R = \frac{2.3}{1 + 0.056d\,\dfrac{m_{Ed}}{m_{RD}}}\, bd\sqrt{f_c^{/}} \text{ ............................................... (8)}$$

When an axial force is applied to the member, the critical crack width may be increased or diminished. To take this phenomenon into account, $m_{Ed}$ has to be replaced by ($m_{Ed}$ –

$m_{Dd}$) and $m_{Rd}$ by ($m_{Rd}$ – $m_{Dd}$), where $m_{Dd}$ is the decompression moment (bending moment causing εs = 0), whose value can be taken as:

$$n_d < 0: m_{Dd} = -n_d\left(\frac{h}{2} - \frac{d}{3}\right)$$
$$n_d > 0: m_{Dd} = -n_d\left(\frac{h}{2} - d'\right) \qquad \text{.......................} (9)$$

Where:

b = Thickness of member (in.).
d = Effective depth (in.).
d′ = Distance from extreme compression fiber to centroid of longitudinal compression reinforcement (in.).
fc′ = Specified concrete uniaxial strength in compression (American practice) (psi).
h = Height of cross section (in.).
$m_{Ed}$ = Design (factored) moment per unit length in critical section (lb.in.).
$m_{Rd}$ = Plastic design (factored) moment per unit length in critical section (lb.in.).
$\varepsilon_s$ = Steel strain.
$n_d$ = Axial force (lb.).
$V_R$ = Shear strength (lb.).

b) Two-way (Punching) shear

ACI 318-08(44) and AASHTO LRFD(22) have the same punching shear formula for non-prestressed slabs and footings, while ACI 318-08(44) introduces the tools accounting for the prestress effect, providing that the critical section is located at “d/2” all around the loading plate area. Hereinafter, the equations proposed for the non-prestressed members:

$$V_c = \left(2 + \frac{4}{\beta}\right)\sqrt{f_c^{'}}b_o d \ \le \ 4\sqrt{f_c^{'}}b_o d$$
$$\le \left(\frac{\alpha_s d}{b_o} + 2\right)\sqrt{f_c^{'}}b_o d \qquad \text{................................} (10) \ \text{(ACI 318-08}^{(44)}$$

Where:

β = Ratio of long sideto short side of the column.
bo = Perimeter of critical section located at distance of d/2 around the column (in).
$\alpha_s$ = 40 for interior columns, 30 for edge columns, and 20 for corner columns.

For prestressed slabs and footings, ACI 318-08(44) provides the following equation:

$$V_c = \left(\beta_\rho \sqrt{f_c^{'}} + 0.3 f_{pc}\right) b_o d + V_p \qquad \text{......................................} \ (11)$$

Where:

$\beta\rho$ = the smaller of 3.5 and ($\alpha_s$ d/bo + 1.5)

FIP[45] Recommendation provides these equations for non-prestressed Two-Way shear design, providing that the critical section is located at “2d” distance all around the loading plate area:

$$P_{RD} = 0.12 \ \xi \ /\left(100 \ f_{ck} \ \rho\right)^{1/3} u_1 \ d \qquad \text{......................................} \ (12)$$

Where:

$P_{RD}$ = Nominal concrete punching shear capacity (N).
$\xi$ = (1 + 200/d) factor for size effect, with d in (mm).
$\rho = \sqrt{\rho_x \rho_y}$

FIP provides the following equations[54] as well to account for the prestress effect:

$$P_{RD_{eff}} = P_{RD} + P_{po} \qquad \text{........................................} \ (13)$$

Where:

$P_{RDeff}$ = Effective nominal concrete punching shear capacity with prestress effect included (N).
$P_{po}$ =Equivalent decompression punching force (N) = $\dfrac{P_{yo}b_x + P_{xo}b_y}{b_x + b_y}$
Pxo, Pyo = Decompression forces corresponding to prestress in x and y direction respectively (N).

$$P_{xo} = \frac{M_{yo}}{M_{yRd}} P_{Rd} \quad ; \quad P_{yo} = \frac{M_{xo}}{M_{xRd}} P_{Rd}$$

$M_{xRd}$ & $M_{yRd}$ = Bending moments at the column face in widths $b_x$ and $b_y$ respectively.
$M_{xo}$ & $M_{yo}$ = Decompression moments in the widths $b_x$ and $b_y$ respectively (N.mm).

$$M_{xo} = \sigma_{cpy} \frac{b_x h^2}{6} \quad \& \quad M_{yo} = \sigma_{cpx} \frac{b_y h^2}{6}$$

$\sigma_{cp} = \dfrac{P}{h}$, calculated for unit width (N/mm/mm).

Muttoni's[47] formulations for the two-way shear strength are as follows:

$$V_R = \frac{8.0}{1+20\dfrac{\psi d}{d_{g0}+d_g}} bd\sqrt{f_c^{/}} \quad \text{..................................} \ (14)$$

Where ψ is the rotation of slab outside the column region. The resulting load rotation relationship is thus:

$$\psi = 0.33\frac{L}{d}\frac{f_y}{E_s}\left(\frac{V_d}{8m_{Rd}}\right)^{3/2} \quad \text{....................} \ (15)$$

Where:

$V_d$ = The factored shear force (lb.)..
dg = Maximum aggregate size (in.).
dg0 = Reference aggregate size (0.63 in).
$V_R$ = Design punching shear strength (lb.).
$m_{Rd}$ = Design moment capacity per unit width (lb.in./in.).
$E_s$ = Modulus of elasticity of reinforcement (psi).
L = Main span of a slab system (in.).

Equation (15) is formulated for intermediate columns; for edge columns, the constant 8 is to be replaced by 4 and for corner columns by 2.

## 5.3- STRUT AND TIE MODELLING (STM)

Figure 56 shows the elastic stress distribution of a bottle-shaped strut as well as the adopted STM. There are two efficiency factors associated with bottle-shaped struts(52). These two factors are based on the reinforcement within the strut. As the compression spreads out from the support, tension is developed. In Figure 56, the compression is applied vertically, and the induced tension is horizontal. When the induced tensile stress exceeds the tensile strength of the concrete, a vertical crack will form. Without any horizontal reinforcement, the strut would split, causing a brittle failure. This phenomenon is the basis of the split cylinder test (ASTM C496(55)) used to determine the tensile strength of concrete. Nevertheless, if sufficient transverse reinforcement exists, brittle failure can be avoided, and the strut can continue to carry load beyond cracking.

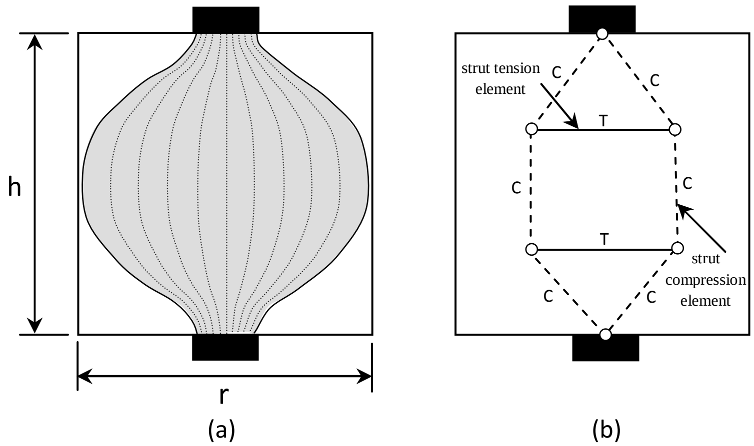


**Figure 56:** a) Bottle-shaped strut; and b) refined Strut.

ACI 318-08[44] provisions provided in Appendix A have been applied in this work. A bottle-shaped strut, Figure 56 (b), is used to model the compression member of a STM with no detailed node geometry needed to be modeled. This model has been promoted after the evaluation of various node capacities; which (the nodes) were found to have more capacity than the other elements in the 3-D truss analogy. Because of the absence of shear reinforcement in the bridge decks, the most sensitive element and consequently the first vulnerable to failure is the tensile element in struts. These are labeled in Figure 56. If either tie fails then the strut will not be able to carry any additional loads. The nominal compressive strength of a strut without longitudinal reinforcement, Fns, was taken as

$$F_{ns} = f_{ce} A_{cs} \quad \text{.......................................................} \; (12)$$

Where:

$A_{cs}$ = The cross sectional area at one end of the strut.

fce = The effective compressive strength of the concrete is taken as:

$f_{ce} = 0.85 \beta_s f_c^{/}$ , $\beta_s = 0.60$ (since strut reinf. does not satisfy Section A.3.3 requirements (ACI318-08[44])

Nominal compressive strength of nodal zones has exactly the same form of eq.(12) for the experiments studied. Nominal strength of a tie, Fnt, is taken as,

$$F_{nt} = A_{ts} f_y + A_{tp}\left(f_{se} + \Delta f_p\right) \text{ ....................................} (13)$$

Where:

$A_{ts}$ = Area of non-prestressed reinforcement in a tie (in.$^2$).
$A_{tp}$ = Area of prestressing steel in a tie (in.$^2$).
$f_{se}$ = Effective stress in prestressing steel (after allowance for all prestress loss) (psi).
$\Delta f_p$ = Increase in stress in prestressing steel due to factored loads (psi).

Tie elements considered in this modeling is either representing steel reinforcements; elements 1 &2 in Figure 57 and Figure 58, or the pure tensile capacity of concrete within the compression struts; elements 3&4 in Figure 57 and 3,4,5&6 in Figure 58. Additionally, the cross sectional area of strut's compression elements were taken as half of their total area magnitude at the loaded nodes. Resultants of the prestress strand forces were placed compressing the rollers at the free ends of the modeled test specimens.

In order to obtain the most accurate information from the STM analysis an event to event (Multistage) analysis technique was used. This allowed the capacity of a member to be found within a STM and then the stiffness provided by the member is removed and then the analysis continues with the remaining members and stiffness. Additionally, while modeling various tests using STM, once a tie representing reinforcement reaches its tensile capacity; an equivalent force in magnitude and direction of that tie will replace it. This procedure is used to account for the yield plateau portion of the stress-strain diagram of the reinforcing steel. On the other hand, once any of the two tension elements (ties) connecting other strut elements together fails; all strut is removed in the next loading stage. A full graphical representation of the Multistage STM analysis technique presented on Figure 63 through Figure 78.

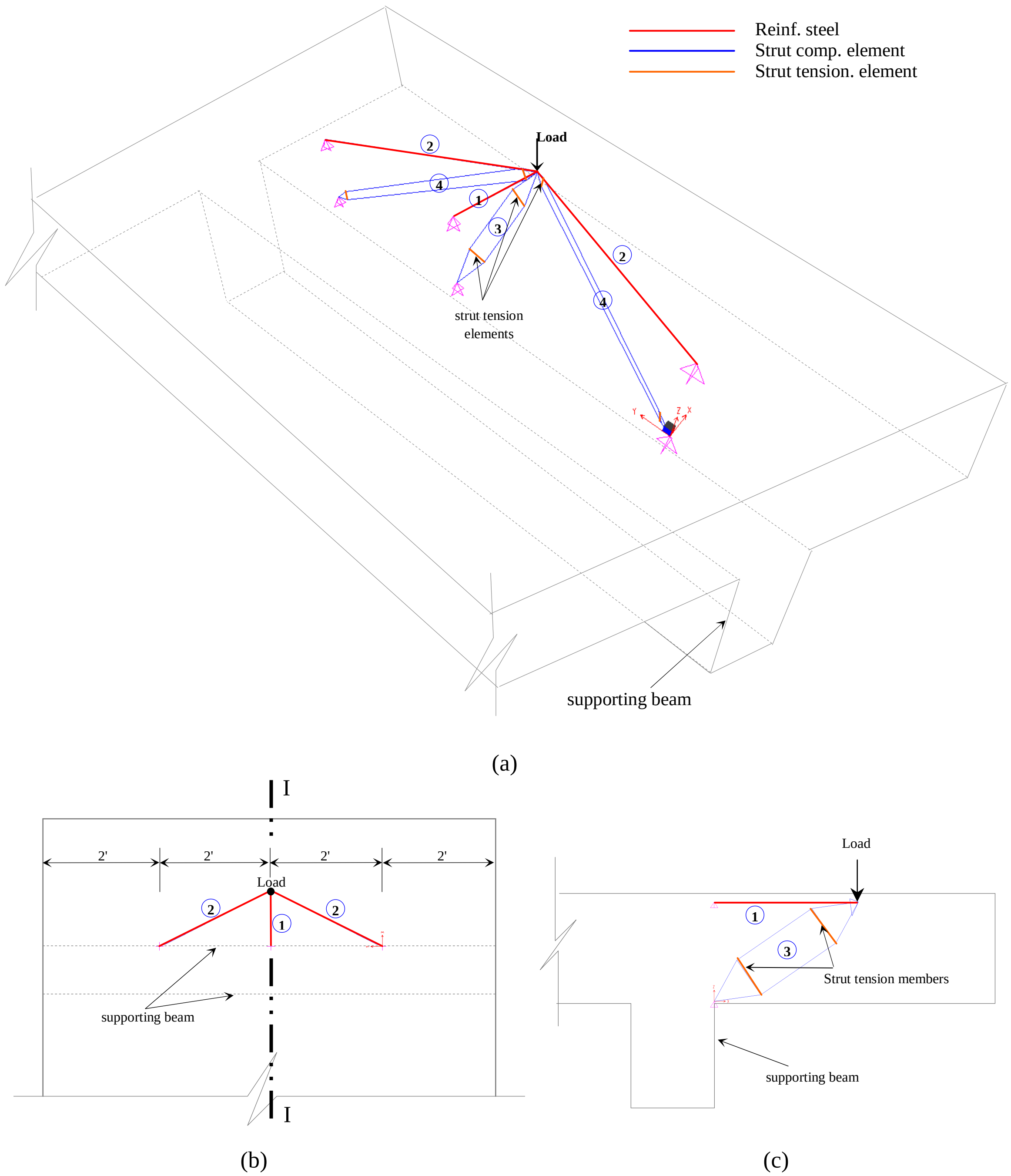


**Figure 57:** STM for overhang specimens: a) 3D view, b) Top plan view, and c) side view at section I-I

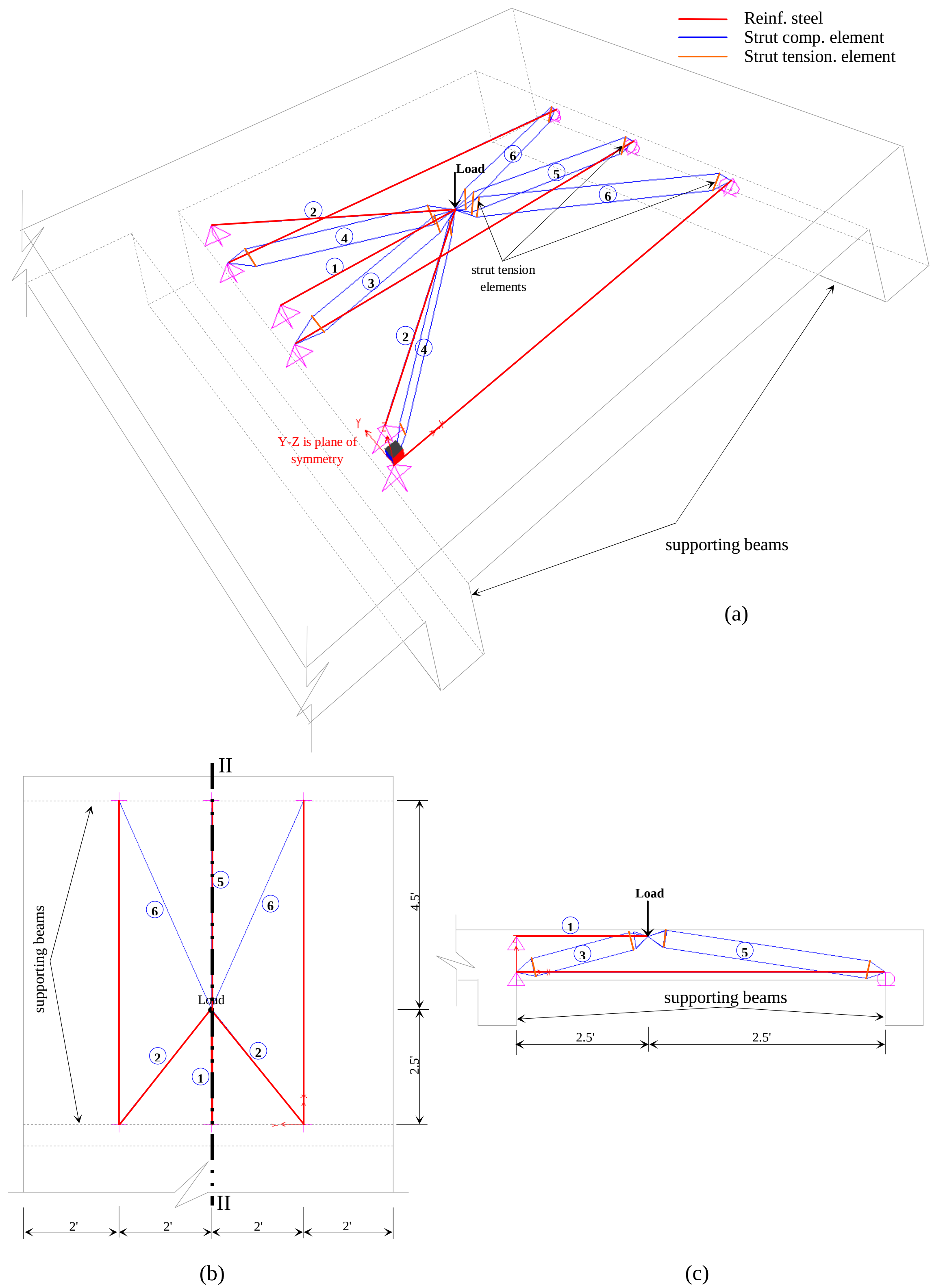


**Figure 58:** STM for welded rebar mats' specimens: a) 3D view, b) Top plan view, and c) side view at section II-II

### 5.3.1- Determination of the tensile capacity of the tie element in the concrete strut

One challenge that has plagued past users of STMs is that there is little guidance on how to determine the tensile capacity of concrete in a compression strut. Because of this lack of guidance it is typical to assume that these elements have no tensile capacity. Although this assumption is not accurate, it is conservative. Without this information it is very challenging to produce STMs that accurately predict the failure of a complex structure.

Based on past experiments and analysis it was found that the failure mode of the 5ft_cip_center experiment is a tension tie failure, Figure 59. Because the compression strut did not fail, it could be analyzed to determine more information about the capacity of the tensile members holding its compression elements together. Since the tensile capacity was measured from concrete sampled during placement, a geometry of the compression strut tension members was determined and subsequently the cross sectional area. This area was found to be 41 in2 (an equivalent diameter of 7.23") for the assumed geometry.

Although, geometrical properties in STM tends to increase strut's force and consequently the tie's as it becomes shallower (which means a higher applied stress), but has been found when using the same reference area that a higher (compared to experiments) failure load is obtained. This was a serious issue for the welded rebar mats where a failure load as high as 170% than the actual load was obtained.

Because of the absence of shear reinforcement, the major element responsible for the strut's strength is the tie, and it is obvious from Figure 60 that as the strut gets very shallow (low slope), the tie length gets smaller and consequently its cross sectional area as well. Accordingly, a factor had to be found to reduce the tie area as the slope of strut gets lower. This factor was taken as the strut angle from horizontal axis referenced to the reference angle and reference area obtained from the evaluation of the tie area for the 5ft CIP overhang loaded at center. In other words, struts tie area is taken proportional to the inclination of the strut taking the angle shown in the Figure 59 as a reference, i.e.;

$$\text{current model area} = 41\text{in.}^2 \text{ x current strut inclination (angle)} / 24.62°$$

Having the area magnitude, the tensile capacity of the strut may be determined!

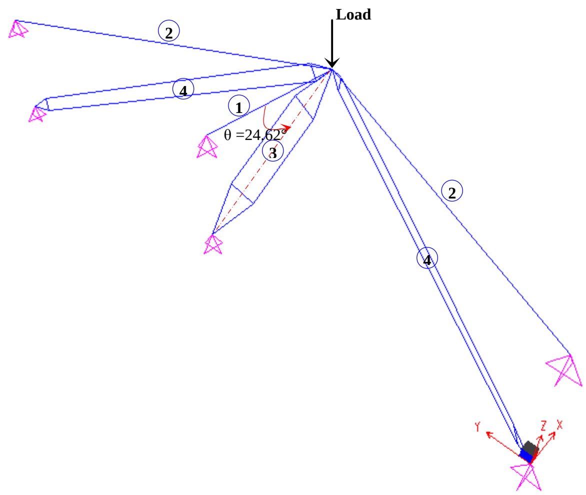


**Figure 59:** STM for 5ft_cip_center overhang test

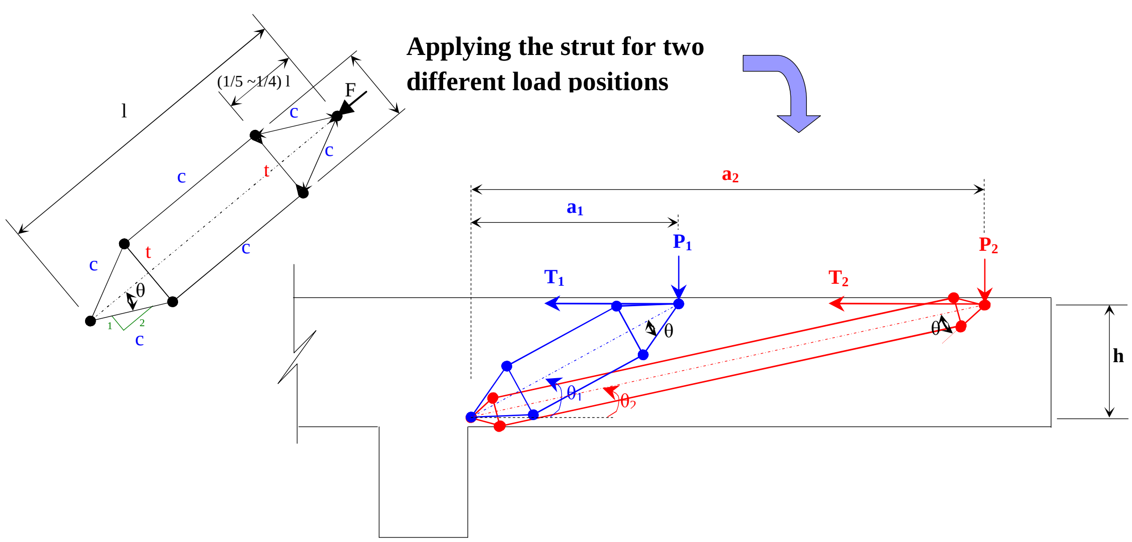


**Figure 60:** Effect of strut inclination on tie lengths and its overall geometry

## 5.4- NUMERICAL APPLICATION

All design equations stated in sections 5.2, and 5.3 are numerically applied in this section. Actual materials data are utilized in equations listed previously. Figure 61 and Figure 62 show an overall graphical comparison of the three design codes and recommendations, STM, and FEM to the experimental data. Section analysis for cracking loads has also been determined for all tests. More comprehensive numerical comparison is provided in tables C.1 through C.4. STM results are provided in Table 11 and Table 12. A full graphical representation of the analysis progression presented in Table 11and Table 12 is displayed on Figure 63 through Figure 78. An overall comparison of the absolute average errors for failure loads predicted by the simple hand methods and FEM are shown in Table 13. Additionally, absolute average errors for cracking loads predicted by section analysis and FEM are presented in Table 14.

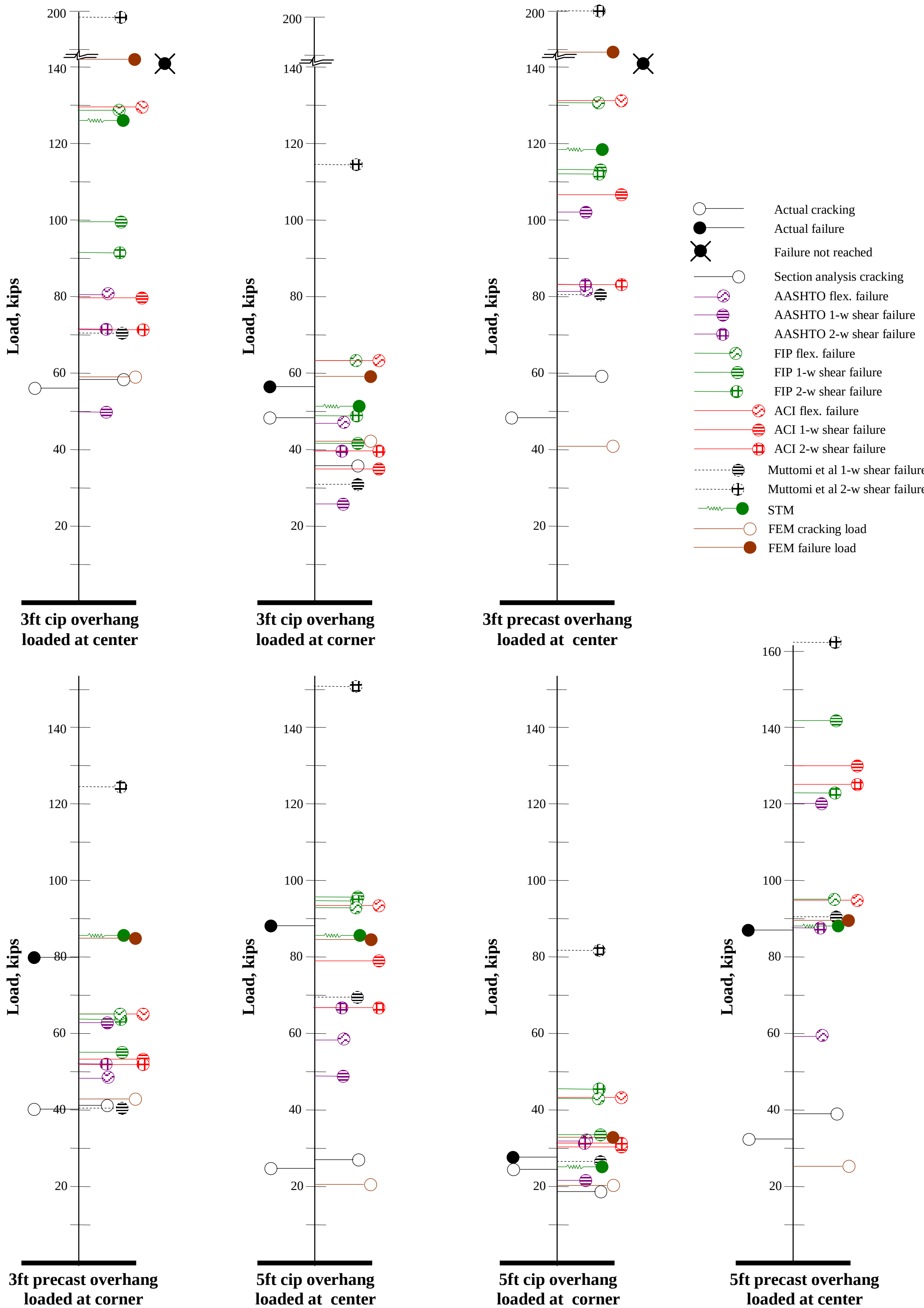


**Figure 61:** Cracking and failure loads for overhang tests

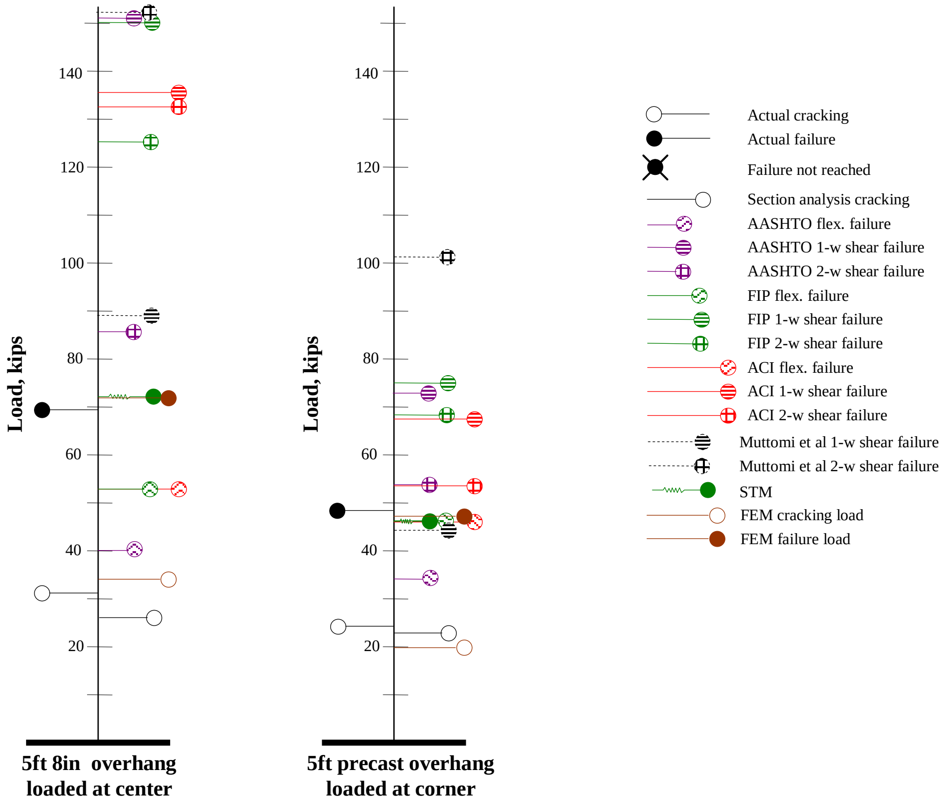


**Figure 61 (*cont.*):** Cracking and failure loads for overhang tests

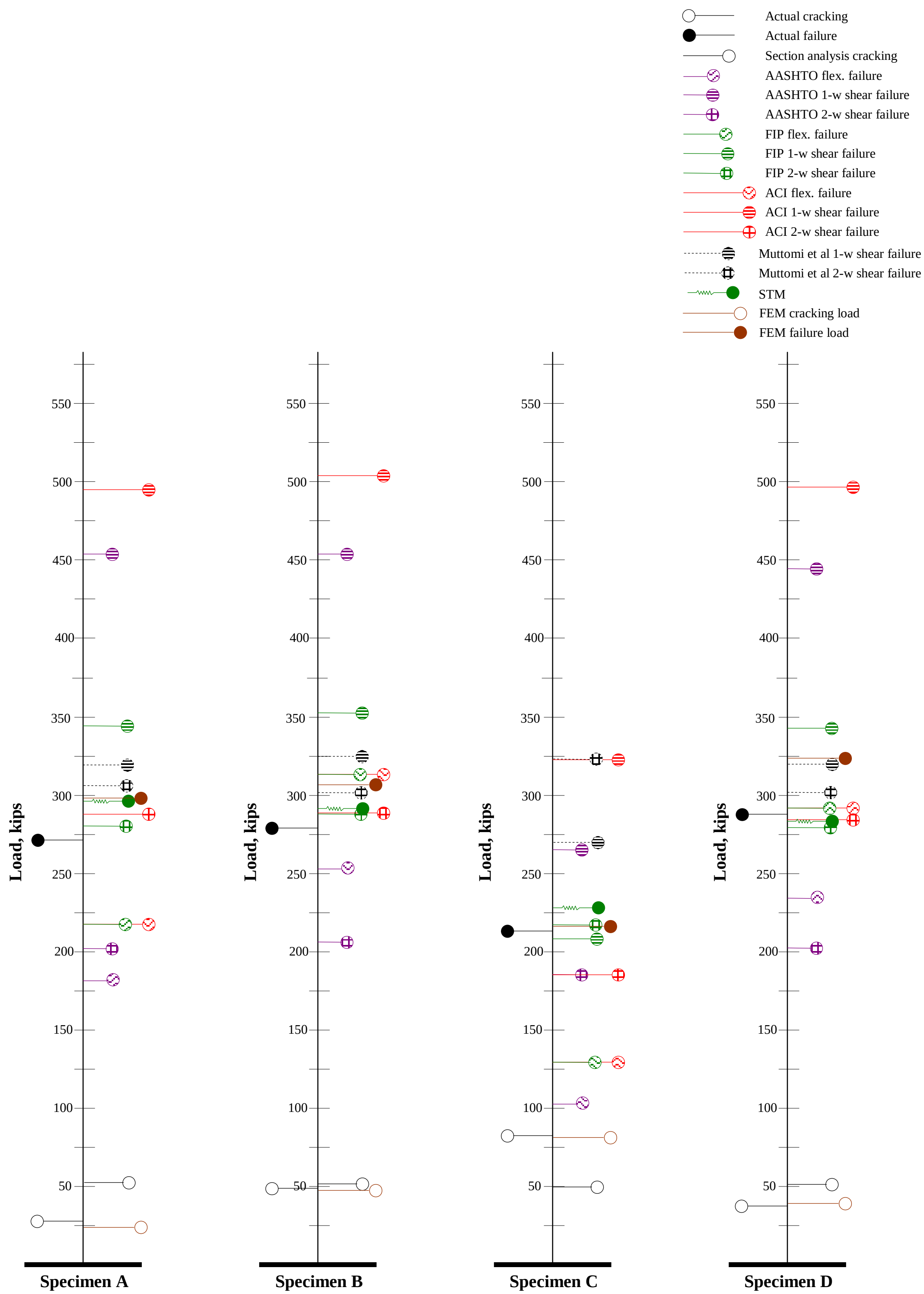


**Figure 62:** Cracking and failure loads for welded rebar mats specimens

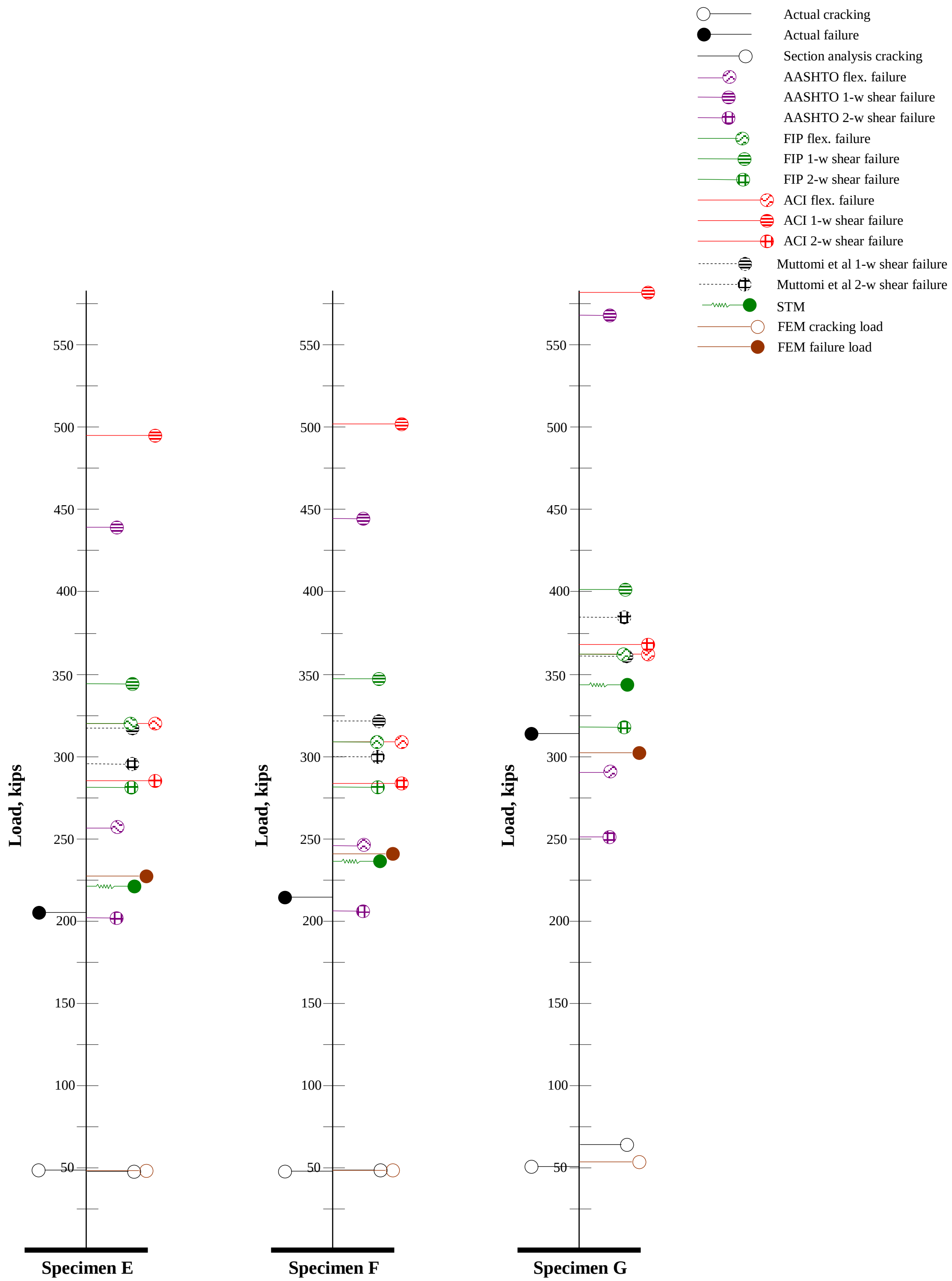


**Figure 62 (*cont.*):** Cracking and failure loads for welded rebar mats specimens

**Table 11:** Determination of failure mode using STM for overhang tests

| Specimen | Failure load predicted by STM, kips | Experimental Failure load, kips | % Difference | Simulated failure sequence/failure load of strut & tie elements, Kips | | | | Failure mode | | Experimentally measured concrete stresses | | | |
|---|---|---|---|---|---|---|---|---|---|---|---|---|---|
| | | | | Short tie ** (1) | Diag. tie ** (2) | Short strut ** (3) | Diag. strut ** (4) | predicted by STM | Experimentally observed | Compressive, psi | | Tensile, psi | |
| | | | | | | | | | | CIP/Precast( stage I) | Precast (Stage II) | CIP/Precast( stage I) | Precast (Stage II) |
| 3ft_cip_center | 127.0 | >103.5 | --- | i | ii | iii-s | iv-s* | Tension failure | --- | 6976 | --- | 660 | --- |
| | | | | 58.0 | 84.5 | 126.6 | 127.0 | | | | | | |
| 3ft_cip_corner | 51.5 | 56.2 | -8.4 | i | | ii-s | iii-s | Comp. strut | Punching | 5371 | --- | 514 | --- |
| | | | | 39.5 | | 50.5 | 51.5 | | | | | | |
| 3ft_pre_center | 118.3 | >96.0 | --- | i | | ii-t | iii-t | Comp. strut | --- | 9098 | 7096 | 729 | 620 |
| | | | | 58.0 | | 77.8 | 118.3 | | | | | | |
| 3ft_pre_corner | 85.5 | 80.0 | 6.9 | i | ii | ii-t | | Comp. strut/Tension | Comp. Strut failure + Punching | 9151 | 6857 | 796 | 550 |
| | | | | 38.5 | 85.5 | 85.5 | | | | | | | |
| 5ft_cip_center | 86.2 | 88.0 | -2.1 | i | ii | iii-s | iv-s* | Tension failure | Tension failure | 5730 | --- | 514 | --- |
| | | | | 41.5 | 75.5 | 84.8 | 86.2 | | | | | | |
| 5ft_cip_corner | 24.8 | 27.5 | -10.0 | | | i-s | ii-s | Comp. strut | | 3369 | --- | 220 | --- |
| | | | | | | 17.3 | 24.8 | | | | | | |
| 5ft_pre_center | 88.0 | 87.0 | 1.2 | i | ii | iii-b* | iii-b* | Tension failure | Tension failure | 9682 | 8740 | 713 | 792 |
| | | | | 41.5 | 87.5 | 88.0 | 88.0 | | | | | | |
| 5’-8”_ center | 72.5 | 69.0 | 5.1 | i | ii | iii-s | iv-s* | Tension failure | Tension failure | 9311 | 9483 | 597 | 597 |
| | | | | 38.0 | 65.3 | 71.9 | 72.5 | | | | | | |
| 5ft_pre_corner | 46.5 | 48.0 | -3.1 | i | | ii-s | iii-s | Comp. strut | | 9311 | 9483 | 597 | 597 |
| | | | | 28.0 | | 42.3 | 46.5 | | | | | | |
| **Absolute error average =** | | | **5.3** | | | | | | | | | | |

- * Very little participation in the ultimate failure
-** Refer to Figure 57
- b designates strut bottom splitting
- t designates strut top splitting
- s designates strut simultaneous top and bottom splitting

**Table 12:** Determination of failure mode using STM for welded rebar mats tests

| Specimen | Failure load predicted by STM, kips | Experimental Failure load, kips | % Difference | Simulated failure sequence/failure load of strut & tie elements, kips | | | | | | Final failure | | Experimentally measured stresses | | | |
|---|---|---|---|---|---|---|---|---|---|---|---|---|---|---|---|
| | | | | | | | | | | | | Compressive, psi | | Tensile, psi | |
| | | | | Short tie ** (1) | Diag. tie ** (2) | 3ft Short strut ** (3) | 3ft Diag. strut ** (4) | 5ft Short strut ** (5) | 5ft Diag. strut ** (6) | predicted by STM | Experimentally observed | CIP | Precast | CIP | Precast |
| Specimen A | 296.9 | 272.0 | 9.1 | | | iii | ii | | i | Comp. strut | Punching | 6490 | 10050 | 540 | 790 |
| | | | | | | 296.9 | 218.6 | | 218.0 | | | | | | |
| Specimen B | 286.7 | 279.0 | 2.8 | iii | v | ii | iv | | i | Comp. strut | Punching | 5220 | 10540 | 410 | 760 |
| | | | | 245.8 | 286.7 | 216.1 | 253.4 | | 176.8 | | | | | | |
| Specimen C | 227.6 | 212.0 | 7.4 | ii | iii | v | iv | | i | Tension/ Comp. strut | Punching | 6240 | ---- | 380 | ---- |
| | | | | 179.2 | 182.1 | 227.6 | 182.4 | | 155.1 | | | | | | |
| Specimen D | 283.9 | 287.0 | -1.1 | iii | iv | ii | v | | i | Comp. strut | Punching @ cip only | 5300 | 10130 | 510 | 770 |
| | | | | 235.5 | 248.6 | 229.2 | 283.9 | | 184.7 | | | | | | |
| Specimen E | 223.4 | 204.0 | 9.5 | iii | iv | ii | v | | i | Comp. strut | P/S panel flex. failure & Support failure | 4500 | 10130 | 430 | 790 |
| | | | | 206.5 | 219.9 | 189.4 | 223.4 | | 155.4 | | | | | | |
| Specimen F | 234.8 | 215.0 | 9.2 | iii | iii | ii | iii | | i | Comp. strut | Splitting & Punching | 4920 | 10380 | 480 | 790 |
| | | | | 234.8 | 234.8 | 200.0 | 234.8 | | 164.0 | | | | | | |
| Specimen G | 344.3 | 314.0 | 9.6 | iv | | i | v | iii | ii | Comp. strut | Punching | 8850 | Not tested | 730 | Not tested |
| | | | | 335.2 | | 228.8 | 344.3 | 286.0 | 234.6 | | | | | | |

**<u>Absolute</u> error average = 7.0**

- All struts failed at the top tension tie
-** Refer to Figure 58

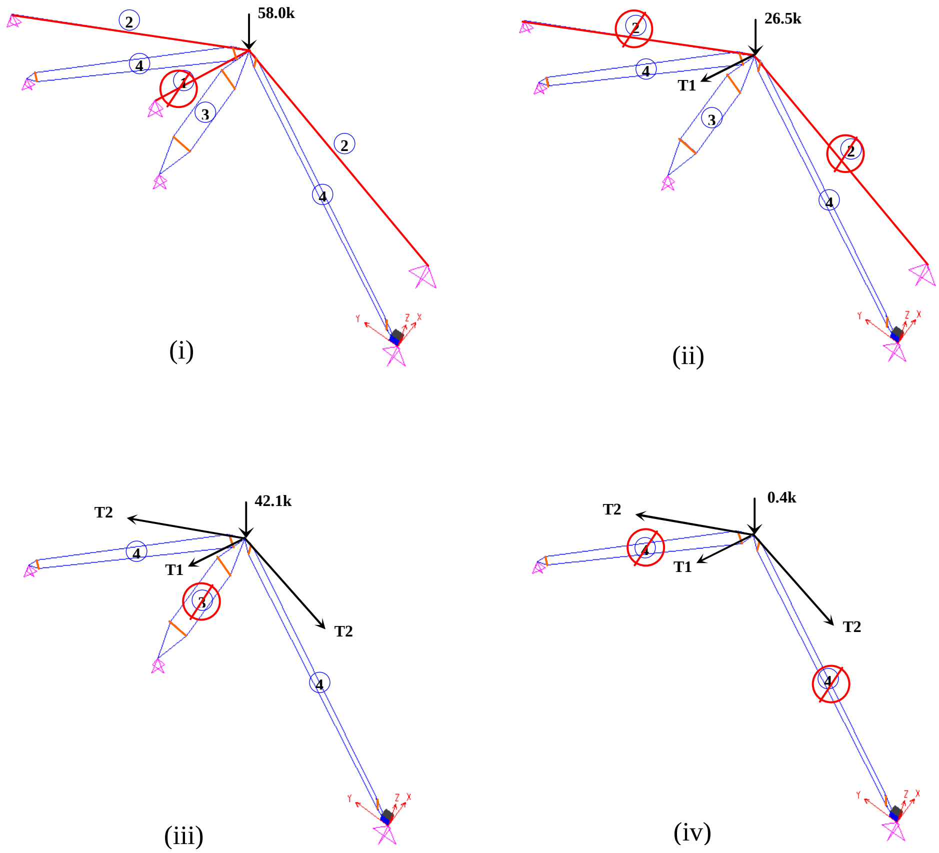


T1 = Equivalent yield force in short tie
T2 = Equivalent yield force in diagonal tie
Failed element

**Figure 63:** Failure sequence predicted by STM for the 3ft CIP overhang loaded at center

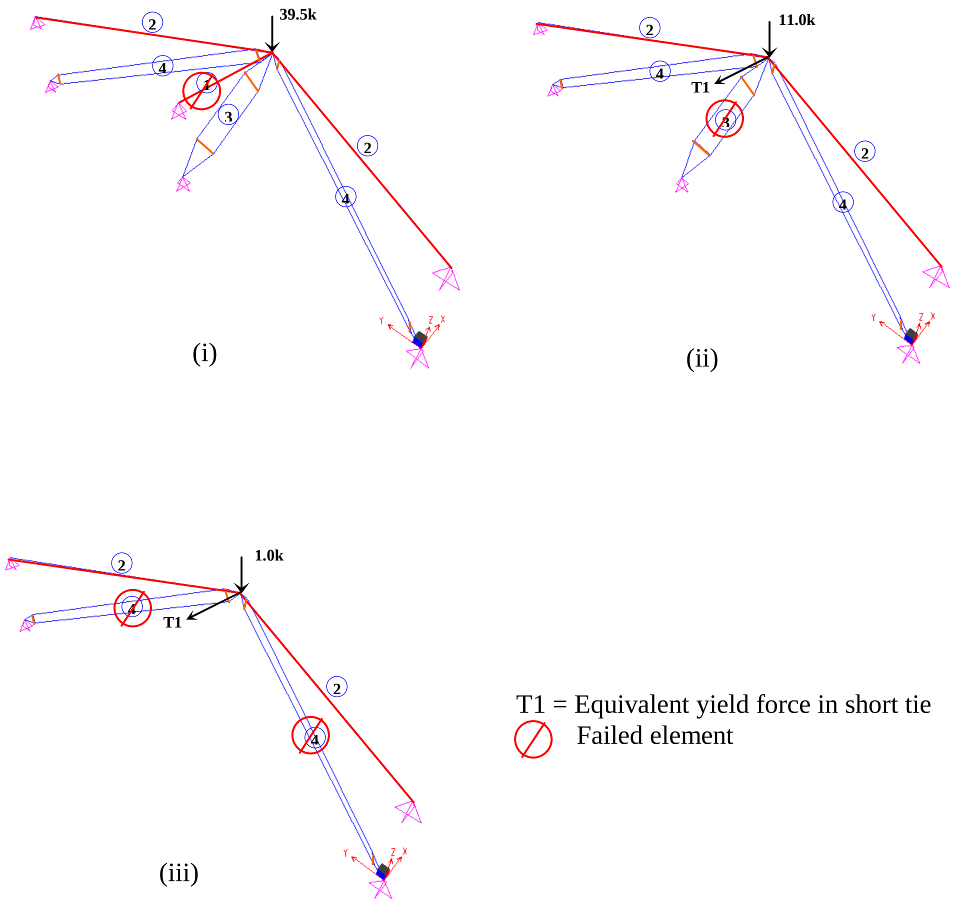


**Figure 64:** Failure sequence predicted by STM for the 3ft CIP overhang loaded at corner

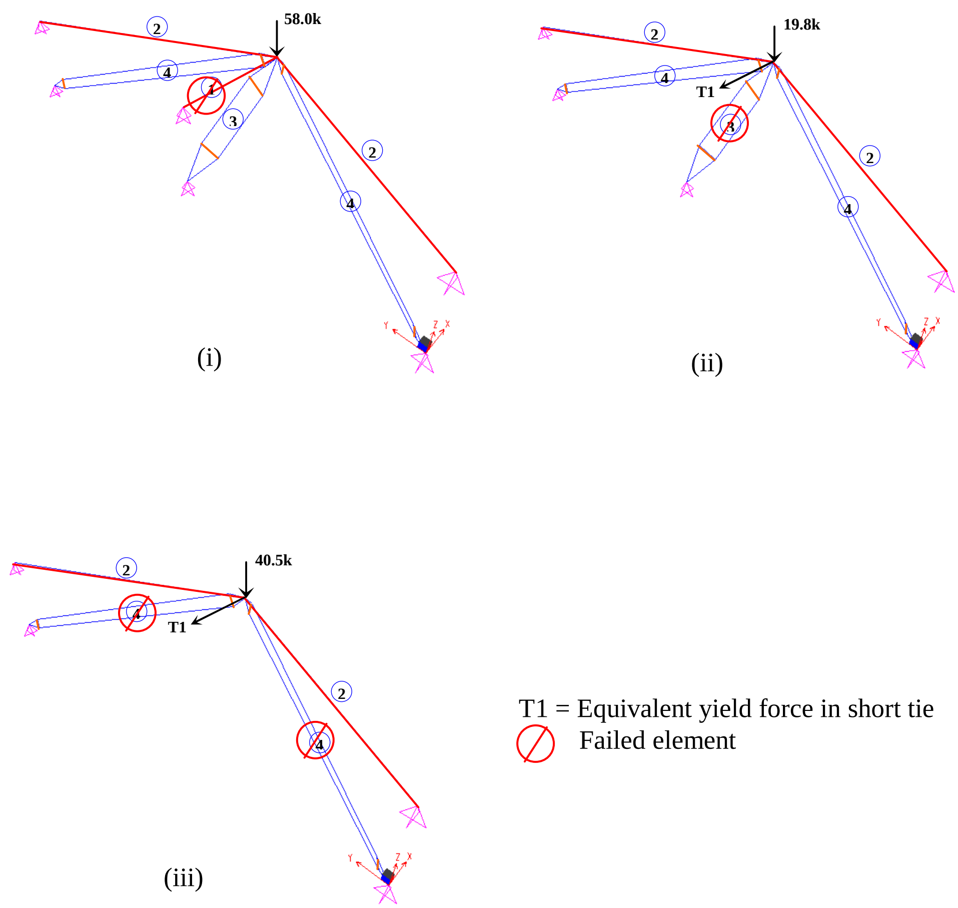


**Figure 65:** Failure sequence predicted by STM for the 3ft Precast overhang loaded at center

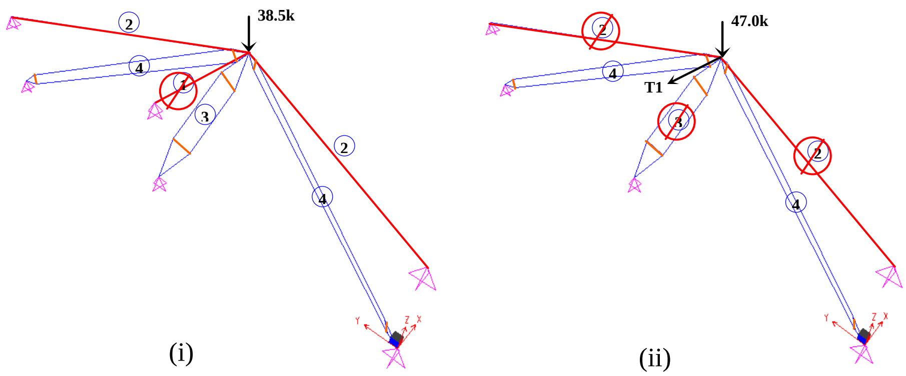


T1 = Equivalent yield force in short tie

Failed element

**Figure 66:** Failure sequence predicted by STM for the 3ft Precast overhang loaded at corner

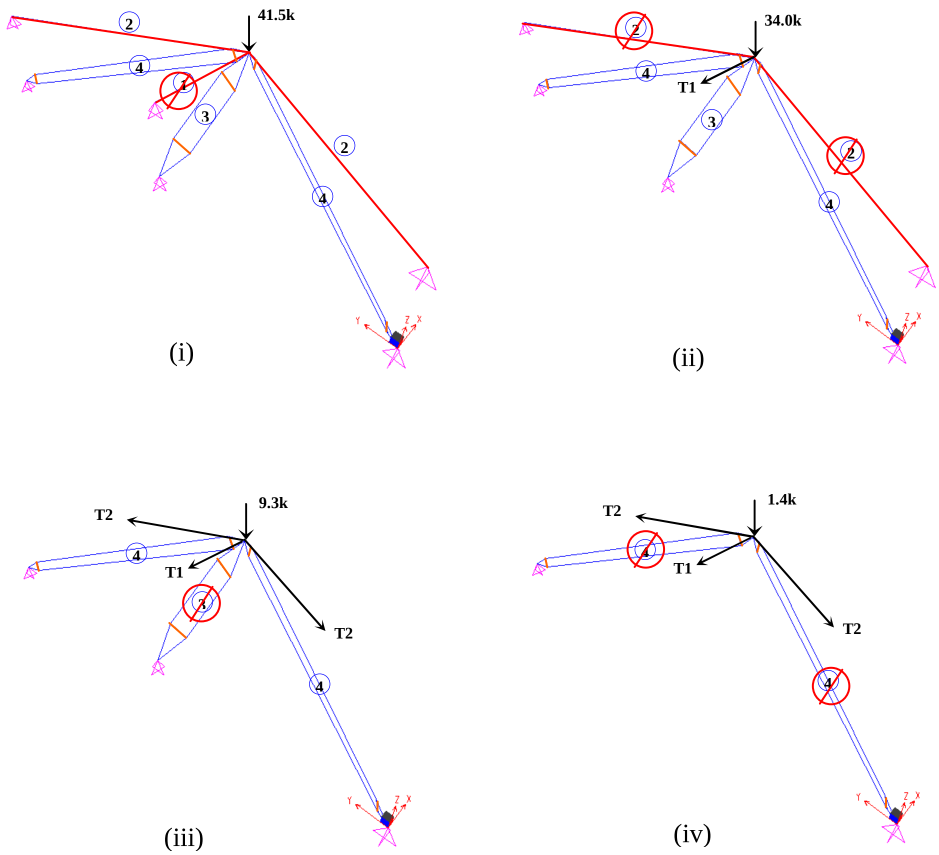


T1 = Equivalent yield force in short tie
T2 = Equivalent yield force in diagonal tie
Failed element

**Figure 67:** Failure sequence predicted by STM for the 5ft CIP overhang loaded at center

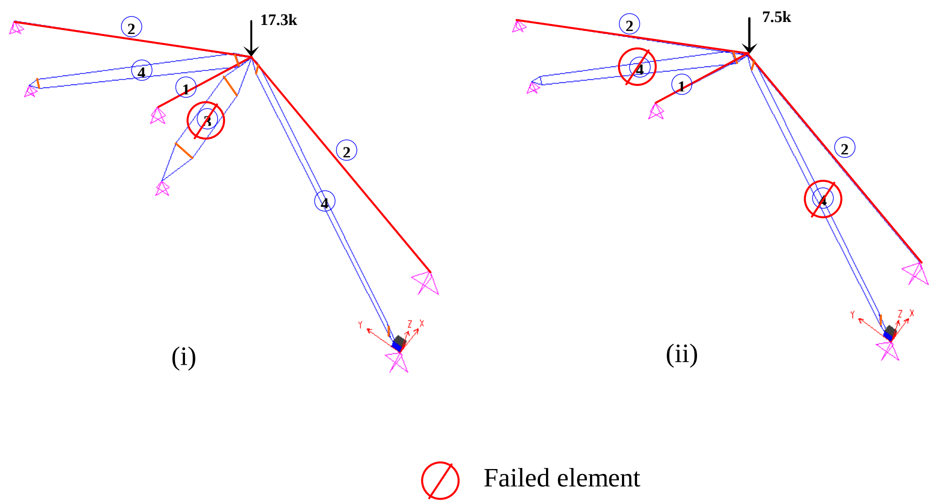


**Figure 68:** Failure sequence predicted by STM for the 5ft CIP overhang loaded at corner

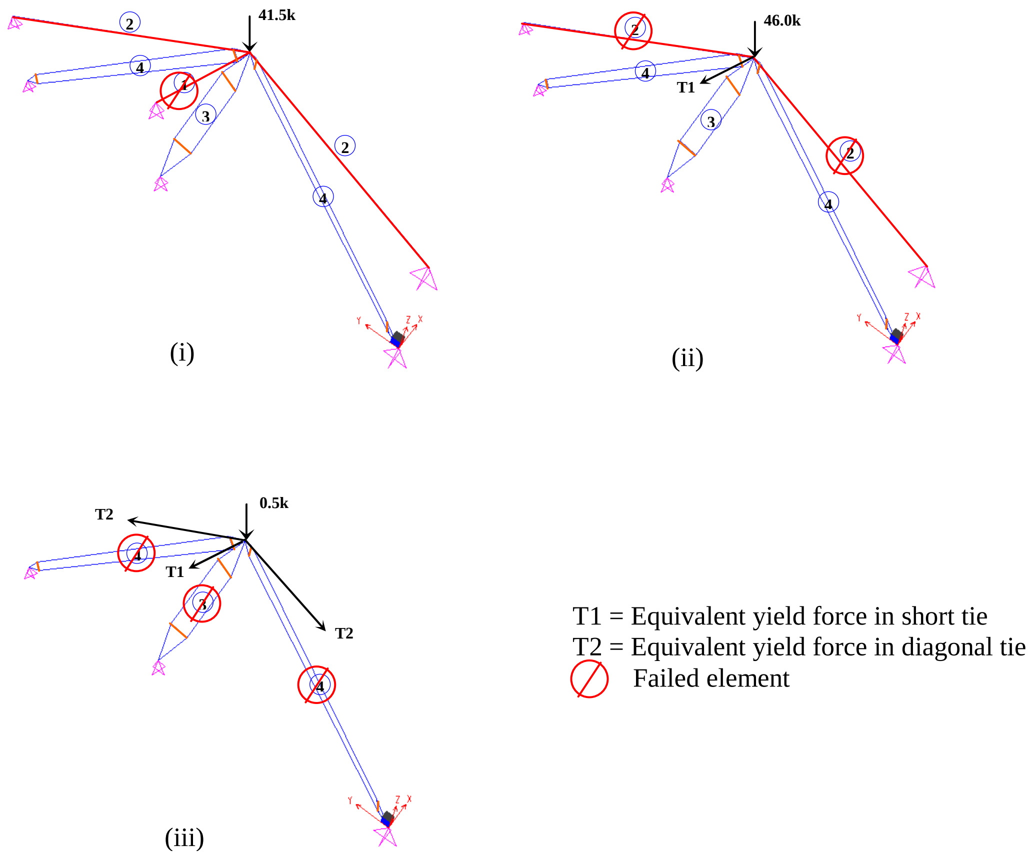


**Figure 69:** Failure sequence predicted by STM for the 5ft Precast overhang loaded at center

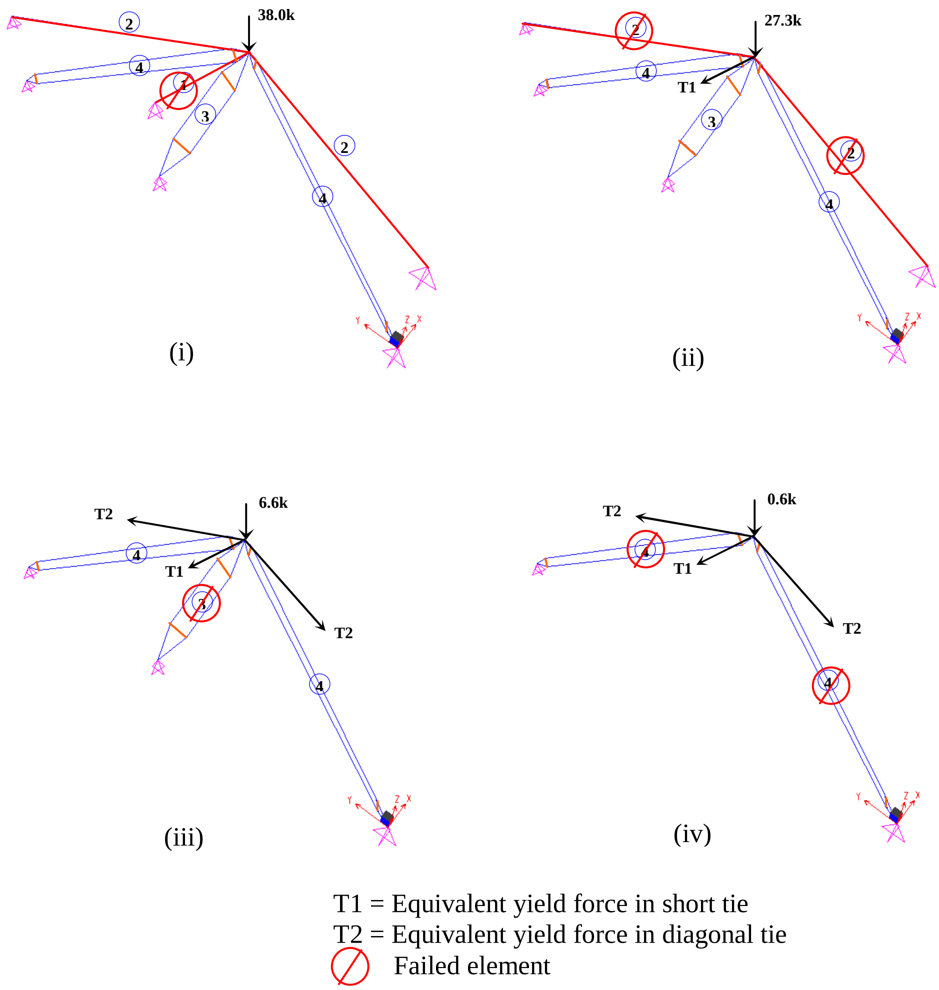


**Figure 70:** Failure sequence predicted by STM for the 5ft-8in overhang loaded at center

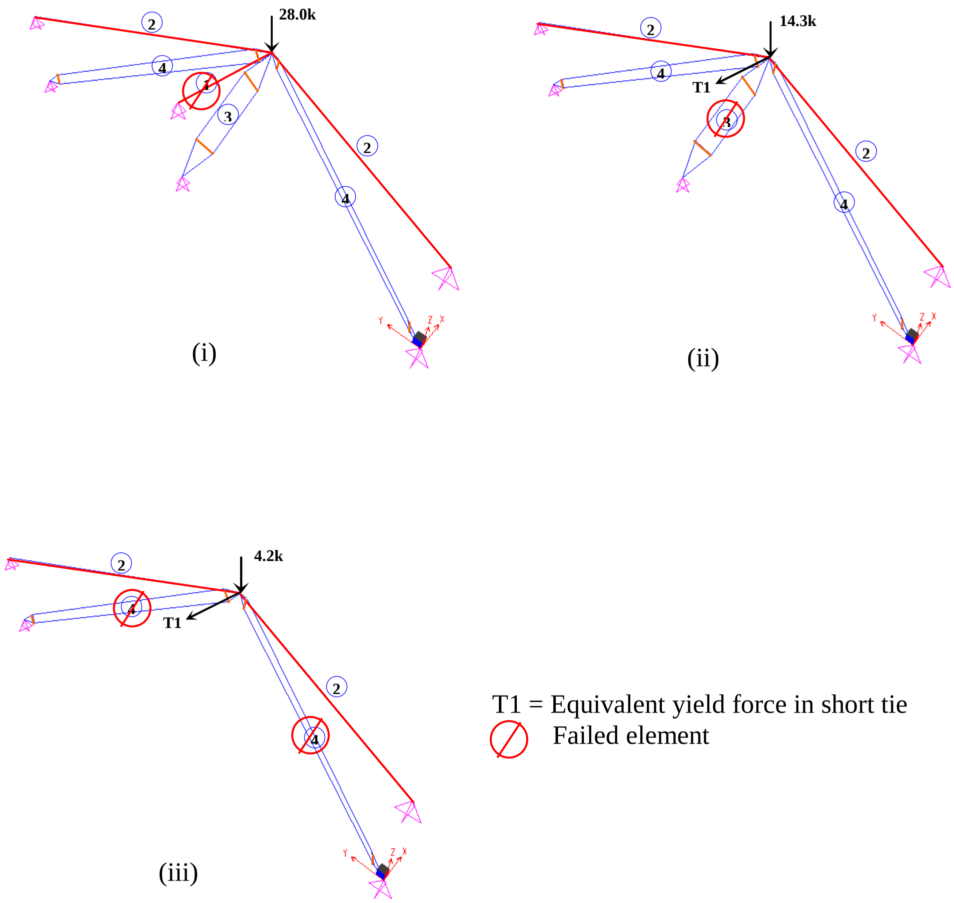


**Figure 71:** Failure sequence predicted by STM for the 5ft Precast overhang loaded at corner

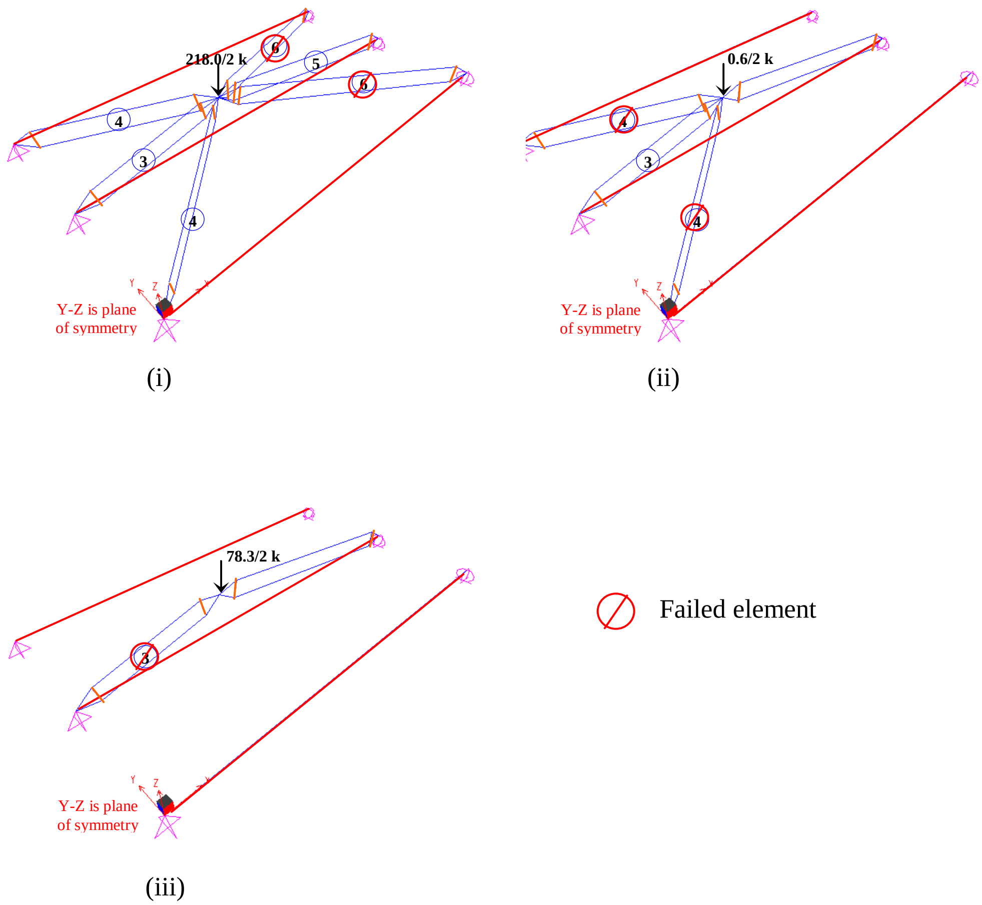


**Figure 72:** Failure sequence predicted by STM for Specimen A

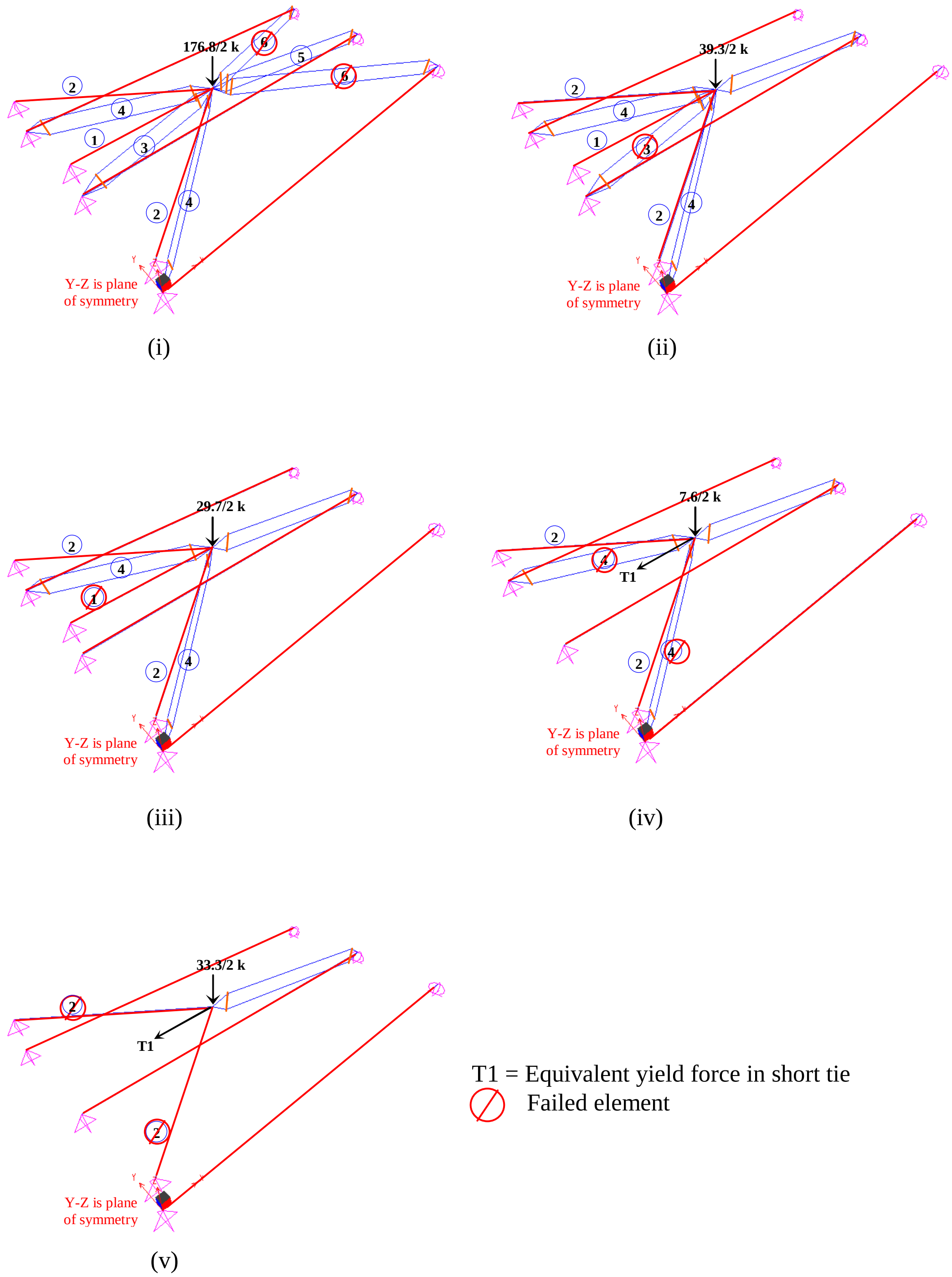


**Figure 73:** Failure sequence predicted by STM for  Specimen B

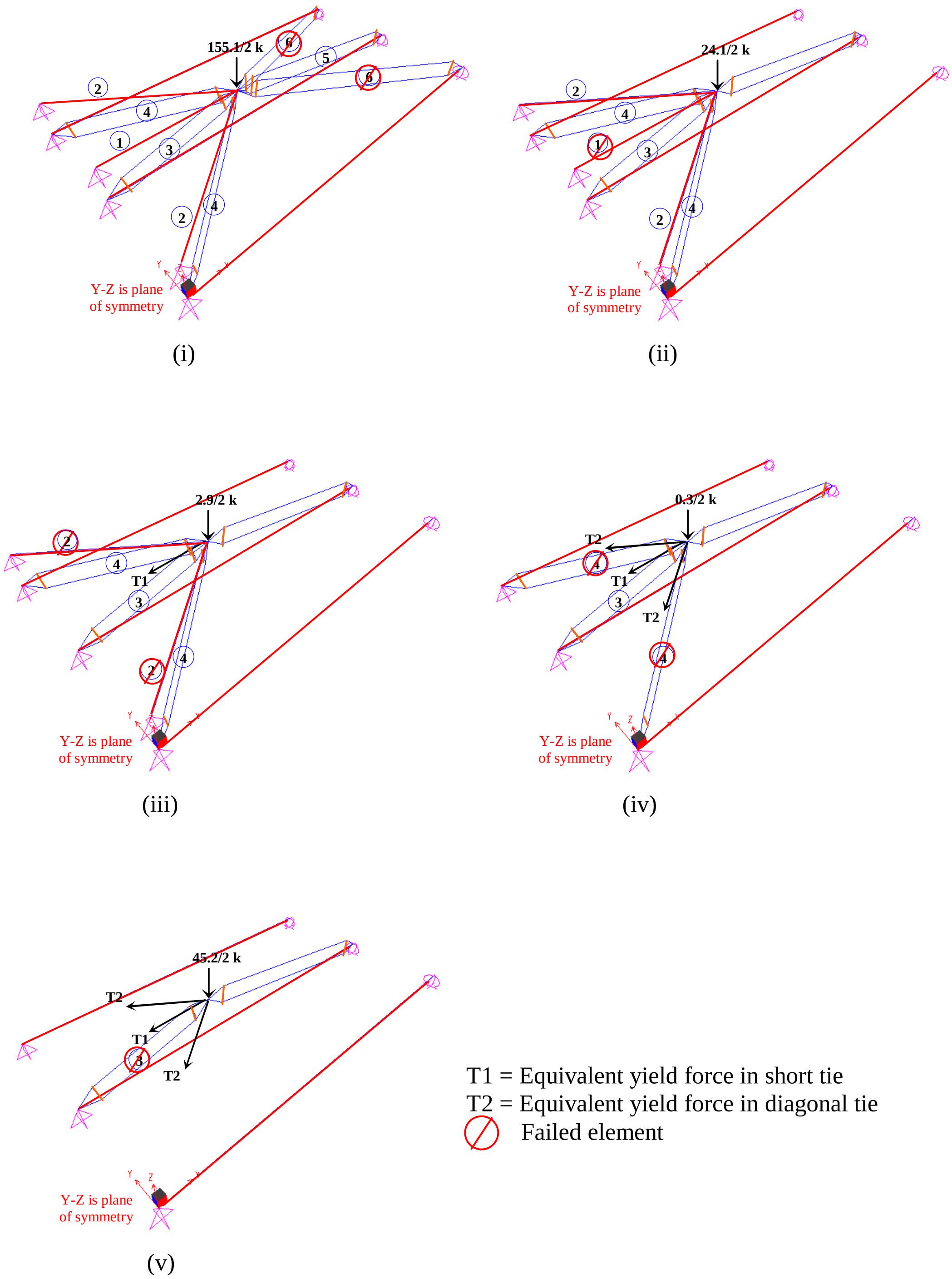


**Figure 74:** Failure sequence predicted by STM for Specimen C

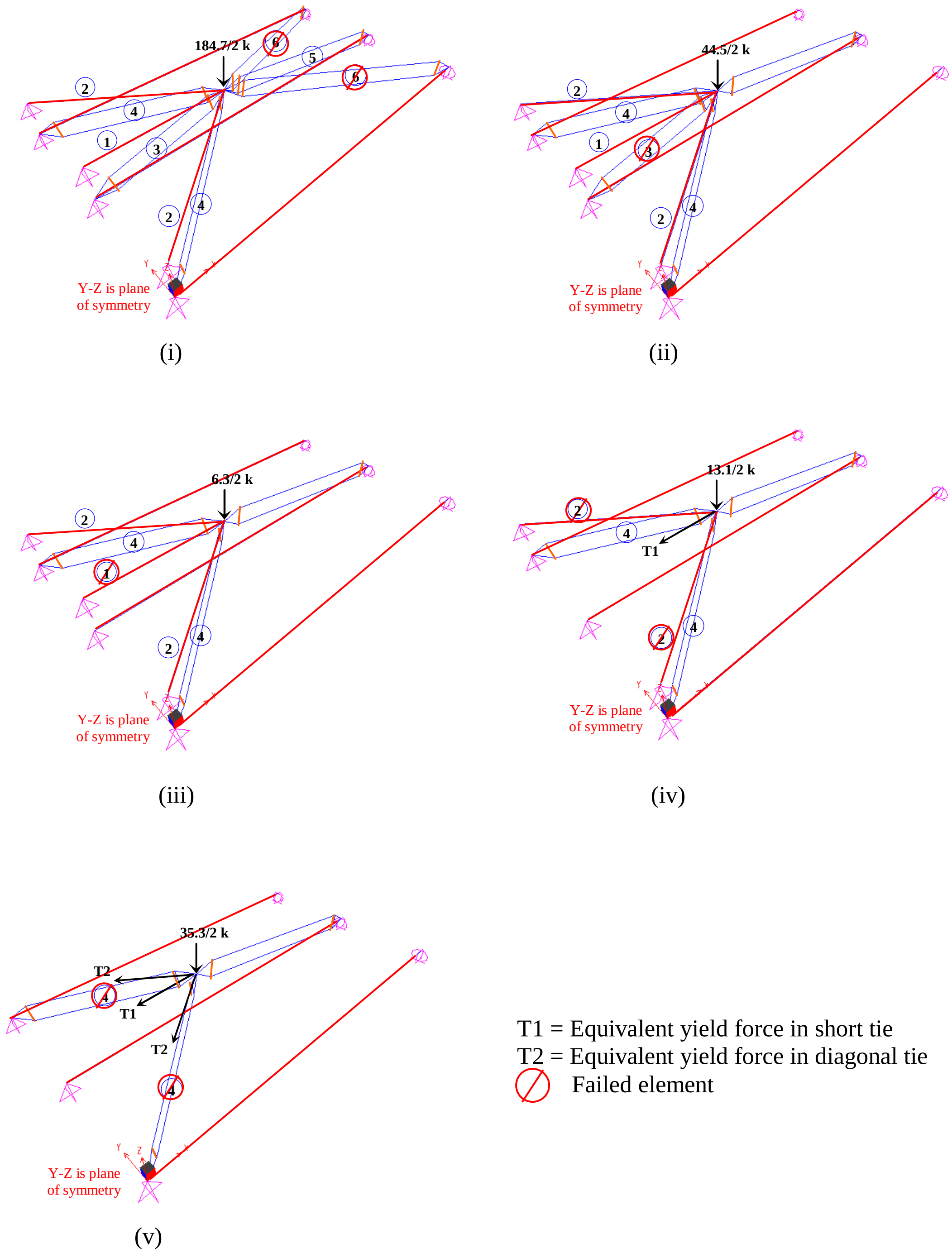


**Figure 75:** Failure sequence predicted by STM for  Specimen D

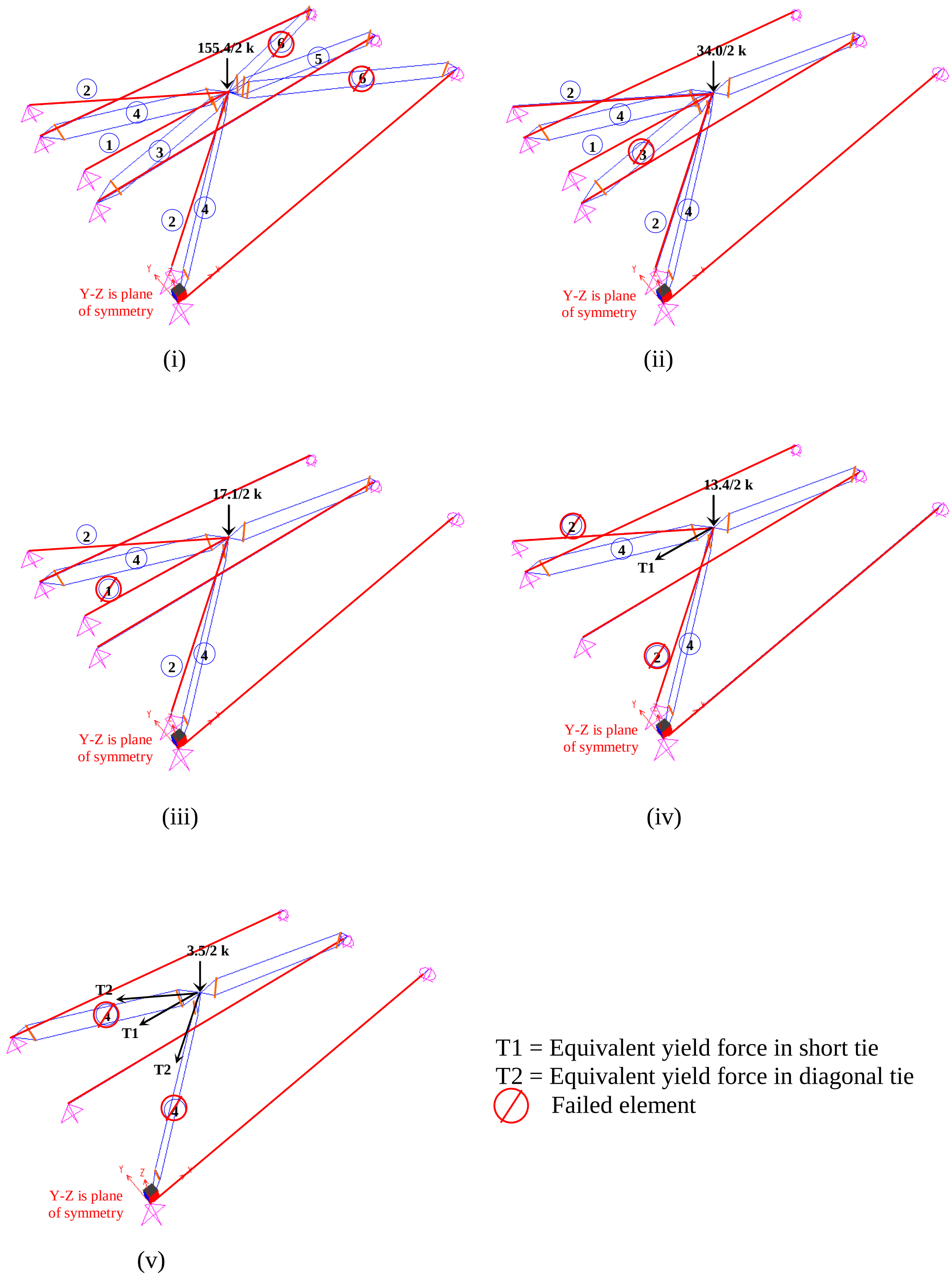


**Figure 76:** Failure sequence predicted by STM for  Specimen E

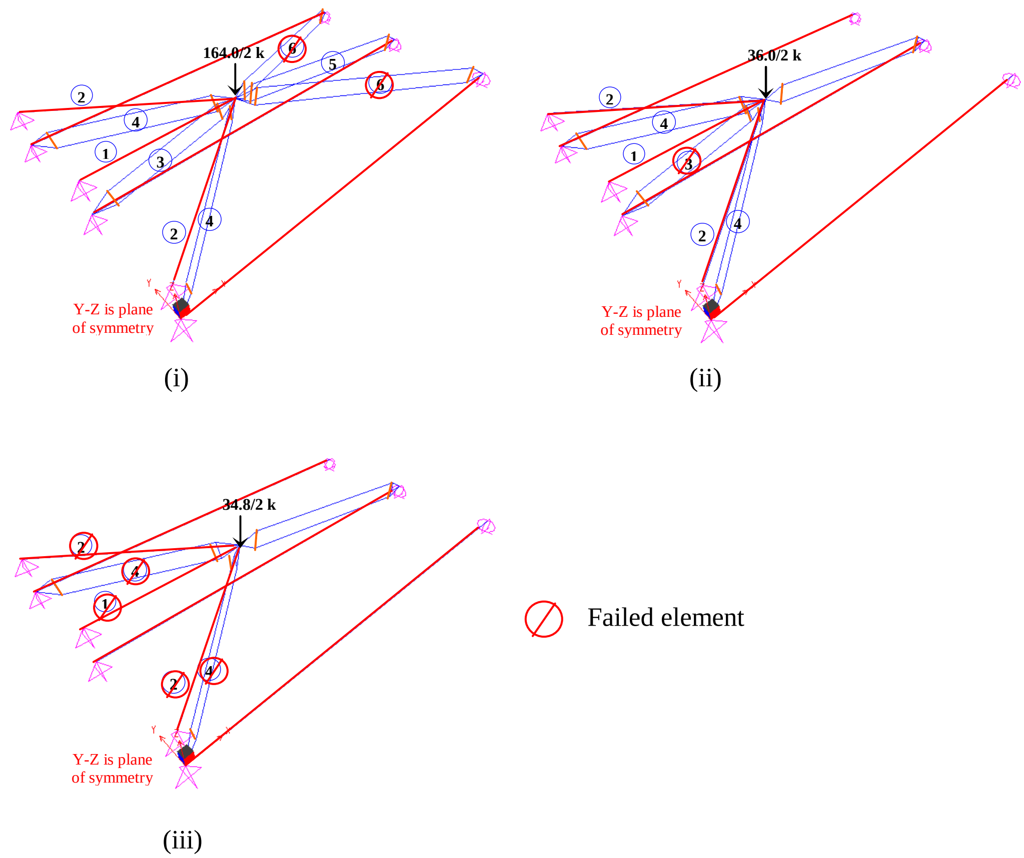


**Figure 77:** Failure sequence predicted by STM for Specimen F

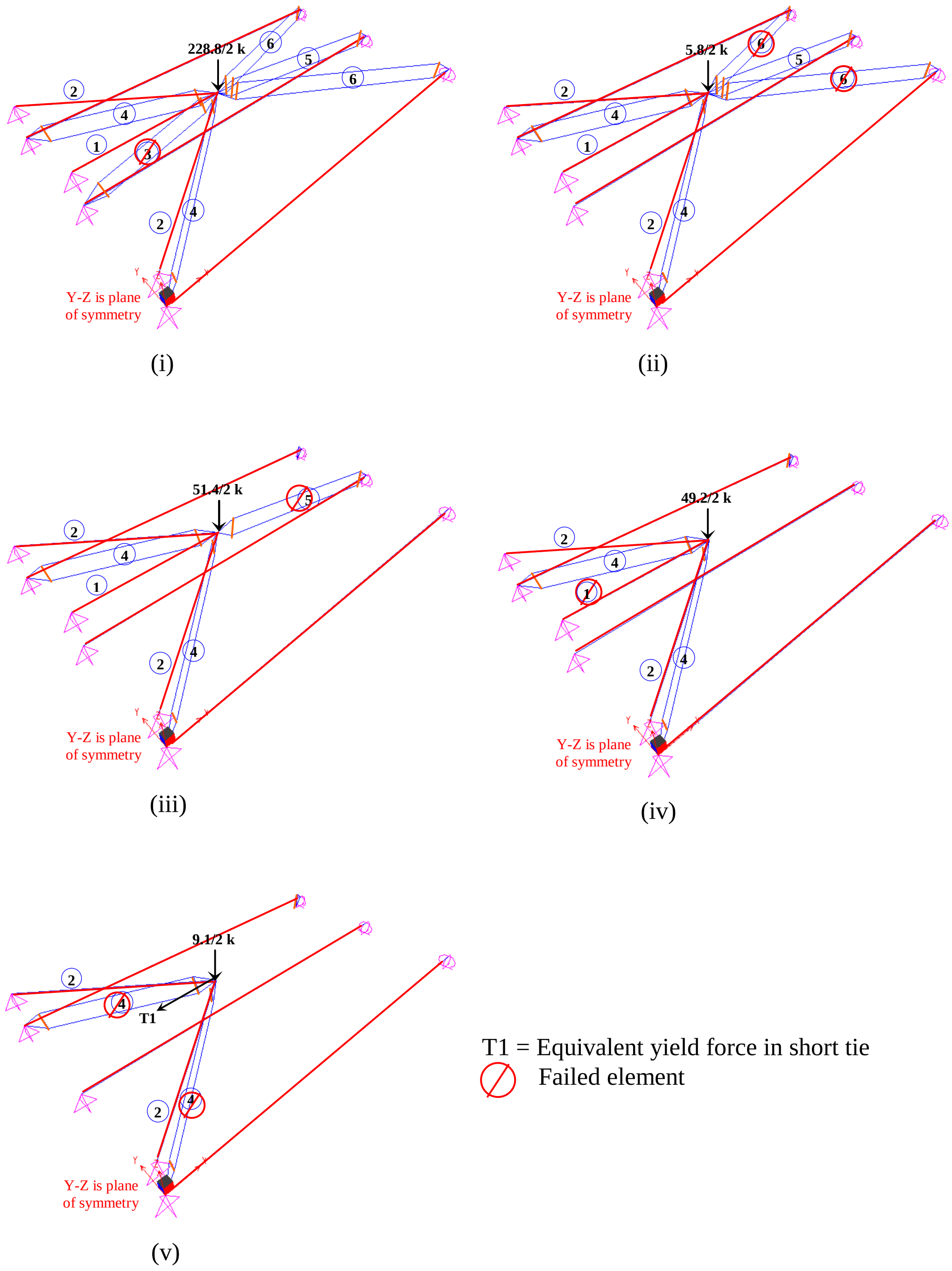


**Figure 78:** Failure sequence predicted by STM for Specimen G

**Table 13:** Summary of failure loads predicted by all analysis methods

| Method | Absolute average % difference (error) from experiments | |
|---|---|---|
| | Overhangs | Welded rebar mats specimens |
| **AASHTO** | 40.27 | 43.81 |
| **FIP** | 16.57 | 31.97 |
| **ACI** | 19.85 | 31.86 |
| **Muttoni and Ruiz** | 22.71 | 26.70 |
| **STM** | 5.30 | 7.00 |
| **FEM** | 6.90 | 8.74 |

**Table 14:** Summary of cracking loads predicted by section analysis and FEM

| Method | Absolute average % difference (error) from experiments | |
|---|---|---|
| | Overhangs | Welded rebar mats specimens |
| **Section Analysis** | 14.27 | 33.45 |
| **FEM** | 12.23 | 4.85 |

## 5.5- DISCUSSION

Recognizing the results obtained by the four design provisions and STM provided in the previous section, the upcoming points should be brought to attention. These discussions are separated according to the overhang and interior loadings. Additionally, in STM, the specimens were pushed until ultimate failure occurred. This mean that if a flexural failure began to occur then the ductility of the system allowed additional loading to be resisted until enough events occur that the system loses its ductility.

### 5.5.1- Overhang tests

Considering Figure 61, Table C.1, Table C.2, Table C.3, Table C.4, Table C.5, and Table 11, the following points may be extracted:

- Although formulations used in flexural capacity and one-way shear determination in both; AASHTO LRFD[22] and ACI 318-08[44] are exactly the same, nevertheless their prediction experienced notable difference in one-way shear and flexural capacity! This absolute difference ranges between 24.12%, and 41.78% with the ACI 318-08[44] magnitudes taken as reference. This is because of the limitations on the effective width placed on cross sections in AASHTO LRFD[22].

- FIP[45] and ACI 318-08[44] flexural capacity predictions are almost identical. This is referred to the small difference in $\beta_1$ factor used in both method.
- Regardless of the failure mode predicted, AASHTO LRFD[22] has the most conservative failure load in all tests. This mentioned difference ranges from 22.08% in the 5ft_cip_corner test to more than 120% in the 3ft_cip_center test.
- Initial and final (destruction) failure modes, and the sequence of failure in general, predicted by all codes are almost the same, with a closer estimation to the actual failure loads is experienced by FIP[45]. Even though some of these predictions are slightly overestimated, the absolute difference of initial failure modes ranges between 5.15% in the 5ft_cip_center test and 25.36% in the 3ft_cip_corner test. Additionally, FIP[45] is the only code that correctly predicted the actual failure mode occurred in the 5ft_cip_center test.
- The predicted failure modes were closer to the measured for the corner testing than the overhang loads at the center. This may be caused by the possible interference of the different failure modes in the corner tests.
- Two-way shear formulations of non-prestressed members provided in AASHTO LRFD[22] is exactly like those provided by ACI 318-08[44]. At the same time, AASHTO LRFD[22] provides no formulae accounting for the prestress effect.
- Cracking loads predicted by section analysis is close to experimental loads with an average absolute difference of 14.16%, a minimum of 3.05% in the 5ft_pre_corner test, and a maximum of 23.47% in the 3ft_cip_corner test.
- Very similar failure sequences, and failure mode definitions to what have been observed in experiments are found using STM, Table 11. In addition, failure loads were very close to experiments with an average absolute difference of 5.23%, a minimum of 1.15% for the 5ft_pre_center test, and a maximum of 10.00% at the 5ft_cip_corner test.

- A conservative one-way shear estimation predicted by the equation proposed by Muttoni and Ruiz[46] compared to ACI 318-08[44] and FIP[45]. In the tests that actually experienced shear failure, these predictions had the greatest difference with an average of 38.21%. Punching shear estimations though, were extremely overestimated with an average difference from the actual failure loads of 123.35%.

### 5.5.2- Welded Rebar Mats Specimens

Considering Figure 62, Tables C.1, C.2, C.3, C.4, C.5, and Table 12, the following points may be extracted:

- Difference in flexural and one-way shear predicted magnitudes persists when using AASHTO LRFD[22] and ACI 318-08[44] using the same formulations. As well, FIP[45] and ACI 318-08[44] flexural estimations are very close.
- The same failure sequence is observed for all design codes in every specimen.
- All codes predicted the first and final failure modes exactly like what have been noticed in experiments.
- AASHTO LRFD[22], as in overhangs, is the most conservative; with a minimum absolute difference of 0.61% in specimen E, and a maximum of 29.35% at D.
- Although in most instances is over-predicting, FIP[45] is the most accurate (closest) design method with a minimum difference of 1.54% in specimen C, and a maximum of 37.60% at E.
- ACI 318-08[44] is providing an upper-limit estimation in these tests; that is their predicted failure magnitudes are the largest in all design codes, even though in some cases like Specimens B & D it behaves as the most accurate (nearest to the actual) code.
- Average cracking loads predicted are fairly close to the actual ones; with an average absolute difference of 33.36%, a minimum of 0.09% at specimen E, and a maximum of 98.00% at A.
- Exactly like overhang modeling, similar failure sequences and modes to experiments were observed when using STM, Table 12. The average absolute

difference is 6.65%, a minimum of -1.08% obtained in specimen D, and a maximum of 9.64% in G.

- Muttoni and Ruiz[46] one-way shear estimations are more conservative alike the behavior in overhang tests. On the other hand, the proposed punching shear equations seem to better estimate the failure loads experienced, but still farther than FIP[45] predictions. This better performance of the punching shear equations support the doubts about the inapplicability of these equations to the overhangs.

## 5.6- CONCLUSIONS

Various design codes are providing design recommendations, most of them are significantly underestimating failure loads (conservative), some are overestimating, but only a few of them are as close to the actual loads. Moreover, some analytical tools, like STM, have been introduced to overcome some of the inconveniences associated with traditional design codes. The following points may be concluded from this study:

- Although failure loads predicted by ACI 318-08[44] was flagged as of conservative estimation in the literature[51], especially if the failure mode is shear, AASHTO LRFD[22] is found using even higher factor of safety in this study; mainly because of the limitations put on the effective slab width. The average absolute difference predicted by ACI 318-08[44] for the overhangs is 20.79%, and 21.66% for the welded rebar mats specimens, while it is 36.84% for overhangs and 23.67% for welded rebar mats specimens when using AASHTO LRFD[22]. This phenomenon stated in literature was not detected in the welded rebar mats specimens; where in most specimens ACI 318-08[44] over-predicted the actual failure loads.
- Even though it slightly over-predicts the failure loads of a few instances in this study, FIP's[45] predicted failure loads are the closest to experiments, especially those actually experienced two-way shear failure. 80% of the tested specimens failed in shear, 90% of them failed due to two-way shear. Two-way shear formulations in FIP[45] and the consideration of the critical section at twice the bridge deck depth around the loaded plate have the major influence on this close result to experiments than the other design codes. Absolute average difference is 16.57% for overhangs, and 19.18% for welded rebar mats specimens.

Additionally, it adequately projected the failure modes experimentally observed in all specimens.

- Cracking loads estimated by basic section analysis are found fairly close to the actual measured ones. An average absolute difference of 14.3% for overhangs, and 33.5% for welded rebar specimens was found.
- STM efficiently predicted actual failure modes, failure sequences, and failure loads in all tests.
- One-way shear design equations proposed by Muttoni and Ruiz(46) are conservative in all tests, while the punching shear equations are over-predicting actual failure loads, and are applicable only to two-end supported slabs.

# CHAPTER VI

# VI. CONCLUSIONS AND RECOMMENDATIONS

This dissertation presents a new precast overhang system that allows for significant improvements in construction speed, economy, and safety while meeting the AASHTO requirements and providing a serviceable structure.

The research performed in the first phase of experimental work evaluated the performance of the precast prestressed full-scale bridge overhang system. Three overhang lengths were tested; 3’, 5’, and 5’-8” under center and corner loading. All specimens provided significant safety factors when comparing the service loading specified to AASHTO to the cracking and ultimate loads. A minimum factor of safety of 1.5 for cracking, and 3.0 at ultimate were both obtained for the 5’ overhang loaded at corner. A greater scattering of cracks in precast overhangs is detected when compared to the cast-in-place overhangs. This was reflected in the reduction in surface strains by an average of 23% between the two systems at the same loading conditions. This reduction in surface strain must lead to a similar reduction in crack sizes. Accordingly, it is recommended that the cantilever on the proposed precast overhang system can be extended in length up to 5’ while still providing satisfactory strength and serviceability performance. By allowing this extension of length of this system, the number of beams on a 30’ roadway can be reduced from four to three. This can lead to a significant savings in the bridge construction costs.

In the second phase, welded rebar mats were used to replace tied reinforcing bars with partial depth panels to improve the economy, constructability, and construction speed of bridge decks. Conventional tied reinforcing and welded rebar mats were used in the test specimens.  Similar ultimate strengths were obtained for all specimens regardless of the amount of top reinforcement existed, but the levels of surface strains are quite different and depends mainly on its amount and distribution. By using a rebar mat with D11 bars at 2.67" spacing transversely and D8 bars at 4" longitudinally with 2" of cover over the beams and then D8 bars at 4" in both transverse and longitudinal directions, a bridge deck can be produced with a sufficient amount of strength and improved durability while using about 30% less steel than a typical bridge deck.  This same steel layout can be used with a clear cover of 3" with equivalent performance in strength and durability to current TxDOT bridge decks. The improved ability of the wire mat help to resist cracking, and consequently could allow an owner either greater construction tolerances for the reinforcement placement or improved crack control and hence long term durability. Therefore, based on the testings in this phase, welded rebar mats can be substituted for tied reinforcing steel in the top mat of a bridge deck while using stay-in-place concrete panels.

The proposed non-linear finite element program has proven successful at modeling the performance of concrete bridge decks with interior and overhang loading. Mesh and load convergence tests have been performed for each specimen to obtain the number of elements and number of loading steps optimum for later on comparisons. For these specimens it was found that a shear reduction factor $\beta$ of 0.20 showed the best correlation with the experimental data. The results obtained were close to the experimental data. Lower average load difference is obtained compared to the average differences of surface strains and deflections. This difference is utmost 50% of the strains absolute average difference. A higher-order brick element would be expected to narrow the mentioned differences, especially what regards to the slow response to follow-up with actual behavior demonstrated in graphs. This recommended element though, would need extensive investigation to justify its use for future work. Additionally, it is foreseen that a shear reduction factor $\beta$ magnitude of 0.18 will provide the best possible results.

In evaluation of the hand methods available, it is found that the STM is the closest, not only in estimating failure loads; but in  predicting the failure sequence and mode as well. Although it sometimes slightly over-predicts failure loads, FIP(45) design recommendation was found the closest to experiments. Furthermore, it satisfactorily estimated the failure modes experimentally observed in all specimens.

Overall, a combination of STM for estimating failure loads and failure progression, in addition to section analysis for cracking prediction is a recommended practice.

Finally, this system has been implemented to build the Rock Creek Bridge in Parker County, Cool, Texas and is performing well. It is being constructed in Ft. Worth on the West 7$^{th}$ St Bridge as well. Additionally, Bridges in Missouri, Texas, and Spain are under design with the system.

# REFERENCES


1. Phares, B., Wipf, T., Bigelow, J., Bowers, R., and Klaiber, F.; "Precast Concrete Elements for Accelerated Bridge Construction: Laboratory Testing, Field Testing, Evaluation of a Precast Concrete Bridge, Madison County Bridge," Research Report TR-561, Iowa State University for Iowa Department of Transportation, Ames, IA, January 2009, 68 pp.
2. Khaleghi, B.; "Use of Precast Concrete Members for Accelerated Bridge Construction in Washington State," Research Report CD 11-S, Transportation Research Board of the National Academies, Washington, D.C., 2005, pp. 187–196.
3. Biswas, M.; "Precast Bridge Deck Design Systems," Special Research Report, PCI Journal, March-April 1986.
4. Sneed, L., Belarbi, A., and You, Y.; "Spalling Solution of Precast-Prestressed Bridge Deck Panels," Research Report OR11-005, Missouri Department of Transportation Research, Development and Technology, Jefferson City, MO, September 2010, 211pp.
5. Shoup, L., Donohue, N., and Lang, M.; "The State of Oklahoma's Bridges," Transportation for America Research Report, Washington, DC, March 2011, 17 pp.
6. Moretti, F. et al.; " FUTURE MOBILITY IN OKLAHOMA: Meeting the State's Need for Safe and Efficient Mobility," TRIP (a national transportation research group) Report, Washington, DC, April 2011, 23 pp.
7. Kwak, H., Filippou, F.; "Finite Element Analysis of Reinforced Concrete Structures Under Monotonic Loads," Research Report UCB/SEMM-90/14, University of California, Berkeley for California Department of Transportation, Berkeley, CA, November 1990, 120pp.
8. Leu, L., Huang, C., M.ASCE, C., and Liao, Y.; "Strut-and-Tie Design Methodology for Three-Dimensional Reinforced Concrete Structures," JOURNAL OF STRUCTURAL ENGINEERING©, ASCE, June 2006, pp. 929-938.

9. ASCE, "Infrastructure Report Card" www.asce.org, 2005.
10. Merrill, B.D.; "Texas' Use of Precast Concrete Stay-in-place Forms for Bridge Decks", Concrete Bridge Conference, 2002.
11. Bieschke, and Klingner, R. E.; "The Effect of Transverse Strand Extensions on the Behavior of Precast Prestressed Panel Bridges", Research Report 303-1F, 1982, Center for Transportation Research, The University of Texas at Austin.
12. Buth, Furr and Jones; "Evaluation of a Prestressed Panel, Cast-In-Place Concrete Bridge", TxDOT Research Report 145-3, 1972.
13. Furr and Jones; "Development Length of Strands in Prestressed Panel Sub-Decks", TxDOT Research Report 145-2, 1970.
14. Furr and Ingram; "Cyclic Load Tests of Composite Prestressed-Reinforced Concrete Panels", TxDOT Research Report 145-4F, 1972.
15. Jones and Furr; "Study of In-Service Bridges Constructed with Prestressed Panel Sub-Decks", TxDOT Research Report 145-1, 1970.
16. Freeby, G. and Ley, T., "Texas' Totally Prefabricated Bridge Superstructures", Transportation Research Board Annual Meeting. Washington, D.C., January, 2005.
17. Badie, S.S., Tadros, M.K. and Girgis, A.F.; "Full-Depth Precast-Concrete Bridge Deck Panel System", NCHRP 12-65, 2006.
18. Scholz, D.P., Wallenfelsz, J.A., Lijeron, C., Roberts-Wollmann, C.L.; "Recommendations for the Connection between Full-Depth Precast Bridge Deck Panel Systems and Precast I-Beams", Virginia Transportation Research Council, 07-CR17, 2007.
19. Hyzak, M.; a personal conversation, Odessa, Texas March 3, 2008.
20. Trejo, D., Hite, M., Mander, J., Ley, T., Mander, T., Henley, M., Scott, R., Patil, S., "Development of a Precast Bridge Deck Overhang System for the Rock Creek Bridge", TTI Research Report 6100-2, 2008.
21. Holowka, M., Dorton, R. A., Csagoly, P.F.; "Punching Shear Strength of Restrained Circular Slabs" Ministry of Transportation and Communications, Toronto, Canada, 1980.

22. AASHTO LRFD, “Bridge Design Specifications and Commentary,” 4th Edition, American Association of State Highway Transportation Officials, Washington, DC, 2007, 1520 pp.
23. Van Landuyt, D., 2010.
24. O'Brien, E. J., Keogh, D. L., and Lehane, B. M.; “Bridge Deck Analysis,” E & FN Spon, London, New York, 1999.
25. Cheung, M. S., Li, W., and Chidiac, S. E.; “Finite Strip Analysis of Bridges” Spon, London ;New York, 1996.
26. Cheung, M. S., Bakht, B., Jaeger, L. G.; “Analysis of Box-Girder Bridge by Grillage and Orthotropic Plate Methods.” Canadian Journal of Civil Engineering, Vol. 9, 1982, pp. 595-601.
27. Fang, I. K., Woreley, J. A., Burns, N. H., and Klingner, R. E.; “Behavior of Ontario-Type Bridge Decks on Steel Girders”, Research Report 350-1, 1986, Center for Transportation Research, The University of Texas at Austin.
28. Cook, R. D., Malkus, D. S., Plesha, M. E., and Witt, R. J; “Concepts and Applications of Finite Element Analysis,” John Wiley & Sons, New York, 4th edition, 2003.
29. Labeas, G. N., Belesis, S. D.;“ Efficient analysis of large-scale structural problems with geometrical non-linearity,” International Journal of Non-Linear Mechanics, Vol. 46, 2011, pp. 1283-1292.
30. Nilson, A. H.;“ Nonlinear Analysis of Reinforced Concrete by the Finite Element Method,” Journal of the American Concrete Institute, Vol. 65, No. 9, September 1969, pp. 757-766.
31. Lin, C. S., and Scordelis, A.; “Nonlinear Analysis of R. C. Shells of General Form,” Journal of the Structural Division, ASCE, No. ST3, Proc. Paper 11164, March 1975.
32. Hand, F. R., Pecknold, D. A., and Schnobrich, W. C.; “Nonlinear Layered Analysis of R. C. Plates and Shells,” Journal of the Structural Division, ASCE, Vol. 99, No. ST7, Proc. Paper 9860, July 1973, pp. 1491-1505.
33. Yuzugullu, O., and Schnobrich, W. C.; “A Numerical Procedure for the Determination of the Behavior of a shear Wall Frame System,” Journal of the American Concrete Institute, Vol. 70, No. 7, July 1973, pp. 474-479.

34. Bashur, F. K., and Darwin, D.; “Nonlinear Model for Reinforced Concrete Slabs,” Journal of the Structural Division, ASCE, Vol. 104, No. ST1, Proc. Paper 13495, January 1978, pp. 157-170.
35. Darwin, D., and Pecknold, D. A.; “Analysis of R. C. Shear Panels Under Cyclic Loading,” Journal of the Structural Division, ASCE, Vol. 102, No. ST2, Proc. Paper 11896, February 1976, pp. 355-369.
36. Kabir, A. F.; “Nonlinear Analysis of Reinforced Concrete Panels, Slabs and Shells for Time Dependent Effects,” UC-SESM Report No. 76-6, University of California at Berkeley, December 1976.
37. Kachlakev, D., Miller, T, Yim, S., Chansawat, K., Potisuk, T.; “Finite Element Modeling of Reinforced Concrete Structures Strengthened with FRP Laminates”, Research Report SPR 316, May 2001, Oregon State University for Oregon Department of Transportation.
38. Frantzeskakis, C., and Theillout, J. N.; “Nonlinear Finite Element Analysis of Reinforced Concrete Structures with a Particular Strategy Following the Cracking Process,” Computers & Structures, Vol. 31, No. 3, pp. 395-412, 1989.
39. Arnesens, A, Sorensen, I., and Bergan, P. G.; “Nonlinear Finite Element Analysis of Reinforced Concrete,” Computers & Structures, Vol. 12, pp. 571-579, 1980.
40. Bergan, P. G., Holand, I.; “Nonlinear Finite Element Analysis of Concrete Structures,” Computer Methods in Applied Mechanics and Engineering, Vol. 17, pp. 443-467, 1979.
41. Shah, S. P., Swartz, S. E., and Ouyang, C.; “Fracture Mechanics of Concrete,” John Wiley & Sons, Inc., New York, New York, 1995.
42. Barzegar, Maddipudi, and Srinivas; “Three-Dimensional Modeling of Concrete Structures. I: Plain Concrete.” Journal of Structural Engineering, 123(10), 1339-1346, 1997.
43. Isenberg, J.; “Finite Element Analysis of Reinforced Concrete Structures II,” ASCE, New York, NY, 1993.
44. ACI Committee 318, “Building Code Requirements for Structural Concrete (ACI 318-08) and Commentary,” American Concrete Institute, Farmington Hills, Michigan, 2008, 465 pp.

45. FIP Commission 3, “Practical Design of Structural Concrete,” FIP Recommendations, Fédération Internationale de la Precontrainte, Laussane, Switzerland, September 1996, 114 pp.
46. Muttoni, A., Ruiz, M; “Shear Strength of Members without Transverse Reinforcement as Function of Critical Shear Crack Width,” ACI Structural Journal, V. 105, No. 2, March-April 2008.
47. Muttoni, A.; “Punching Shear Strength of Reinforced Concrete Slabs without Transverse Reinforcement,” ACI Structural Journal, V. 105, No. 4, July-August 2008.
48. Oliveira, D. R., Regan, P. E., and Melo, G. S.; “Punching resistance of RC slabs with rectangular columns,” Mag Concrete Res, V. 40, No. 3, pp. 123-138, 2004.
49. Regan, P. E., Rezai-Jorabi, H.; “Shear resistance of one-way slabs under concentrated loads,” ACI Structural Journal, V. 85, No. 2, 1988, Farmington Hills, Mich.
50. Sherwood, E. G., Lubell, A. S., Bentz, E. C., and Collins, M. P.; “One-way shear strength of thick slabs and wide beams,” ACI Structural Journal, V. 103, No. 6, pp. 794-802, 1988, Farmington Hills, Mich.
51. Guandalini, S., Burdet, O., and Muttoni, A.; “Punching Tests of Slabs with Low Reinforcement Ratios,” ACI Structural Journal, V. 106, No. 1, January-February 2009.
52. Brown, M. D., Sankovich, C. L., Bayrak, O., and Jirsa, J. O.; “Behavior and Efficiency of Bottle-Shaped Struts,” ACI Structural Journal, V. 103, No. 3, May-June 2006.
53. Quintero-Febres, C., Parra-Montesinos, G., and Wight, J.; “Strength of Struts in Deep Concrete Members Designed Using Strut-and-Tie Method,” ACI Structural Journal, V. 103, No. 4, July-August 2006.
54. FIP Commission on Practical Design, “Design of Post-tensioned Slabs and Foundation Rafts,” FIP Recommendations, Fédération Internationale de la Precontrainte, Laussane, Switzerland, May 1998, 44 pp.
55. ASTM C496; “Standard Test Method for Splitting Tensile Strength of Cylindrical Concrete Specimens, ” ASTM International, West Conshohocken, Pa., Sept. 1996, 5 pp.

56. Swiss Society of Engineers and Architects; “SIA Code 262 for Concrete Structures,” Zürich, Switzerland, 2003, 94 pp.

# APPENDIX A: Crack Maps and Demec Gauge Layout for Welded Rebar Mats Bridge Decks

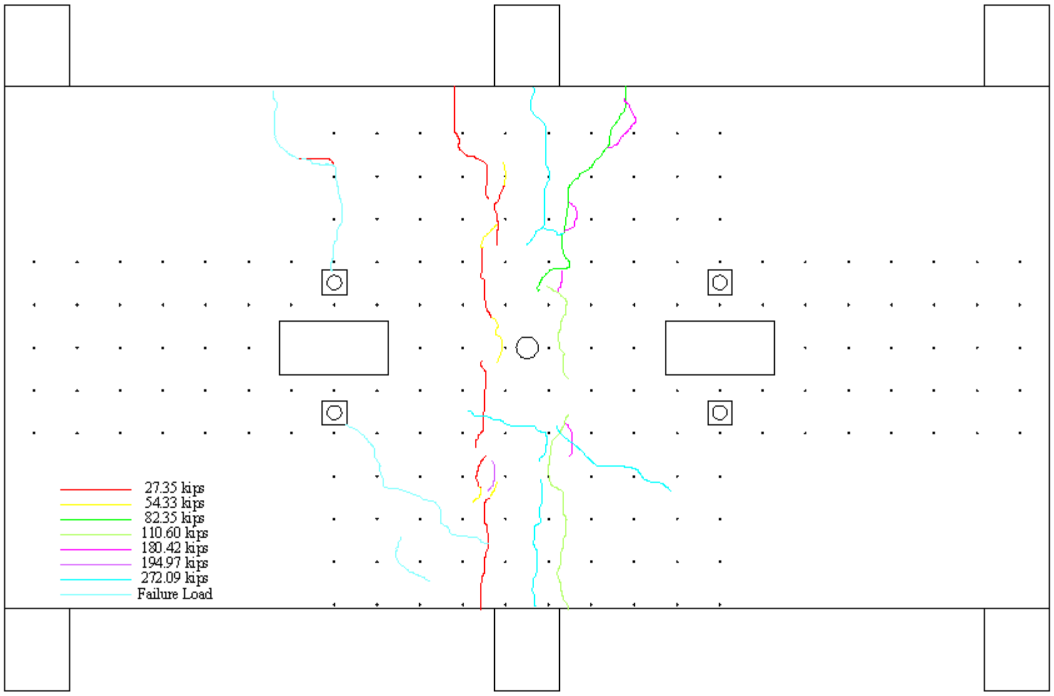

**Figure A.1:** Crack map for specimen A

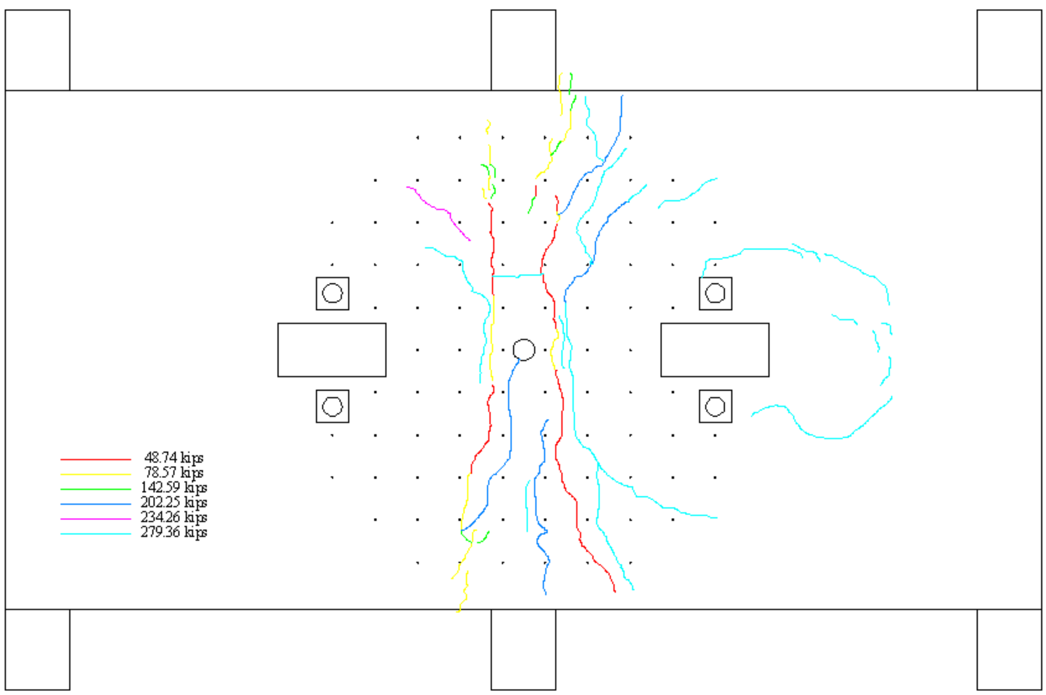

**Figure A.2:** Crack map for specimen B

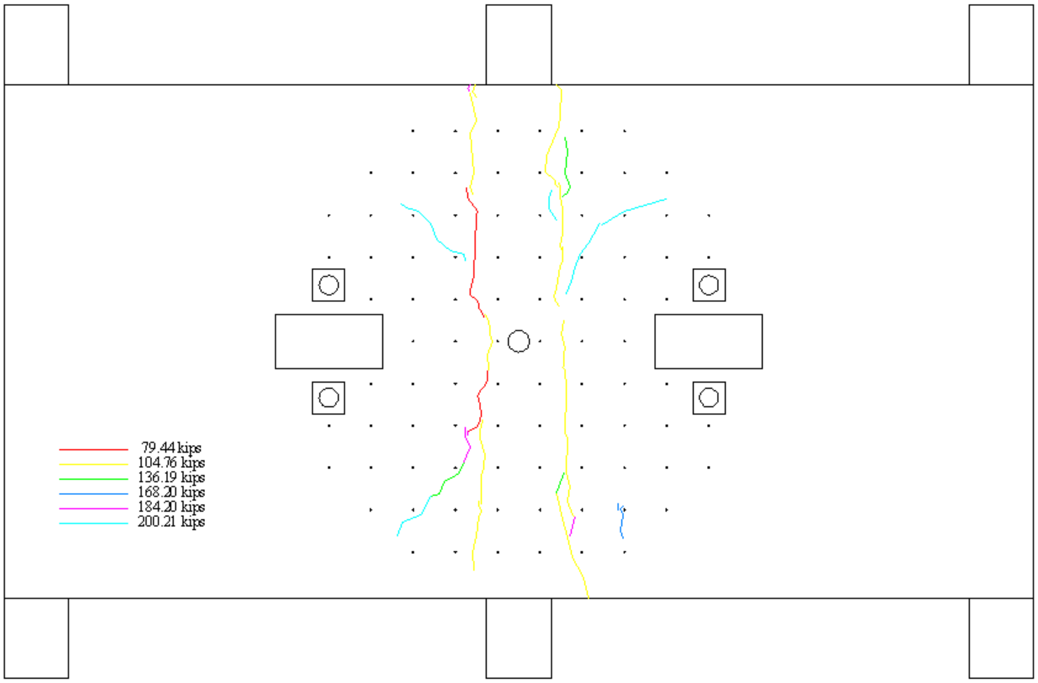


**Figure A.3:** Crack map for specimen C

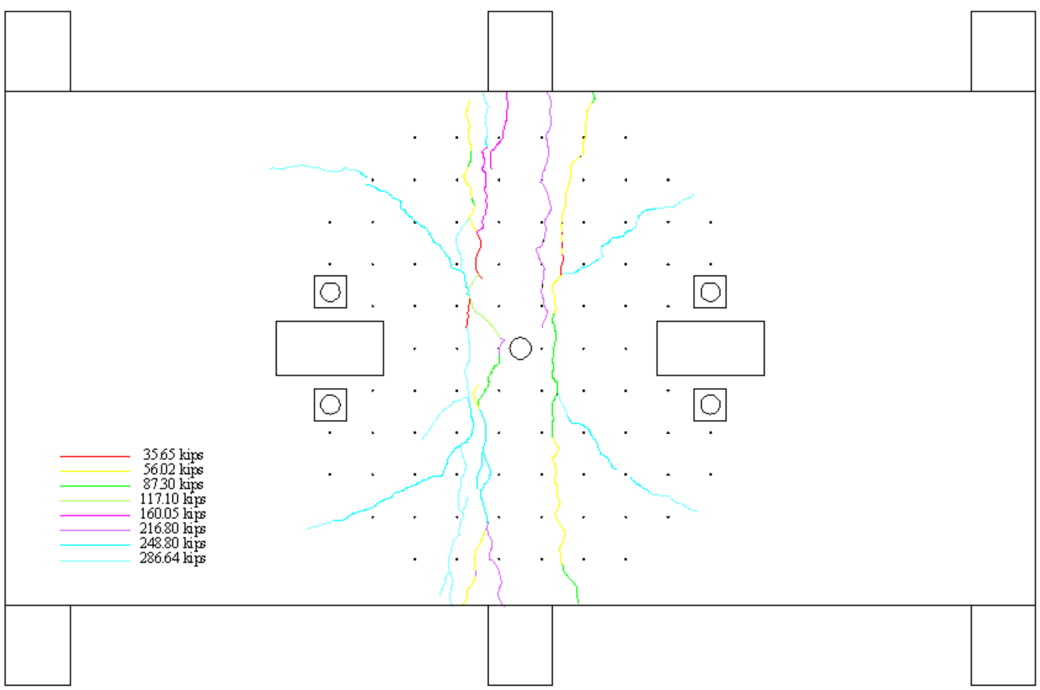


**Figure A.4:** Crack map for specimen D

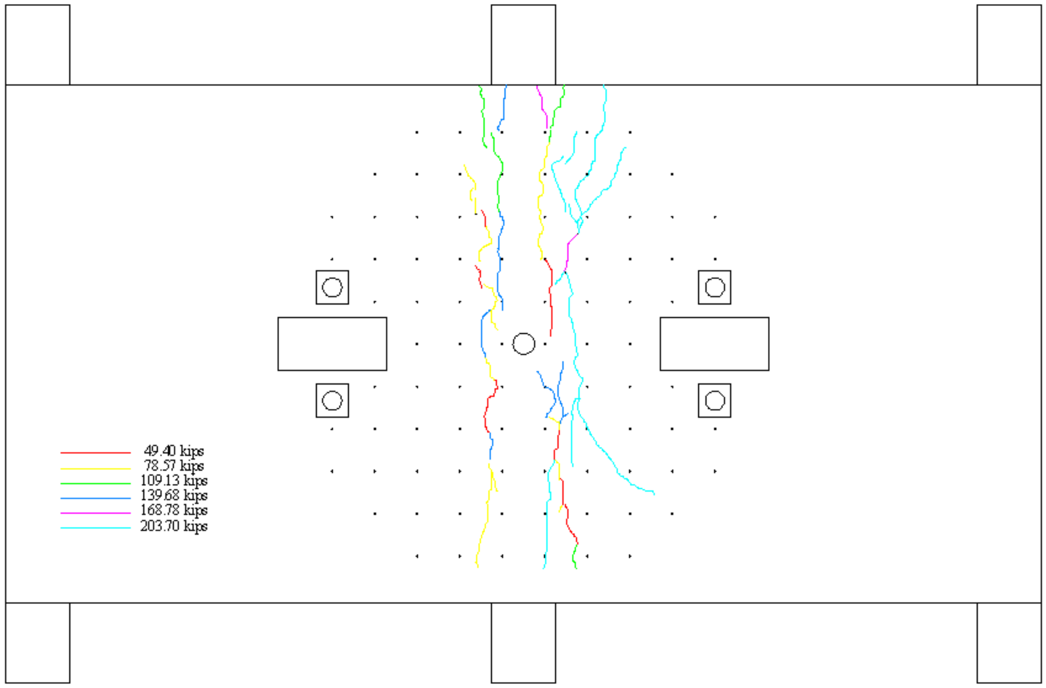


**Figure A.5:** Crack map for specimen E

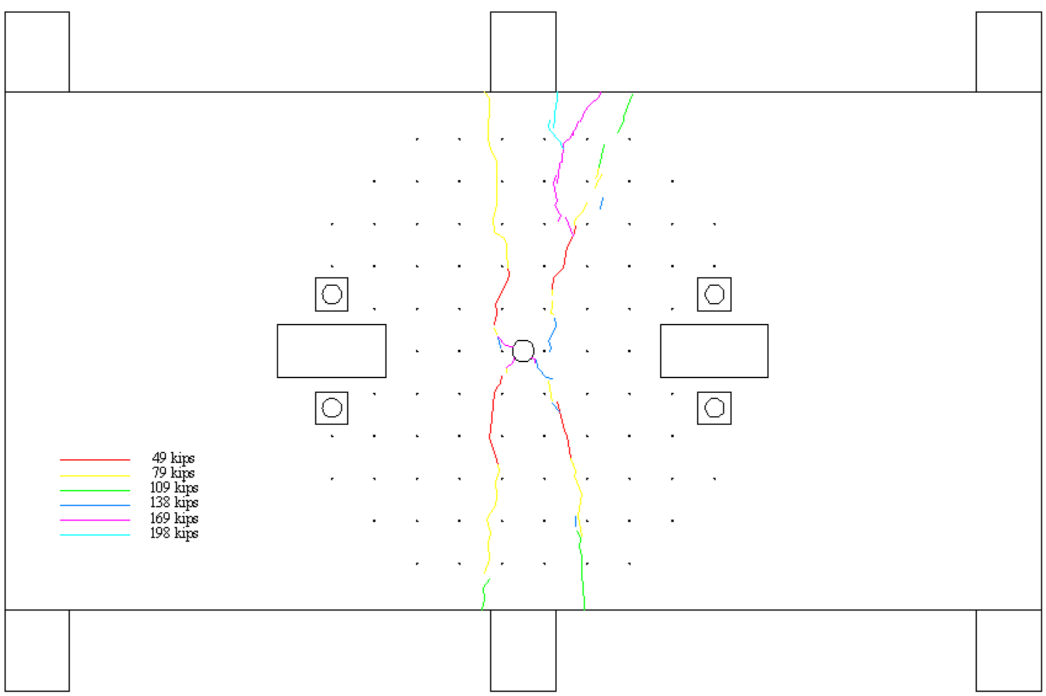


**Figure A.6:** Crack map for specimen F

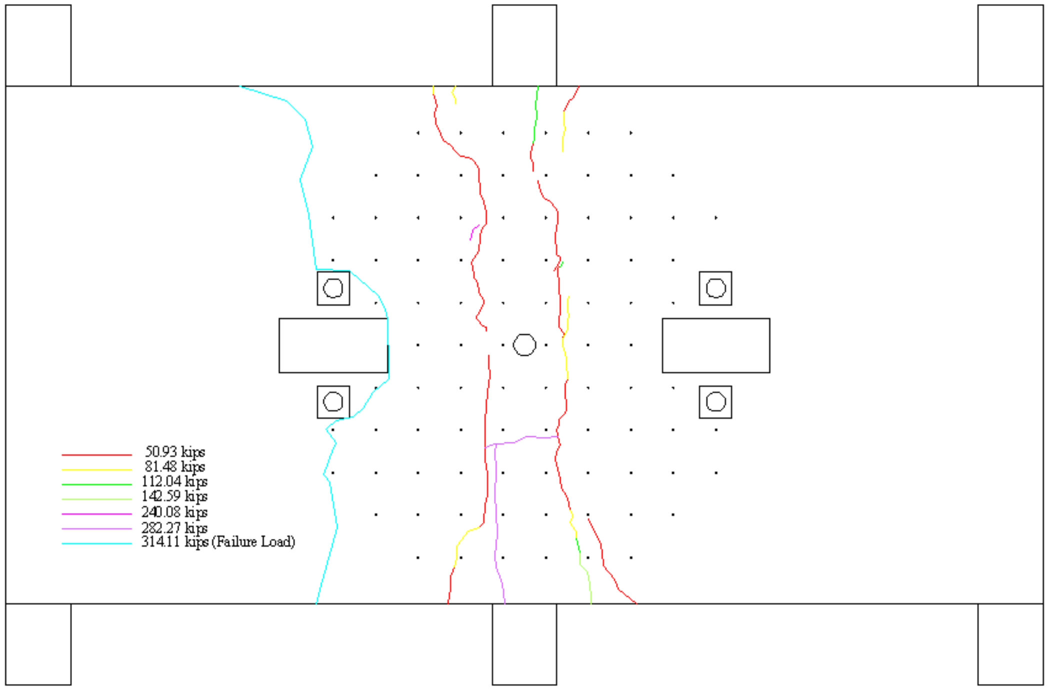


**Figure A.7:** Crack map for specimen G

# APPENDIX B: Finite Element Modeling Graphs

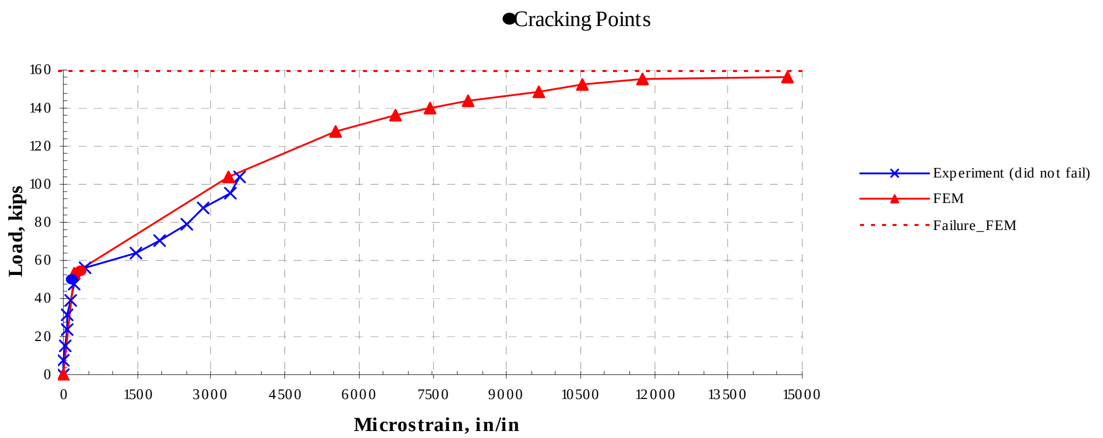


DEMEC 14

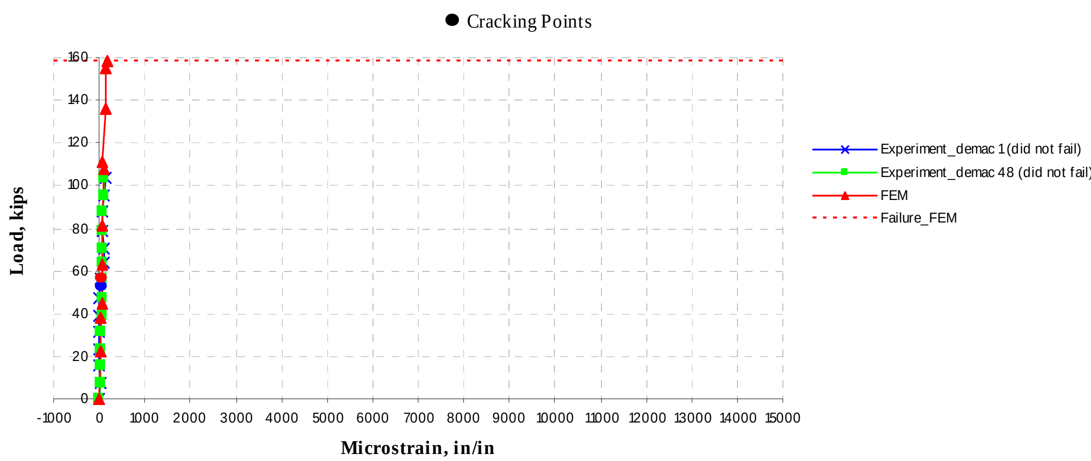


DEMECs 1&48

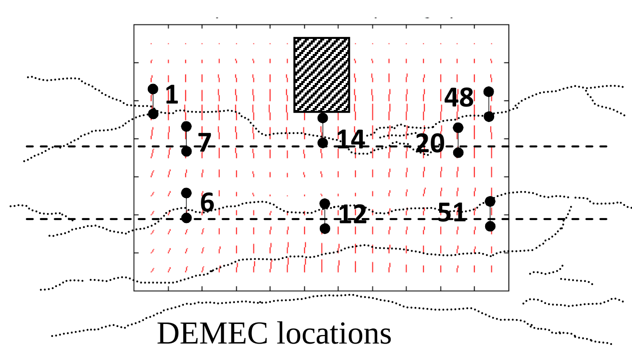


DEMEC locations

**Figure B.1:** FEM (β = 0.20) vs. experimental strain measurements at different DEMEC locations for the 3ft_cip_center bridge deck

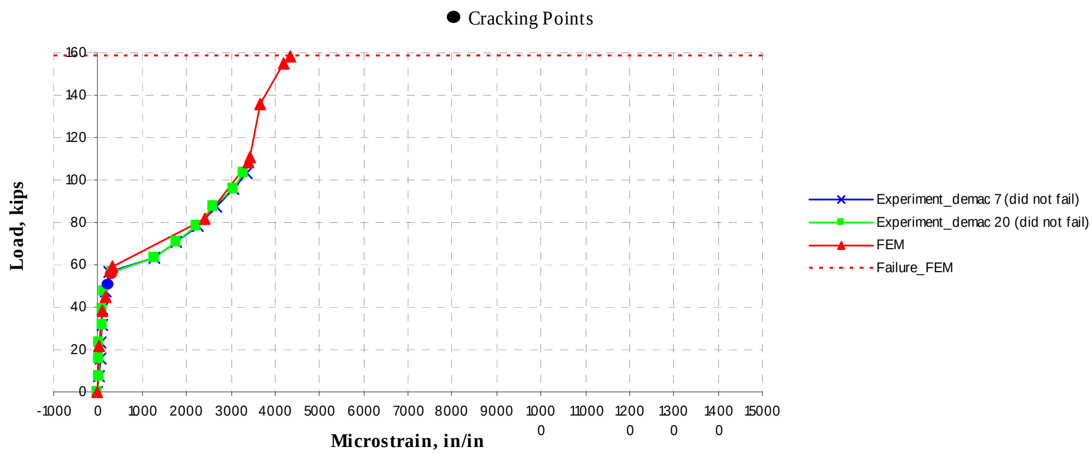


DEMECs 7&20

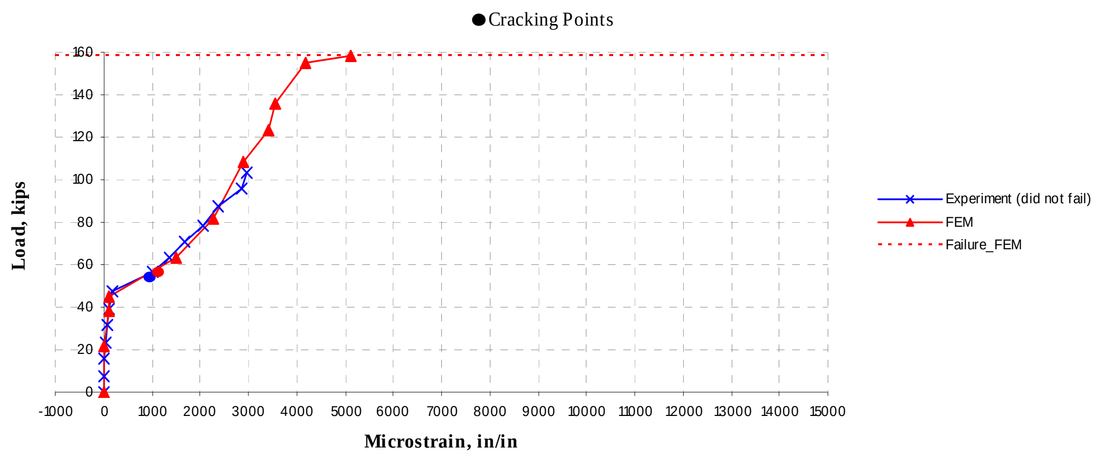


DEMEC 12

**Figure B.1 (*cont.*):** FEM (β = 0.20) vs. experimental strain measurements at different DEMEC locations for the 3ft_cip_center bridge deck

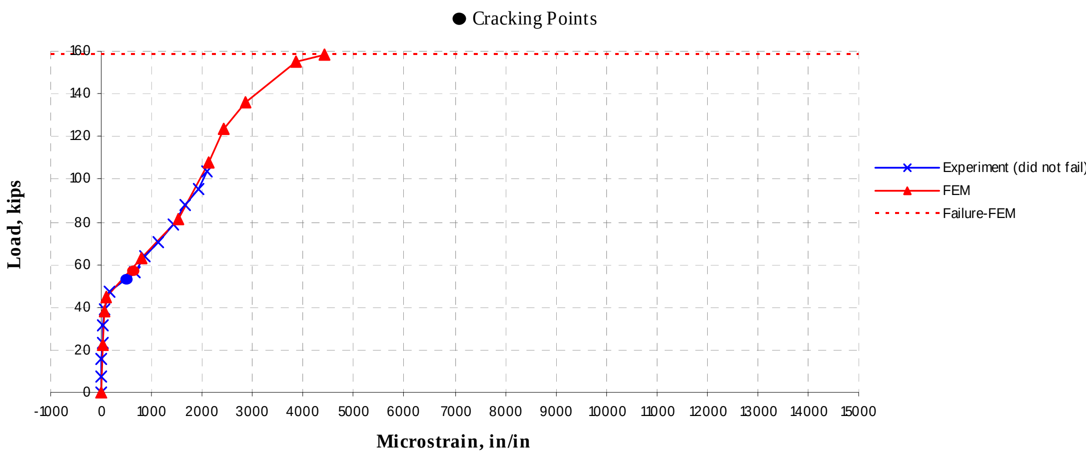


DEMEC 6

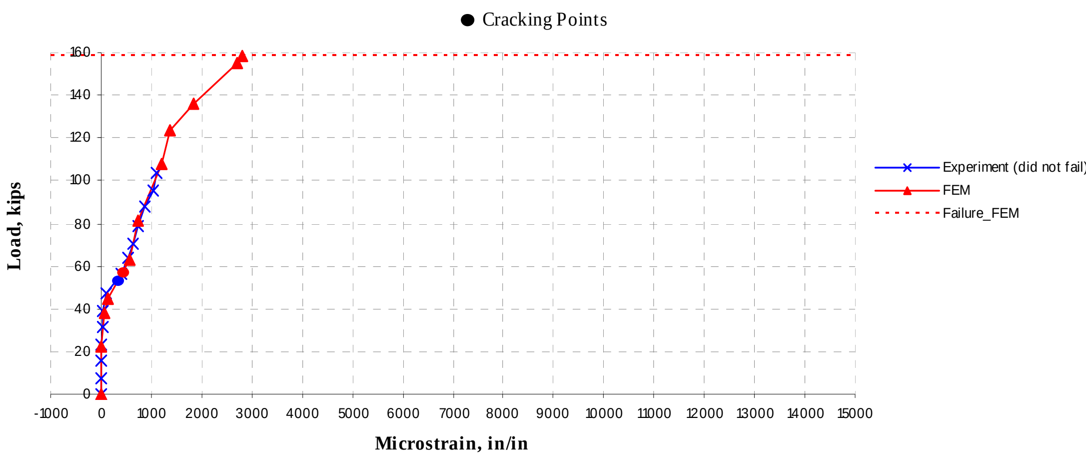


DEMEC 51

**Figure B.1 (*cont.*):** FEM (β = 0.20) vs. experimental strain measurements at different DEMEC locations for the 3ft_cip_center bridge deck

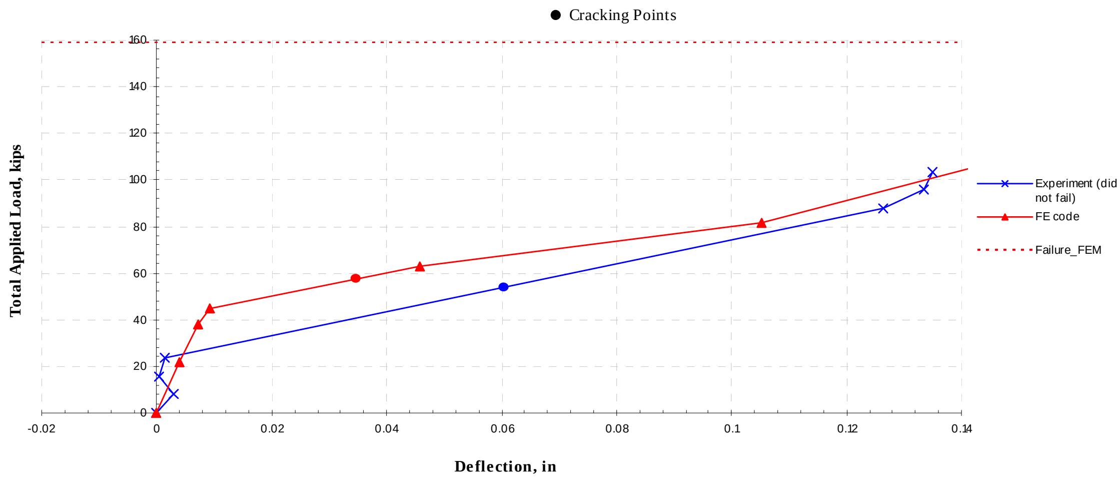


gauge 1

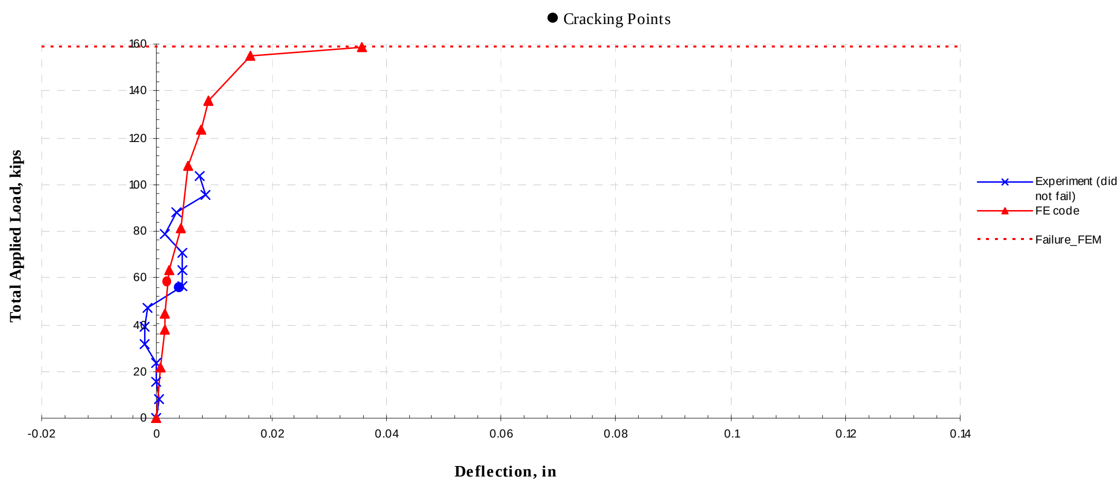


gauge 2

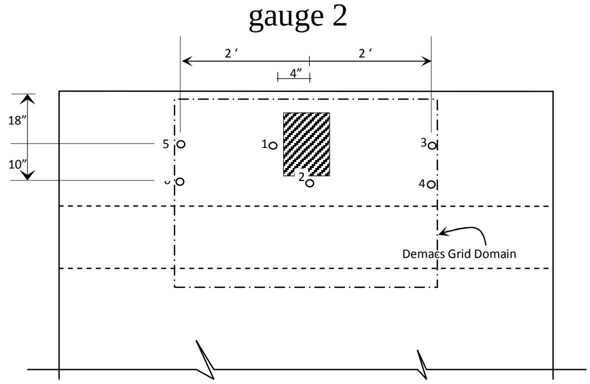


locations of deflection gauges

**Figure B.2:** FEM (β = 0.20) vs. experimental deflection measurements at different locations for the 3ft_cip_center bridge deck

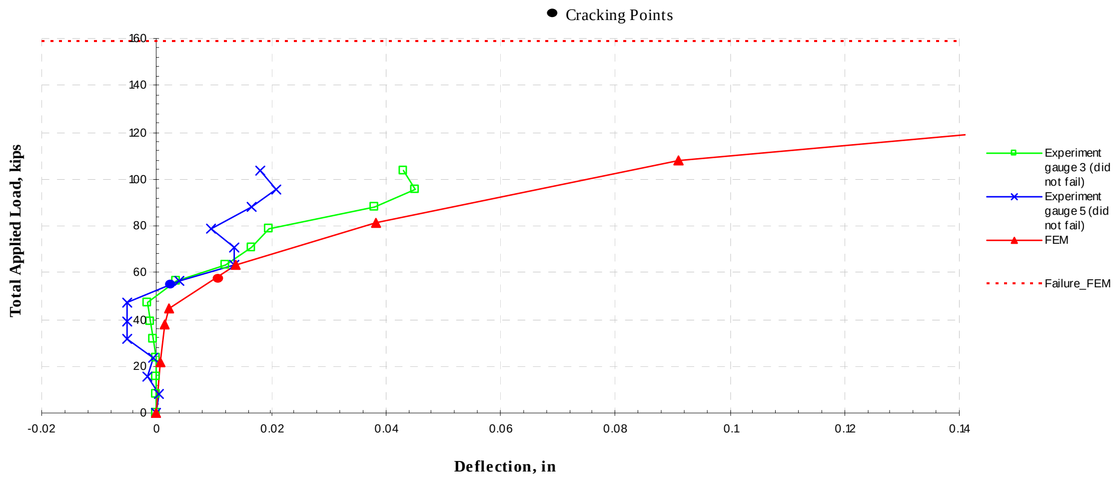


gauges 3&5

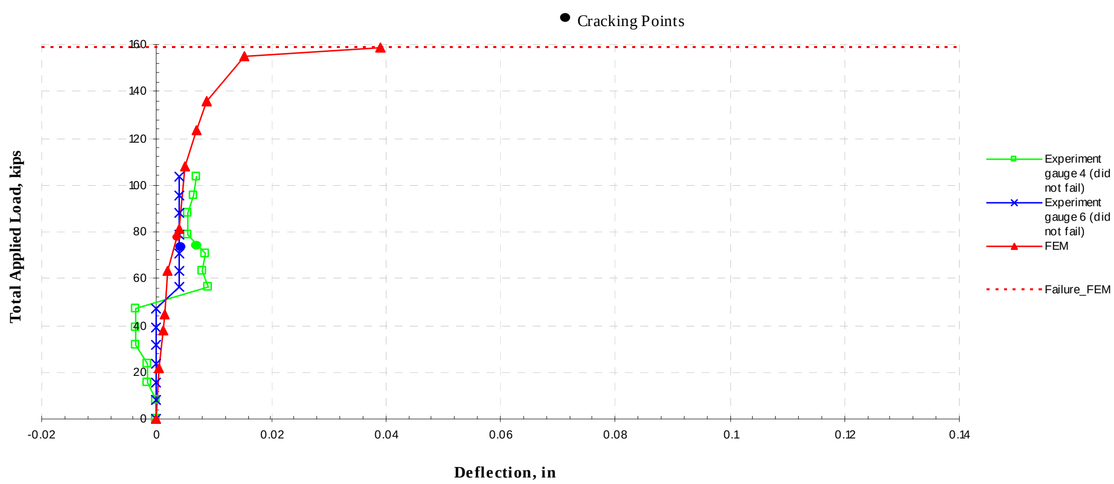


gauges 4&6

**Figure B.2 (*cont.*):** FEM (β = 0.20) vs. experimental deflection measurements at different locations for the 3ft_cip_center bridge deck

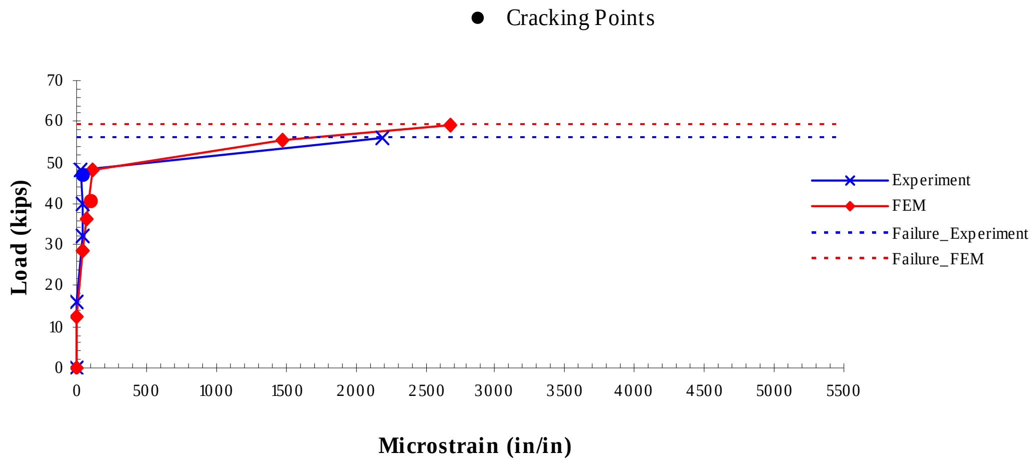


** FE value was taken at a location 1.61" off from mentioned DEMEC number

DEMEC 13

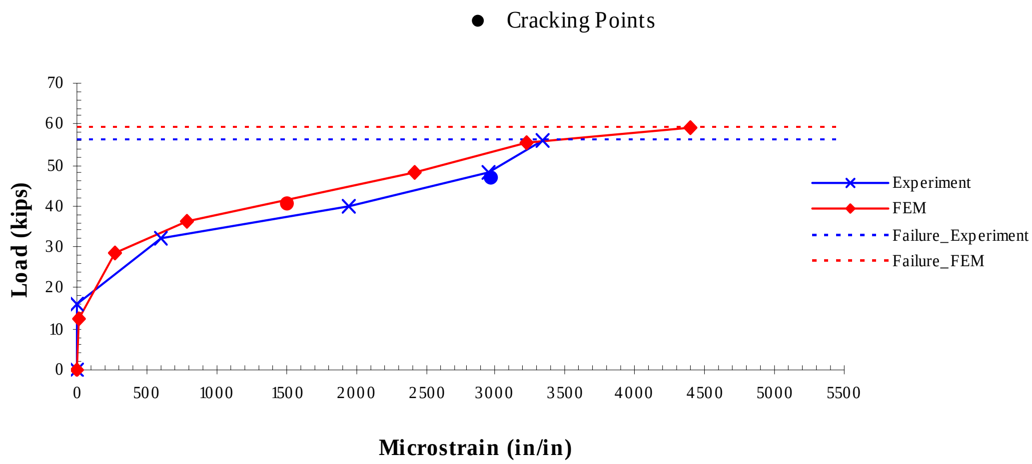


DEMEC 26

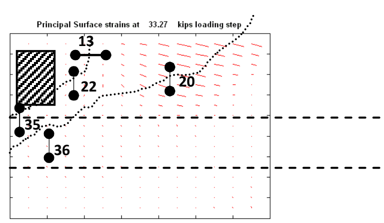


DEMEC locations

**Figure B.3:** FEM (β = 0.20) vs. experimental strain measurements at different DEMEC locations for the 3ft_cip_corner bridge deck

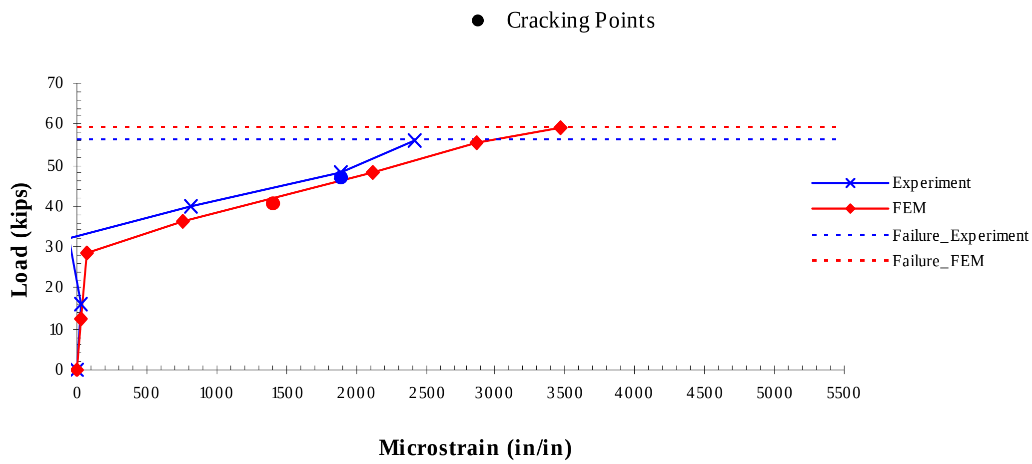


DEMEC 20

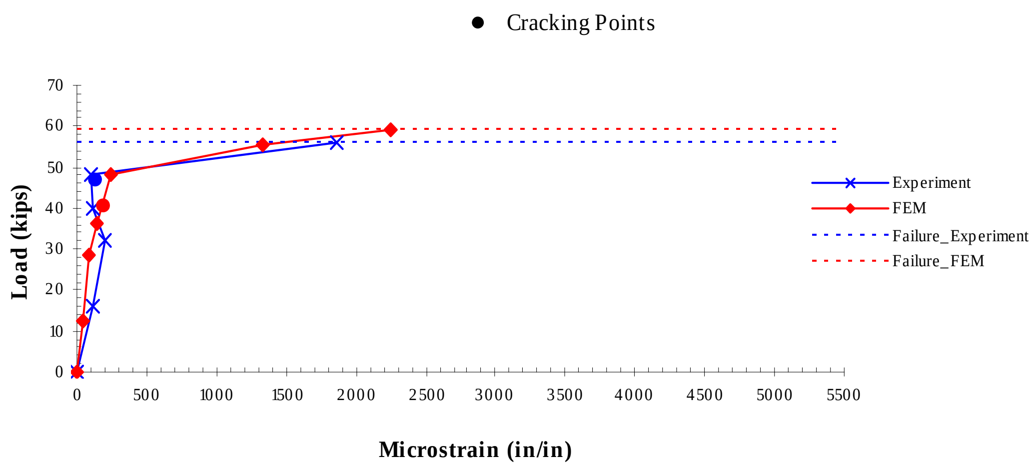


DEMEC 22

**Figure B.3 (*cont.*):** FEM (β = 0.20) vs. experimental strain measurements at different DEMEC locations for the 3ft_cip_corner bridge deck

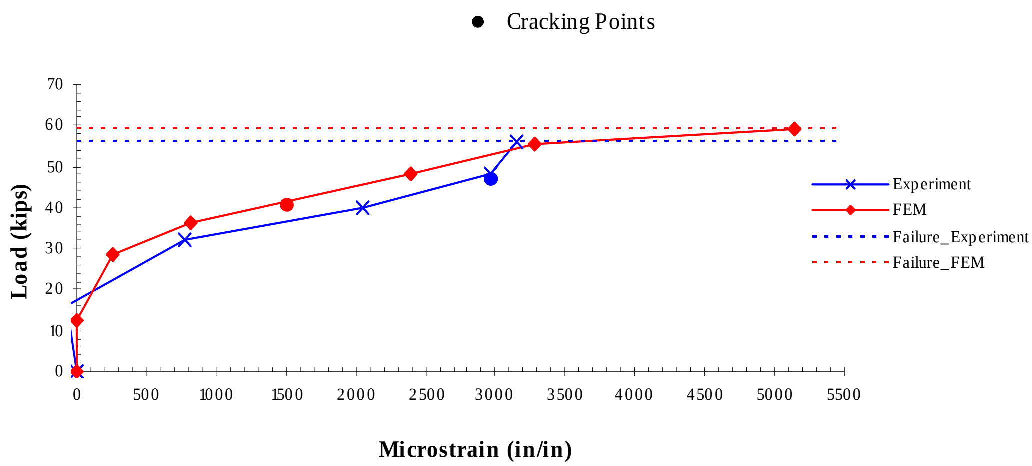


DEMEC 35

**Figure B.3 (*cont.*):** FEM (β = 0.20) vs. experimental strain measurements at different DEMEC locations for the 3ft_cip_corner bridge deck

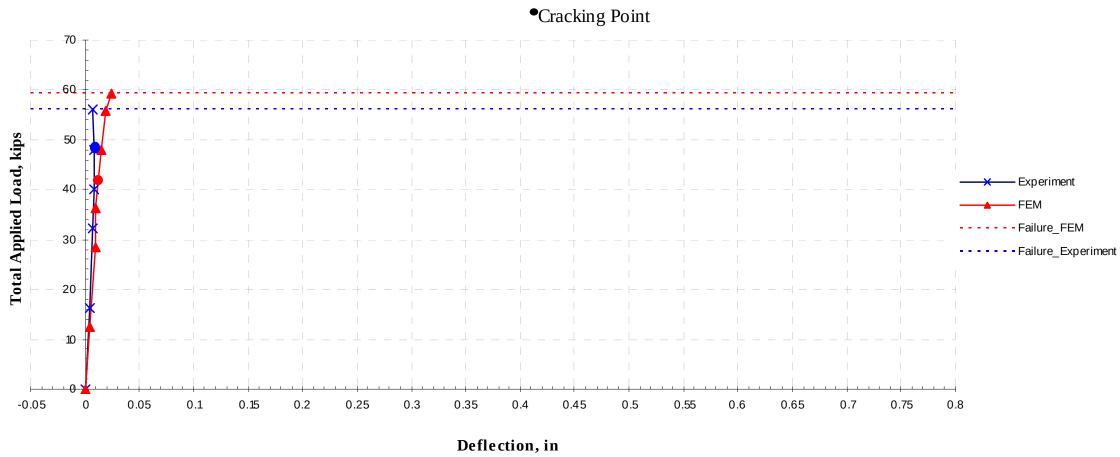


gauge 1

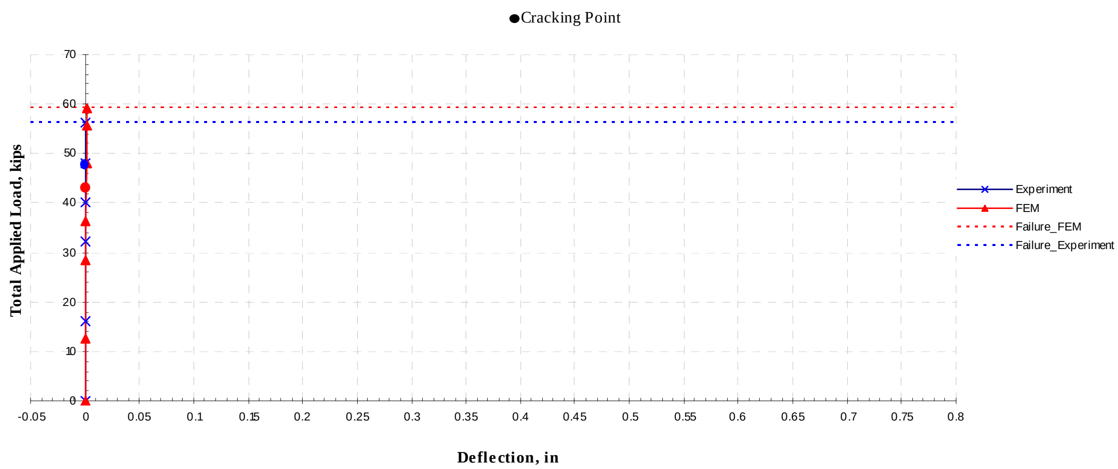


gauge 2

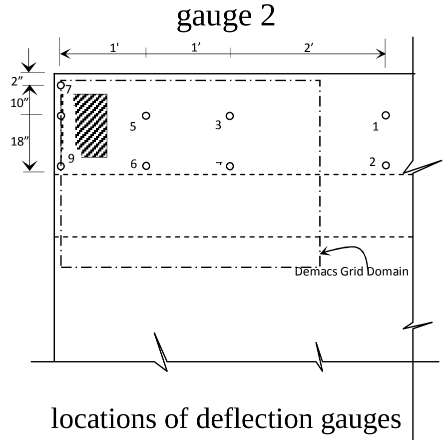


locations of deflection gauges

**Figure B.4:** FEM (β = 0.20) vs. experimental deflection measurements at different locations for the 3ft_cip_corner bridge deck

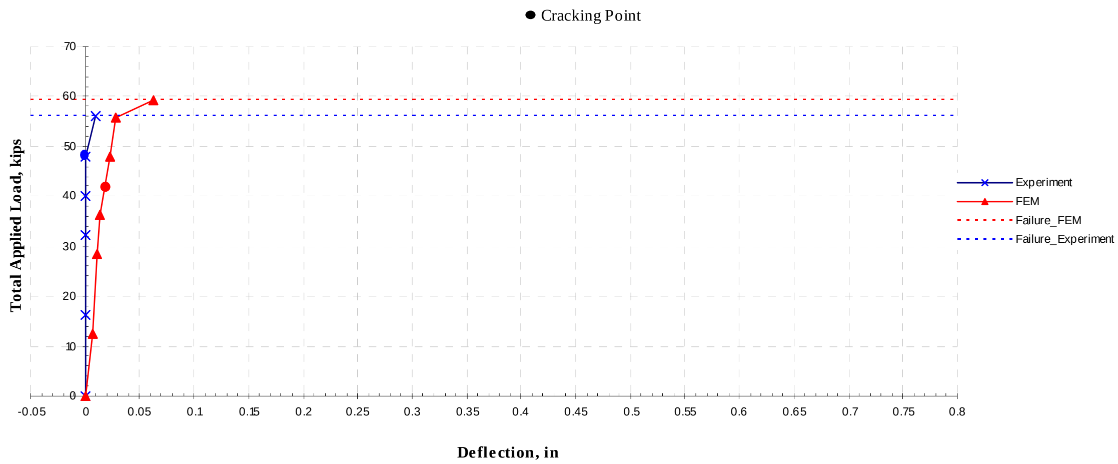


gauge 3

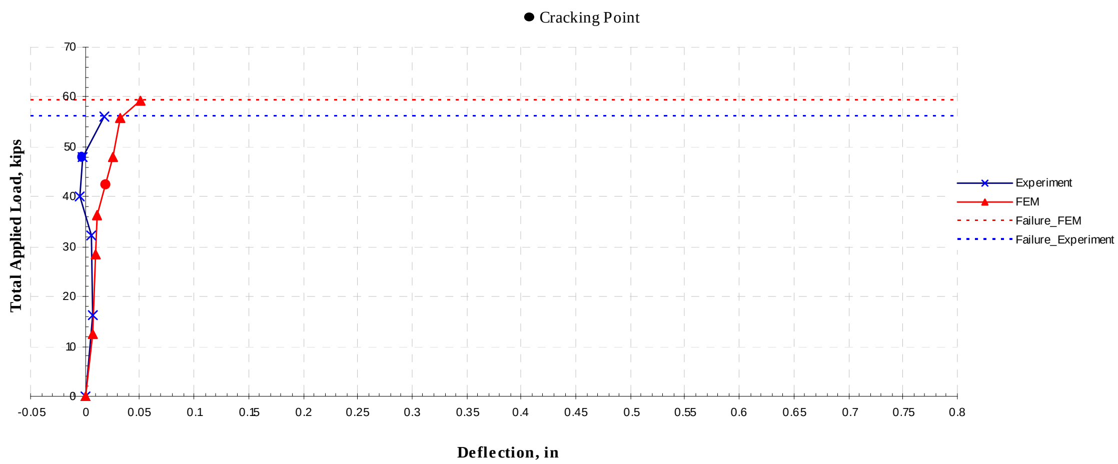


gauge 4

**Figure B.4 (*cont.*):** FEM (β = 0.20) vs. experimental deflection measurements at different locations for the 3ft_cip_corner bridge deck

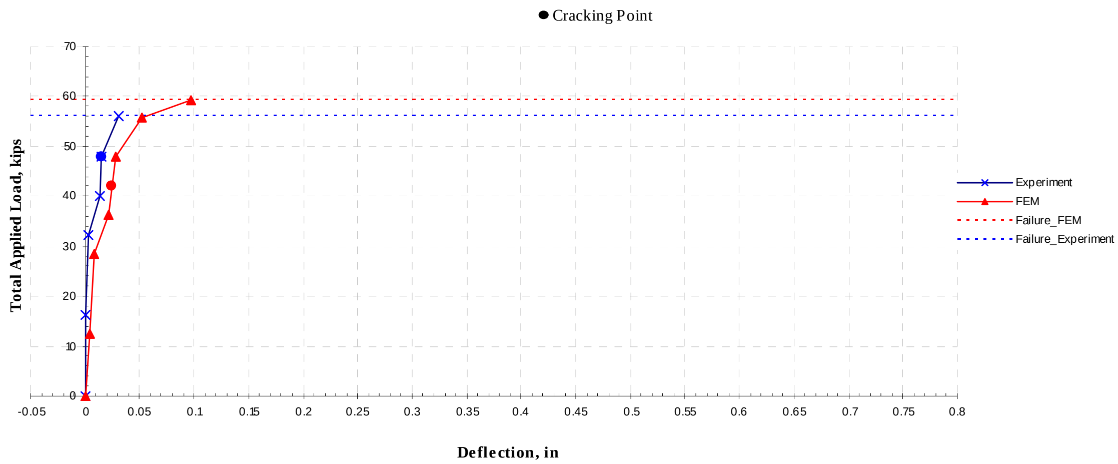


gauge 5

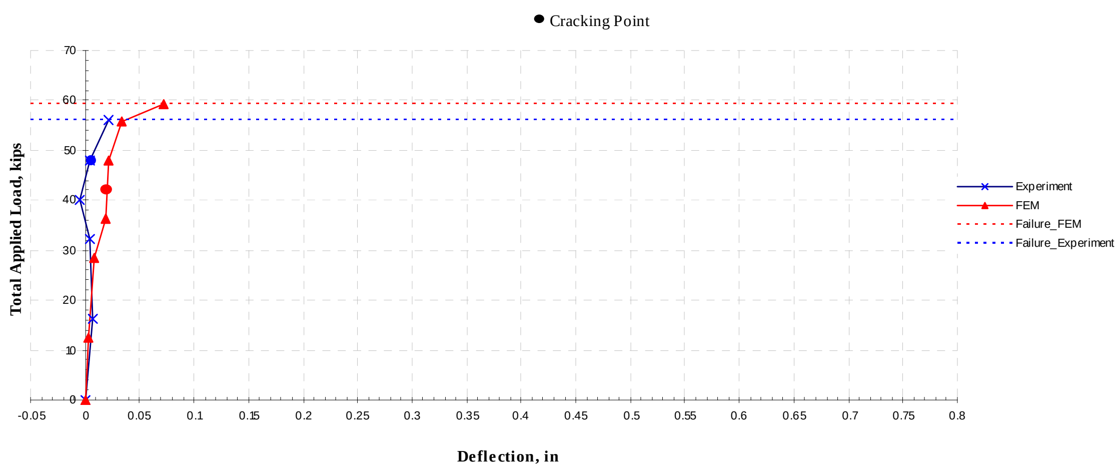


gauge 6

**Figure B.4 (*cont.*):** FEM (β = 0.20) vs. experimental deflection measurements at different locations for the 3ft_cip_corner bridge deck

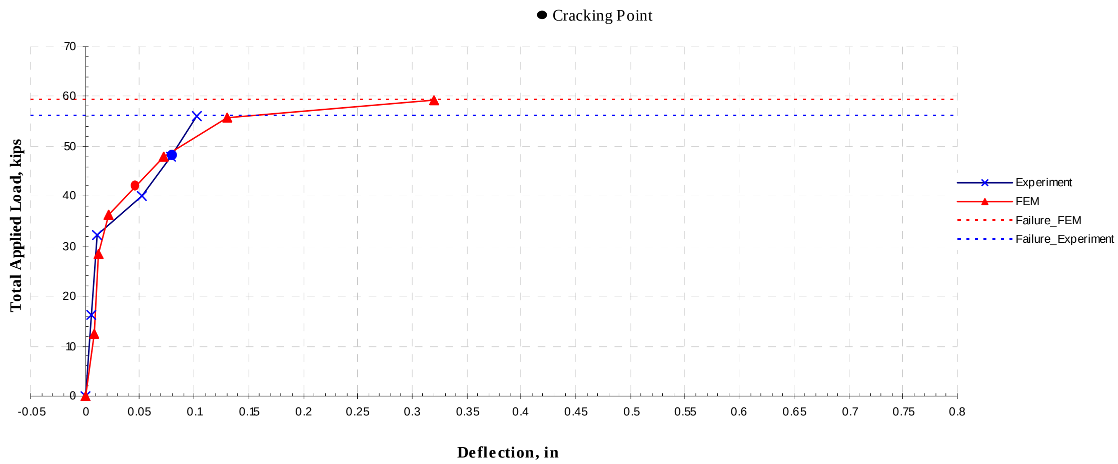


gauge 7

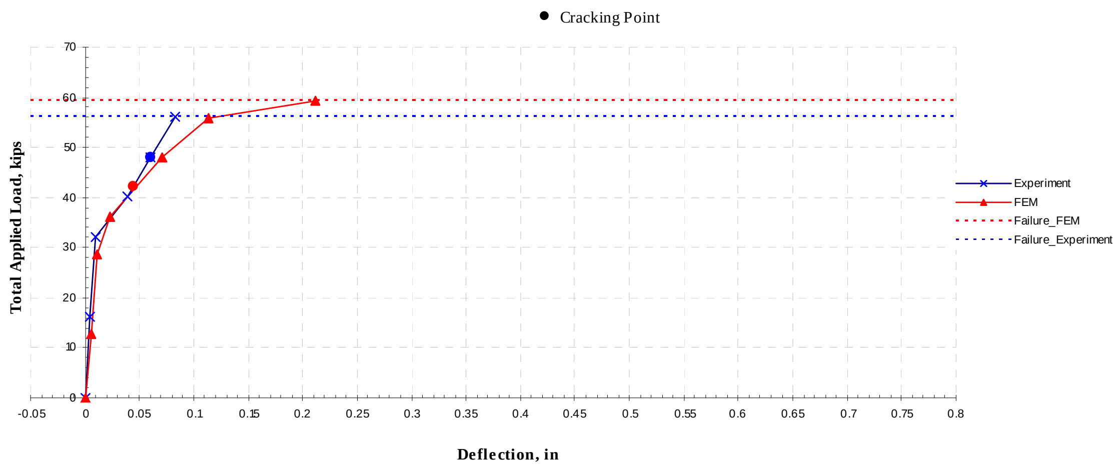


gauge 8

**Figure B.4 (*cont.*):** FEM (β = 0.20) vs. experimental deflection measurements at different locations for the 3ft_cip_corner bridge deck

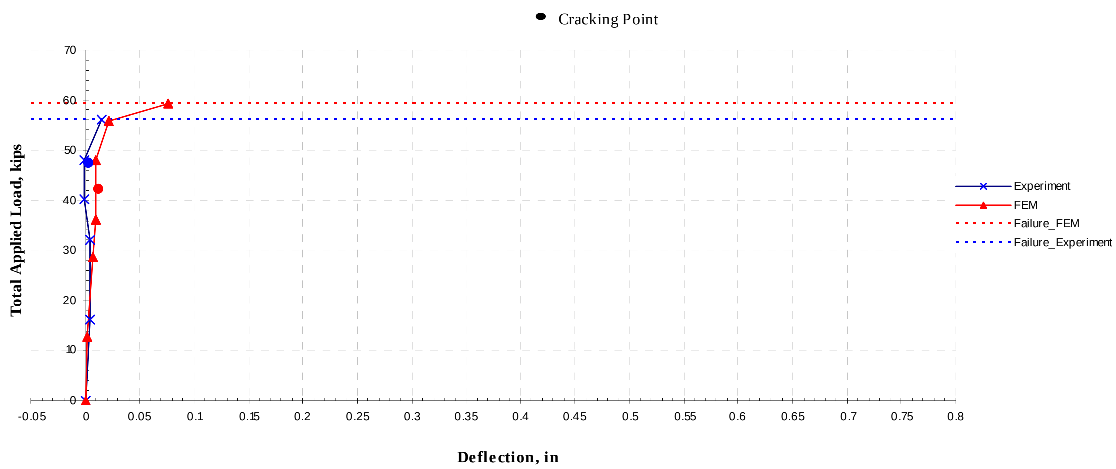


gauge 9

**Figure B.4 (*cont.*):** FEM (β = 0.20) vs. experimental deflection measurements at different locations for the 3ft_cip_corner bridge deck

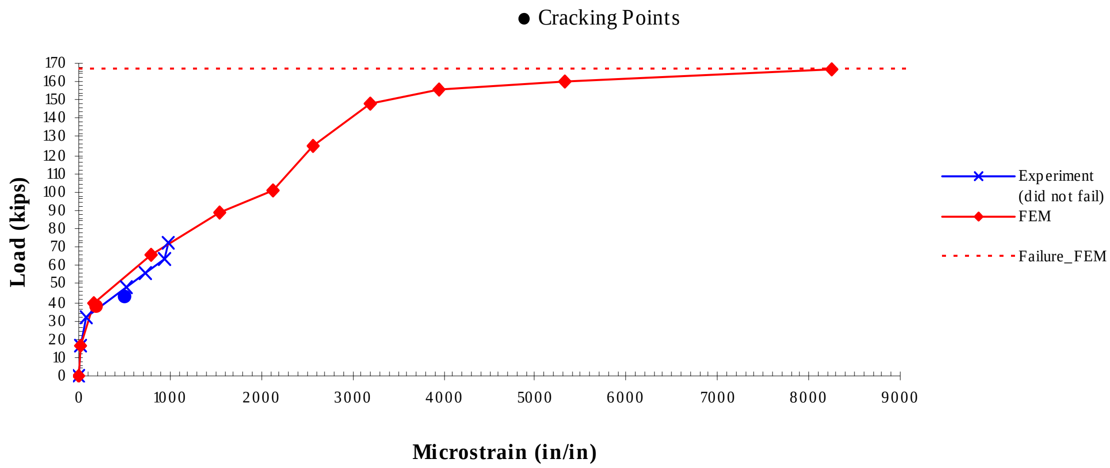


DEMEC 41

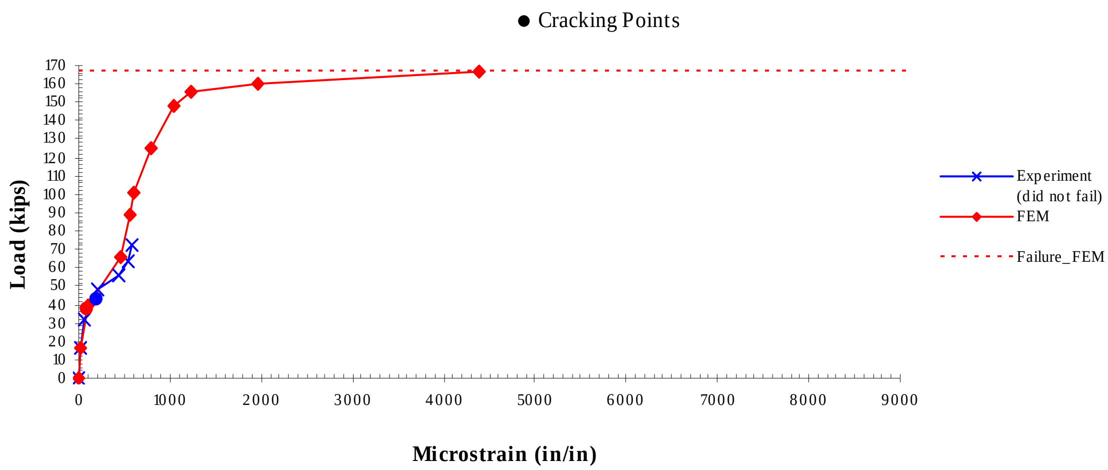


DEMEC 29

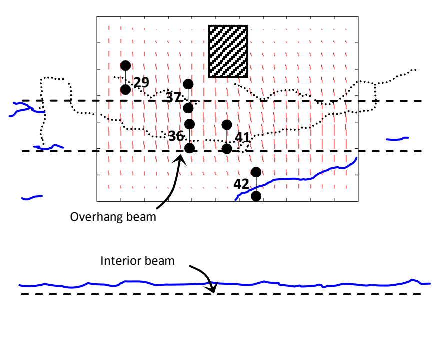


DEMEC locations

**Figure B.5:** FEM (β = 0.20) vs. experimental strain measurements at different DEMEC locations for the 3ft_pre_center bridge deck

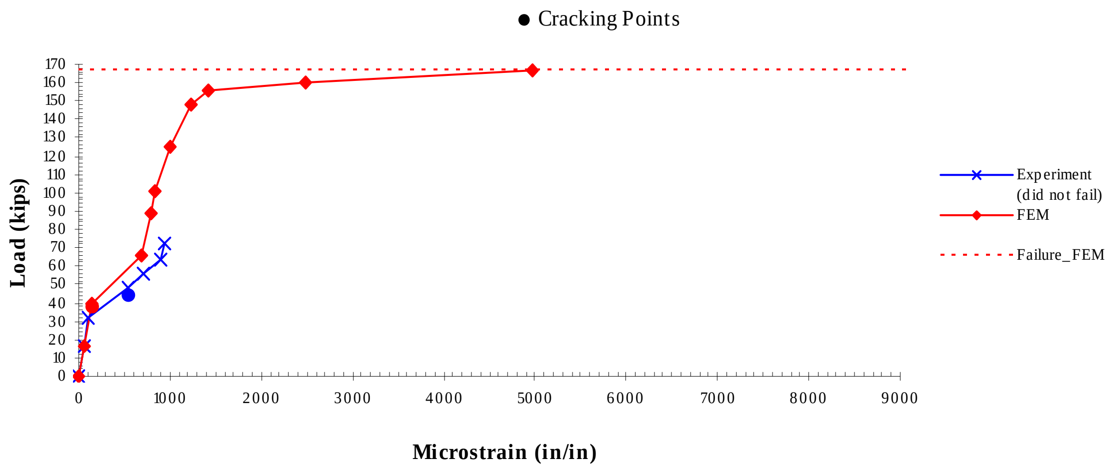


DEMEC 36

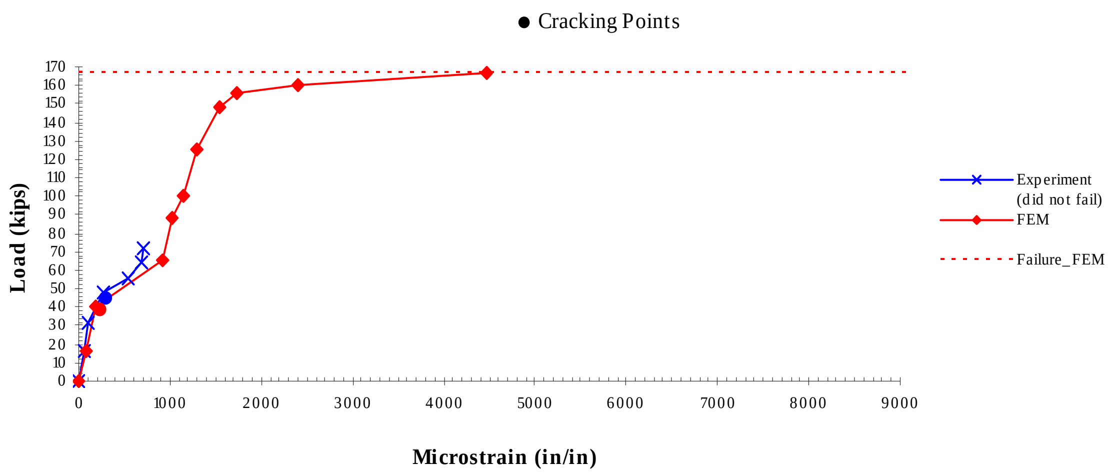


DEMEC 37

**Figure B.5 (*cont.*):** FEM (β = 0.20) vs. experimental strain measurements at different DEMEC locations for the 3ft_pre_center bridge deck

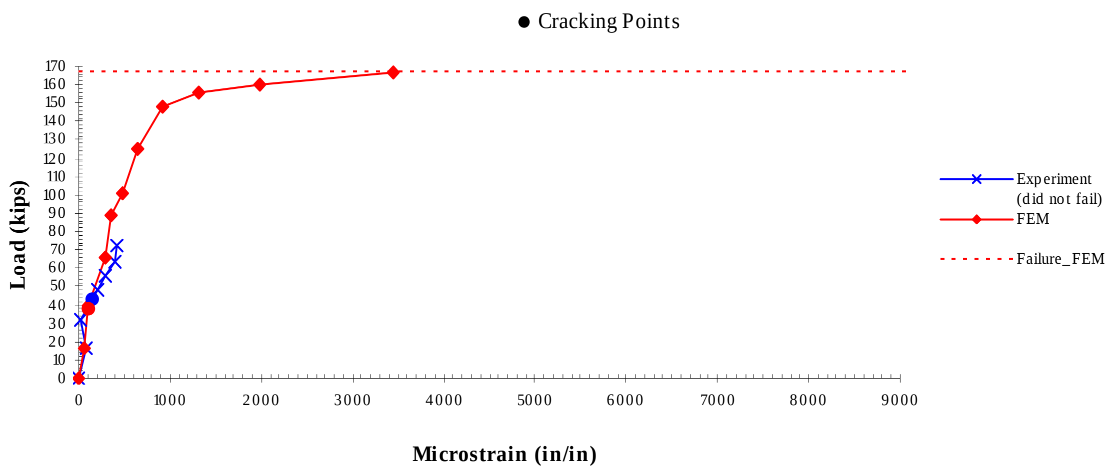


DEMEC 42

**Figure B.5 (*cont.*):** FEM (β = 0.20) vs. experimental strain measurements at different DEMEC locations for the 3ft_pre_center bridge deck

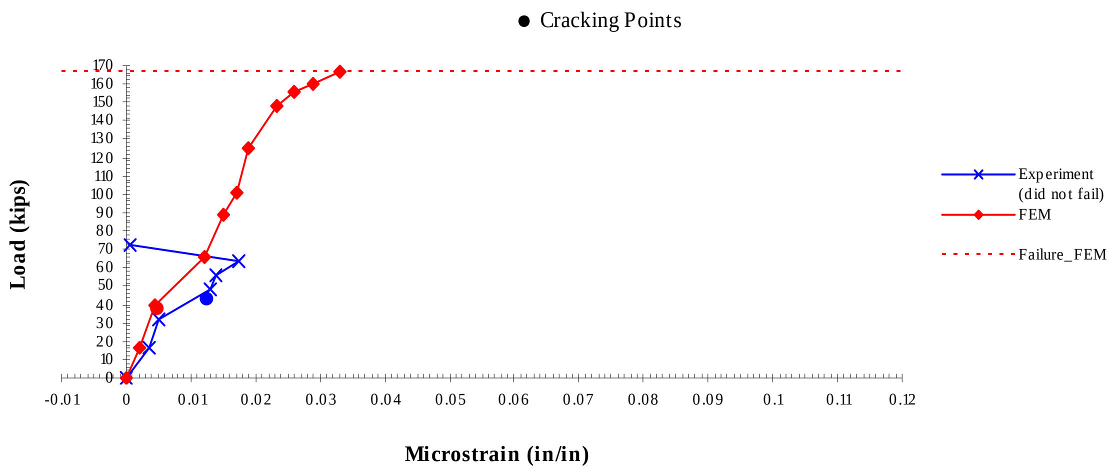


gauge 1

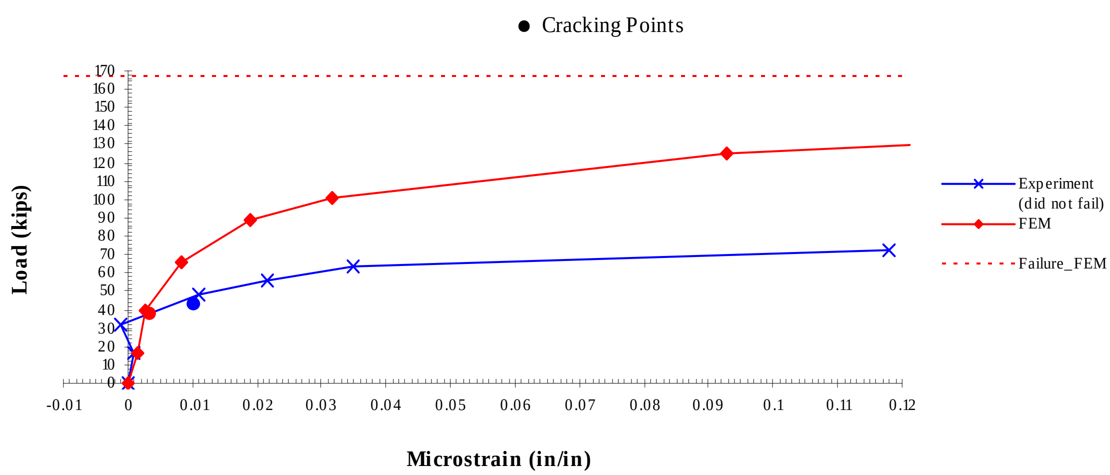


gauge 2

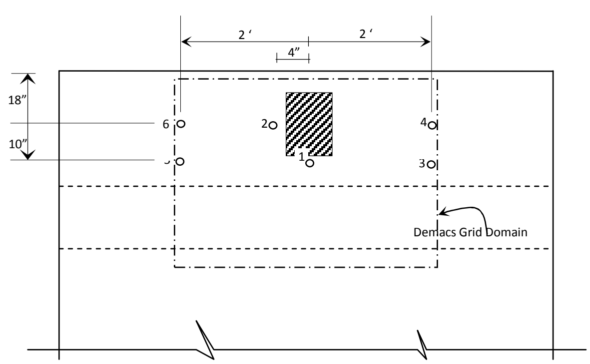


locations of deflection gauges

**Figure B.6:** FEM (β = 0.20) vs. experimental deflection measurements at different locations for the 3ft_pre_center bridge deck

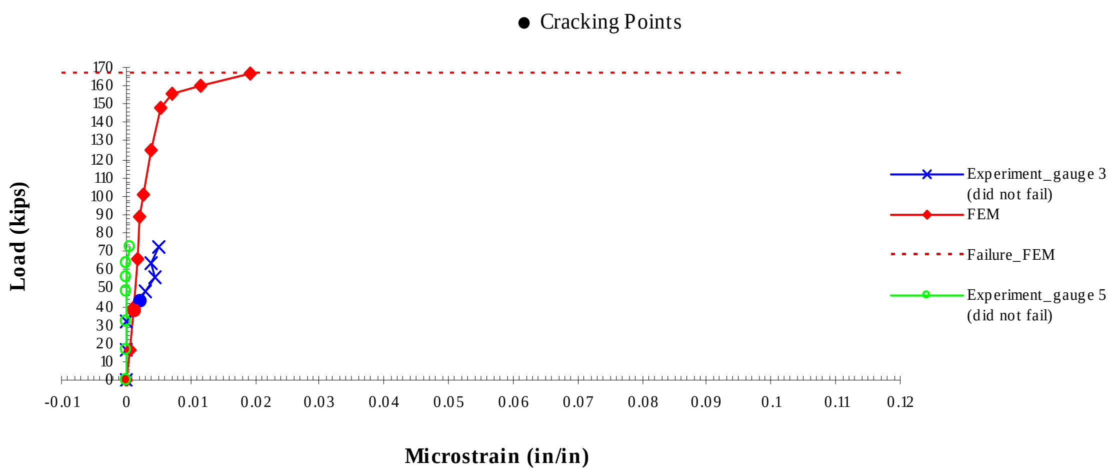


gauges 3&5

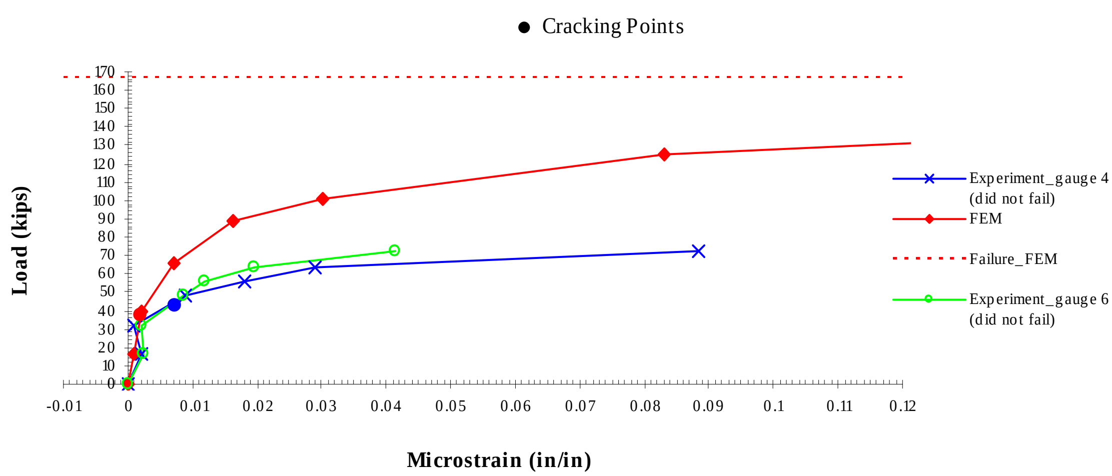


gauges 4&6

**Figure B.6 (*cont.*):** FEM (β = 0.20) vs. experimental deflection measurements at different locations for the 3ft_pre_center bridge deck

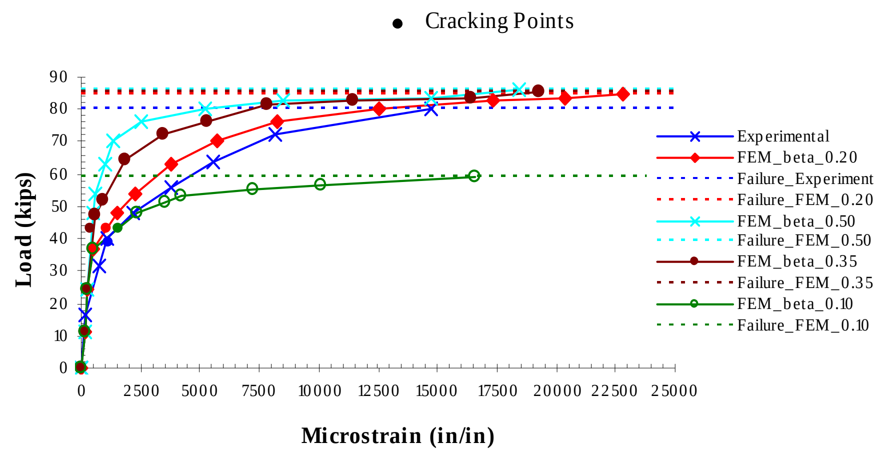


DEMEC 35

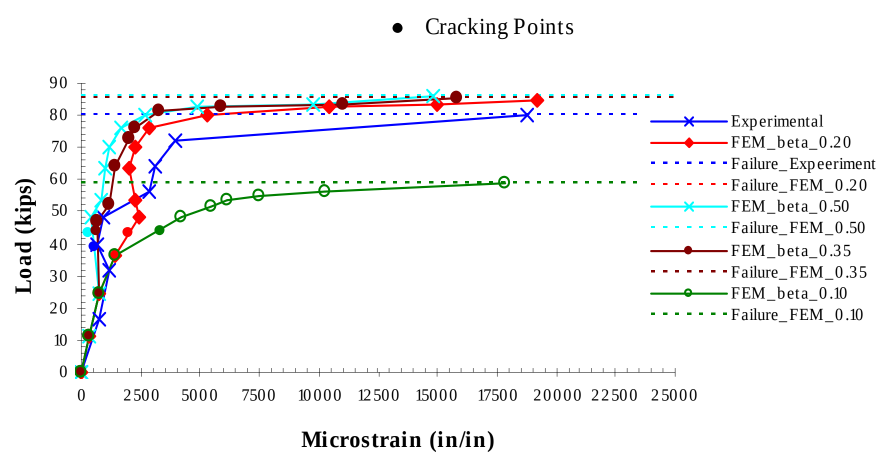


DEMEC 12

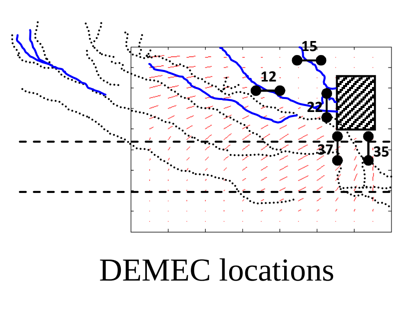


DEMEC locations

**Figure B.7:** Effect of the reduction shear factor; β on strain measurements at different DEMEC locations for the 3ft_pre_corner bridge deck

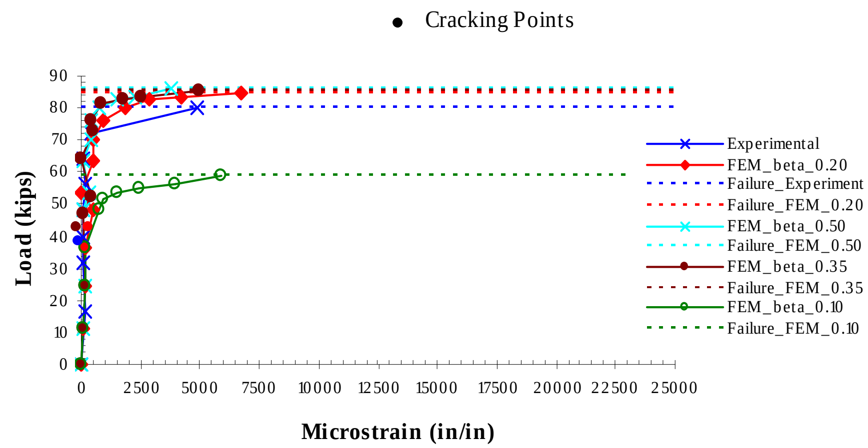


DEMEC 15

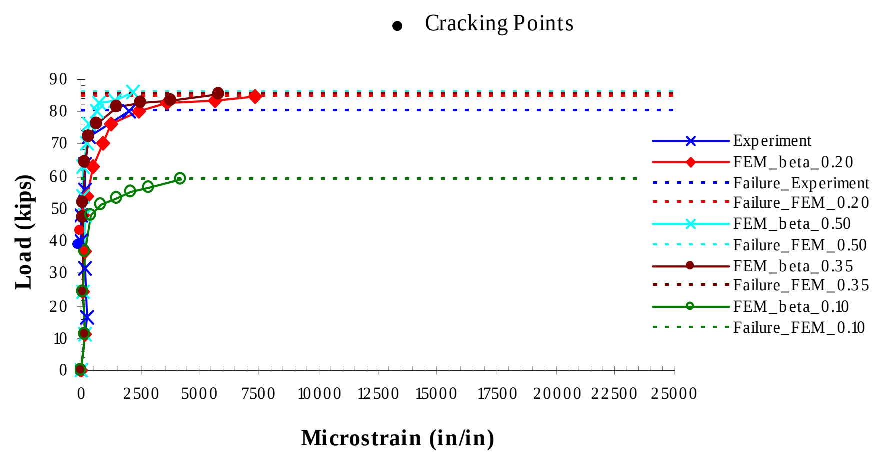


DEMEC 22

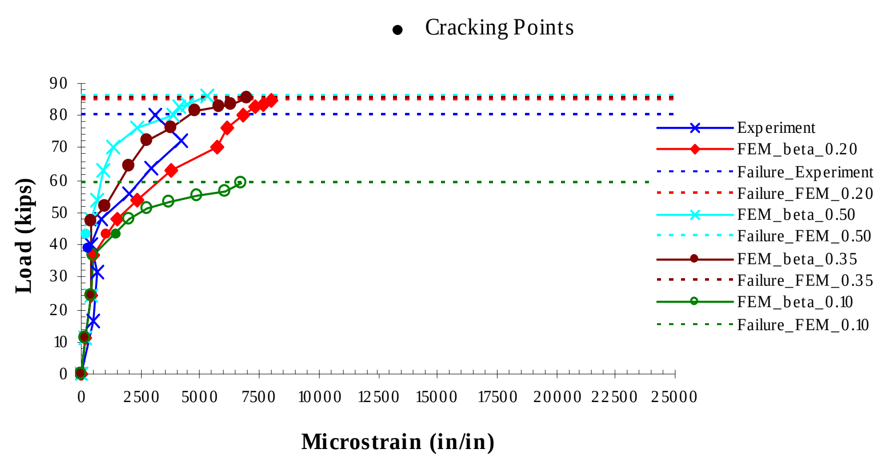


DEMEC 37

**Figure B.7 (*cont.*):** Effect of the reduction shear factor; β on strain measurements at different DEMEC locations for the 3ft_pre_corner bridge deck

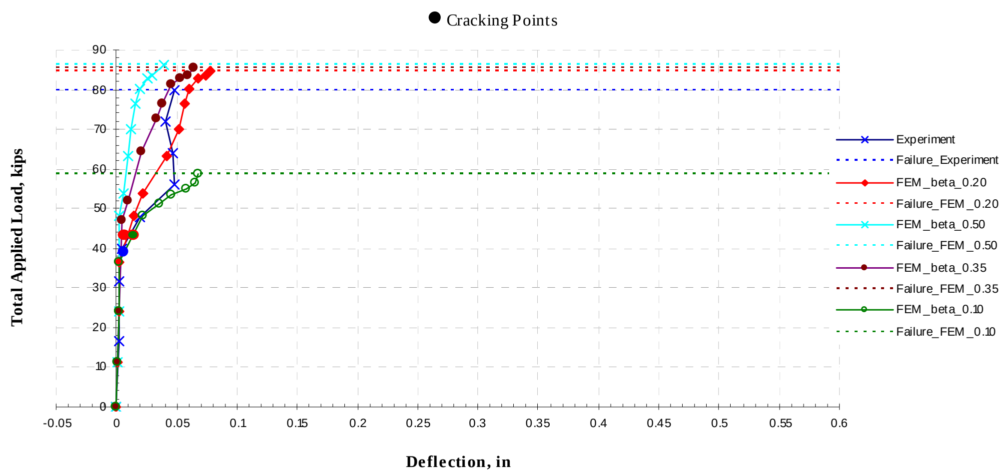


gauge 1

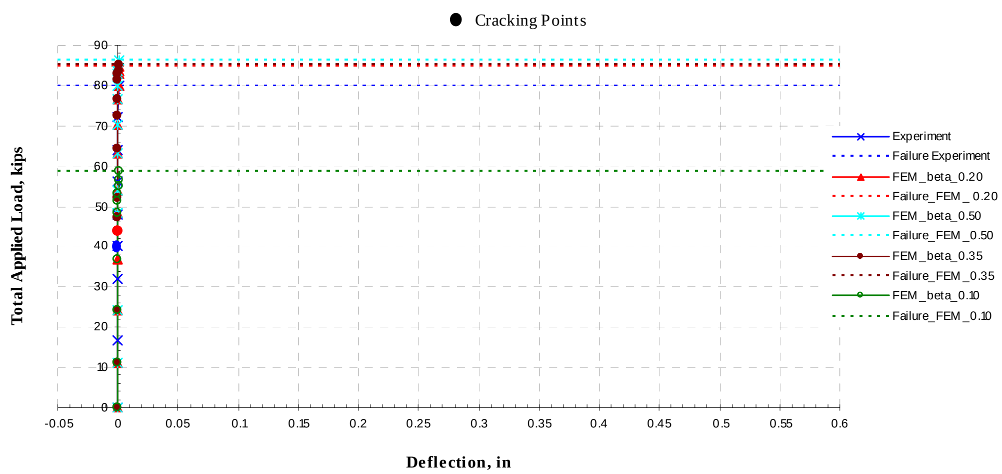


gauge 2 (very small deflections)

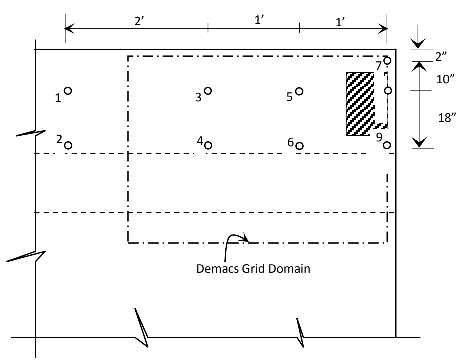


locations of deflection gauges

**Figure B.8:** Effect of the reduction shear factor; β on deflection measurements at different locations for the 3ft_pre_corner bridge deck

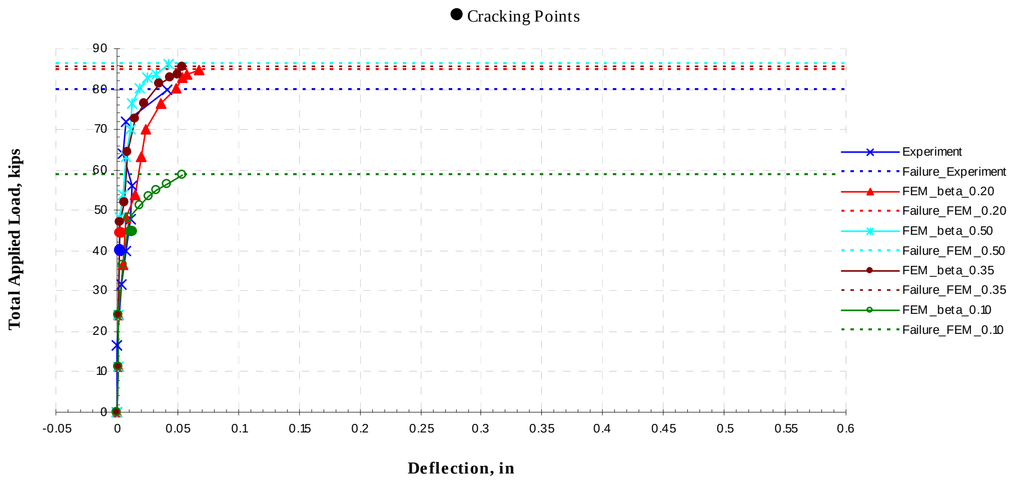


gauge 3

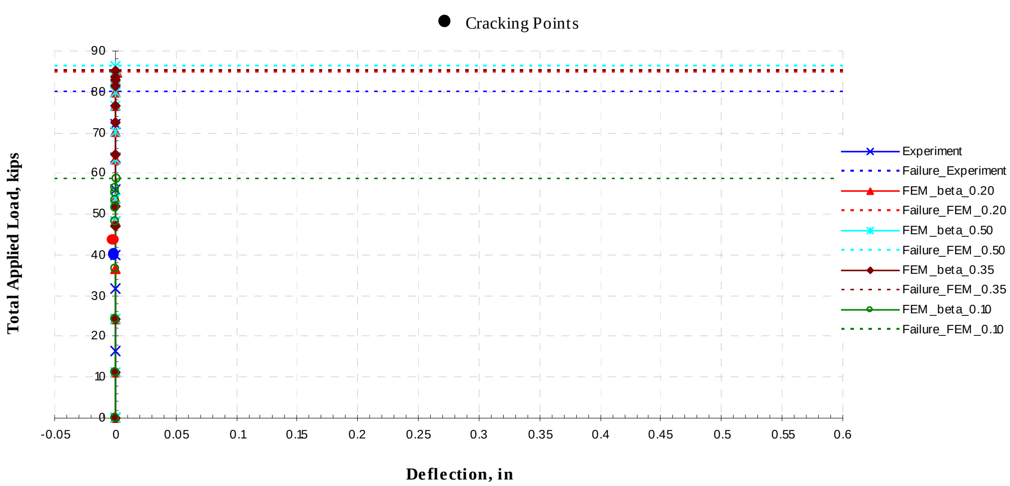


gauge 4 (very small deflections)

**Figure B.8 (*cont.*):** Effect of the reduction shear factor; β on deflection measurements at different locations for the 3ft_pre_corner bridge deck

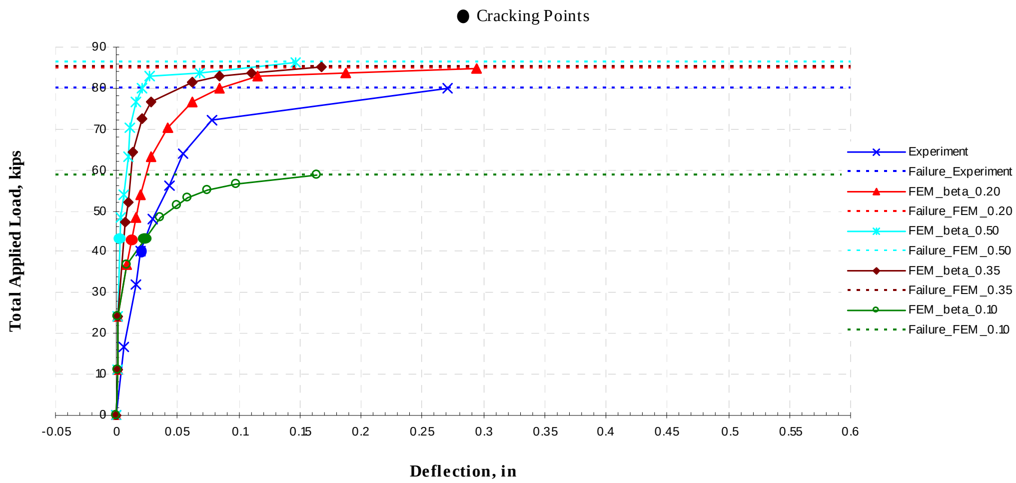


gauge 5

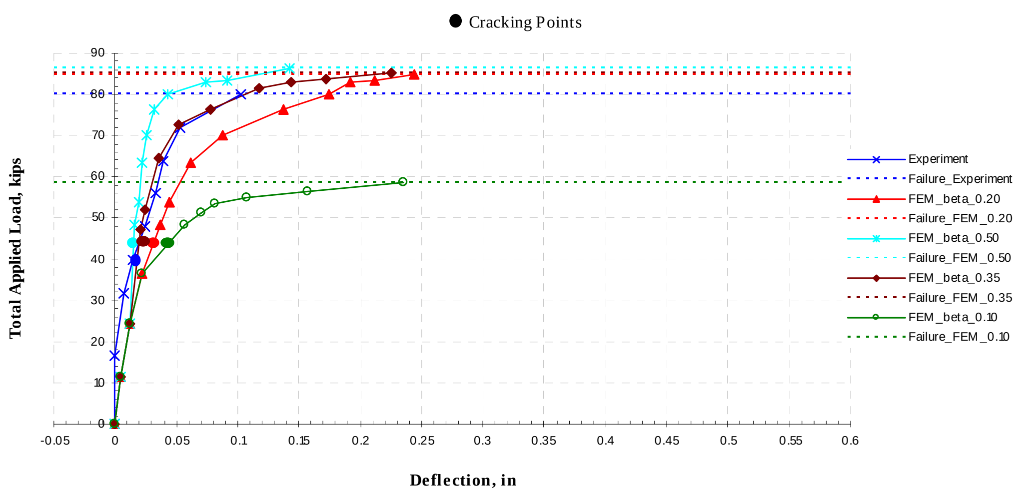


gauge 6

**Figure B.8 (*cont.*):** Effect of the reduction shear factor; β on deflection measurements at different locations for the 3ft_pre_corner bridge deck

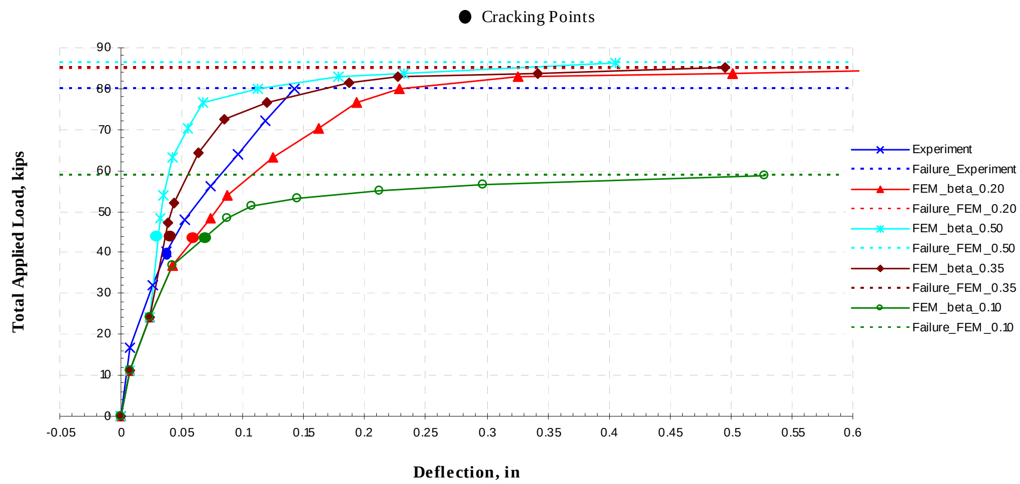


gauge 7

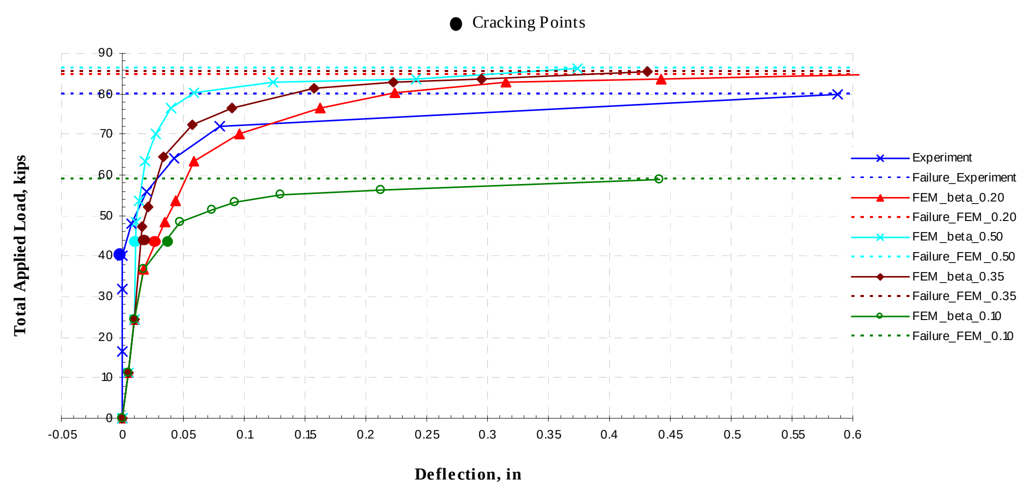


gauge 8

**Figure B.8 (*cont.*):** Effect of the reduction shear factor; β on deflection measurements at different locations for the 3ft_pre_corner bridge deck

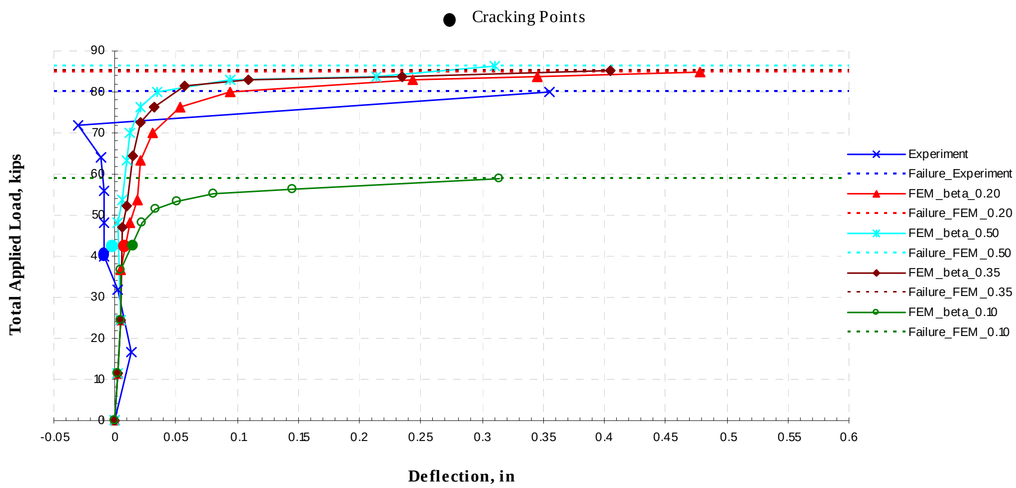


gauge 9

**Figure B.8 (*cont.*):** Effect of the reduction shear factor; β on deflection measurements at different locations for the 3ft_pre_corner bridge deck

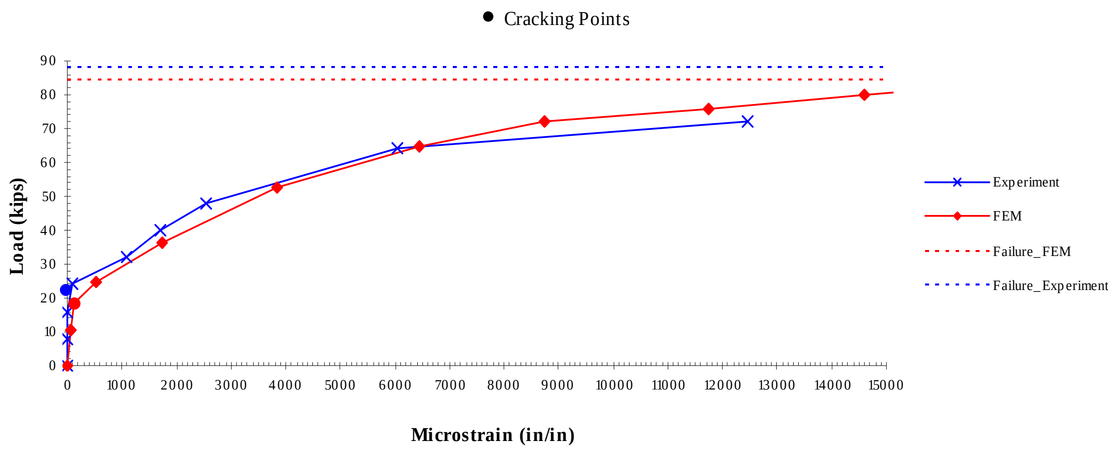


DEMEC 58 (FE value was taken at a location 1" off from mentioned DEMEC number)

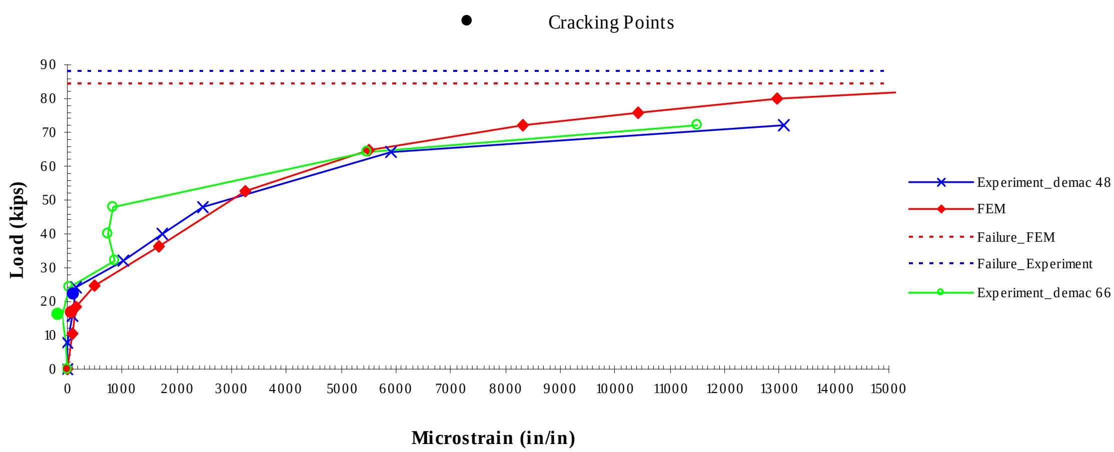


DEMECs 48&66

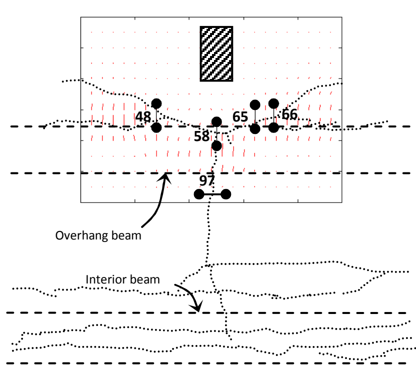


DEMEC locations

**Figure B.9:** FEM (β = 0.20) vs. experimental strain measurements at different DEMEC locations for the 5ft_cip_center bridge deck

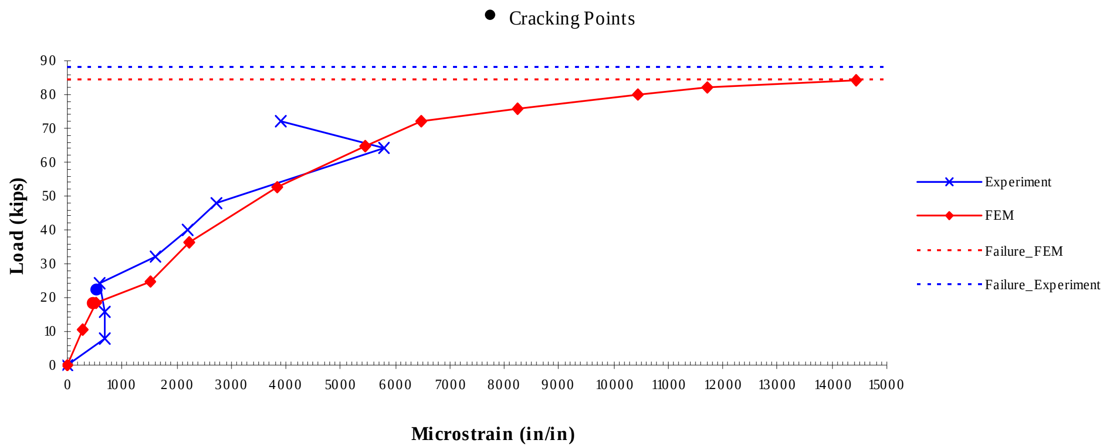


DEMEC 65

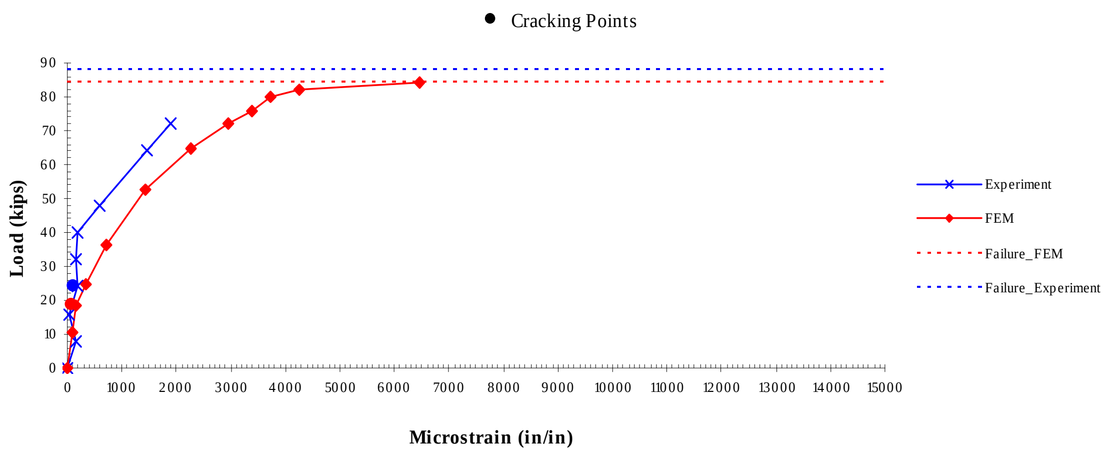


DEMEC 97

**Figure B.9 (*cont.*):** FEM ($\beta$ = 0.20) vs. experimental strain measurements at different DEMEC locations for the 5ft_cip_center bridge deck

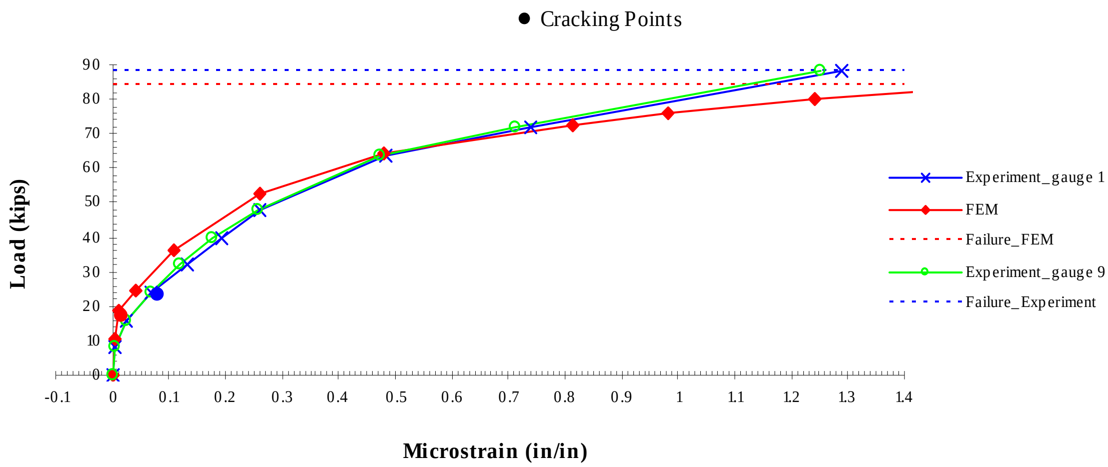


gauges 1&9

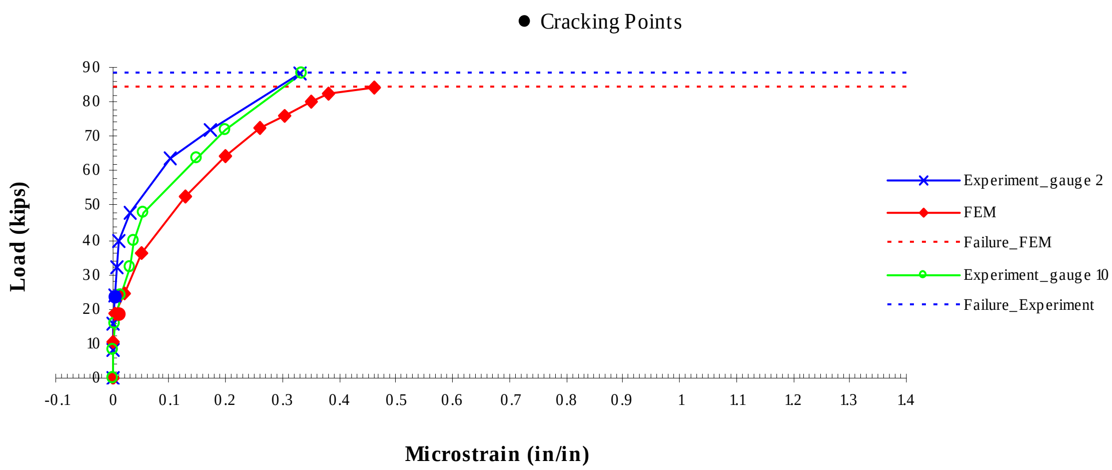


gauges 2&10

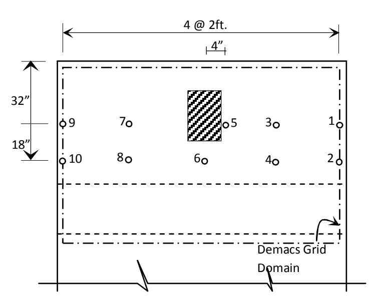


locations of deflection gauges

**Figure B.10:** FEM (β = 0.20) vs. experimental deflection measurements at different locations for the 5ft_cip_center bridge deck

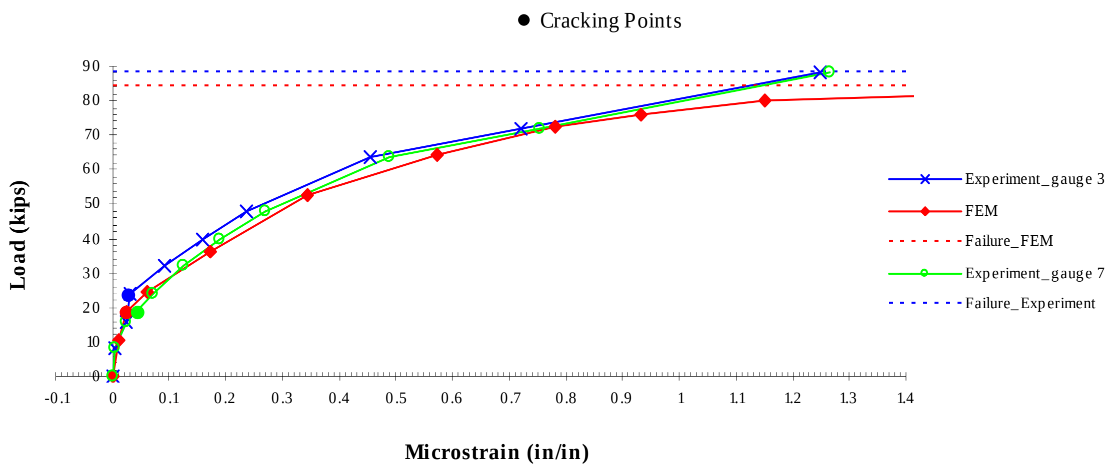


gauges 3&7

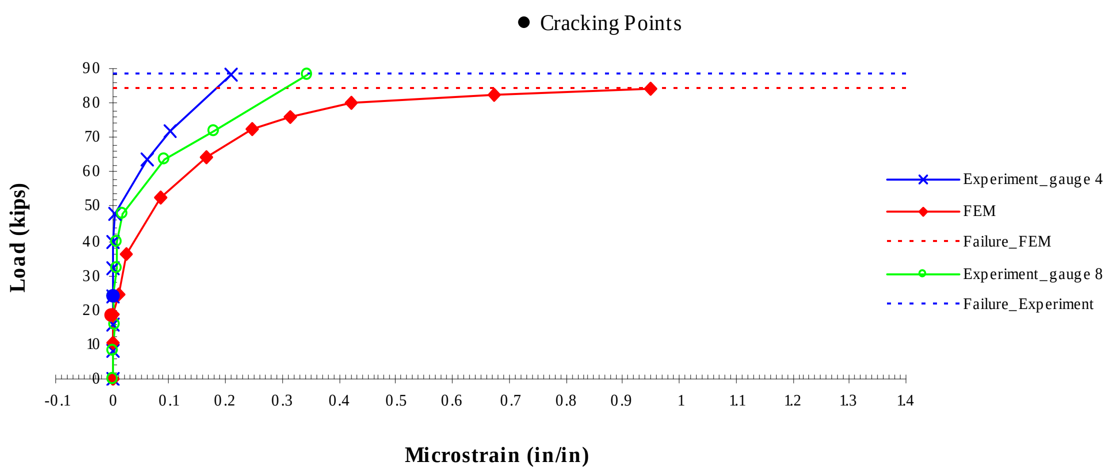


gauges 4&8

**Figure B.10 (*cont.*):** FEM (β = 0.20) vs. experimental deflection measurements at different locations for the 5ft_cip_center bridge deck

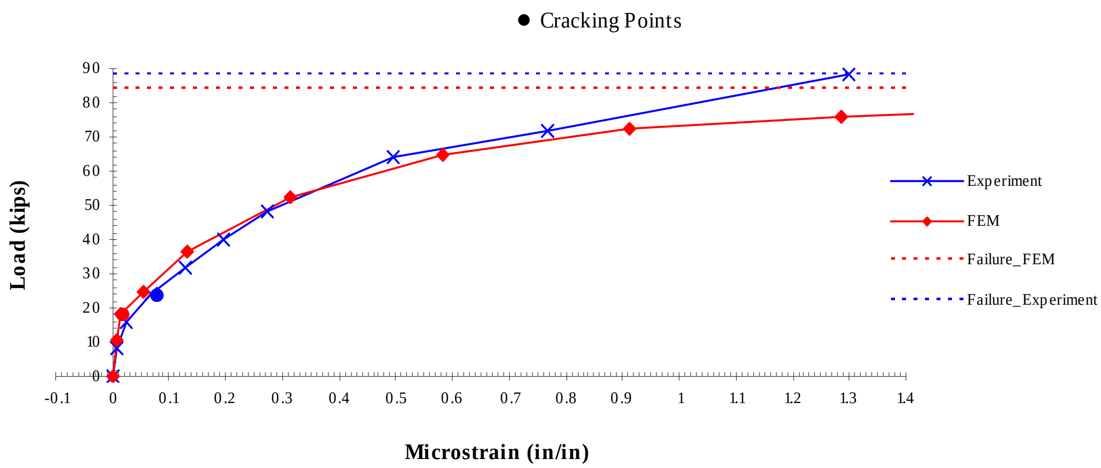


gauge 5

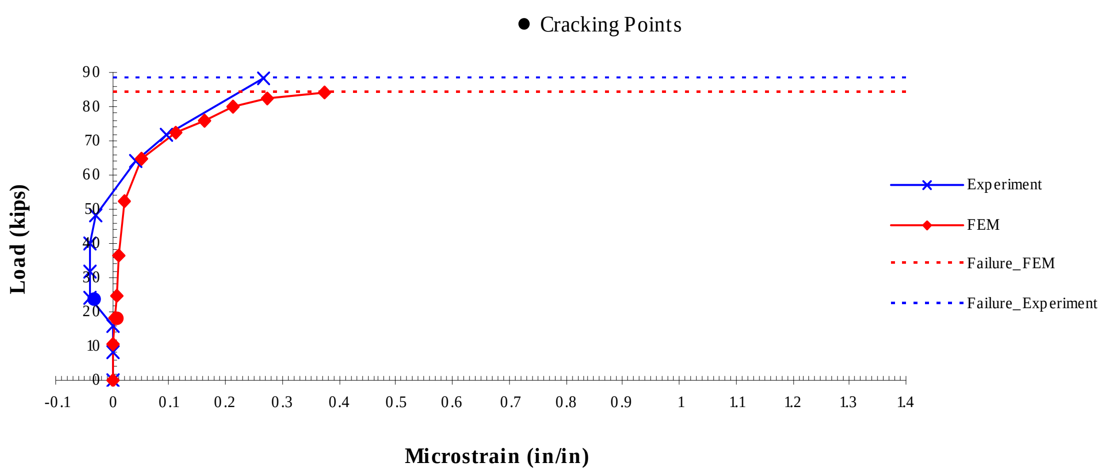


gauge 6

**Figure B.10 (*cont.*):** FEM (β = 0.20) vs. experimental deflection measurements at different locations for the 5ft_cip_center bridge deck

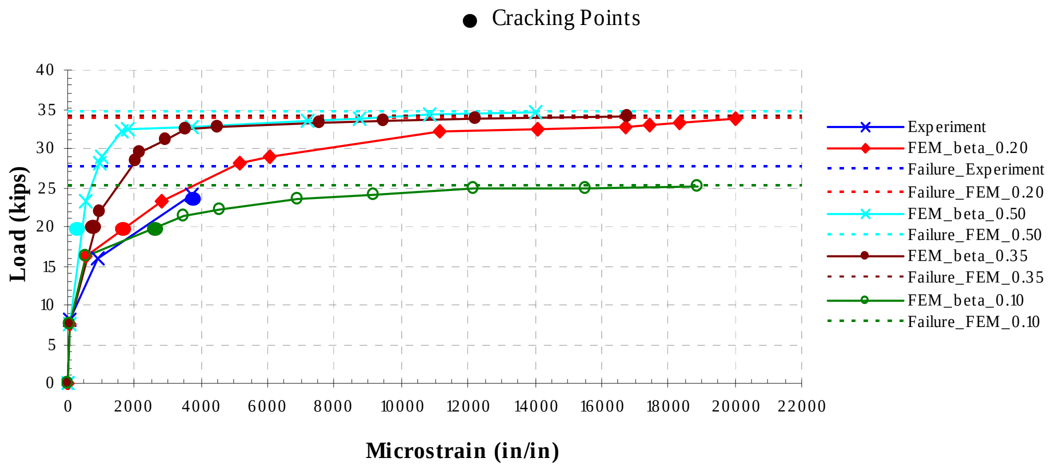


DEMEC 5

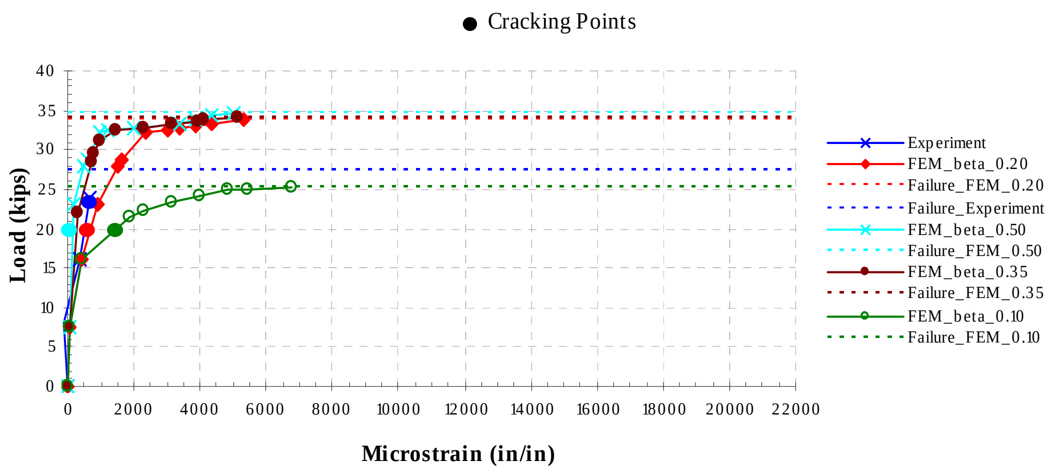


DEMEC 1

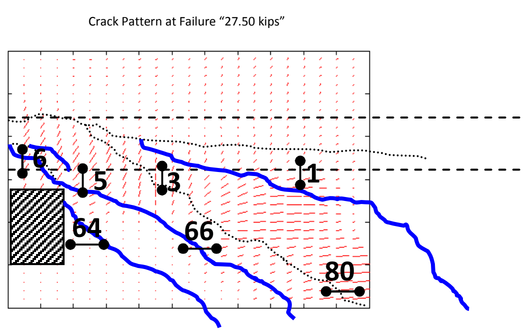


DEMEC locations

**Figure B.11:** Effect of the reduction shear factor; β on strain measurements at different DEMEC locations for the 5ft_cip_corner bridge deck

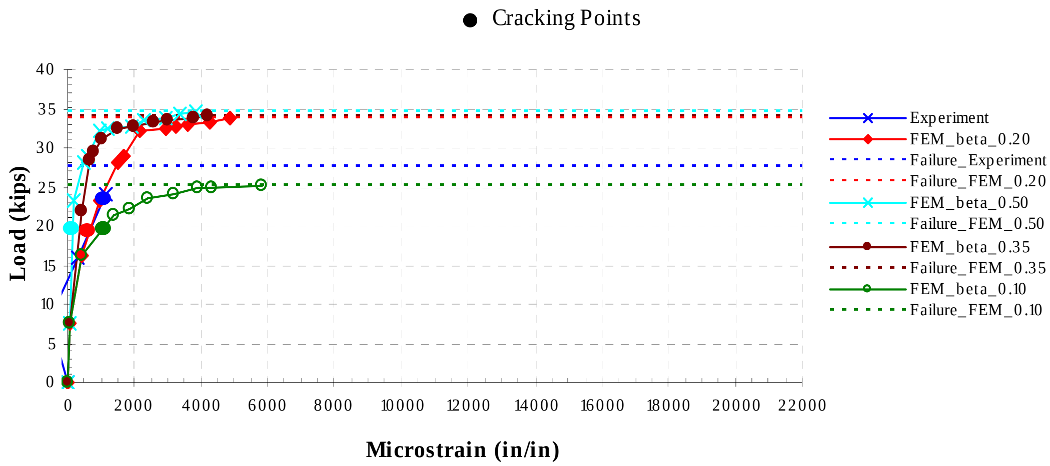


DEMEC 3

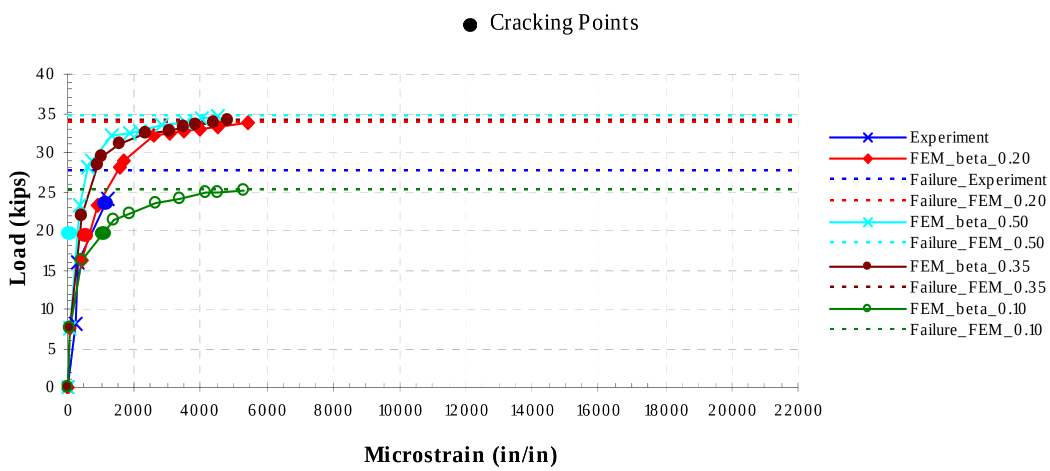


DEMEC 6

**Figure B.11 (*cont.*):** Effect of the reduction shear factor; β on strain measurements at different DEMEC locations for the 5ft_cip_corner bridge deck

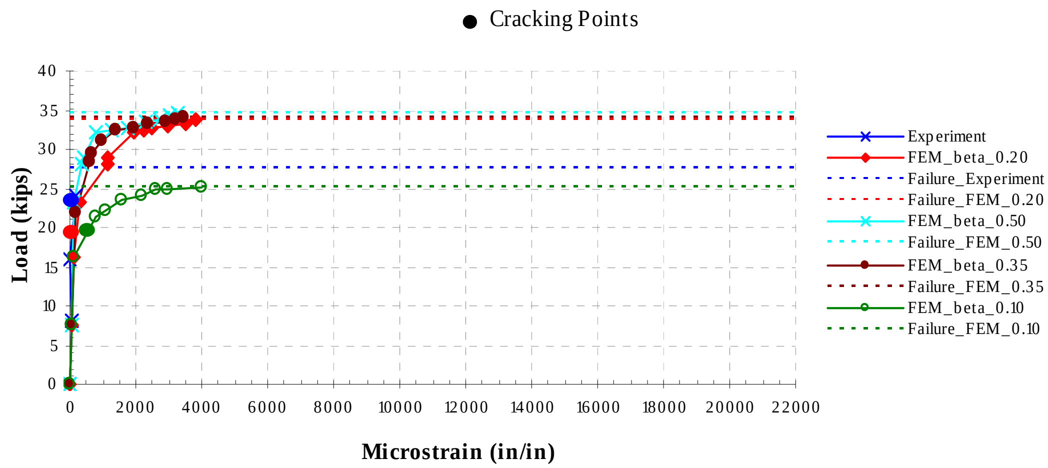


DEMEC 64

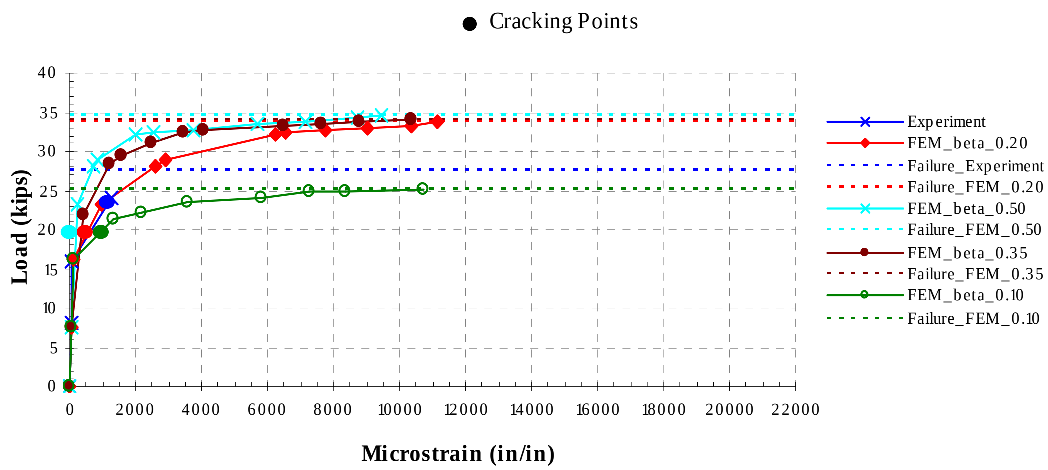


DEMEC 66

**Figure B.11 (*cont.*):** Effect of the reduction shear factor; β on strain measurements at different DEMEC locations for the 5ft_cip_corner bridge deck

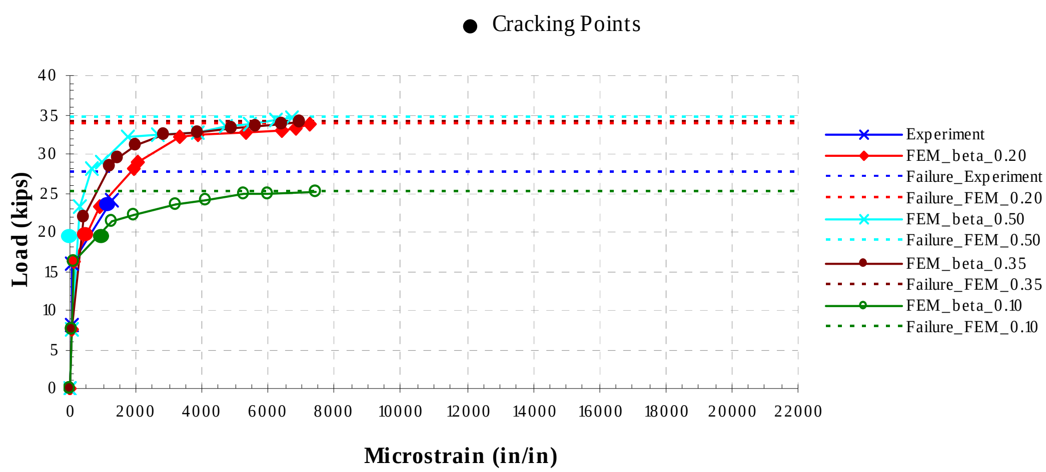


DEMEC 80

**Figure B.11 (*cont.*):** Effect of the reduction shear factor; β on strain measurements at different DEMEC locations for the 5ft_cip_corner bridge deck

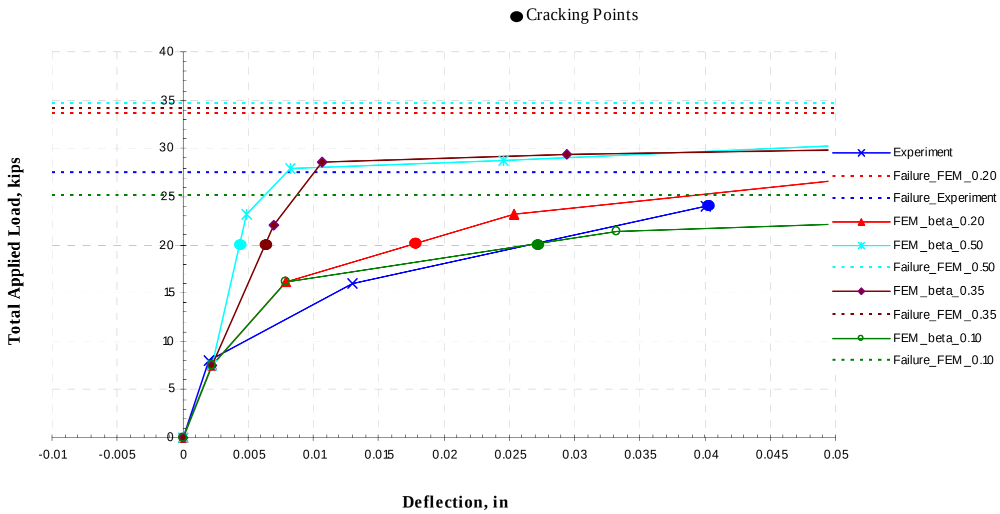


gauge 1

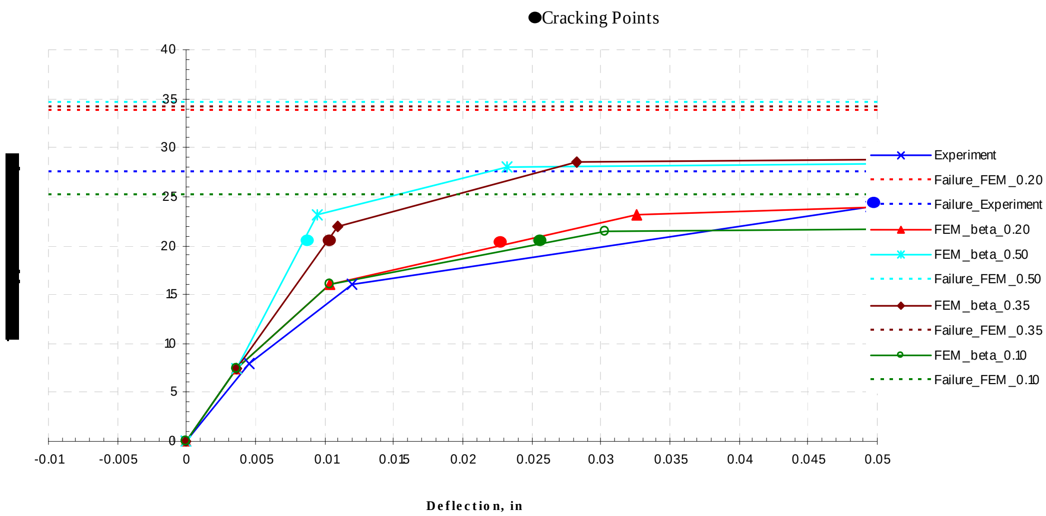


gauge 2

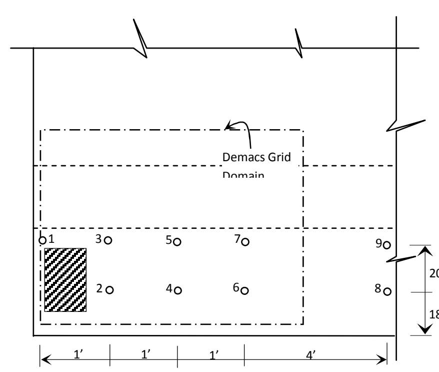


locations of deflection gauges

**Figure B.12:** Effect of the reduction shear factor; β on deflection measurements at different locations for the 5ft_cip_corner bridge deck

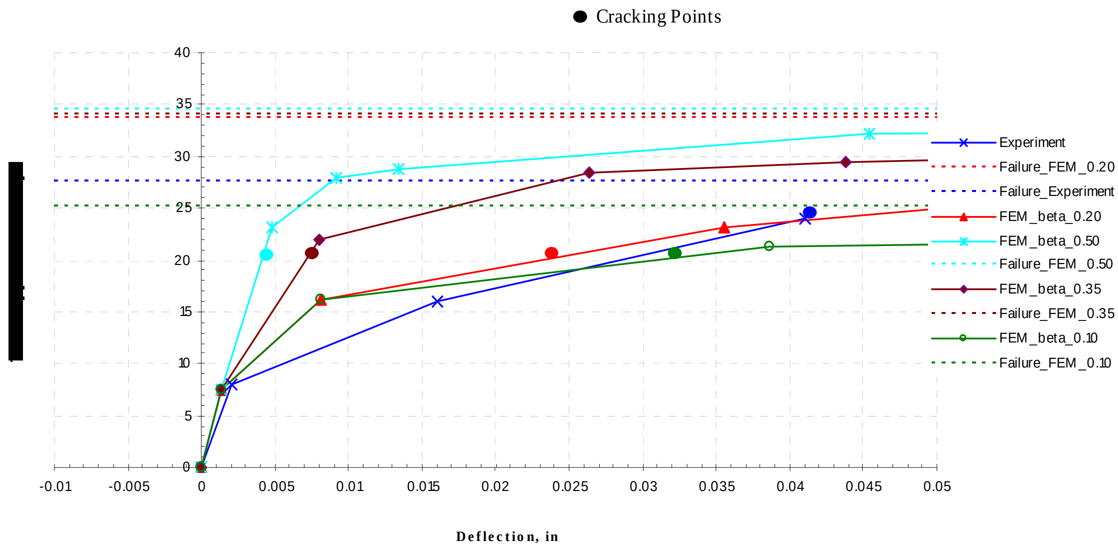


gauge 3

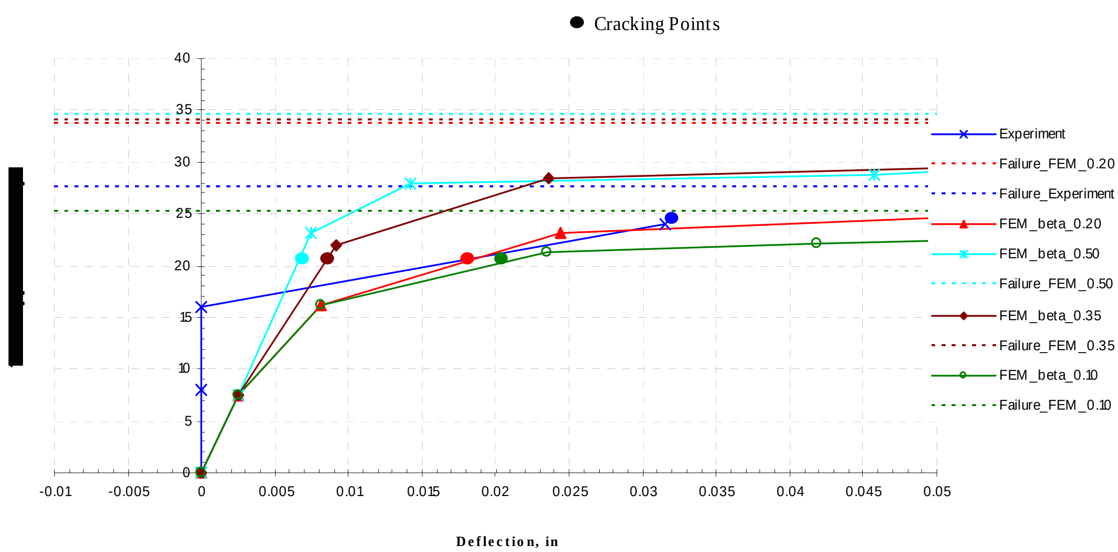


gauge 4

**Figure B.12 (*cont.*):** Effect of the reduction shear factor; β on deflection measurements at different locations for the 5ft_cip_corner bridge deck

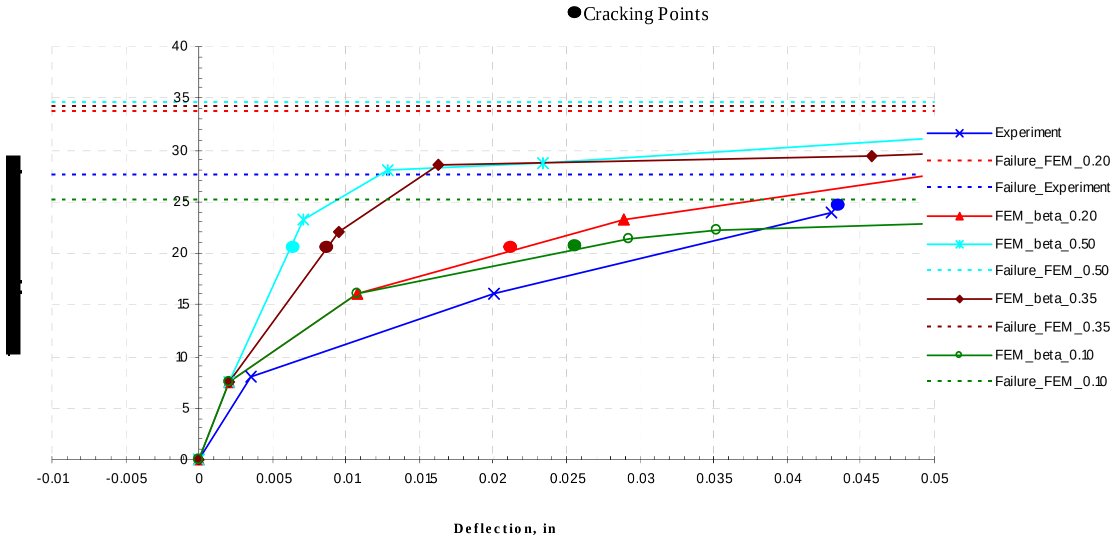


gauge 5

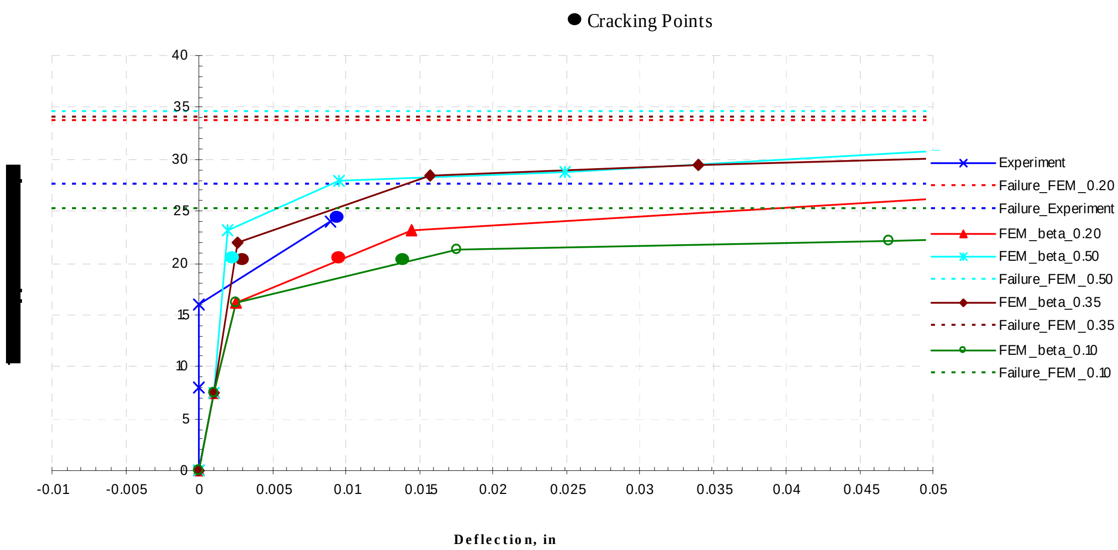


gauge 6

**Figure B.12 (*cont.*):** Effect of the reduction shear factor; β on deflection measurements at different locations for the 5ft_cip_corner bridge deck

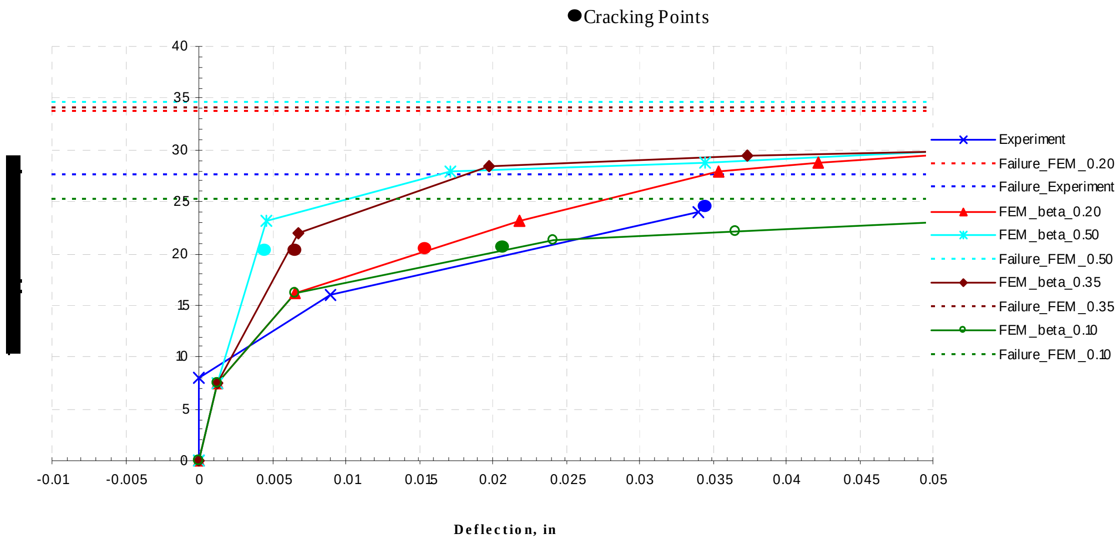


gauge 7

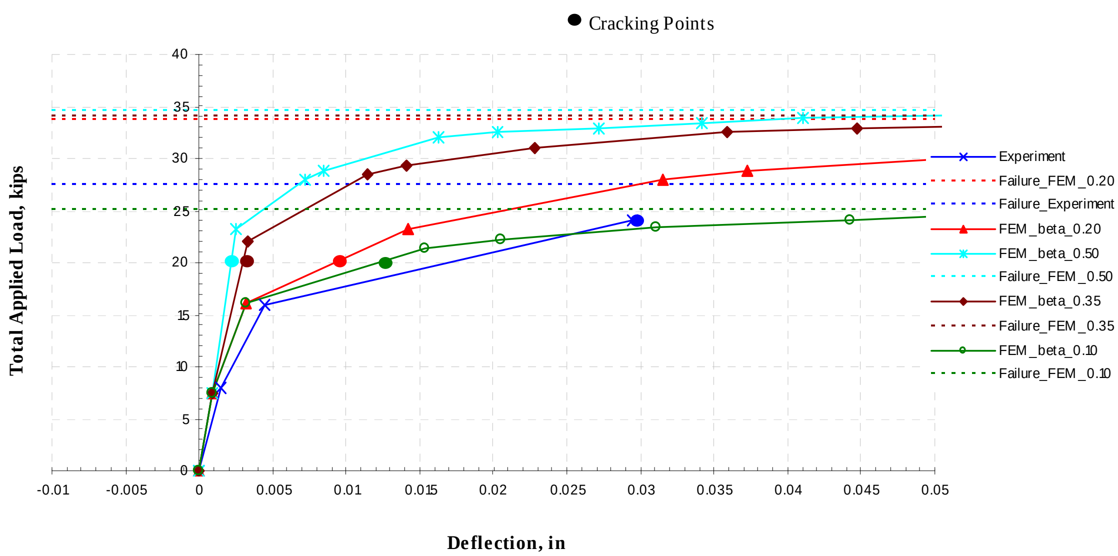


gauge 8

**Figure B.12 (*cont.*):** Effect of the reduction shear factor; β on deflection measurements at different locations for the 5ft_cip_corner bridge deck

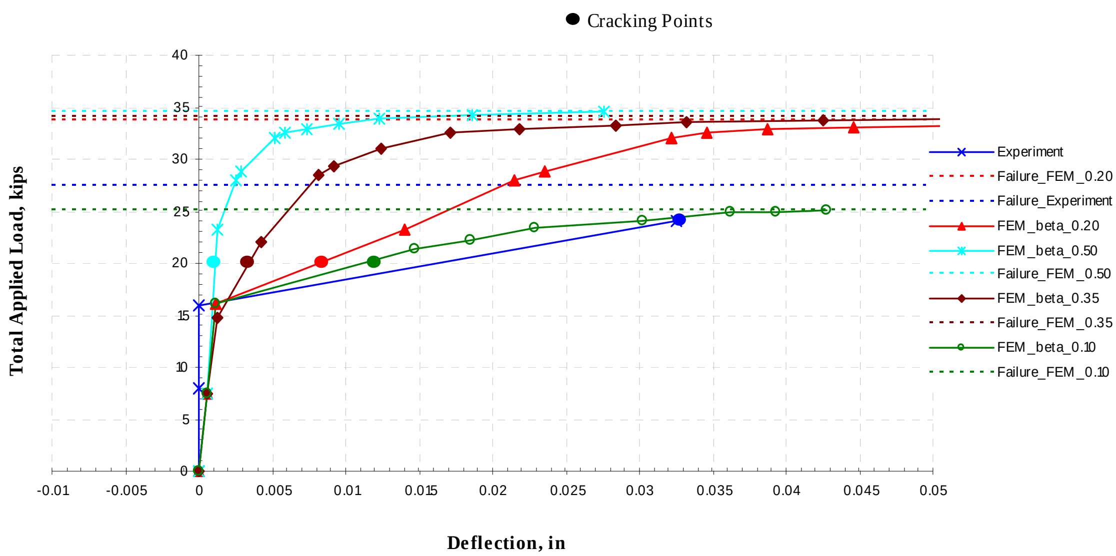


gauge 9

**Figure B.12 (*cont.*):** Effect of the reduction shear factor; β on deflection measurements at different locations for the 5ft_cip_corner bridge deck

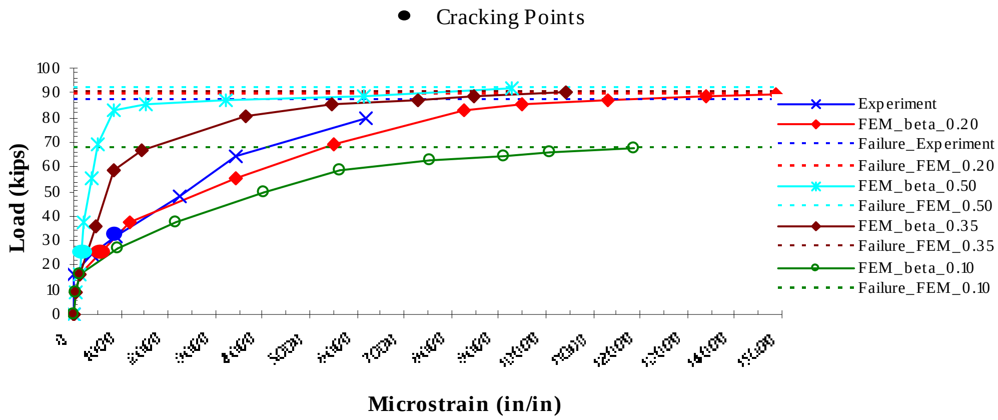


DEMEC 58

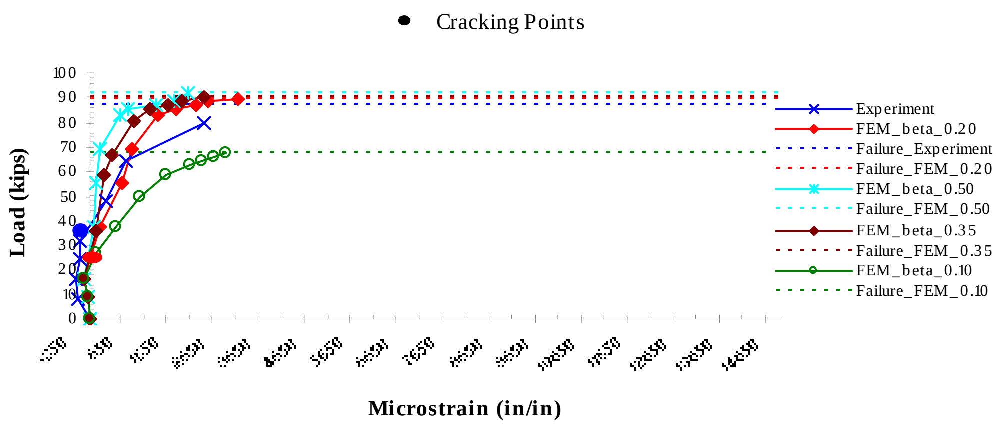


DEMEC 3

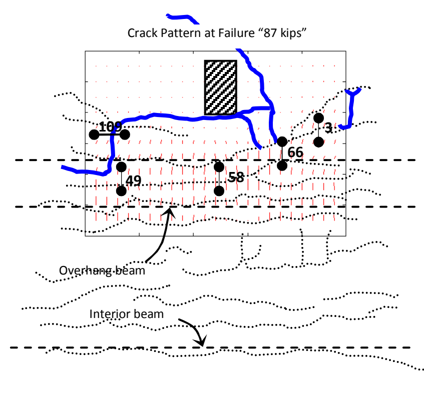


DEMEC locations

**Figure B.13:** Effect of the reduction shear factor; β on strain measurements at different DEMEC locations for the 5ft_pre_center bridge deck

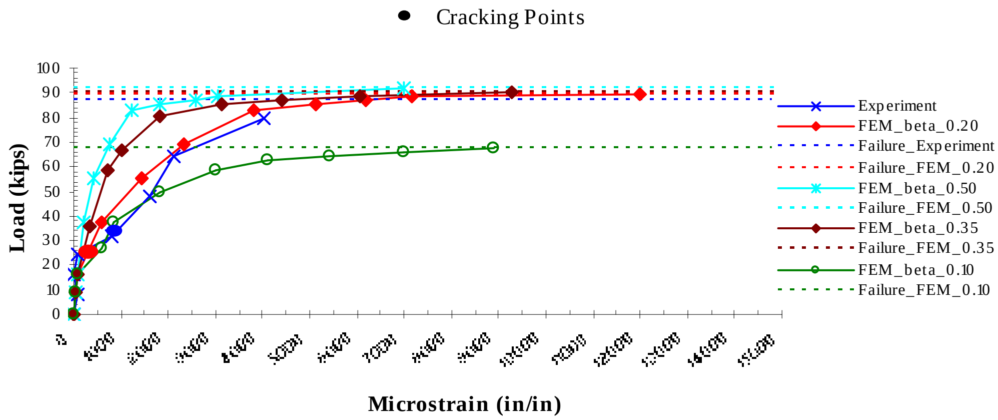


DEMEC 49

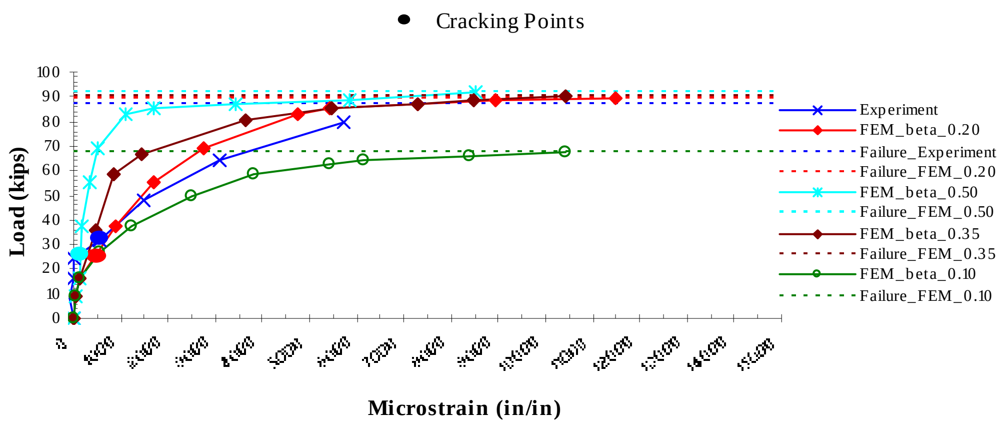


DEMEC 66

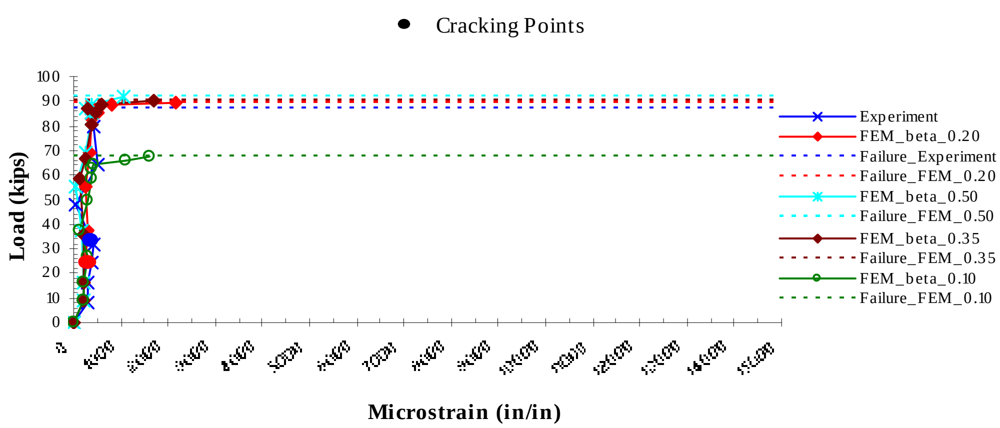


DEMEC 109

**Figure B.13 (*cont.*):** Effect of the reduction shear factor; β on strain measurements at different DEMEC locations for the 5ft_pre_center bridge deck

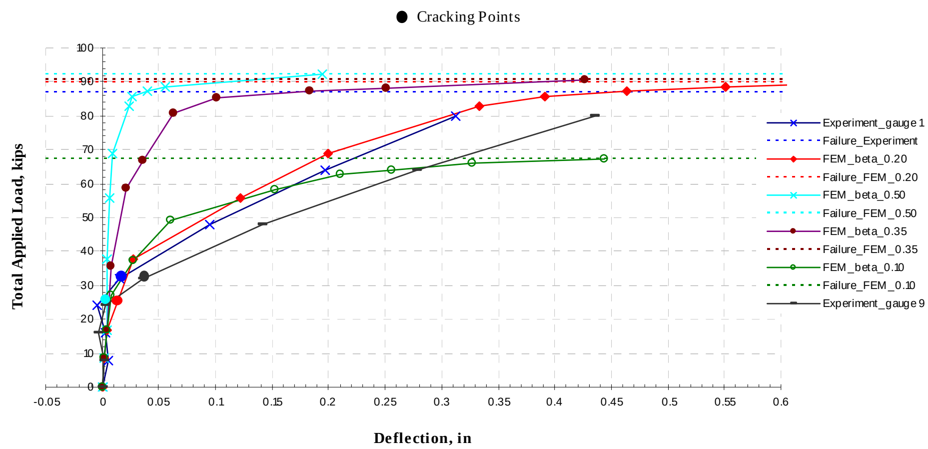


gauges 1&9

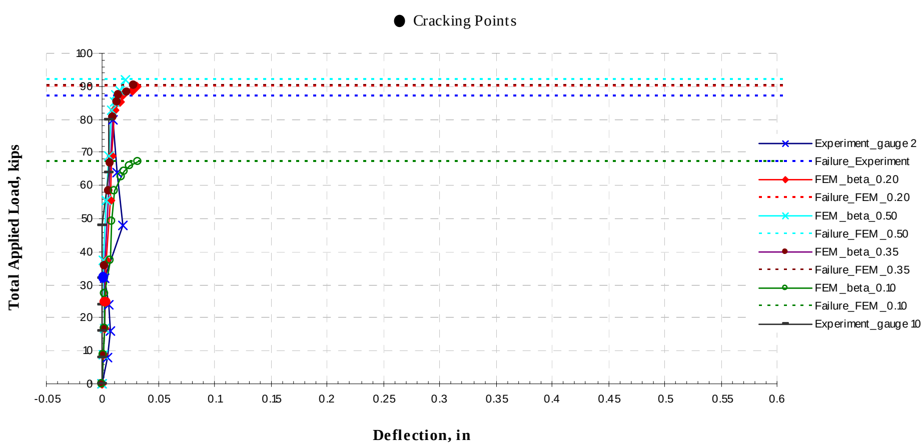


gauges 2&10

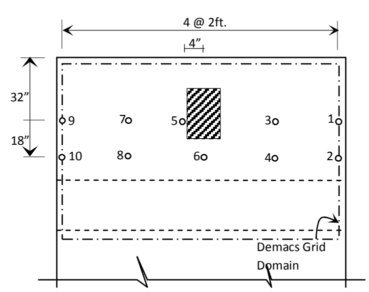


locations of deflection gauges

**Figure B.14:** Effect of the reduction shear factor; β on deflection measurements at different locations for the 5ft_pre_center bridge deck

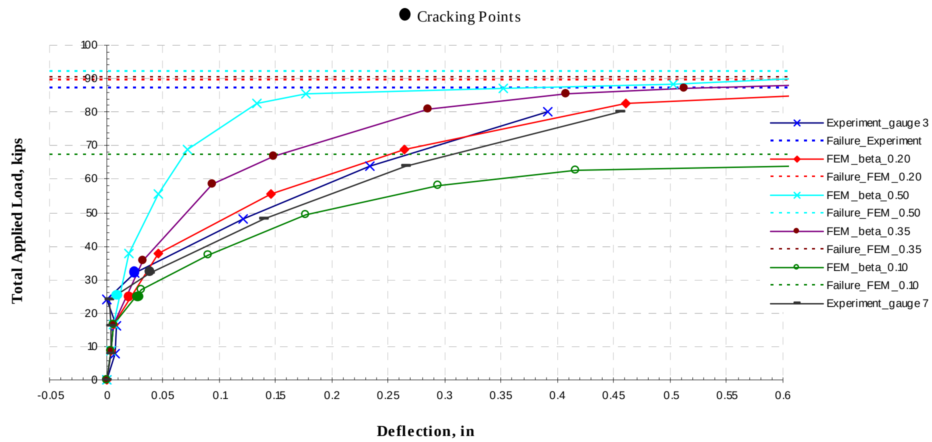


gauges 3&7

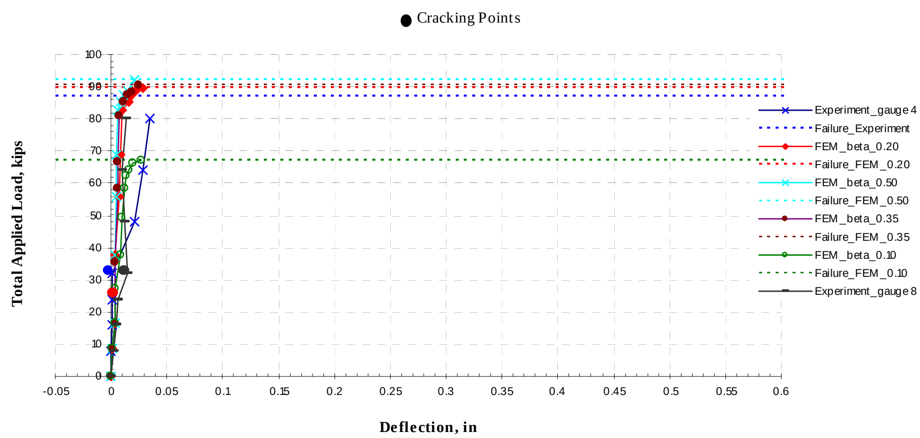


gauges 4&8

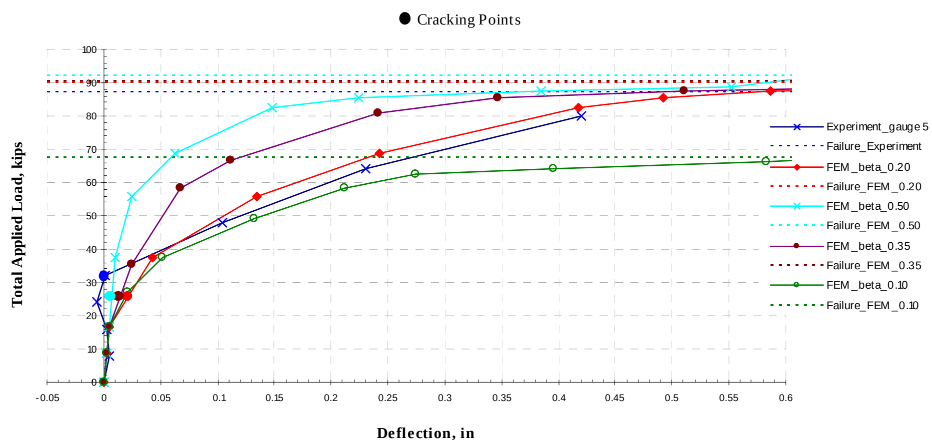


gauge 5

**Figure B.14 (*cont.*):** Effect of the reduction shear factor; β on deflection measurements at different locations for the 5ft_pre_center bridge deck

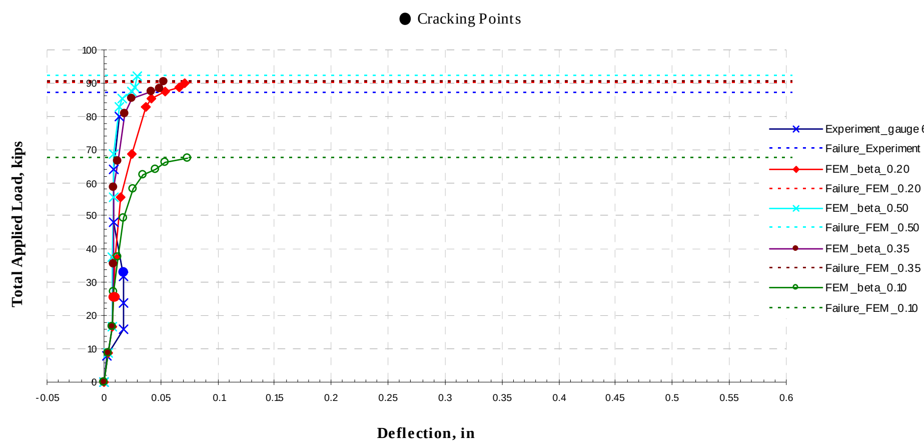


gauge 6

**Figure B.14 (*cont.*):** Effect of the reduction shear factor; β on deflection measurements at different locations for the 5ft_pre_center bridge deck

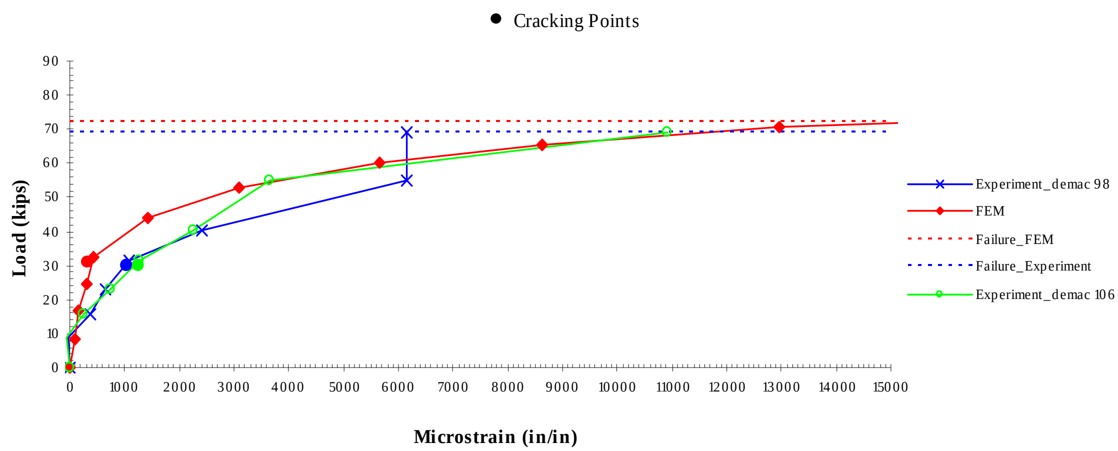


DEMECs 98 & 106

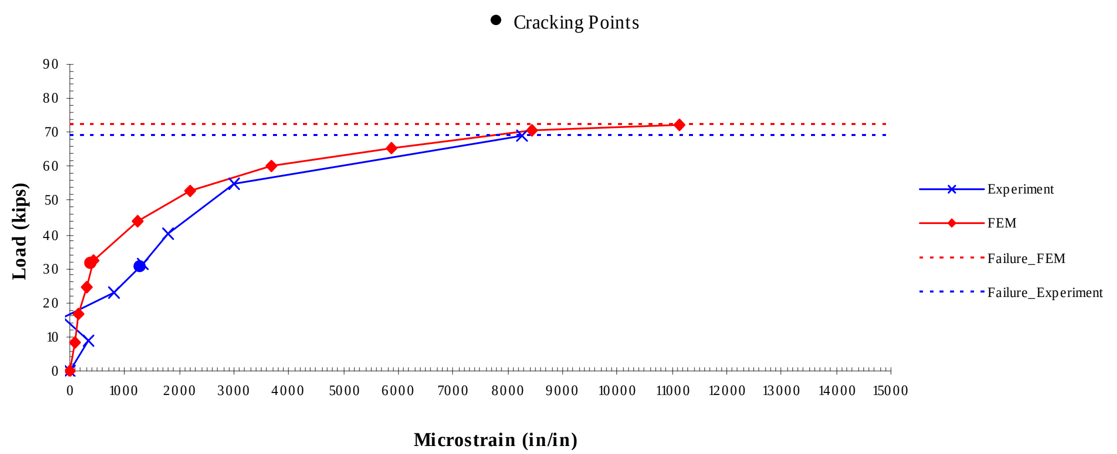


DEMEC 84

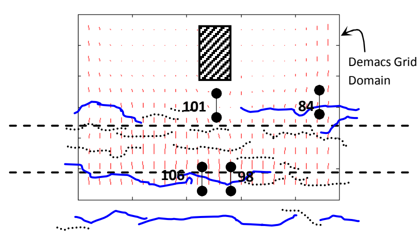


DEMEC locations

**Figure B.15:** FEM (β = 0.20) vs. experimental strain measurements at different DEMEC locations for the 5ft 8in_center bridge deck

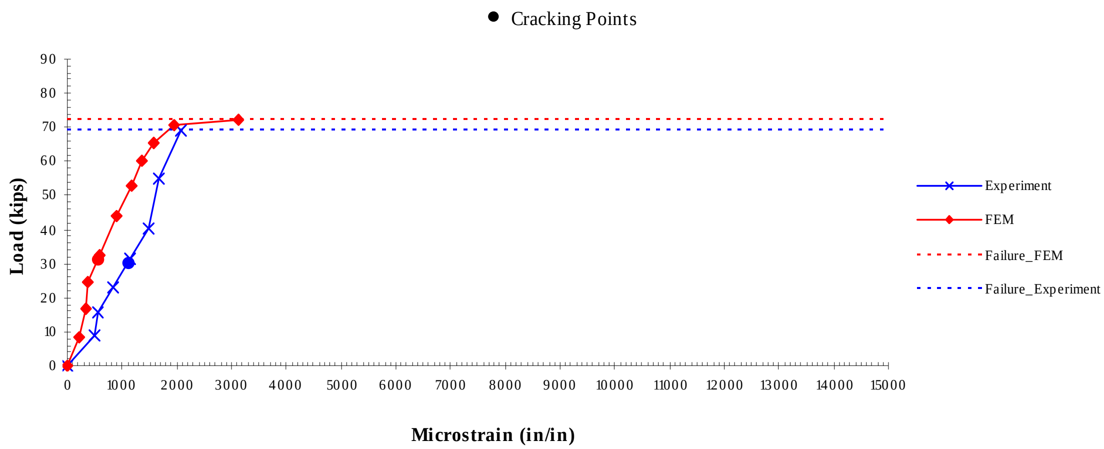


DEMEC 101

**Figure B.15 (*cont.*):** FEM (β = 0.20) vs. experimental strain measurements at different DEMEC locations for the 5ft 8in_center bridge deck

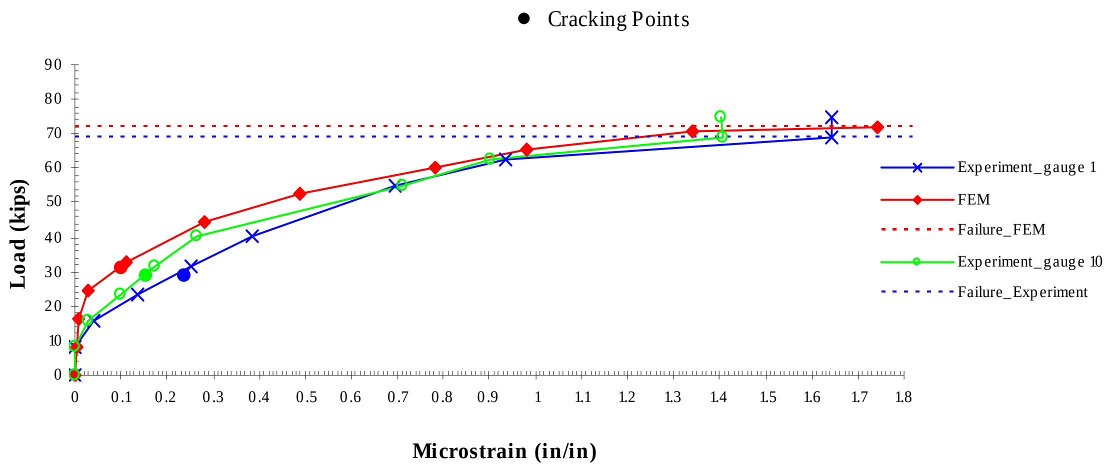


gauges 1&10

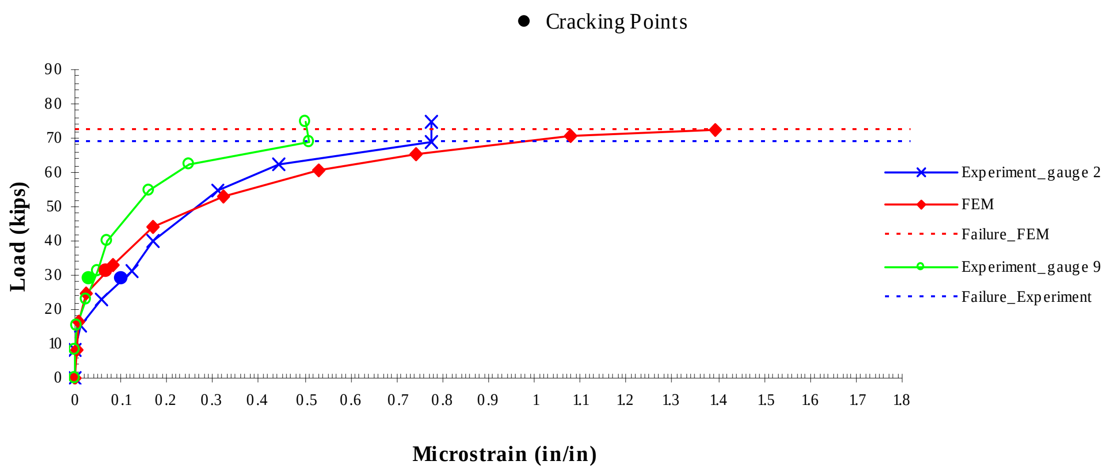


gauges 2&9

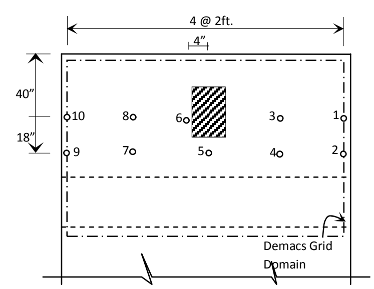


locations of deflection gauges

**Figure B.16:** FEM (β = 0.20) vs. experimental deflection measurements at different locations for the 5ft 8in_center bridge deck

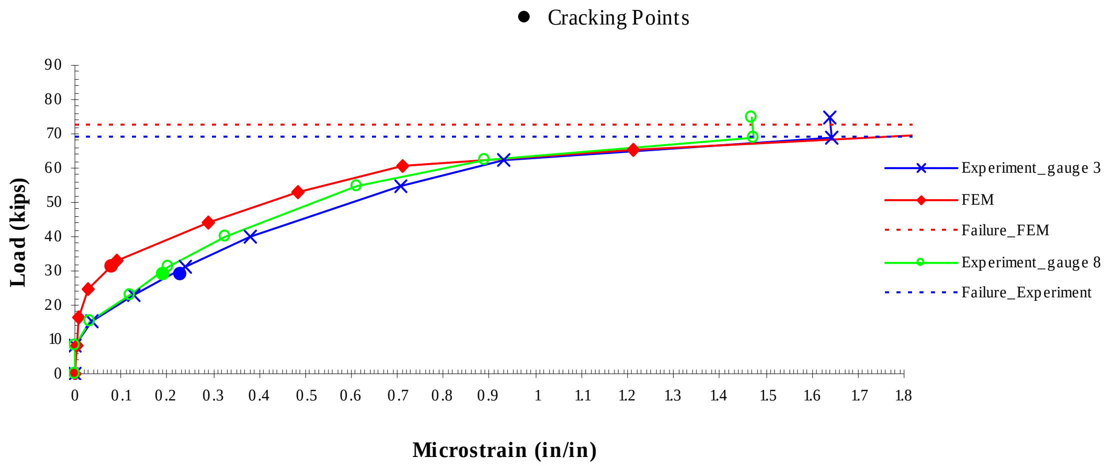


gauges 3&8

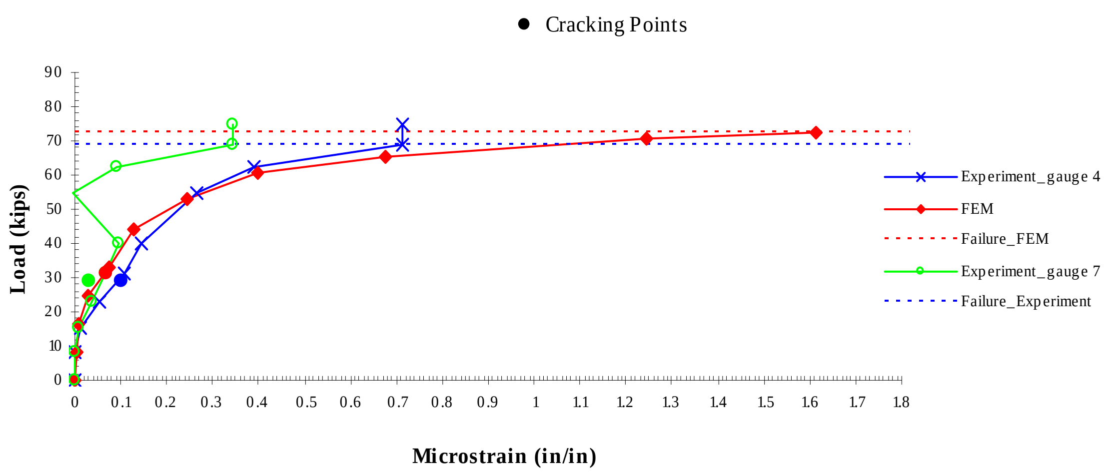


gauges 4&7

**Figure B.16 (*cont.*):** FEM (β = 0.20) vs. experimental deflection measurements at different locations for the 5ft 8in_center bridge deck

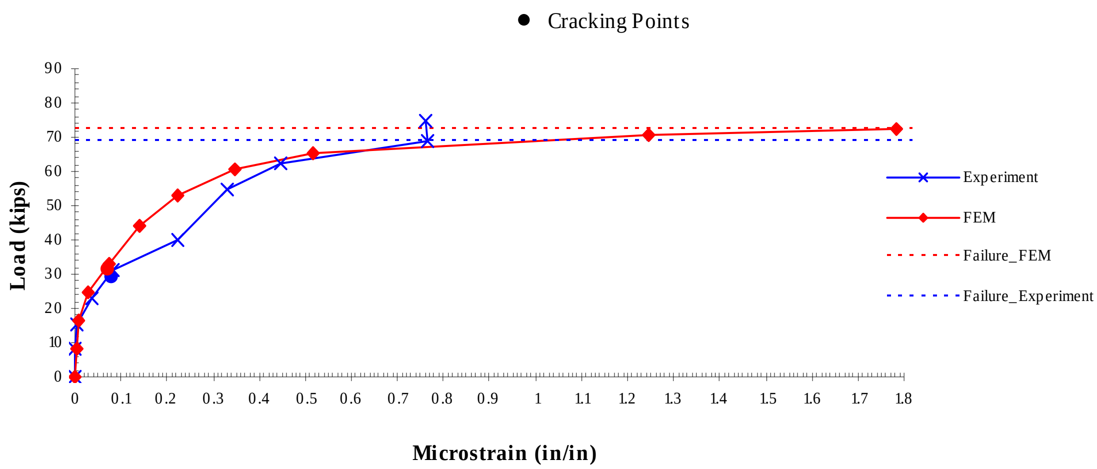


gauge 5

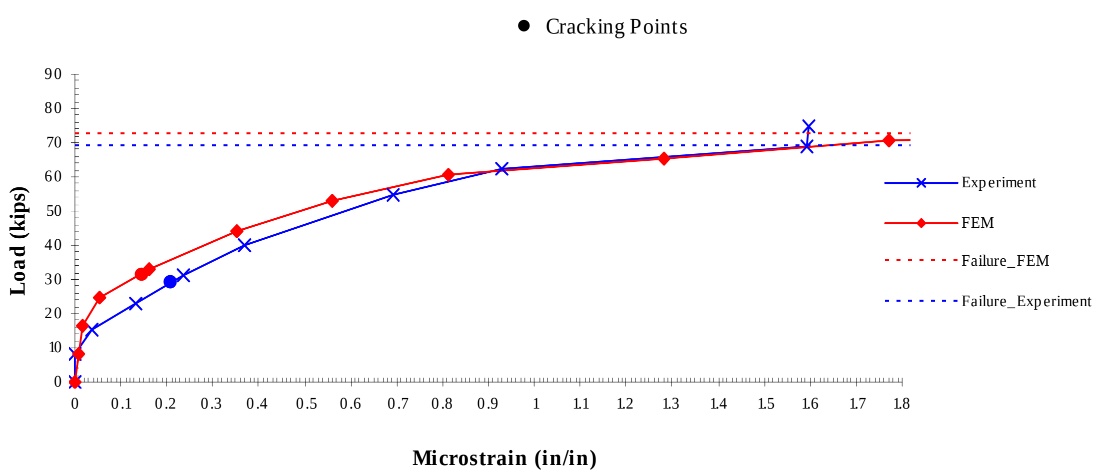


gauge 6

**Figure B.16 (*cont.*):** FEM (β = 0.20) vs. experimental deflection measurements at different locations for the 5ft 8in_center bridge deck

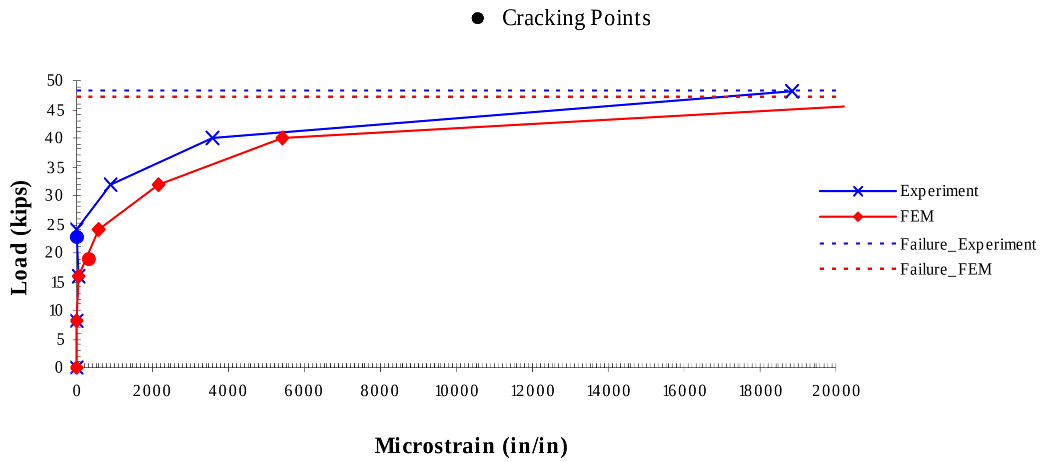


DEMEC 6

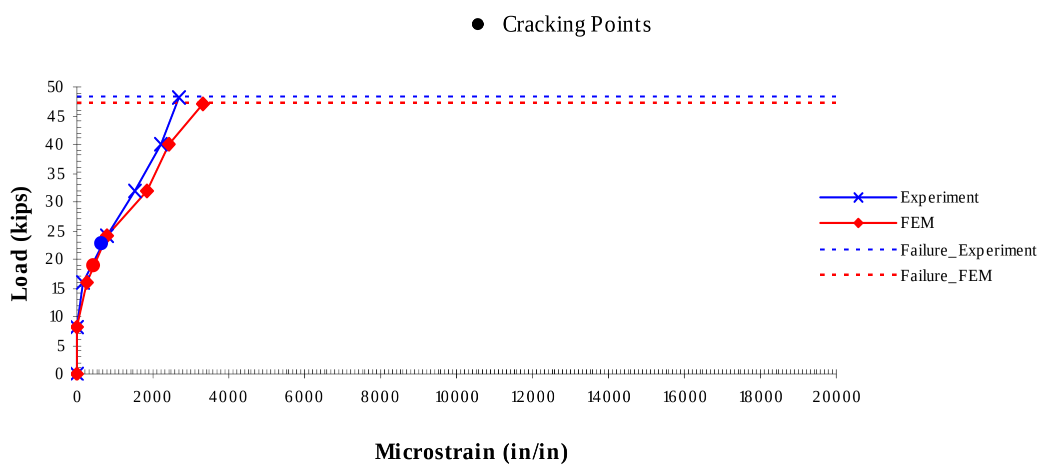


DEMEC 4

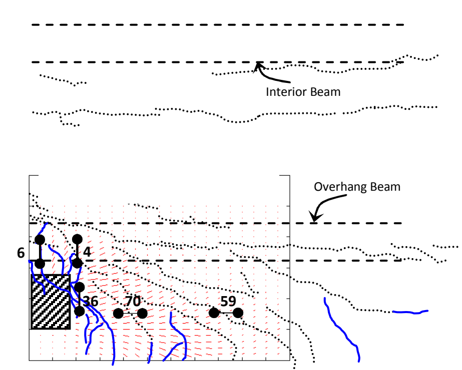


DEMEC locations

**Figure B.17:** FEM (β = 0.20) vs. experimental strain measurements at different DEMEC locations for the 5ft_pre_corner bridge deck

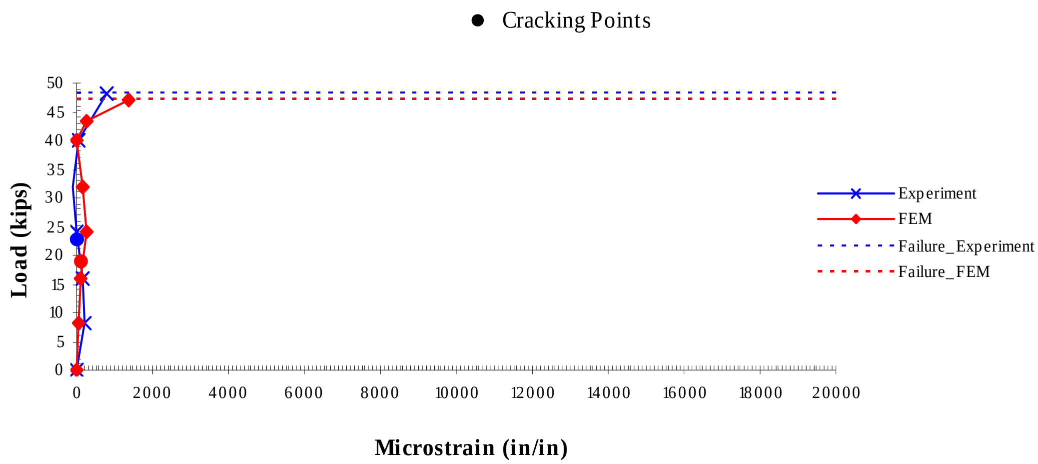


DEMEC 36

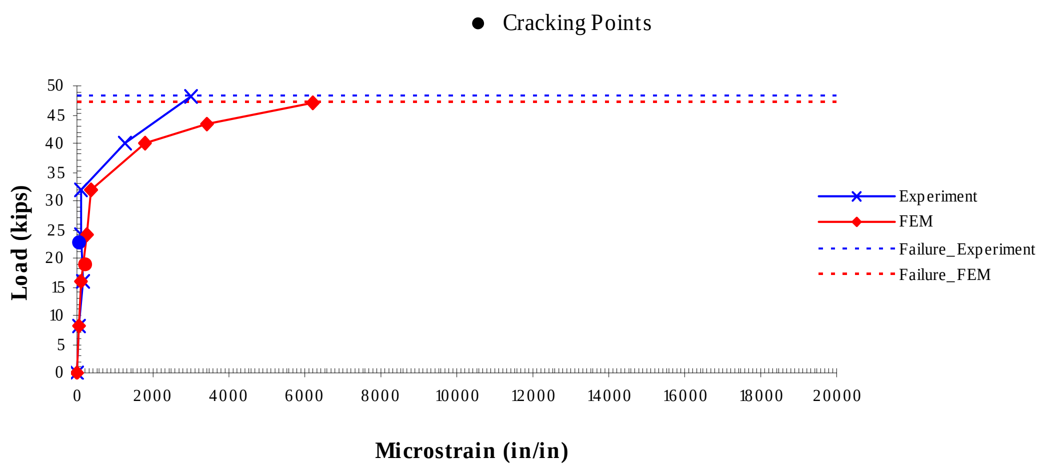


DEMEC 59

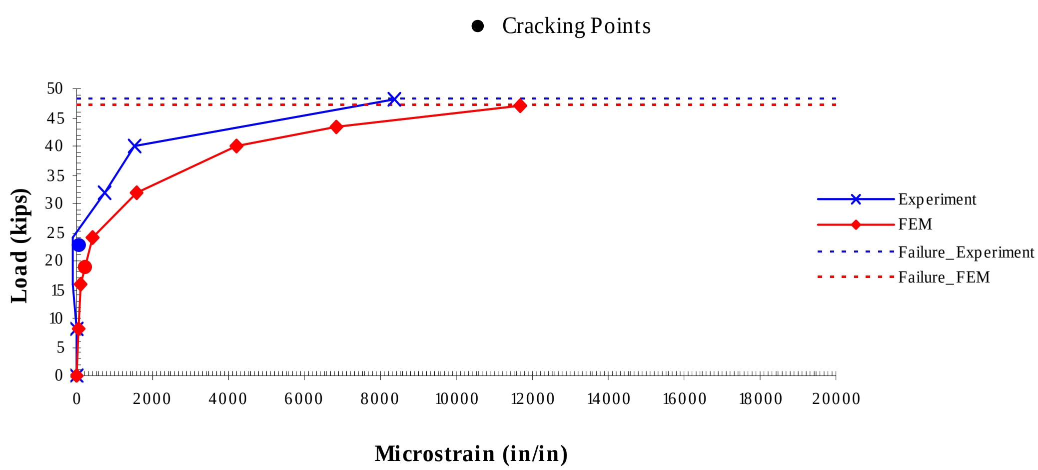


DEMEC 70

**Figure B.17 (*cont.*):** FEM ($\beta$ = 0.20) vs. experimental strain measurements at different DEMEC locations for the 5ft_pre_corner bridge deck

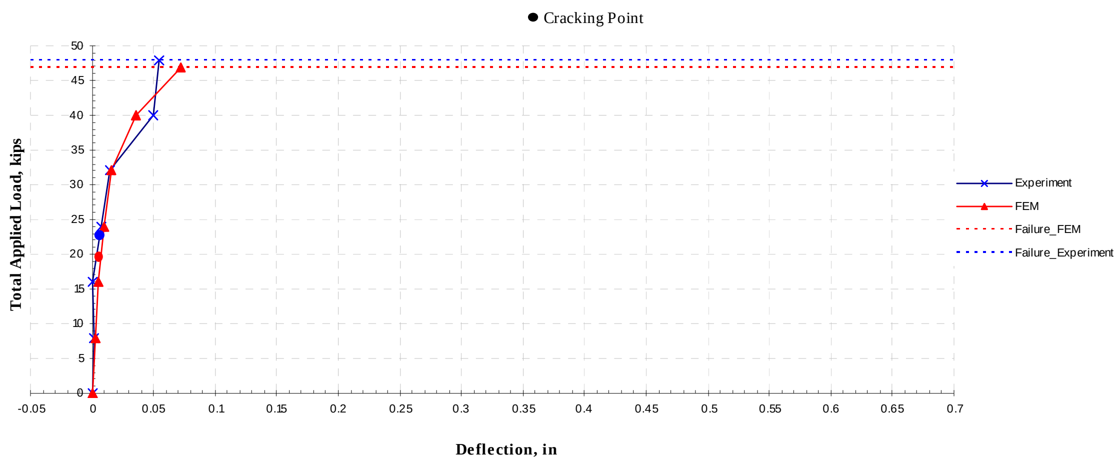


gauge 1

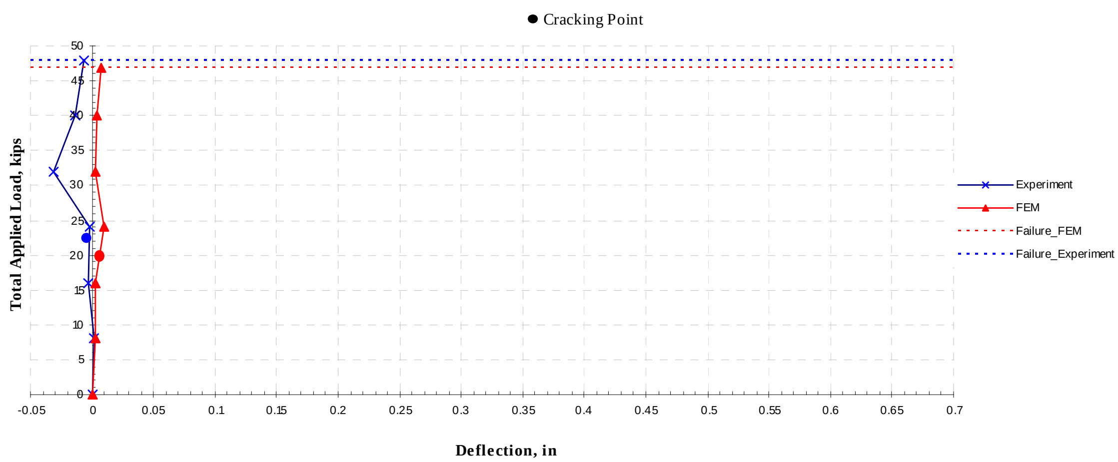


gauge 2

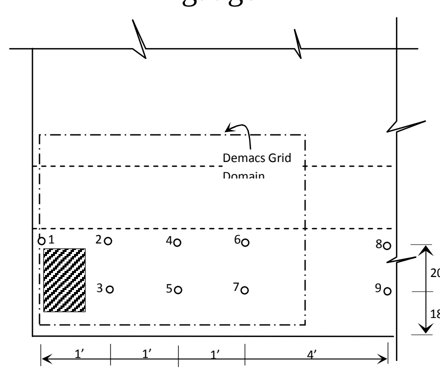


locations of deflection gauges

**Figure B.18:** FEM (β = 0.20) vs. experimental deflection measurements at different locations for the 5ft_pre_corner bridge deck

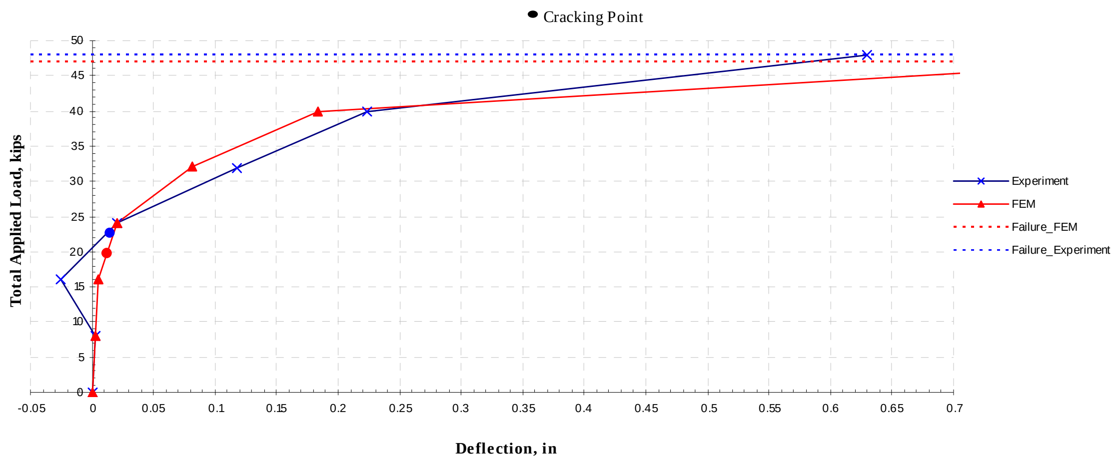


gauge 3

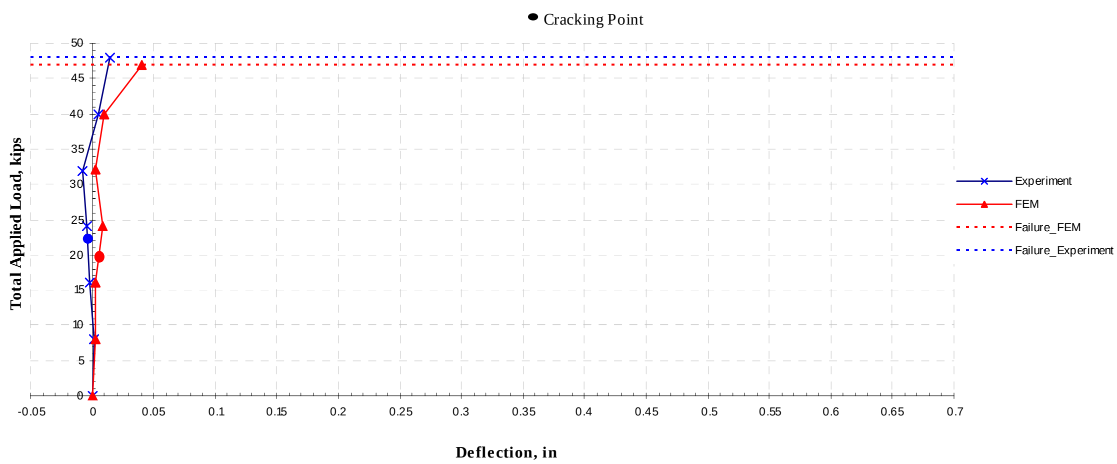


gauge 4

**Figure B.18 (*cont.*):** FEM (β = 0.20) vs. experimental deflection measurements at different locations for the 5ft_pre_corner bridge deck

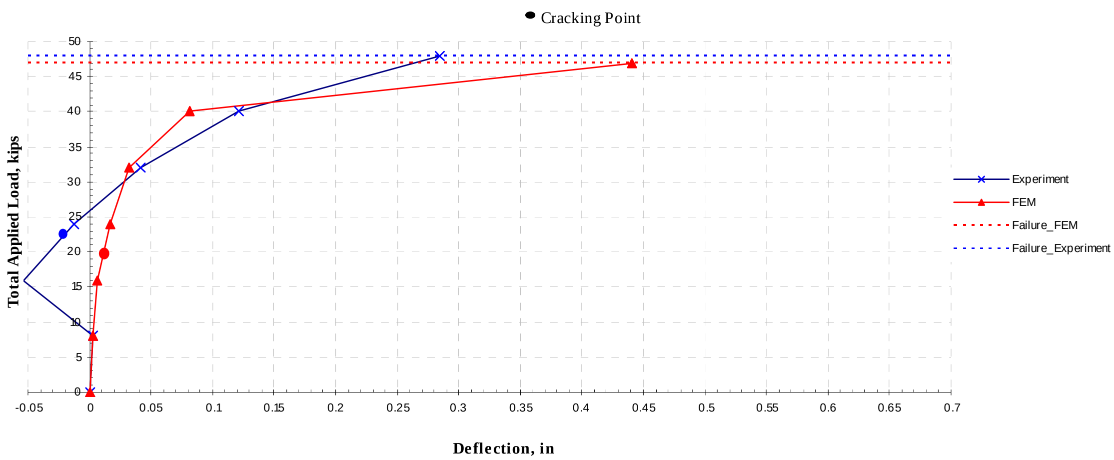


gauge 5

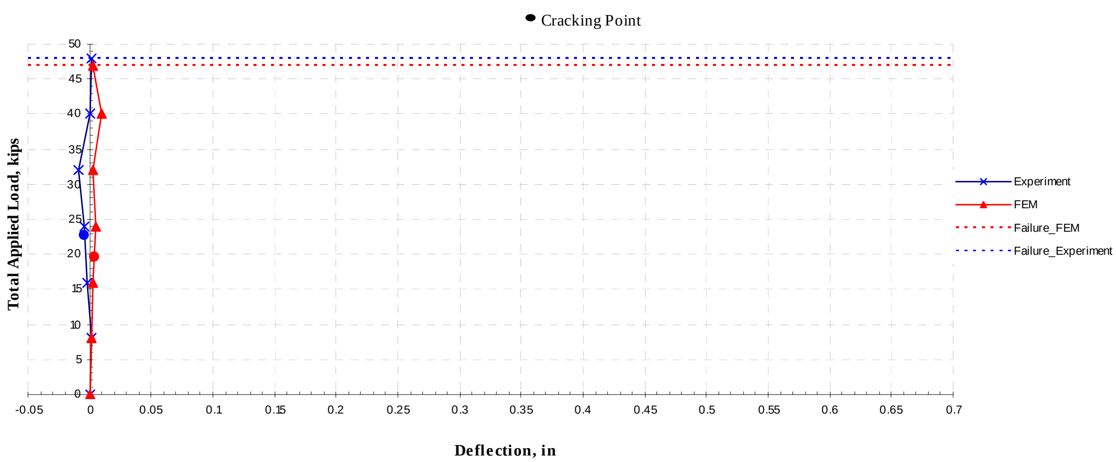


gauge 6

**Figure B.18 (*cont.*):** FEM (β = 0.20) vs. experimental deflection measurements at different locations for the 5ft_pre_corner bridge deck

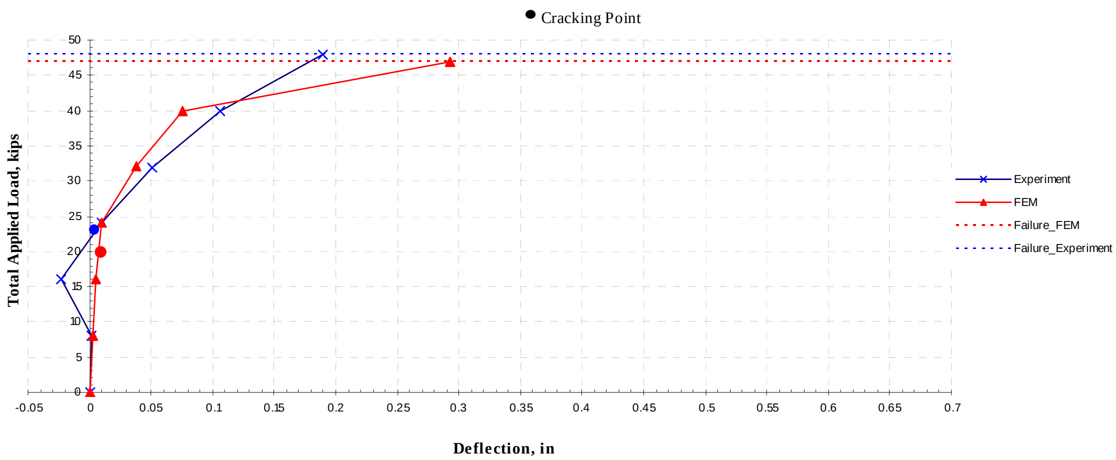


gauge 7

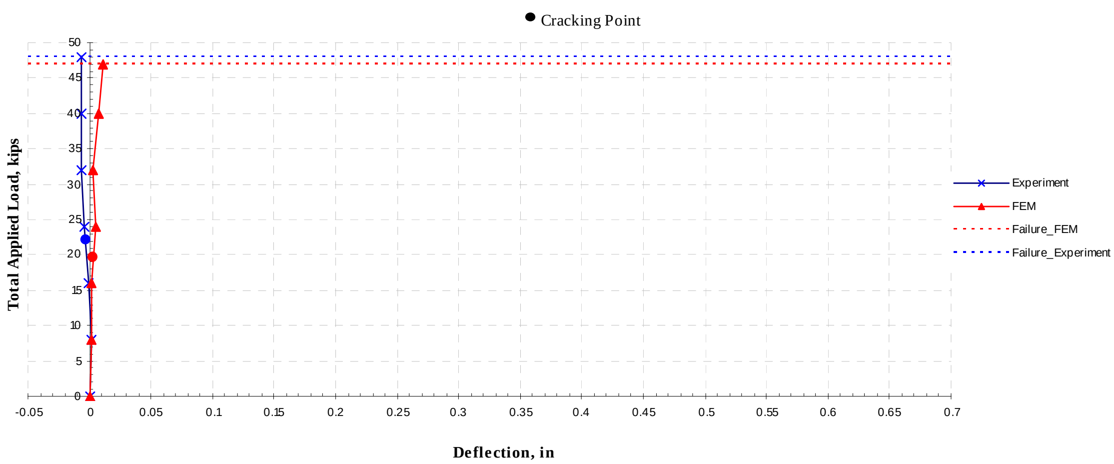


gauge 8

**Figure B.18 (*cont.*):** FEM (β = 0.20) vs. experimental deflection measurements at different locations for the 5ft_pre_corner bridge deck

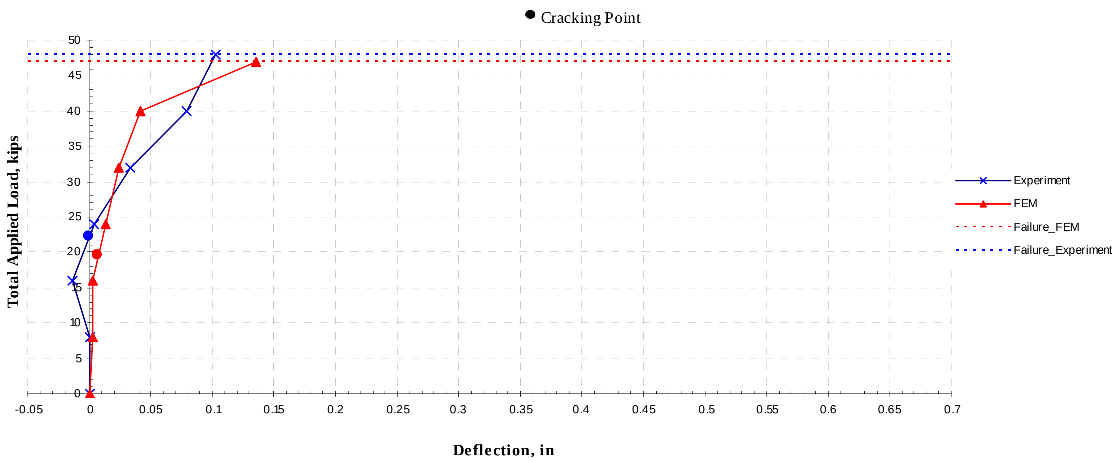


gauge 9

**Figure B.18 (*cont.*):** FEM (β = 0.20) vs. experimental deflection measurements at different locations for the 5ft_pre_corner bridge deck

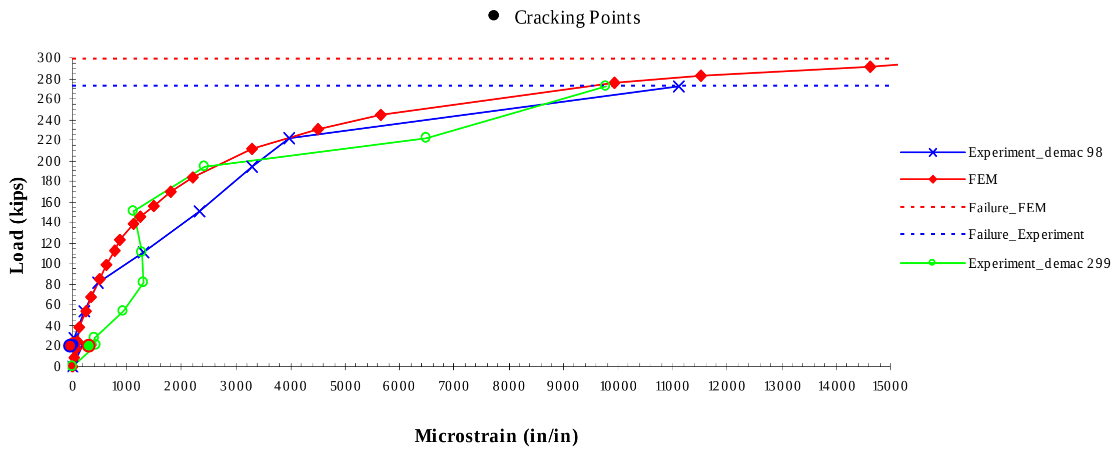


DEMECs 98 &299

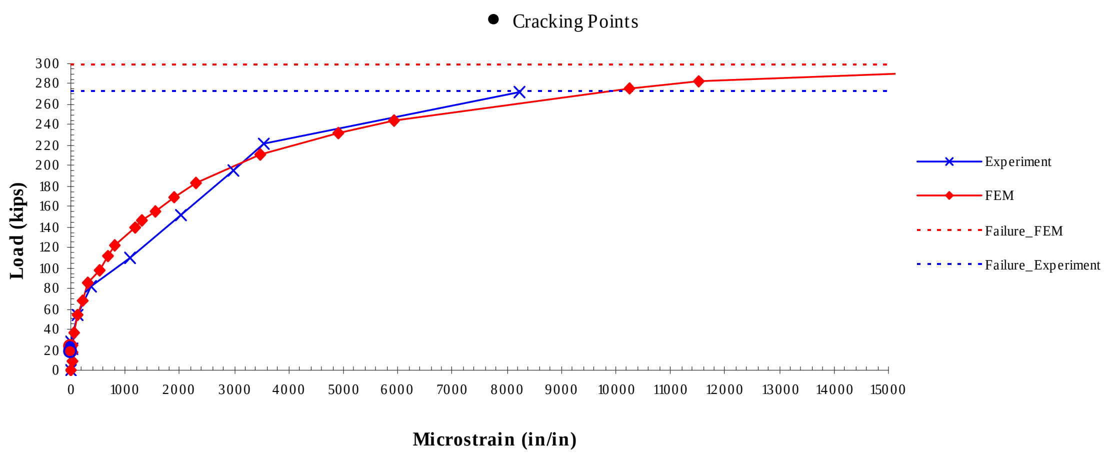


DEMEC 77

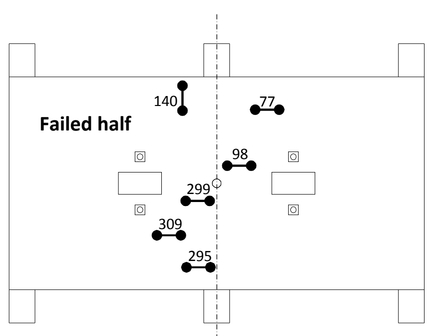


DEMEC locations

**Figure B.19:** FEM (β = 0.20) vs. experimental strain measurements at different DEMEC locations for Specimen A

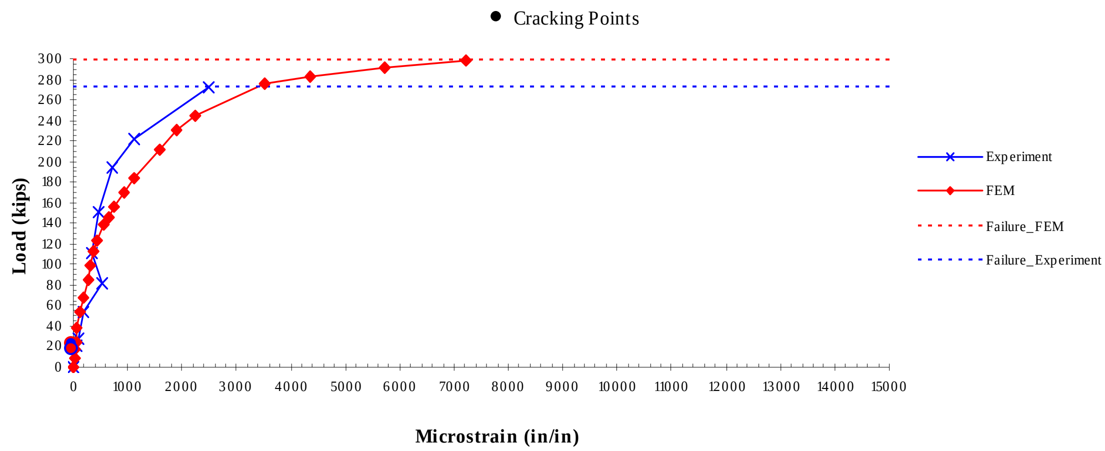


DEMEC 140

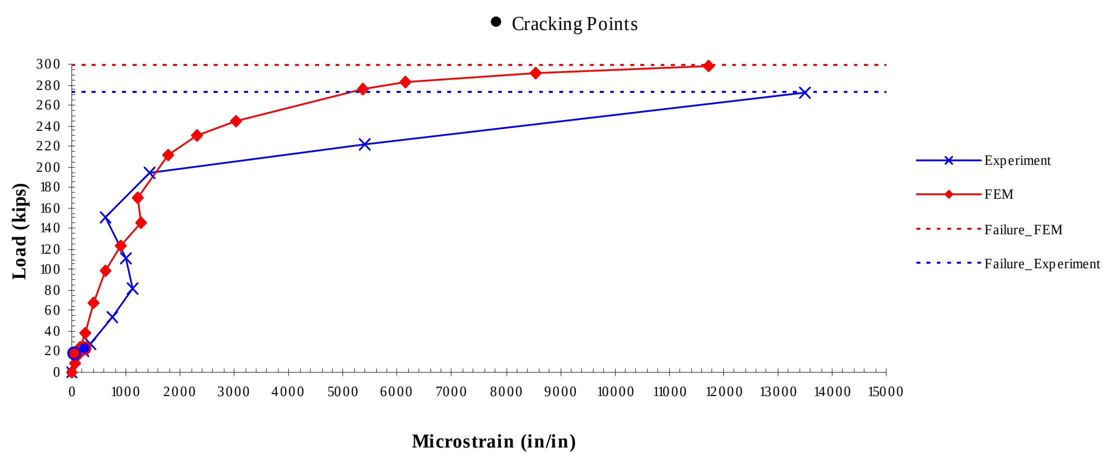


DEMEC 295

**Figure B.19 (*cont.*):** FEM (β = 0.20) vs. experimental strain measurements at different DEMEC locations for Specimen A

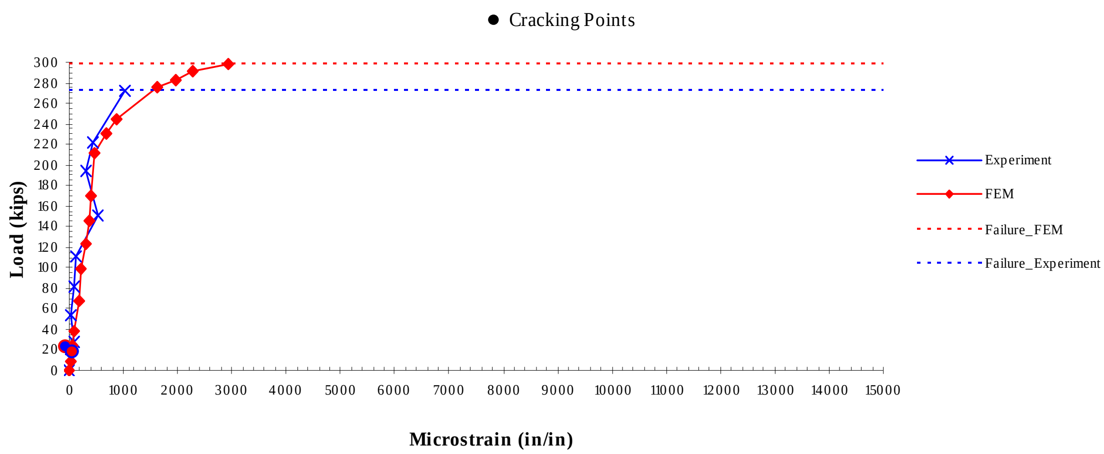


DEMEC 309

**Figure B.19 (*cont.*):** FEM (β = 0.20) vs. experimental strain measurements at different DEMEC locations for Specimen A

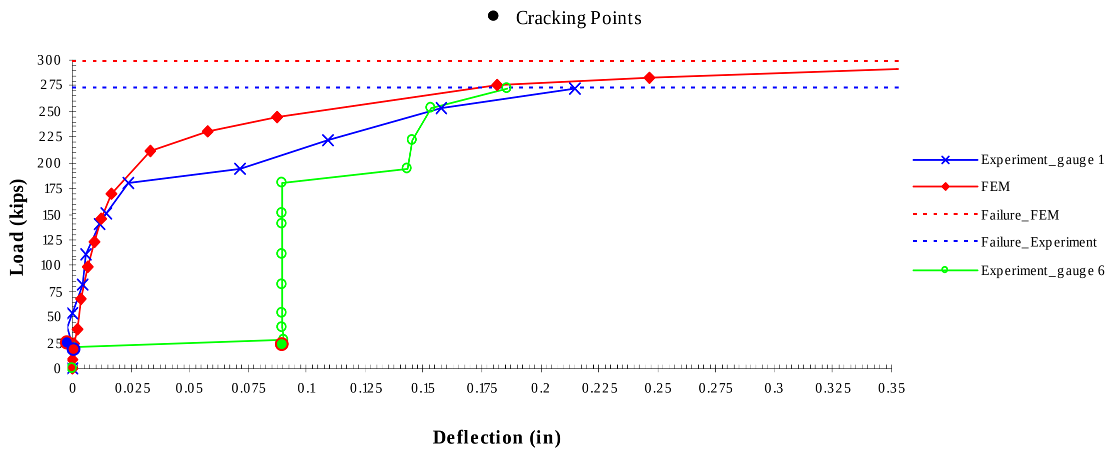


gauges 1 & 6

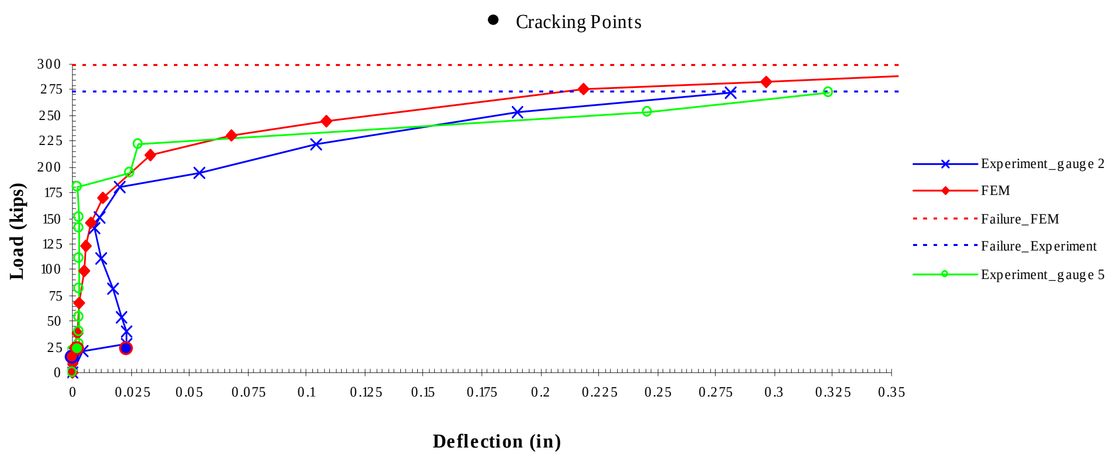


gauges 2 & 5

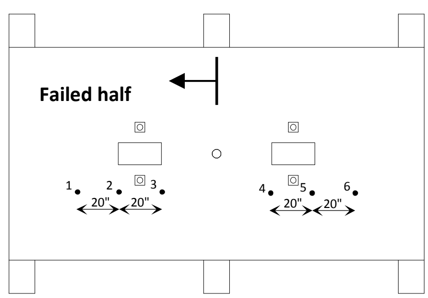


locations of deflection gauges

**Figure B.20:** FEM (β = 0.20) vs. experimental deflection measurements at different locations for Specimen A

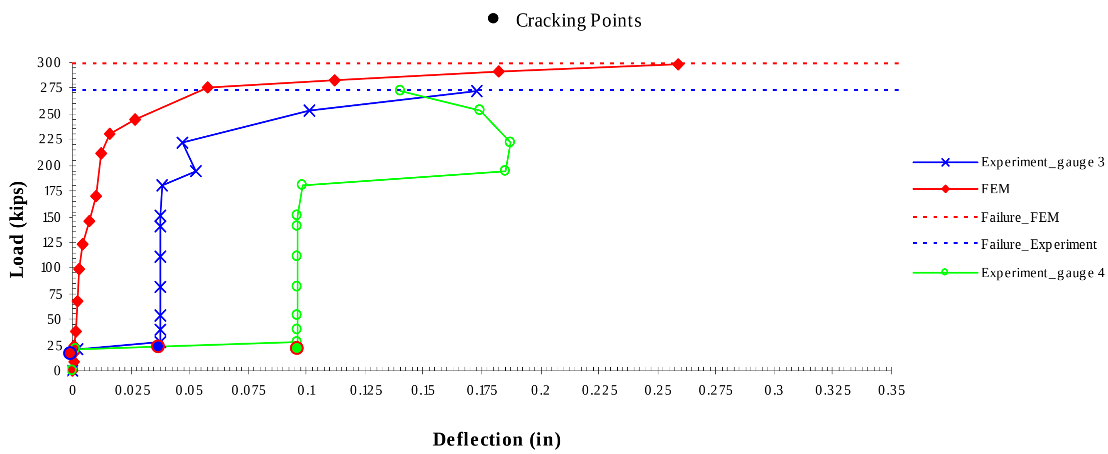


gauges 3 & 4

**Figure B.20 (*cont.*):** FEM (β = 0.20) vs. experimental deflection measurements at different locations for Specimen A

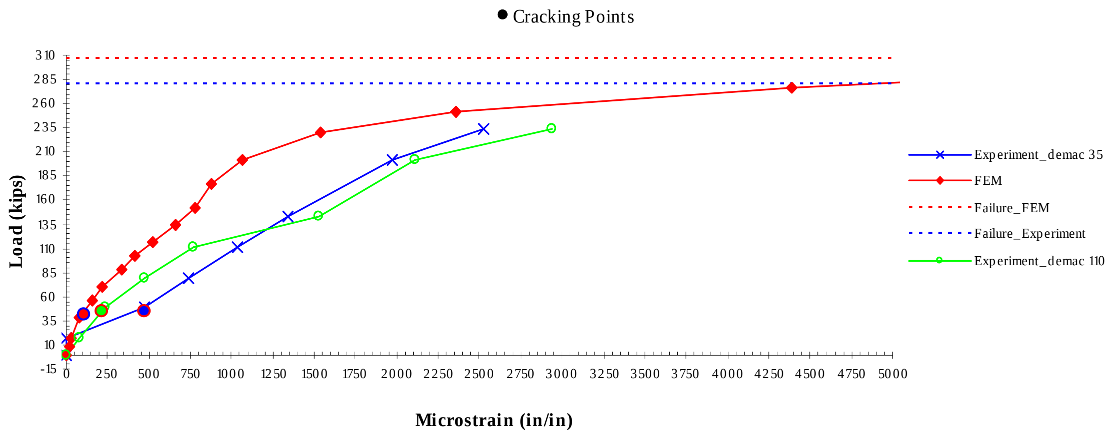


DEMECs 35 & 110

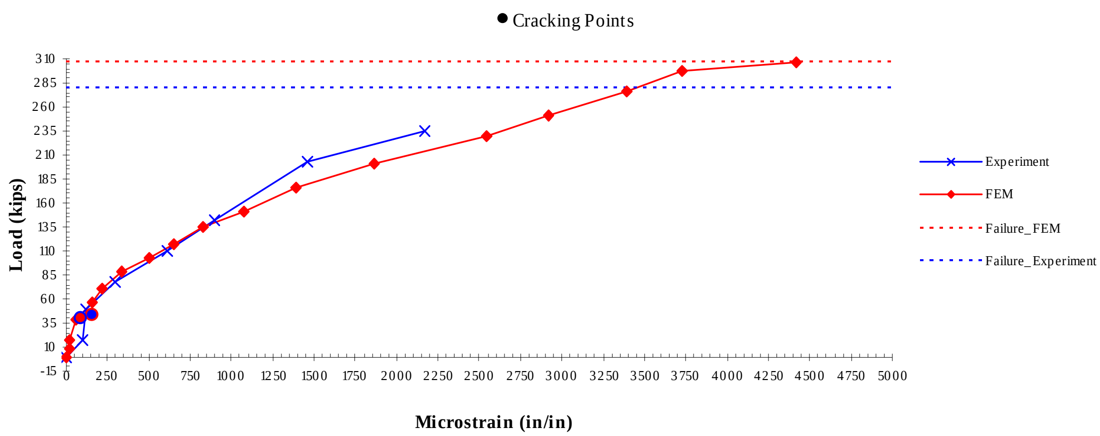


DEMEC 10

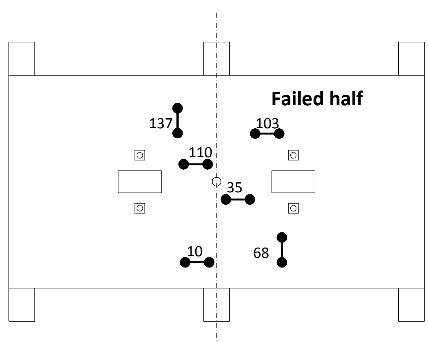


DEMEC locations

**Figure B.21:** FEM (β = 0.20) vs. experimental strain measurements at different DEMEC locations for Specimen B

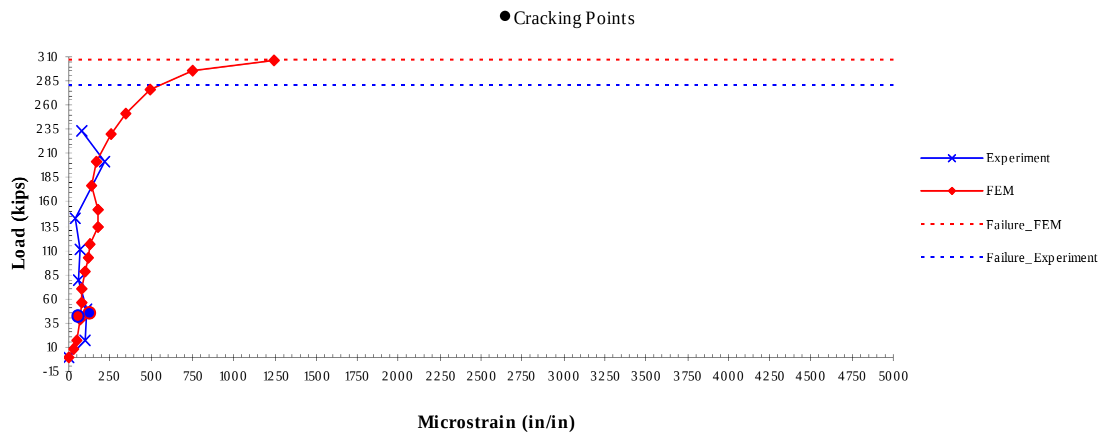


DEMEC 68

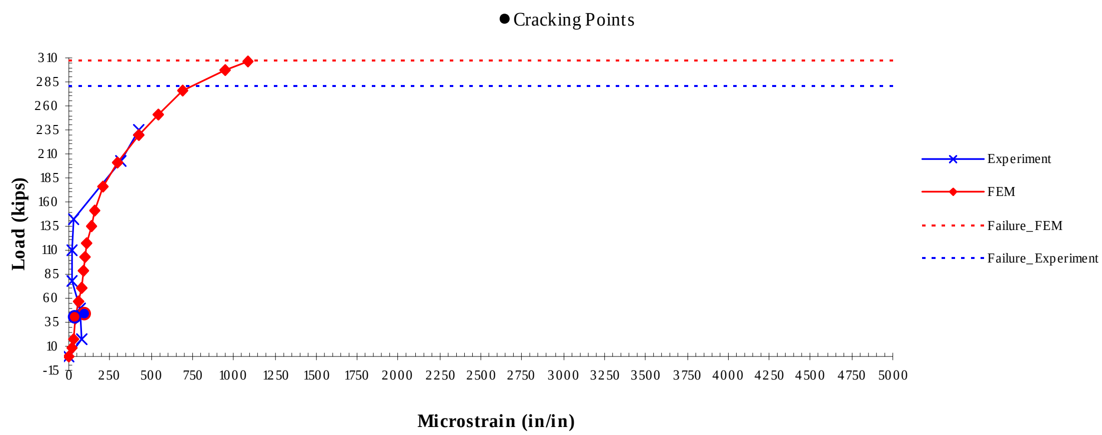


DEMEC 103

**Figure B.21 (*cont.*):** FEM ($\beta$ = 0.20) vs. experimental strain measurements at different DEMEC locations for Specimen B

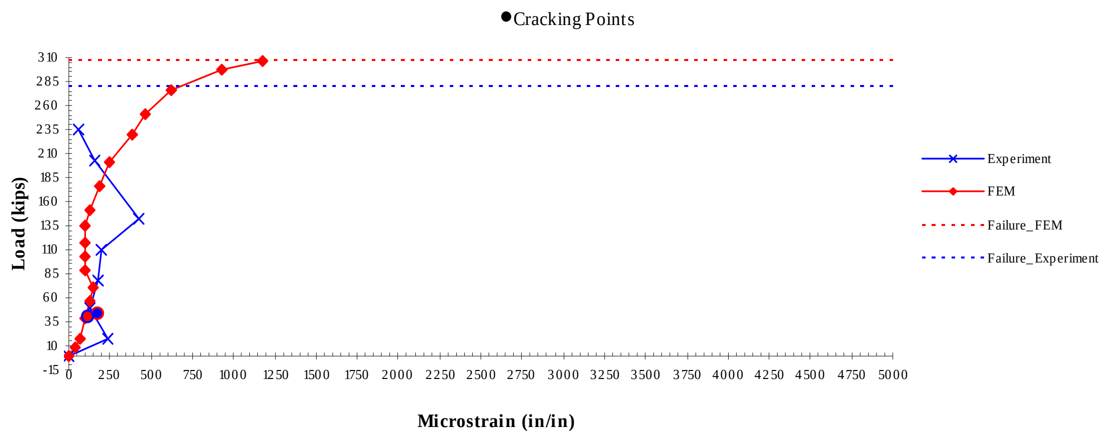


DEMEC 137

**Figure B.21 (*cont.*):** FEM (β = 0.20) vs. experimental strain measurements at different DEMEC locations for Specimen B

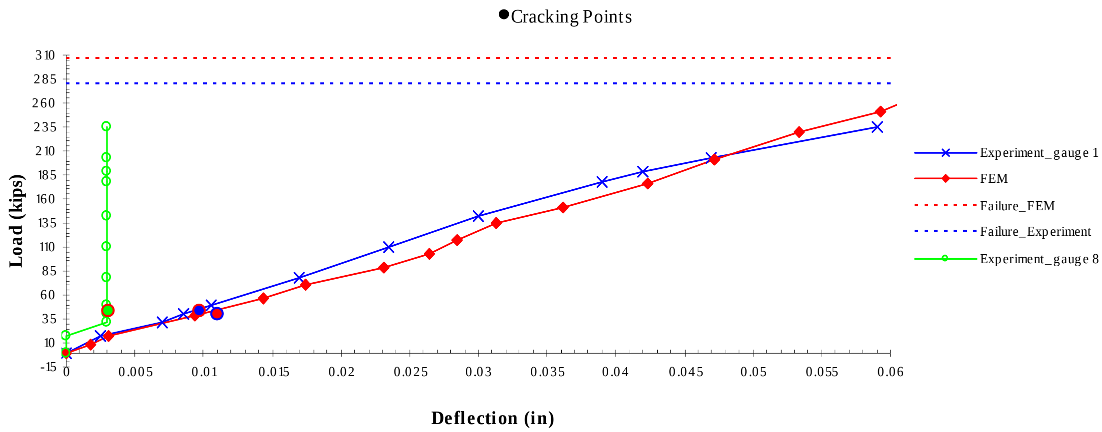


gauges 1 & 8

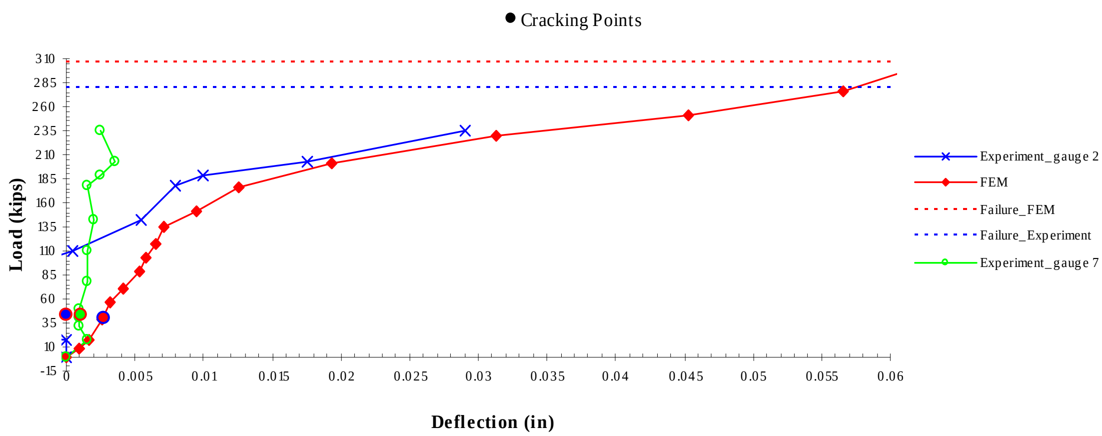


gauges 2 & 7

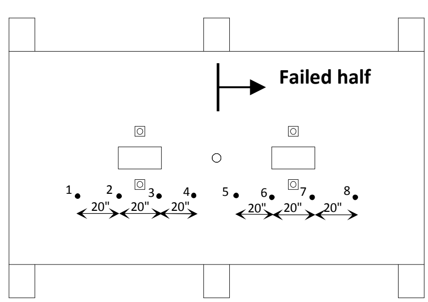


locations of deflection gauges

**Figure B.22:** FEM (β = 0.20) vs. experimental deflection measurements at different locations for Specimen B

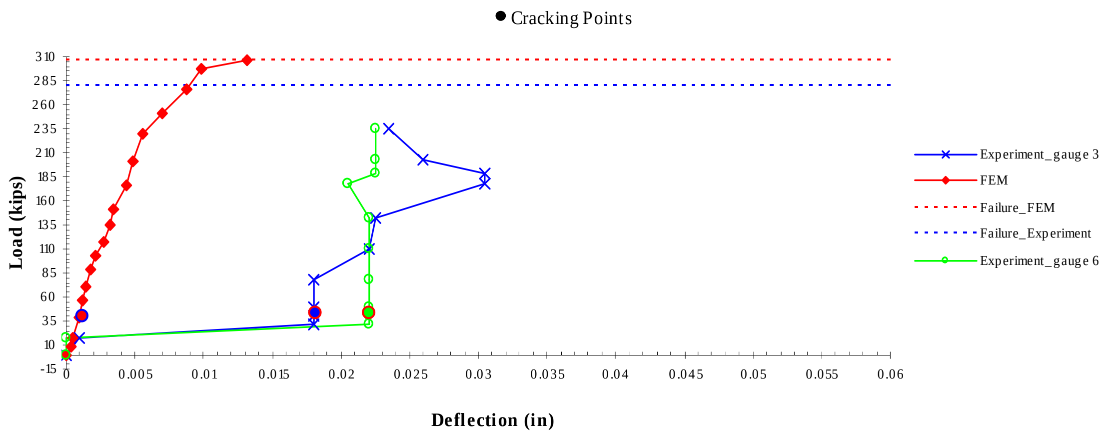


gauges 3 & 6

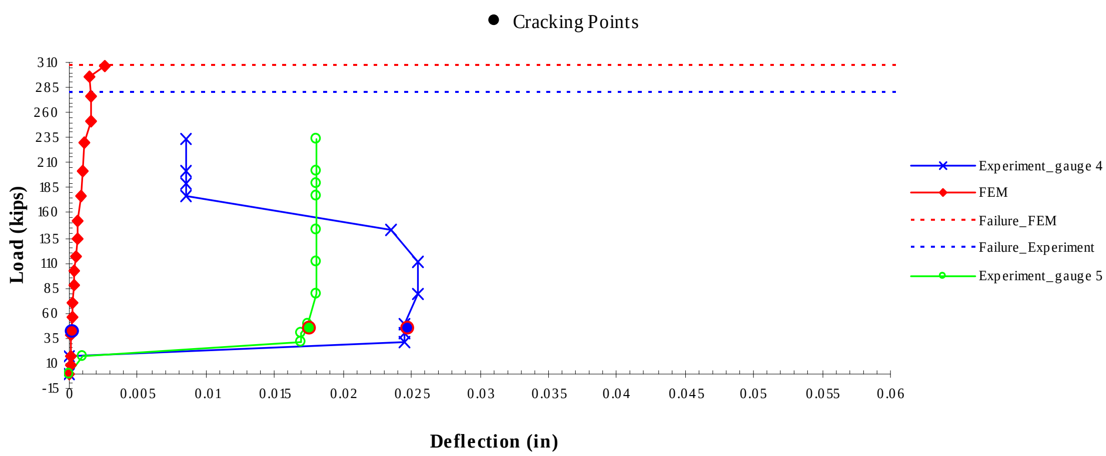


gauges 4 & 5

**Figure B.22 (*cont.*):** FEM (β = 0.20) vs. experimental deflection measurements at different locations for Specimen B

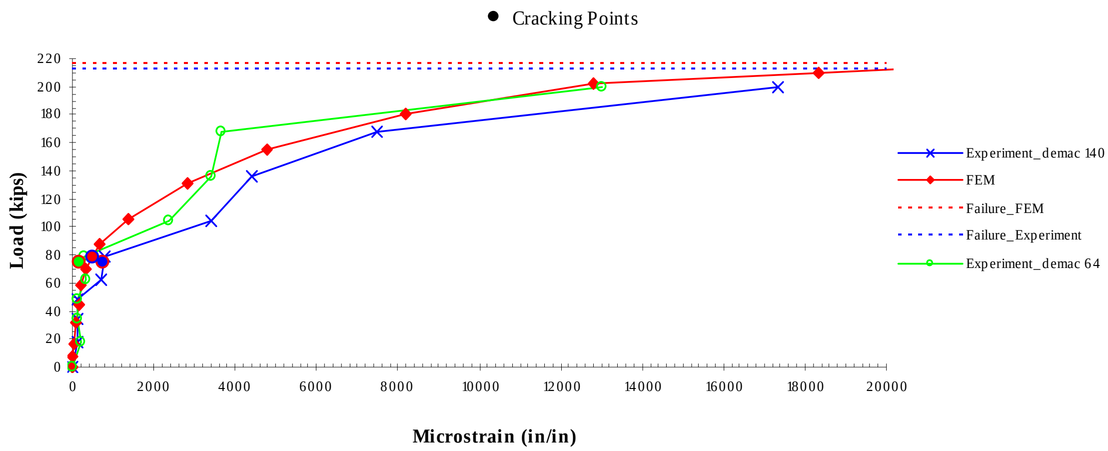


DEMECs 140 & 64

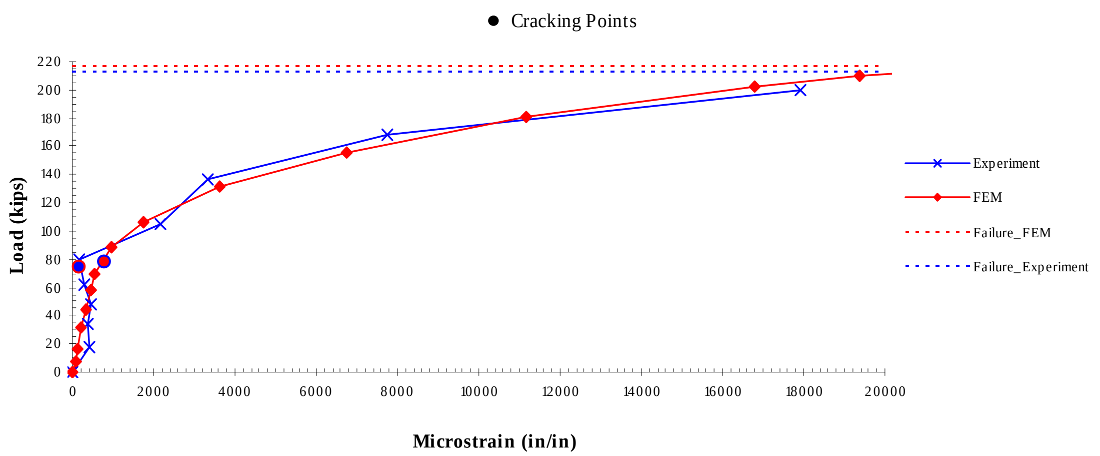


DEMEC 62

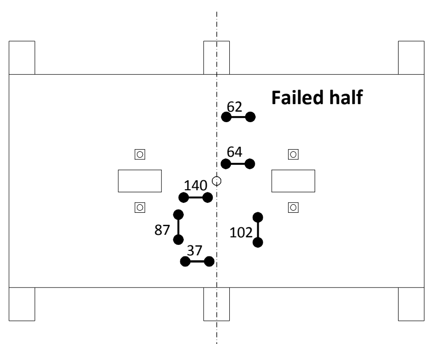


DEMEC locations

**Figure B.23:** FEM (β = 0.20) vs. experimental strain measurements at different DEMEC locations for Specimen C

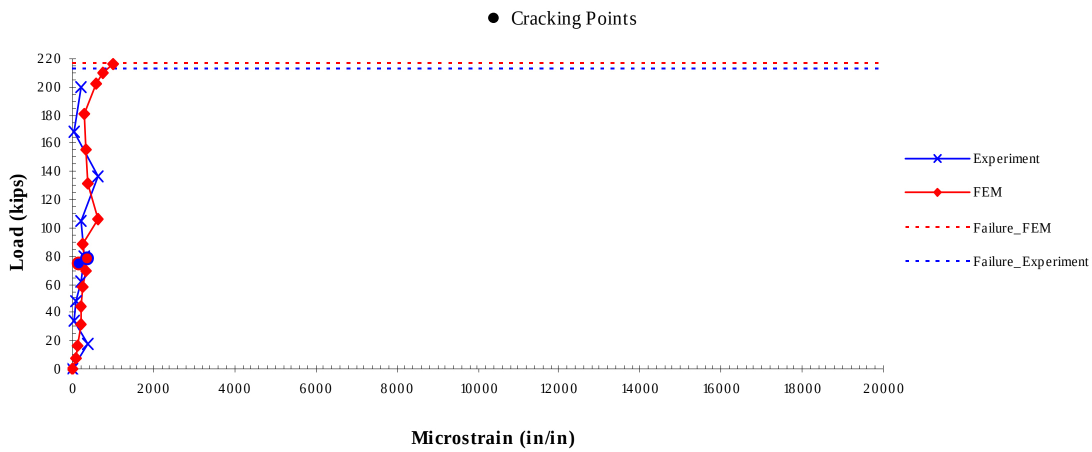


DEMEC 87

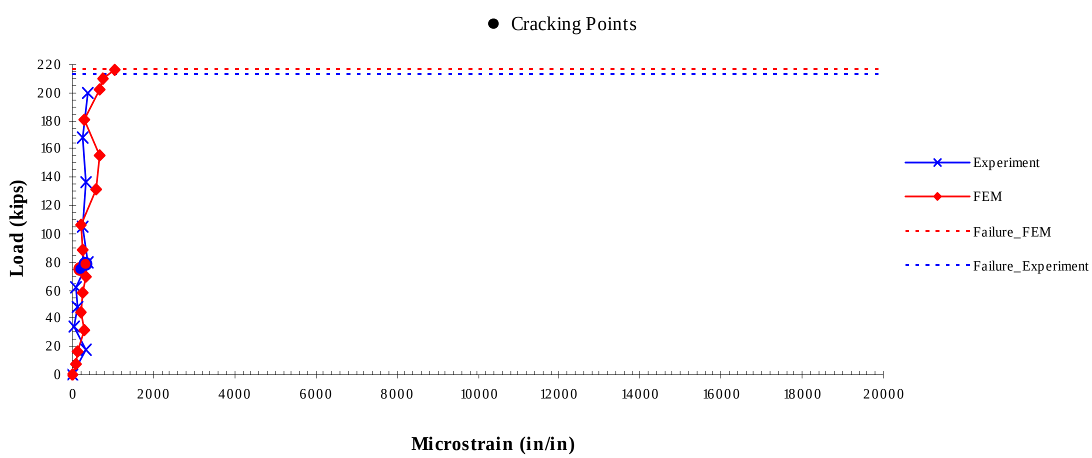


DEMEC 102

**Figure B.23 (*cont.*):** FEM (β = 0.20) vs. experimental strain measurements at different DEMEC locations for Specimen C

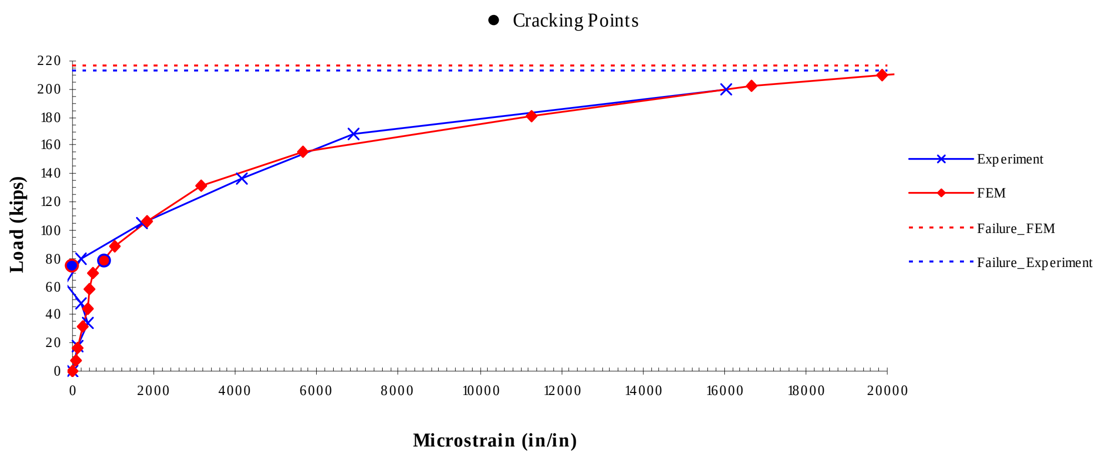


DEMEC 137

**Figure B.23 (*cont.*):** FEM (β = 0.20) vs. experimental strain measurements at different DEMEC locations for Specimen C

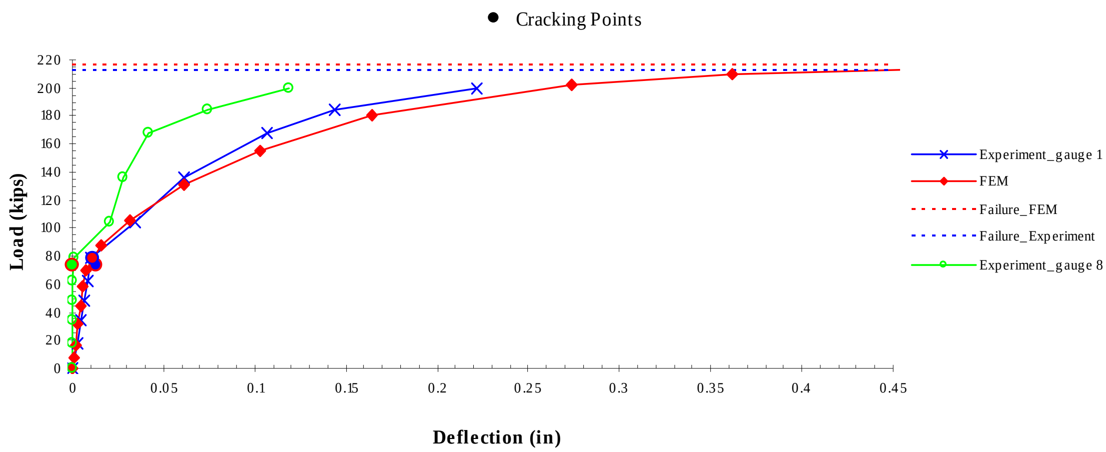


gauges 1 & 8

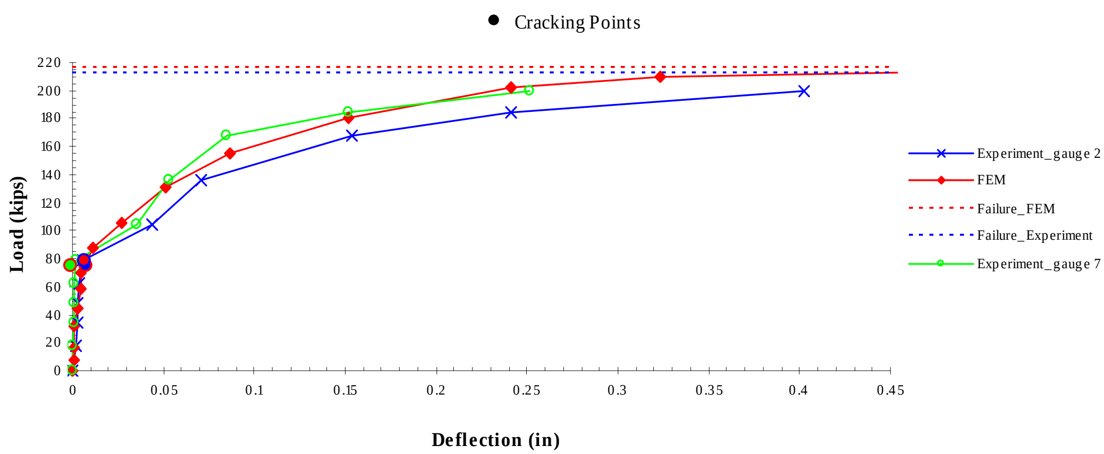


gauges 2 & 7

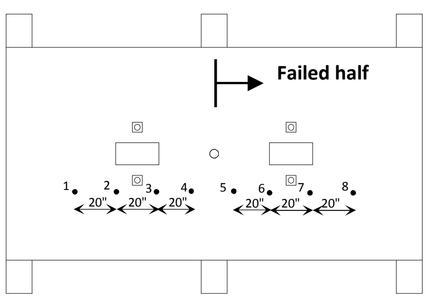


locations of deflection gauges

**Figure B.24:** FEM (β = 0.20) vs. experimental deflection measurements at different locations for Specimen C

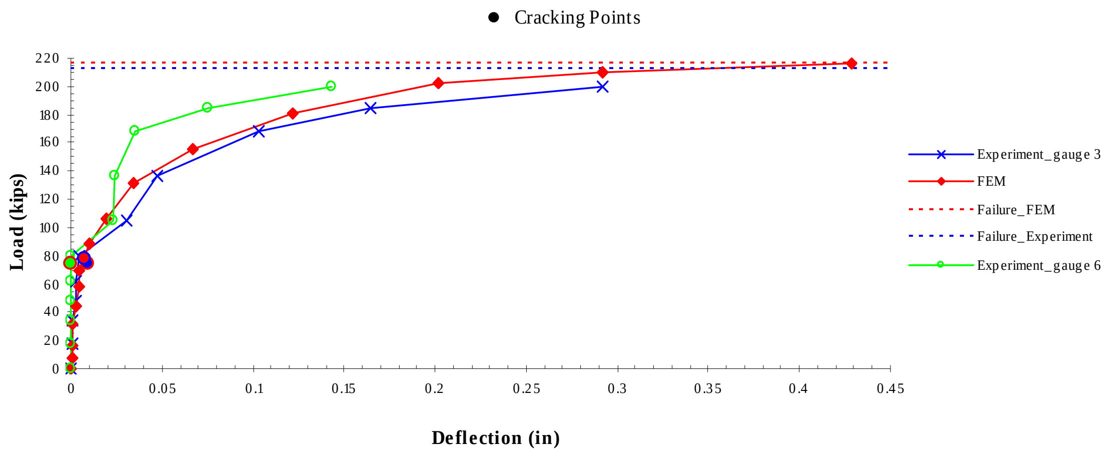


gauges 3 & 6

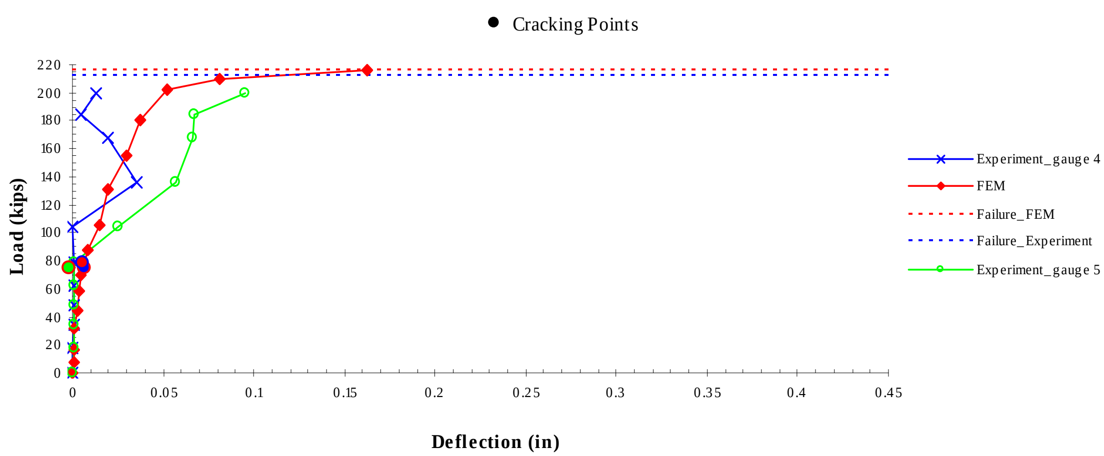


gauges 4 & 5

**Figure B.24 (*cont.*):** FEM (β = 0.20) vs. experimental deflection measurements at different locations for Specimen C

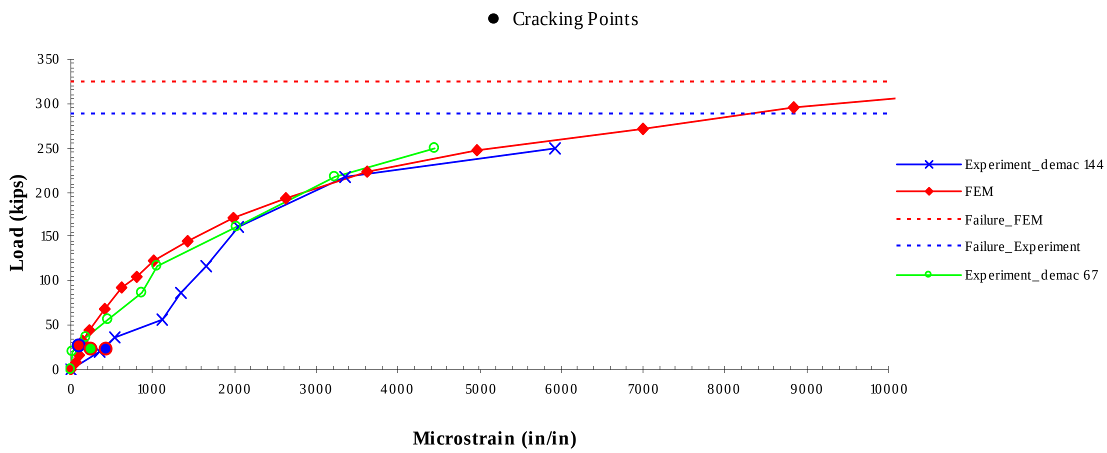


DEMECs 144 & 67

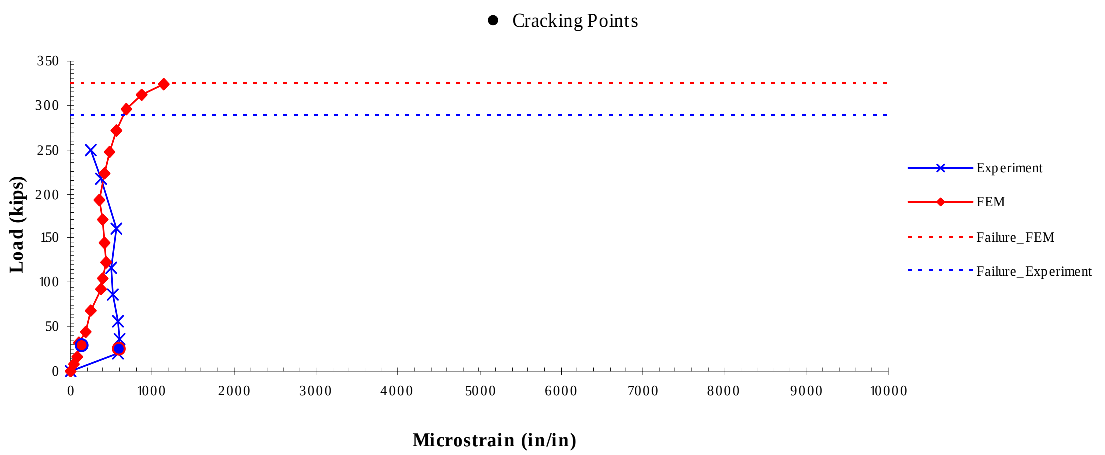


DEMEC 12

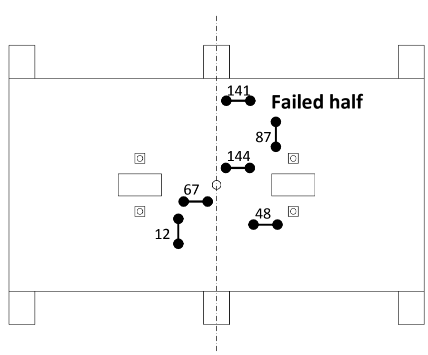


DEMEC locations

**Figure B.25:** FEM (β = 0.20) vs. experimental strain measurements at different DEMEC locations for Specimen D

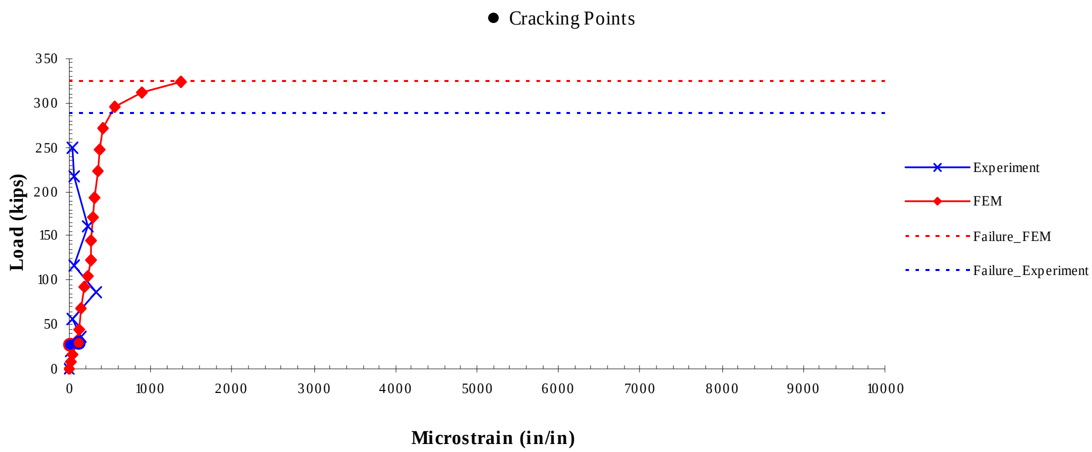


DEMEC 48

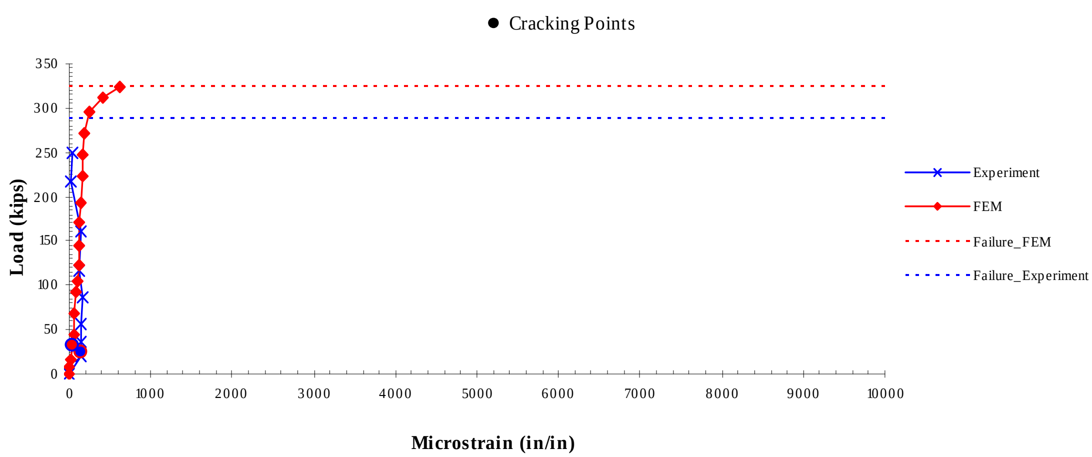


DEMEC 87

**Figure B.25 (*cont.*):** FEM (β = 0.20) vs. experimental strain measurements at different DEMEC locations for Specimen D

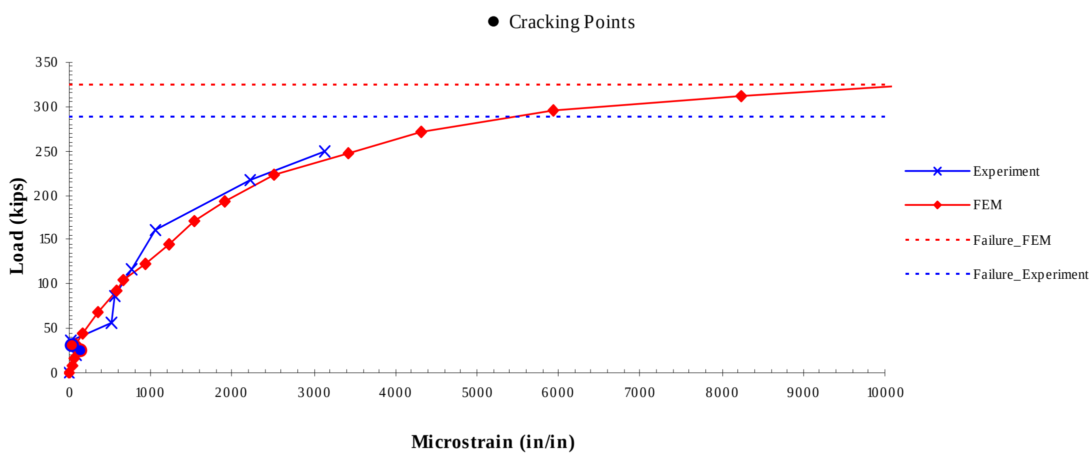


DEMEC 141

**Figure B.25 (*cont.*):** FEM (β = 0.20) vs. experimental strain measurements at different DEMEC locations for Specimen D

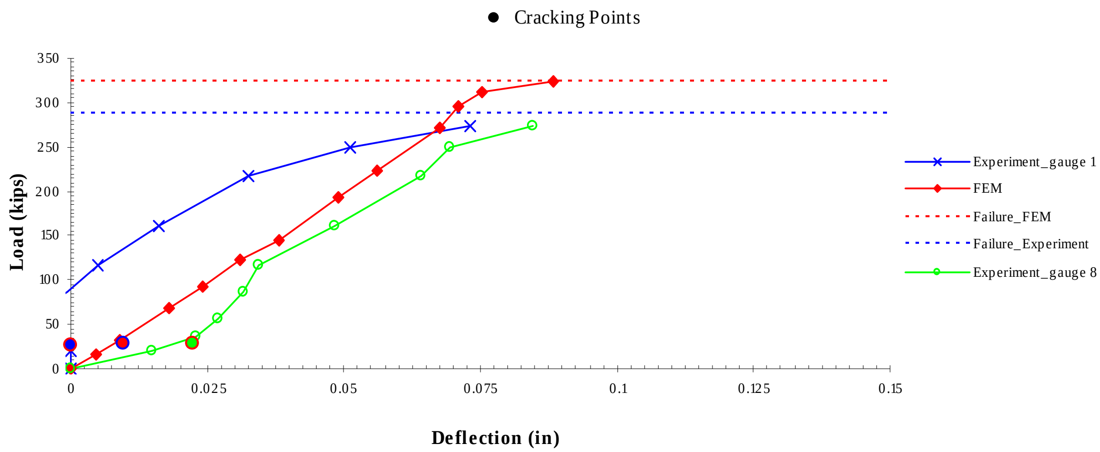


gauges 1 & 8

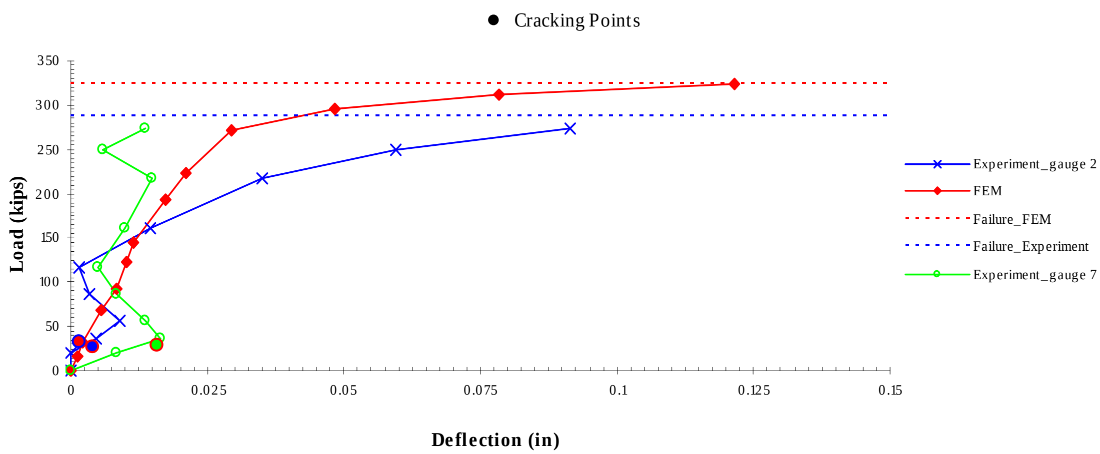


gauges 2 & 7

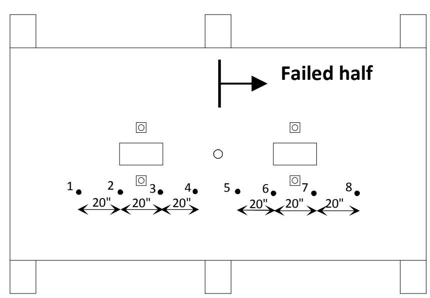


locations of deflection gauges

**Figure B.26:** FEM (β = 0.20) vs. experimental deflection measurements at different locations for Specimen D

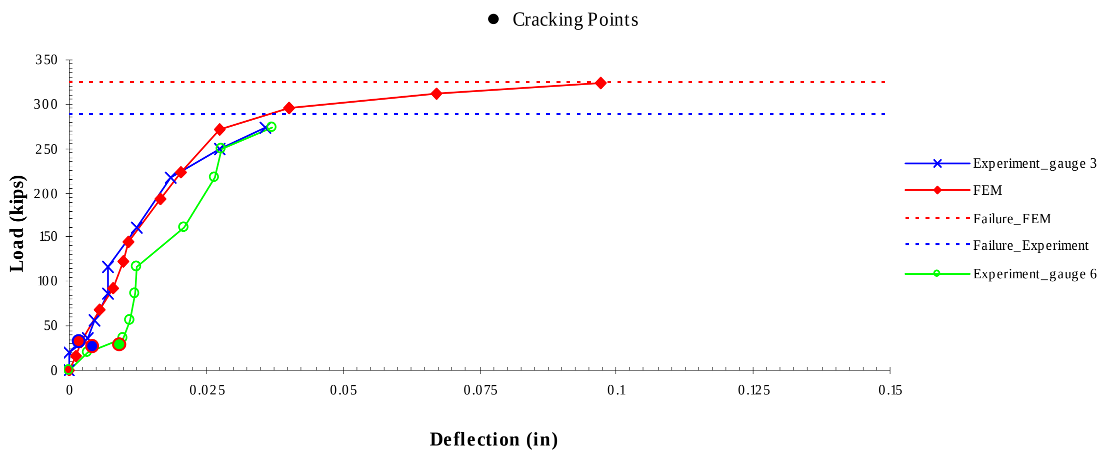


gauges 3 & 6

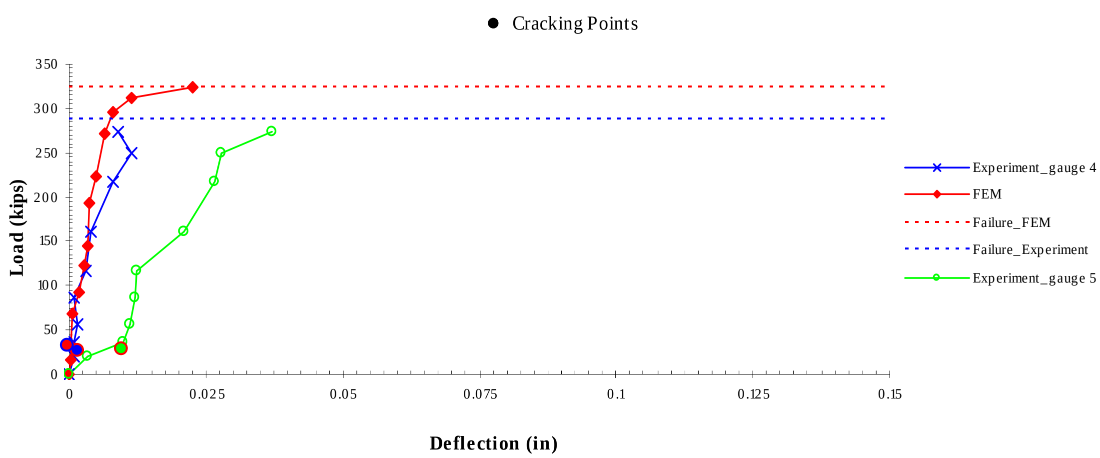


gauges 4 & 5

**Figure B.26 (*cont.*):** FEM (β = 0.20) vs. experimental deflection measurements at different locations for Specimen D

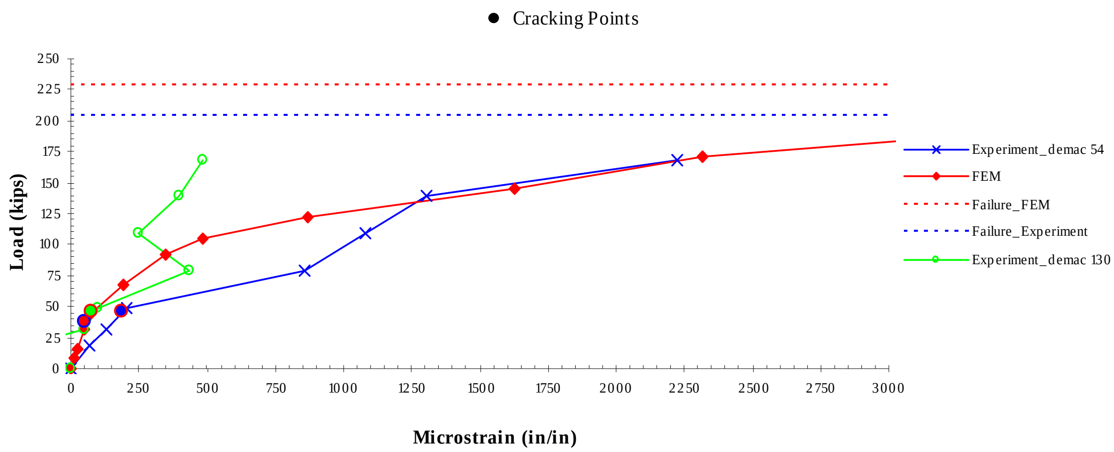


DEMECs 54 & 130

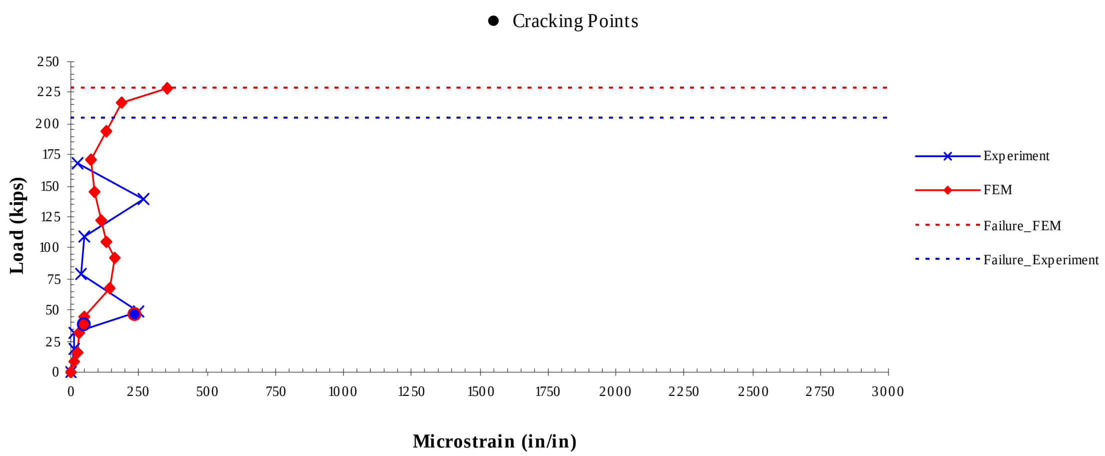


DEMEC 47

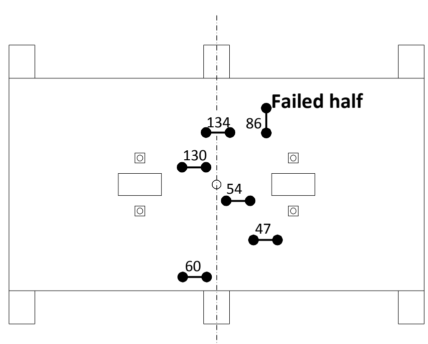


DEMEC locations

**Figure B.27:** FEM (β = 0.20) vs. experimental strain measurements at different DEMEC locations for Specimen E

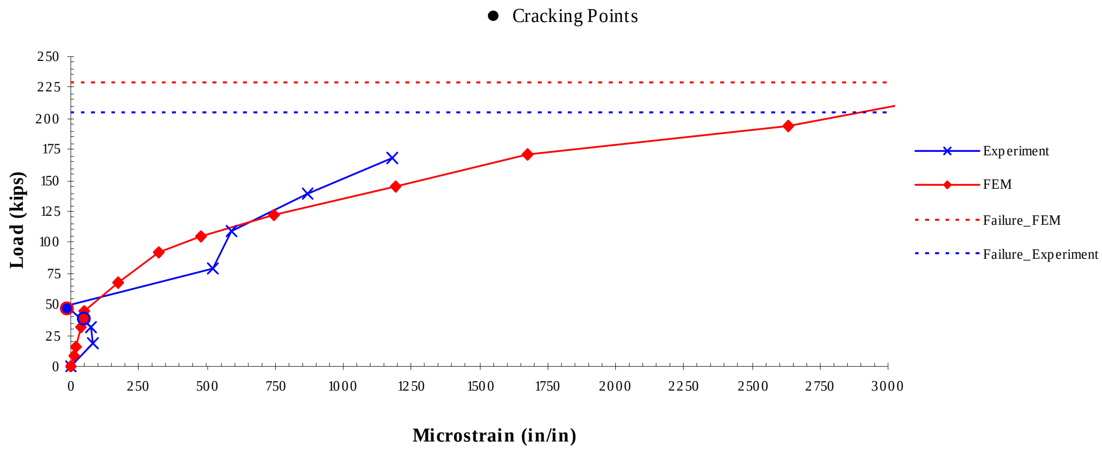


DEMEC 60

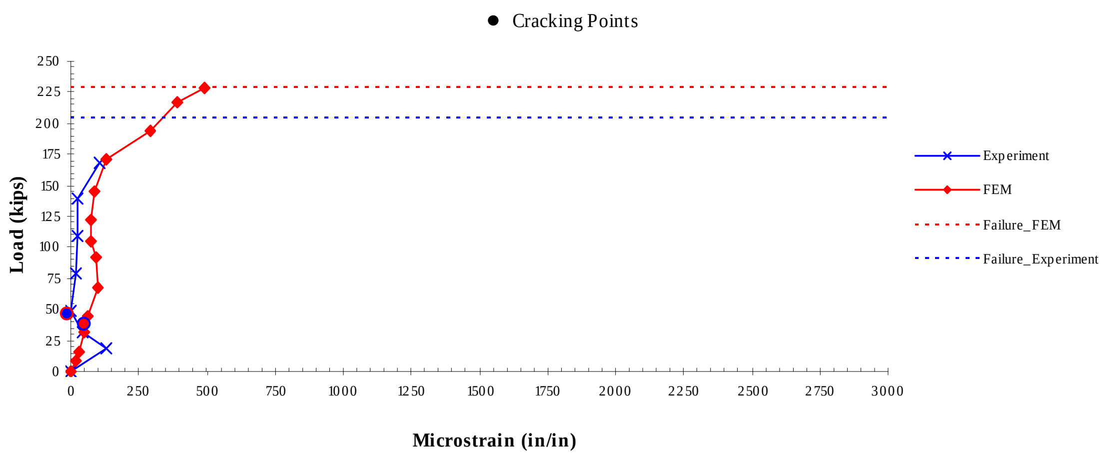


DEMEC 86

**Figure B.27( *cont.*):** FEM (β = 0.20) vs. experimental strain measurements at different DEMEC locations for Specimen E

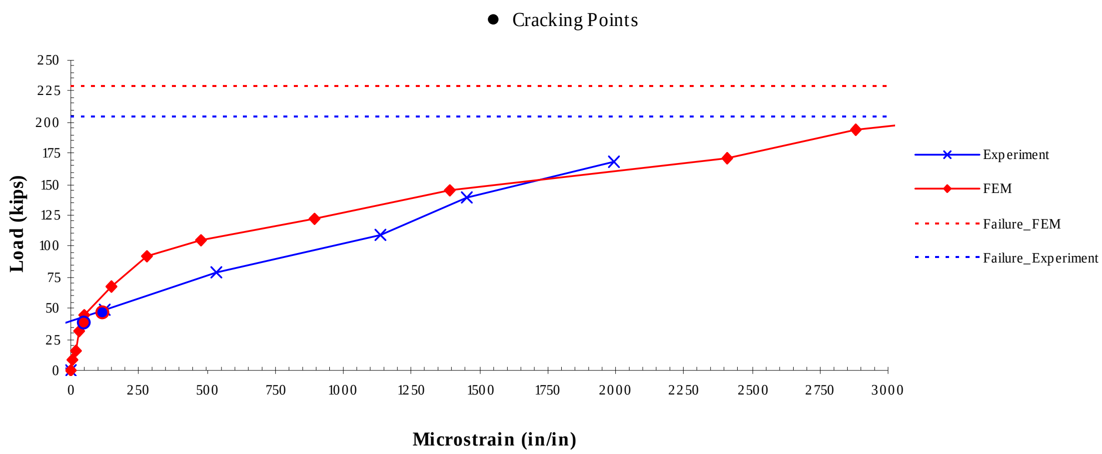


DEMEC 134

**Figure B.27( *cont.*):** FEM (β = 0.20) vs. experimental strain measurements at different DEMEC locations for Specimen E

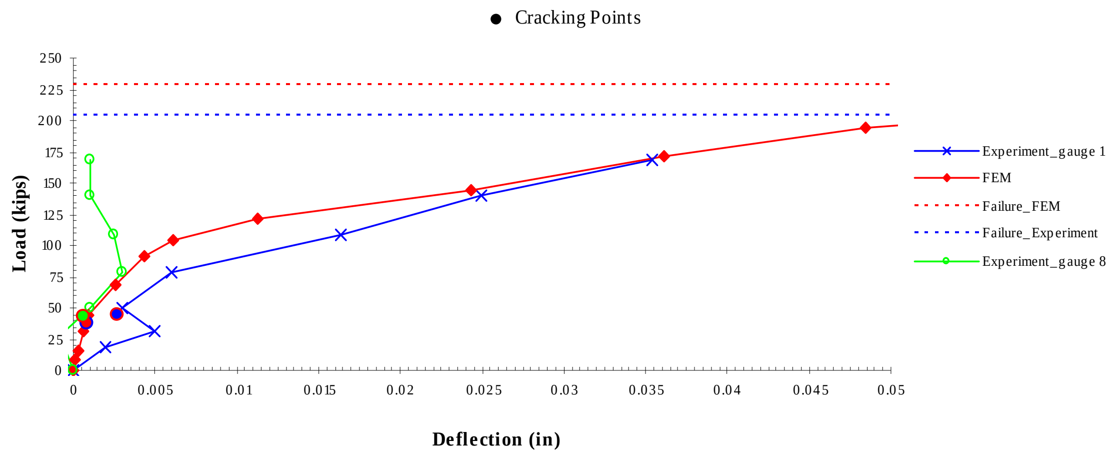


gauges 1 & 8

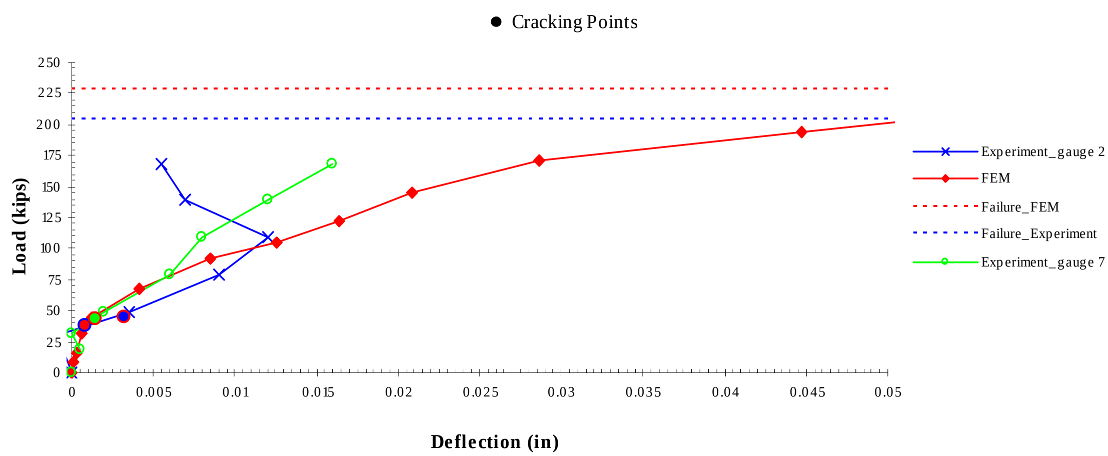


gauges 2 & 7

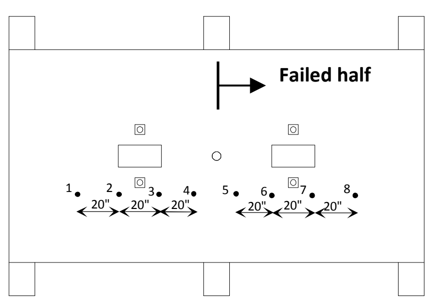


locations of deflection gauges

**Figure B.28:** FEM (β = 0.20) vs. experimental deflection measurements at different locations for Specimen E

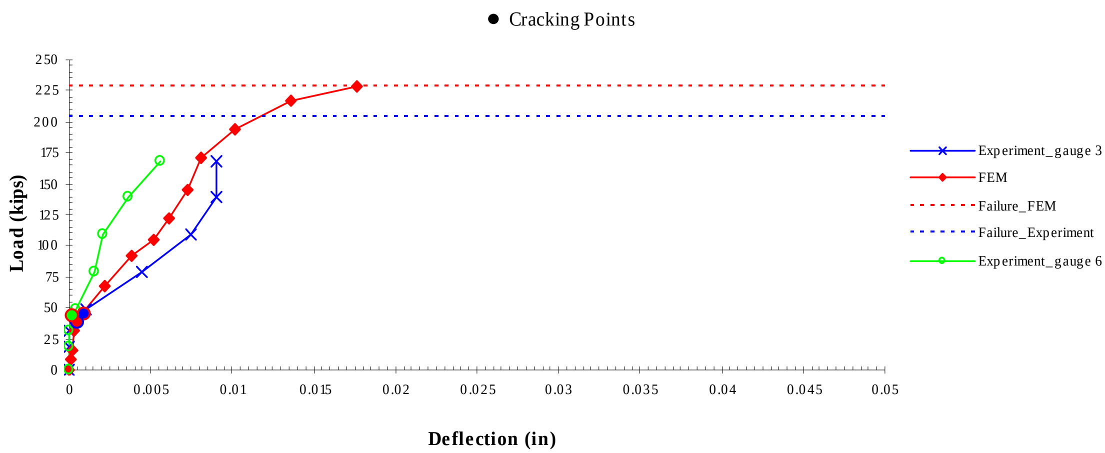


gauges 3 & 6

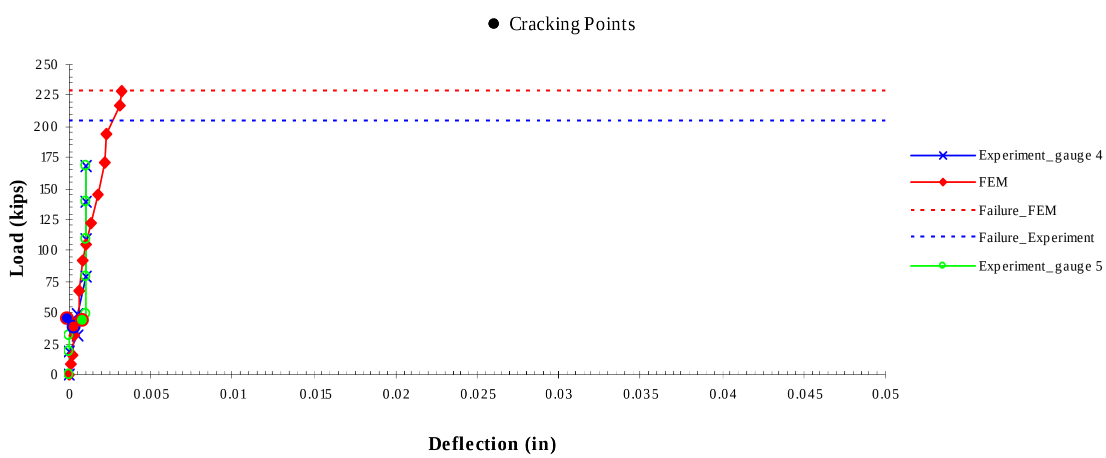


gauges 4 & 5

**Figure B.28 (*cont.*):** FEM (β = 0.20) vs. experimental deflection measurements at different locations for Specimen E

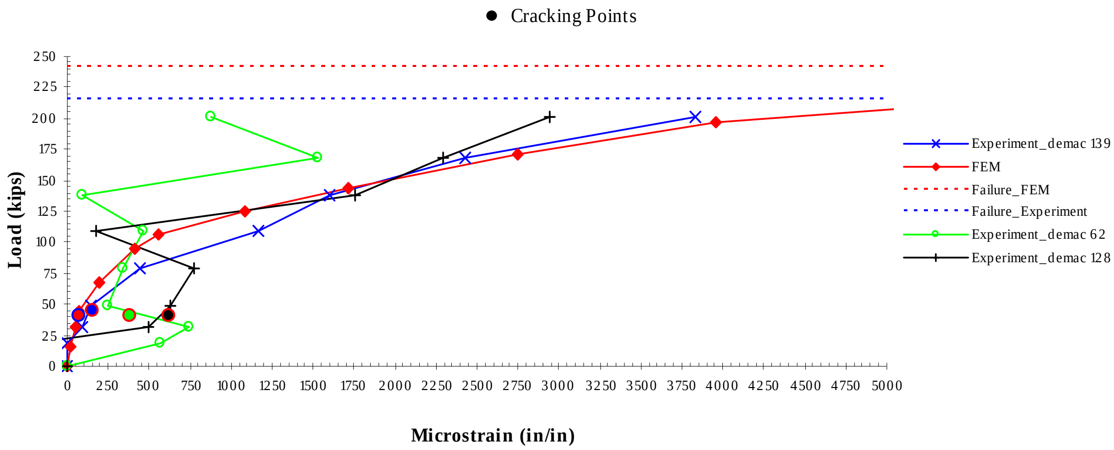


DEMECs 139. 62 & 128

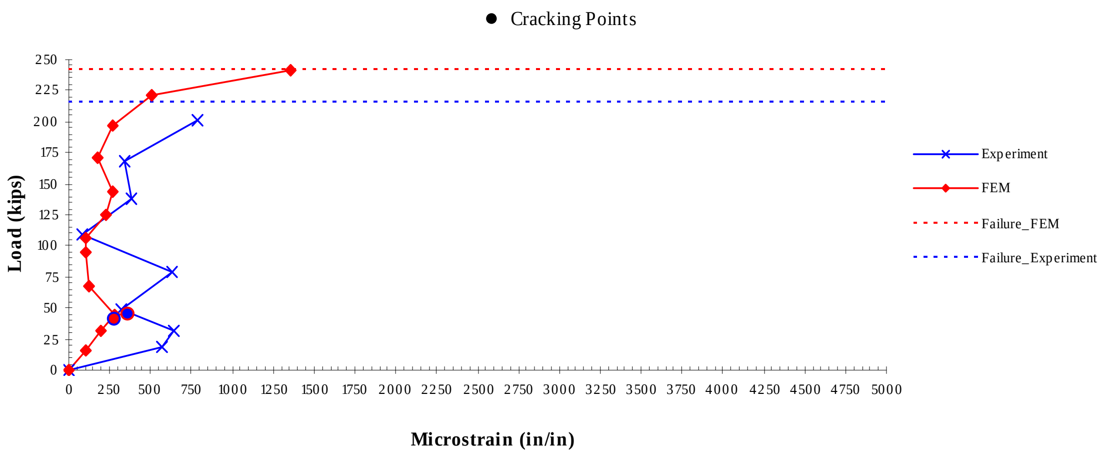


DEMEC 58

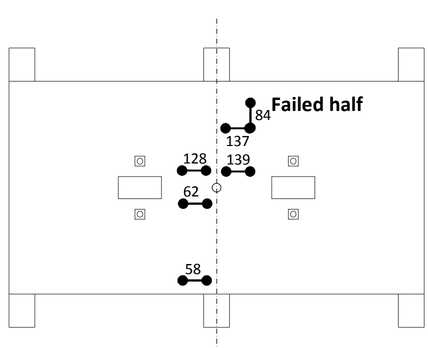


DEMEC locations

**Figure B.29:** FEM (β = 0.20) vs. experimental strain measurements at different DEMEC locations for Specimen F

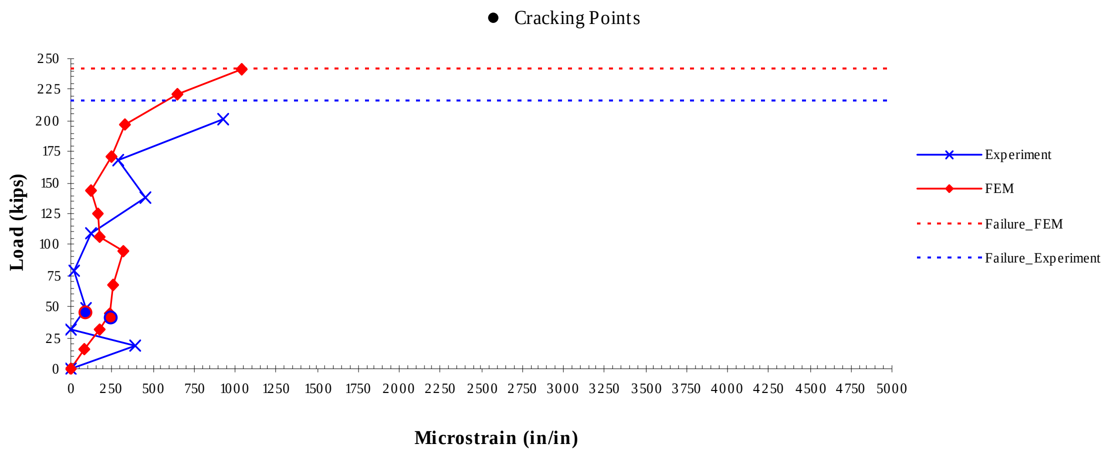


DEMEC 84

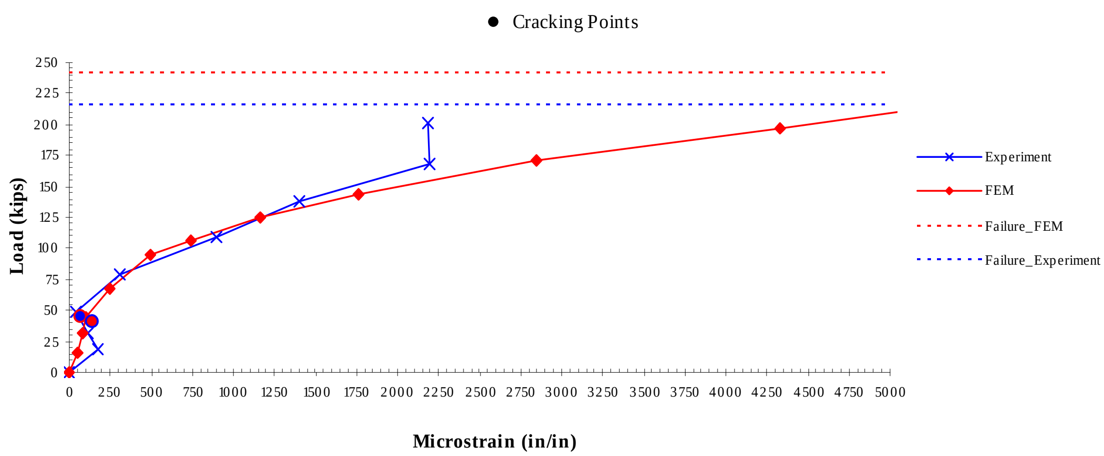


DEMEC 137

**Figure B.29 (*cont.*):** FEM ($\beta$ = 0.20) vs. experimental strain measurements at different DEMEC locations for Specimen F

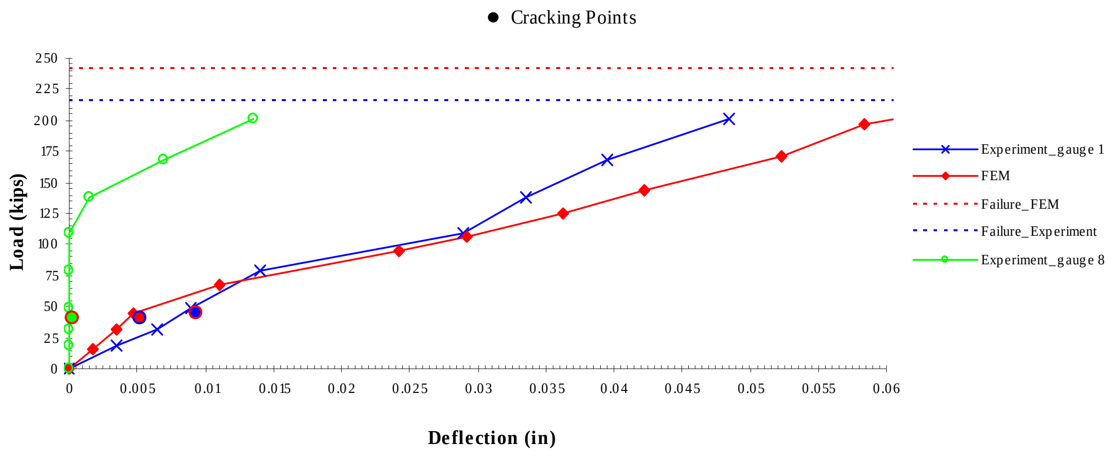


gauges 1 & 8

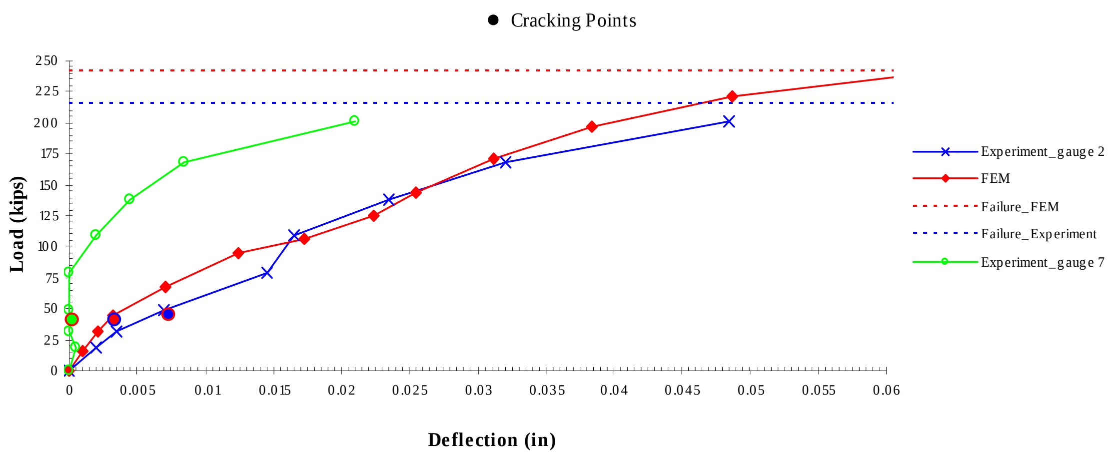


gauges 2 & 7

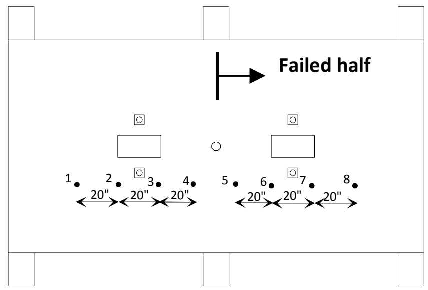


locations of deflection gauges

**Figure B.30:** FEM (β = 0.20) vs. experimental deflection measurements at different locations for Specimen F

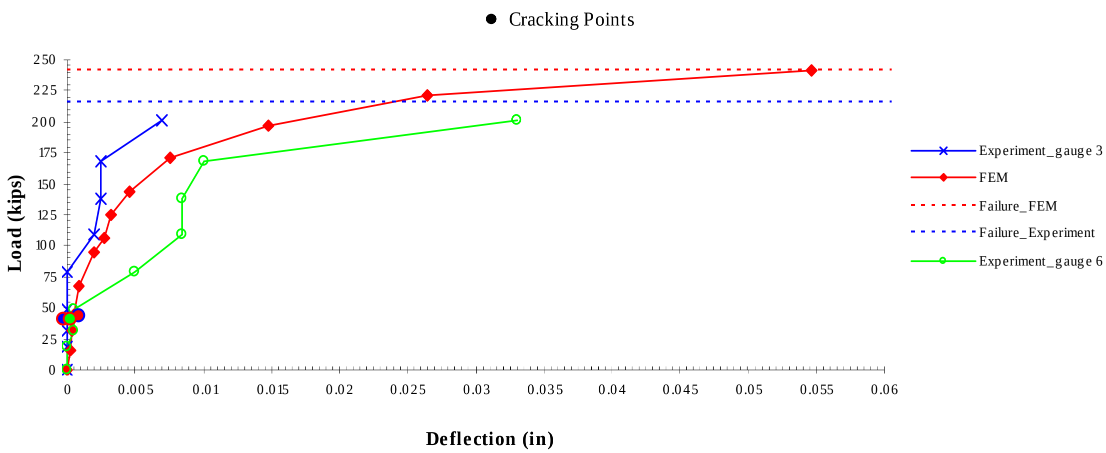


gauges 3 & 6

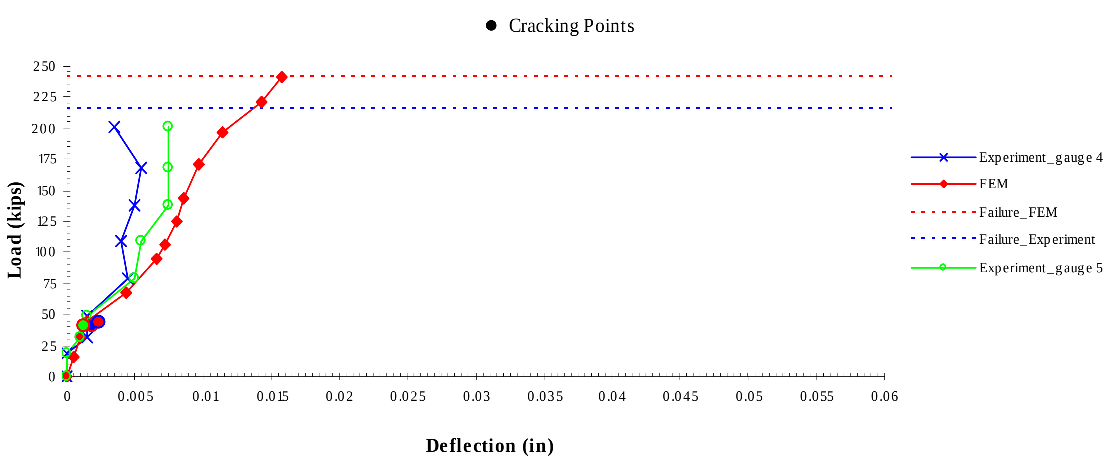


gauges 4 & 5

**Figure B.30 (*cont.*):** FEM ($\beta$ = 0.20) vs. experimental deflection measurements at different locations for Specimen F

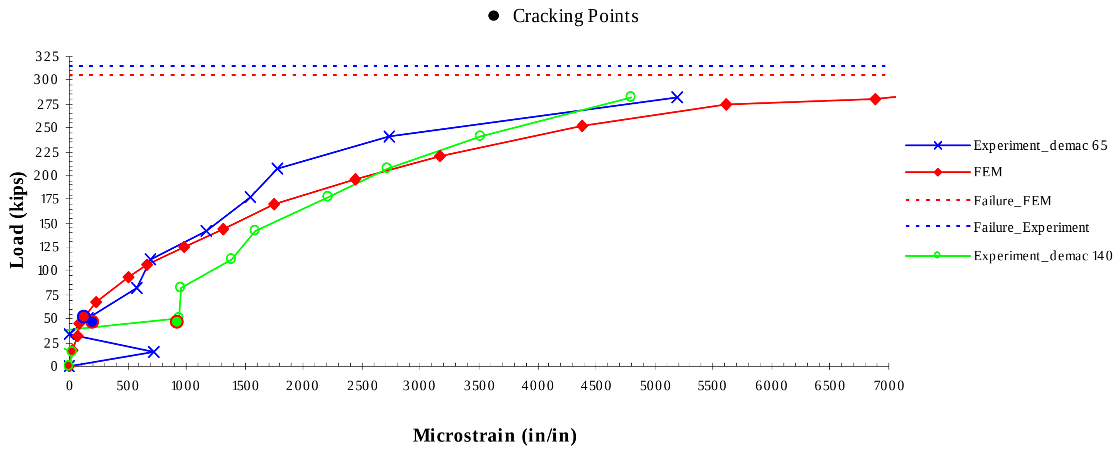


DEMECs 65 & 140

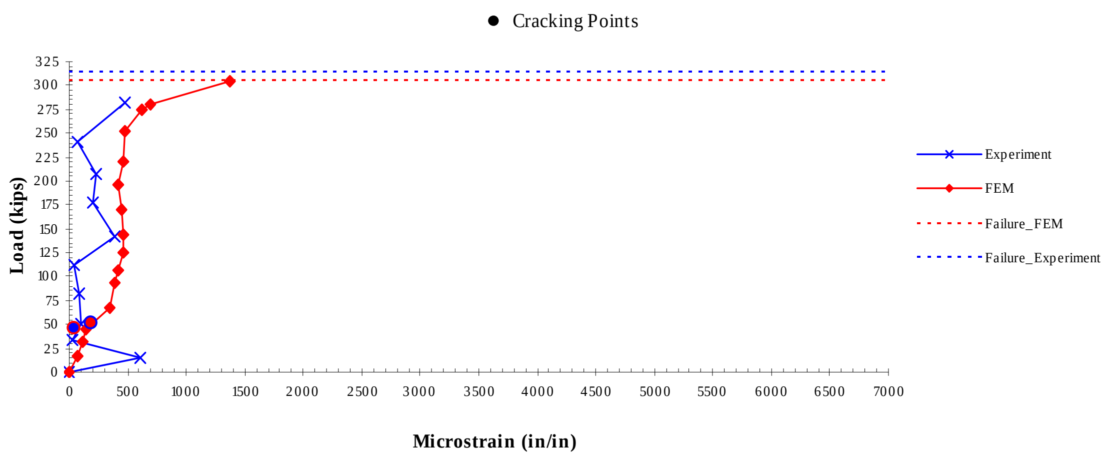


DEMEC 17

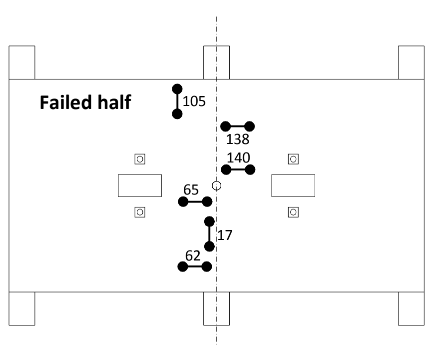


DEMEC locations

**Figure B.31:** FEM (β = 0.20) vs. experimental strain measurements at different DEMEC locations for Specimen G

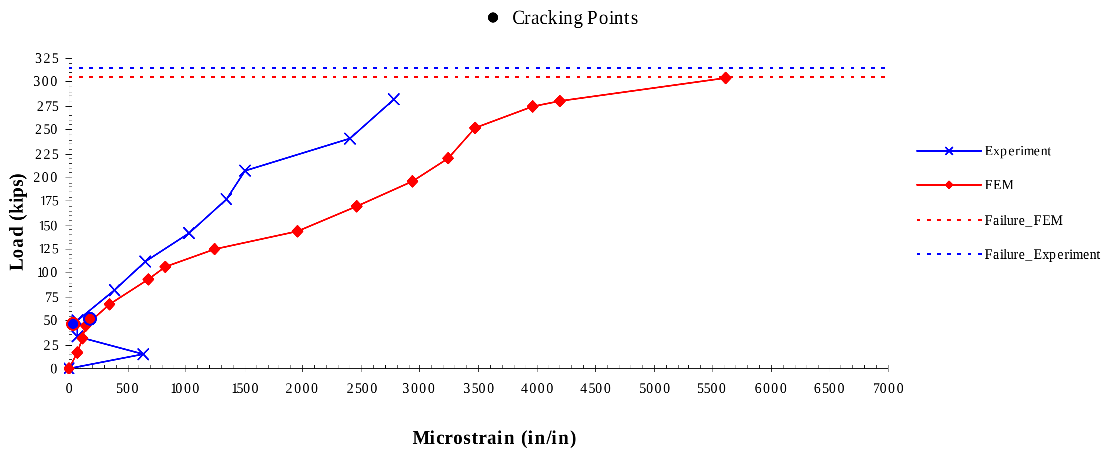


DEMEC 62

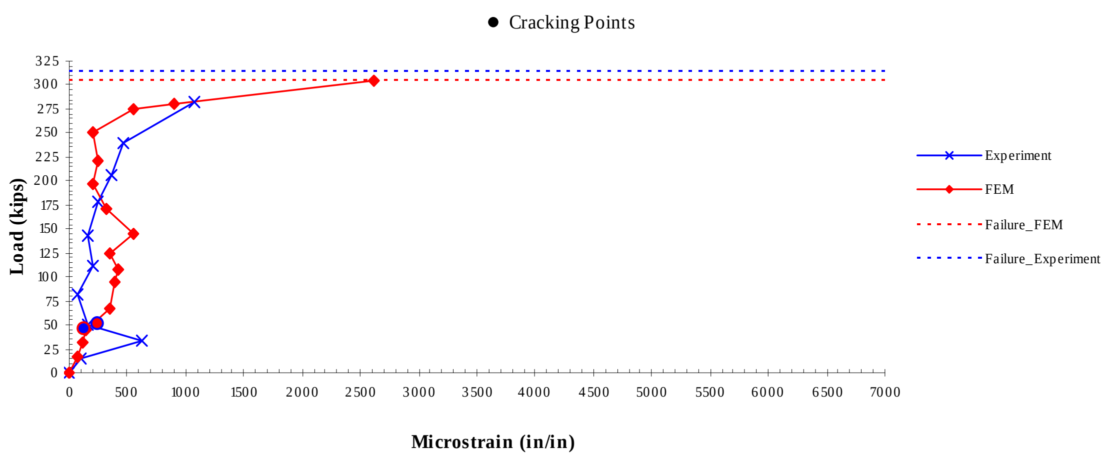


DEMEC 105

**Figure B.31 (*cont.*):** FEM (β = 0.20) vs. experimental strain measurements at different DEMEC locations for Specimen G

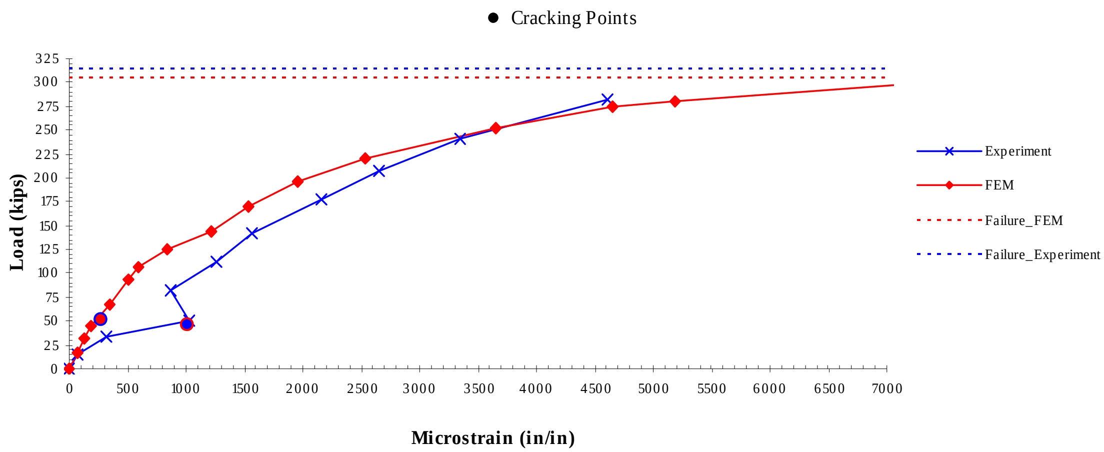


DEMEC 138

**Figure B.31 (*cont.*):** FEM (β = 0.20) vs. experimental strain measurements at different DEMEC locations for Specimen G

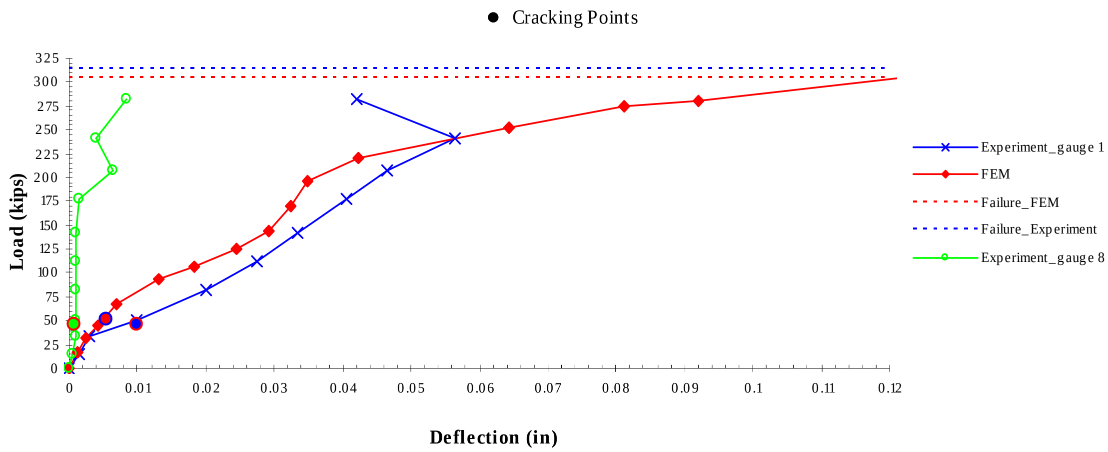


gauges 1 & 8

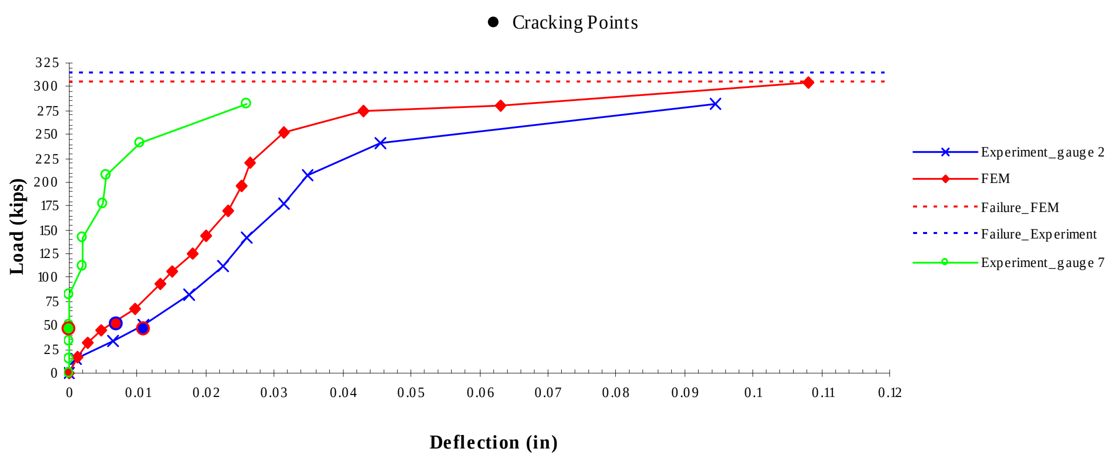


gauges 2 & 7

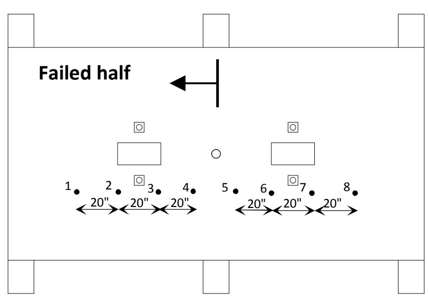


locations of deflection gauges

**Figure B.32:** FEM (β = 0.20) vs. experimental deflection measurements at different locations for Specimen G

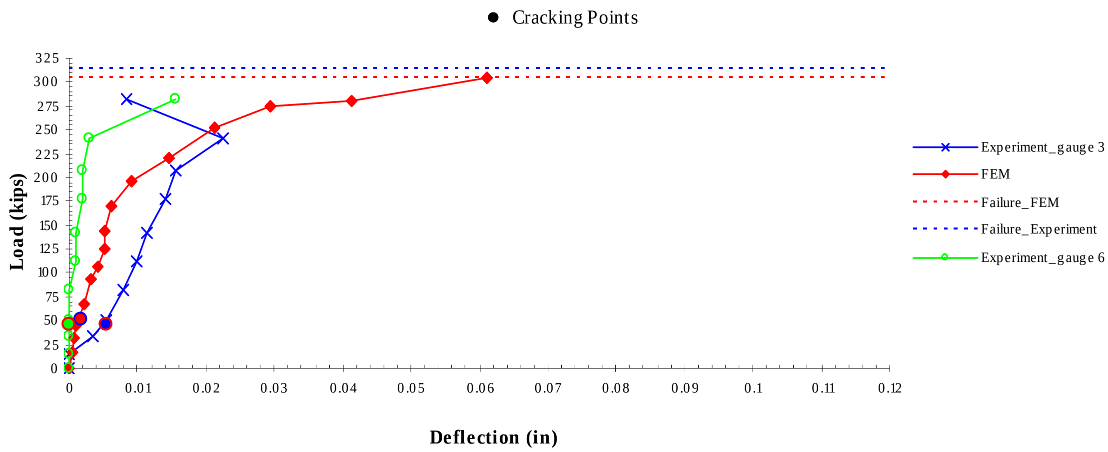


gauges 3 & 6

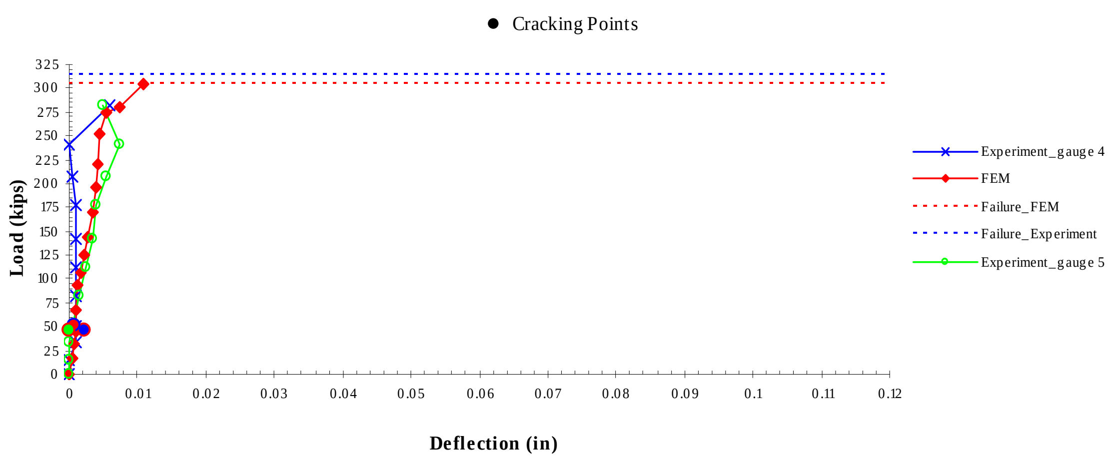


gauges 4 & 5

**Figure B.32 (*cont.*):** FEM (β = 0.20) vs. experimental deflection measurements at different locations for Specimen G

# APPENDIX C: Simplified Hand Methods' Tables

**Table C.1:** Comparison of Cracking Loads; section analysis to experiments

| Specimen | Cracking Load predicted by Section Analysis | | Experiments | | Actual Failure description |
|---|---|---|---|---|---|
| | Top surface | | Cracking Load, kips | Failure load, kips | |
| | Load, kips | % Diff. | | | |
| **3ft_cip_center** | 58.6 | 4.1 | 56.3 | >103.5 | --- |
| **3ft_cip_corner** | 36.7 | -23.5 | 48.0 | 56.2 | Punching |
| **3ft_pre_center** | 59.2 | 23.4 | 48.0 | >96.0 | --- |
| **3ft_pre_corner** | 41.6 | 4.0 | 40.0 | 80.0 | Comp. Strut failure + Punching |
| **5ft_cip_center** | 26.8 | 11.8 | 24.0 | 88.0 | Tension failure |
| **5ft_cip_corner** | 18.5 | -22.8 | 24.0 | 27.5 | |
| **5ft_pre_center** | 39.2 | 22.3 | 32.0 | 87.0 | Tension failure |
| **5ft 8in_center** | 27.1 | -13.6 | 31.4 | 69.0 | Tension failure |
| **5ft_pre_corner** | 23.3 | -3.1 | 24.0 | 48.0 | |
| **Specimen_A** | 53.6 | 98.3 | 27.0 | 272.0 | Punching (South side) |
| **Specimen_B** | 51.5 | 5.1 | 49.0 | 279.0 | Punching (South side) |
| **Specimen_C** | 50.3 | -36.3 | 79.0 | 212.0 | Punching (South side) |
| **Specimen_D** | 51.1 | 42.0 | 36.0 | 287.0 | Punching @ cip only(South side) |
| **Specimen_E** | 49.0 | -0.1 | 49.0 | 204.0 | P/S panel flex. failure & Support failure (south side) |
| **Specimen_F** | 49.5 | 1.1 | 49.0 | 215.0 | South side splitting & Punching |
| **Specimen_G** | 77.1 | 51.2 | 51.0 | 314.0 | Punching (north side) |

**Table C.2:** Comparison of AASHTO LRFD[22] failure loads to experimental loads

| Specimen | Failure Load Analysis – AASHTO LRFD: Neg. Moment region flexural capacity | | Pos. Moment region flexural capacity | | One way shear capacity Eq 2 (Eq 5.8.3.3-3 in AASHTO) | | One way shear capacity Eqs 5&6 (Eq 5.8.3.4.3-1 in AASHTO) | | Punching shear capacity Eq 10 (Eq 5.13.3.6.3-1 in AASHTO) | | Experiments | | Actual Failure description |
|---|---|---|---|---|---|---|---|---|---|---|---|---|---|
| | Load , kips | % Diff. | Load , kips | % Diff. | Load, kips | % Diff. | Load, kips | % Diff. | Load, kips | % Diff. | Cracking Load, kips | Failure load, kips | |
| **3ft_cip_center** | 80.8 | *** | n/a | *** | 50.0 | *** | n/a | *** | 72.9 | *** | 56.3 | >103.5 | --- |
| **3ft_cip_corner** | 47.0 | -16.4 | n/a | *** | 25.9 | -53.9 | n/a | *** | 39.9 | -28.9 | 48.0 | 56.2 | Punching |
| **3ft_pre_center** | 81.9 | *** | n/a | *** | 50.4 | *** | 102.7 | *** | 83.3 | *** | 48.0 | >96.0 | --- |
| **3ft_pre_corner** | 48.4 | -39.5 | n/a | *** | 29.3 | -63.4 | 63.7 | -20.4 | 52.1 | -34.8 | 40.0 | 80.0 | Comp. Strut failure + Punching |
| **5ft_cip_center** | 58.1 | -34.0 | n/a | *** | 49.4 | -43.9 | n/a | *** | 67.3 | -23.6 | 24.0 | 88.0 | Tension failure |
| **5ft_cip_corner** | 32.2 | 17.3 | n/a | *** | 22.1 | -19.7 | n/a | *** | 32.1 | 16.7 | 24.0 | 27.5 | |
| **5ft_pre_center** | 59.7 | -31.4 | n/a | *** | 61.0 | -29.9 | 120.2 | 38.2 | 87.4 | 0.5 | 32.0 | 87.0 | Tension failure |
| **5ft 8in_center** | 40.0 | -42.0 | n/a | *** | 75.8 | 9.9 | 151.2 | 119.1 | 85.7 | 24.3 | 31.4 | 69.0 | Tension failure |
| **5ft_pre_corner** | 34.8 | -27.5 | n/a | *** | 37.0 | -22.9 | 73.5 | 53.2 | 53.4 | 11.2 | 24.0 | 48.0 | |
| **Specimen_A** | 0.0 | *-* | 180.0 | -33.8 | 303.1 | 11.5 | 453.5 | 66.7 | 202.0 | -25.8 | 27.0 | 272.0 | Punching (South side) |
| **Specimen_B** | 148.4 | -46.8 | 252.1 | -9.7 | 310.4 | 11.3 | 453.1 | 62.4 | 206.8 | -25.9 | 49.0 | 279.0 | Punching (South side) |
| **Specimen_C** | 48.8 | -77.0 | 103.1 | -51.4 | 266.2 | 25.6 | n/a | *** | 183.2 | -13.6 | 79.0 | 212.0 | Punching (South side) |
| **Specimen_D** | 109.6 | -61.8 | 232.6 | -19.0 | 304.3 | 6.0 | 445.4 | 55.2 | 202.8 | -29.4 | 36.0 | 287.0 | Punching @ cip only(South side) |
| **Specimen_E** | 162.1 | -20.5 | 256.4 | 25.7 | 304.3 | 49.2 | 438.1 | 114.8 | 202.8 | -0.6 | 49.0 | 204.0 | P/S panel flex. failure & Support failure (south side) |
| **Specimen_F** | 140.5 | -34.7 | 247.0 | 14.9 | 308.1 | 43.3 | 445.7 | 107.3 | 205.2 | -4.5 | 49.0 | 215.0 | South side splitting & Punching |
| **Specimen_G** | 147.7 | -53.0 | 290.8 | -7.4 | 359.4 | 14.5 | 568.8 | 81.2 | 250.9 | -20.1 | 51.0 | 314.0 | Punching (north side) |

**Table C.3:** Comparison of ACI 318-08[44] failure loads to experimental loads

| Specimen | Failure Load Analysis | | | | | | | | | | | | Experi ments | Actual Failure description |
|---|---|---|---|---|---|---|---|---|---|---|---|---|---|---|
| | ACI 318-08 | | | | | | | | | | | | | |
| | Neg. Moment region flexural capacity | | Pos. Moment region flexural capacity | | One way shear capacity Eq 2 (Eq 11-3 in ACI) | | One way shear capacity Eq 3 (Eq 11-4 in ACI) | | One way shear capacity Eq 4 (Eq 11-9 in ACI) | | Punching shear capacity Eq10&11 (Eqs 11-31, 11-32, 11-33, 11-34 in ACI) | | | |
| | Load, kips | % Diff. | Load, kips | % Diff. | Load, kips | % Diff. | Load, kips | % Diff. | Load, kips | % Diff. | Load, kips | % Diff. | Failure load, kips | |
| 3ft_cip_center | 129.4 | *** | n/a | *** | 79.9 | *** | n/a | *** | n/a | *** | 72.9 | *** | >103.5 | --- |
| 3ft_cip_corner | 63.6 | 13.2 | n/a | *** | 35.1 | -37.6 | n/a | *** | n/a | *** | 39.9 | -28.9 | 56.2 | Punching |
| 3ft_pre_center | 131.1 | *** | n/a | *** | n/a | *** | 107.7 | *** | 176.0 | *** | 83.3 | *** | >96.0 | --- |
| 3ft_pre_corner | 65.5 | -18.1 | n/a | *** | n/a | *** | 52.9 | -33.8 | 87.8 | 9.7 | 52.1 | -34.8 | 80.0 | Comp. Strut failure + Punching |
| 5ft_cip_center | 92.9 | 5.6 | n/a | *** | 79.0 | -10.3 | n/a | *** | n/a | *** | 67.3 | -23.6 | 88.0 | Tension failure |
| 5ft_cip_corner | 44.2 | 60.8 | n/a | *** | 30.3 | 10.1 | n/a | *** | n/a | *** | 32.1 | 16.7 | 27.5 | |
| 5ft_pre_center | 95.6 | 9.8 | n/a | *** | n/a | *** | 130.4 | 49.8 | 139.7 | 60.6 | 125.5 | 44.2 | 87.0 | Tension failure |
| 5ft 8in_center | 53.6 | -22.3 | n/a | *** | n/a | *** | 135.8 | 96.8 | 92.5 | 34.1 | 132.3 | 91.7 | 69.0 | Tension failure |
| 5ft_pre_corner | 47.7 | -0.6 | n/a | *** | n/a | *** | 67.9 | 41.4 | 70.5 | 46.8 | 53.4 | 11.2 | 48.0 | |
| Specimen_A | 0.0 | *-* | 219.3 | -19.4 | n/a | *** | 493.5 | 81.4 | 506.9 | 86.4 | 288.4 | 6.0 | 272.0 | Punching (South side) |
| Specimen_B | 197.9 | -29.1 | 315.7 | 13.2 | n/a | *** | 505.4 | 81.2 | 509.6 | 82.7 | 284.8 | 2.1 | 279.0 | Punching (South side) |
| Specimen_C | 65.0 | -69.3 | 128.4 | -39.4 | 324.3 | 53.0 | n/a | *** | n/a | *** | 183.2 | -13.6 | 212.0 | Punching (South side) |
| Specimen_D | 146.1 | -49.1 | 289.8 | 1.0 | n/a | *** | 495.5 | 72.6 | 507.4 | 76.8 | 284.8 | -0.8 | 287.0 | Punching @ cip only(South side) |
| Specimen_E | 216.2 | 6.0 | 321.8 | 57.7 | n/a | *** | 495.5 | 142.9 | 507.4 | 148.7 | 284.8 | 39.6 | 204.0 | P/S panel flex. failure & Support failure (south side) |
| Specimen_F | 187.3 | -12.9 | 309.1 | 43.8 | n/a | *** | 501.6 | 133.3 | 508.7 | 136.6 | 284.8 | 32.5 | 215.0 | South side splitting & Punching |
| Specimen_G | 197.0 | -37.3 | 362.9 | 15.6 | n/a | *** | 585.2 | 86.4 | 670.5 | 113.5 | 370.4 | 18.0 | 314.0 | Punching (north side) |

**Table C.4:** Comparison of FIP[45] Recommendations failure loads to experimental loads

| Specimen | Failure Load Analysis – FIP Recommendations: Neg. Moment region flexural capacity | | Pos. Moment region flexural capacity | | One way shear capacity Eq 7 (Eq 6.7.2 in FIP) | | Punching shear capacity Eqs 12&13 (Eq 6.7.4 in FIP) | | Experiments | | Actual Failure description |
|---|---|---|---|---|---|---|---|---|---|---|---|
| | Load, kips | % Diff. | Load, kips | % Diff. | Load, kips | % Diff. | Load, kips | % Diff. | Cracking Load, kips | Failure load, kips | |
| **3ft_cip_center** | 128.9 | *** | n/a | *** | 99.9 | *** | 92.6 | *** | 56.3 | >103.5 | --- |
| **3ft_cip_corner** | 63.3 | 12.6 | n/a | *** | 42.0 | -25.4 | 49.0 | -12.8 | 48.0 | 56.2 | Punching |
| **3ft_pre_center** | 130.7 | *** | n/a | *** | 113.7 | *** | 112.4 | *** | 48.0 | >96.0 | --- |
| **3ft_pre_corner** | 65.4 | -18.3 | n/a | *** | 55.6 | -30.6 | 63.8 | -20.2 | 40.0 | 80.0 | Comp. Strut failure + Punching |
| **5ft_cip_center** | 92.5 | 5.2 | n/a | *** | 95.6 | 8.6 | 94.8 | 7.7 | 24.0 | 88.0 | Tension failure |
| **5ft_cip_corner** | 43.9 | 59.6 | n/a | *** | 33.5 | 22.0 | 45.3 | 64.8 | 24.0 | 27.5 | |
| **5ft_pre_center** | 95.3 | 9.6 | n/a | *** | 142.5 | 63.8 | 123.1 | 41.5 | 32.0 | 87.0 | Tension failure |
| **5ft 8in_center** | 53.5 | -22.5 | n/a | *** | 150.4 | 118.0 | 125.8 | 82.3 | 31.4 | 69.0 | Tension failure |
| **5ft_pre_corner** | 47.6 | -0.9 | n/a | *** | 75.2 | 56.7 | 68.4 | 42.4 | 24.0 | 48.0 | |
| **Specimen_A** | 0.0 | *-* | 218.2 | -19.8 | 342.2 | 25.8 | 280.0 | 3.0 | 27.0 | 272.0 | Punching (South side) |
| **Specimen_B** | 197.4 | -29.2 | 314.2 | 12.6 | 352.2 | 26.2 | 284.2 | 1.9 | 49.0 | 279.0 | Punching (South side) |
| **Specimen_C** | 64.9 | -69.4 | 128.2 | -39.5 | 209.3 | -1.3 | 215.3 | 1.5 | 79.0 | 212.0 | Punching (South side) |
| **Specimen_D** | 145.9 | -49.2 | 288.4 | 0.5 | 343.0 | 19.5 | 280.7 | -2.2 | 36.0 | 287.0 | Punching @ cip only(South side) |
| **Specimen_E** | 215.7 | 5.7 | 320.0 | 56.9 | 343.0 | 68.1 | 280.7 | 37.6 | 49.0 | 204.0 | P/S panel flex. failure & Support failure (south side) |
| **Specimen_F** | 186.8 | -13.1 | 307.5 | 43.0 | 348.6 | 62.1 | 282.8 | 31.6 | 49.0 | 215.0 | South side splitting & Punching |
| **Specimen_G** | 196.5 | -37.4 | 361.9 | 15.3 | 400.7 | 27.6 | 319.5 | 1.8 | 51.0 | 314.0 | Punching (north side) |

**Table C.5:** Muttoni and Ruiz[46,47] critical shear crack equations

| Specimen | Failure Load Analysis | | | | Experiments | | Actual Failure description |
|---|---|---|---|---|---|---|---|
| | One way shear capacity Eq 8 | | Punching shear capacity Eq 14 | | | | |
| | Load, kips | % Diff. | Load, kips | % Diff. | Cracking Load, kips | Failure load, kips | |
| **3ft_cip_center** | 70.5 | *** | 198.4 | *** | 56.3 | >103.5 | --- |
| **3ft_cip_corner** | 30.9 | -45.0 | 114.5 | 103.7 | 48.0 | 56.2 | Punching |
| **3ft_pre_center** | 80.5 | *** | 200.5 | *** | 48.0 | >96.0 | --- |
| **3ft_pre_corner** | 40.4 | -49.6 | 124.1 | 55.2 | 40.0 | 80.0 | Comp. Strut failure + Punching |
| **5ft_cip_center** | 69.7 | -20.8 | 150.7 | 71.3 | 24.0 | 88.0 | Tension failure |
| **5ft_cip_corner** | 26.7 | -2.9 | 81.9 | 197.8 | 24.0 | 27.5 | |
| **5ft_pre_center** | 90.6 | 4.1 | 163.4 | 87.8 | 32.0 | 87.0 | Tension failure |
| **5ft 8in_center** | 89.6 | 29.9 | 152.6 | 121.1 | 31.4 | 69.0 | Tension failure |
| **5ft_pre_corner** | 44.8 | -6.7 | 101.6 | 111.6 | 24.0 | 48.0 | |
| **Specimen_A** | 318.1 | 17.0 | 306.6 | 12.7 | 27.0 | 272.0 | Punching (South side) |
| **Specimen_B** | 325.8 | 16.8 | 301.7 | 8.2 | 49.0 | 279.0 | Punching (South side) |
| **Specimen_C** | 271.6 | 28.1 | 324.7 | 53.2 | 79.0 | 212.0 | Punching (South side) |
| **Specimen_D** | 319.4 | 11.3 | 301.8 | 5.2 | 36.0 | 287.0 | Punching @ cip only(South side) |
| **Specimen_E** | 319.4 | 56.6 | 297.1 | 45.6 | 49.0 | 204.0 | P/S panel flex. failure & Support failure (south side) |
| **Specimen_F** | 323.3 | 50.4 | 300.0 | 39.5 | 49.0 | 215.0 | South side splitting & Punching |
| **Specimen_G** | 362.0 | 15.3 | 384.8 | 22.5 | 51.0 | 314.0 | Punching (north side) |

VITA

Mostafa Farhat Ghashgesh

Candidate for the Degree of

Doctor of Philosophy

Thesis: INVESTIGATIONS OF A PRECAST BRIDGE DECK SYSTEM

Major Field: Civil Engineering

Biographical:

Personal Data: Born in Tripoli, Libya on October 20th 1973, the son of Farhat Ghashgesh and Salma Atahhah.

Education:

Completed the requirements for the Doctor of Philosophy in Civil Engineering at Oklahoma State University, Stillwater, Oklahoma in July, 2012.

Completed the requirements for the Master of Science in Civil Engineering at Al-Fateh University, Tripoli, Libya in 2002.

Completed the requirements for the Bachelor of Science in Civil Engineering at Al-Fateh University, Tripoli, Libya in 1996.

Experience:

2008: Employed by Oklahoma State University as a Graduate Research Assistant.
2006: Cooperative with Libya Telecom and Technology Company (LTT).
2005: Cooperative with Al-Jamahiriya Consultation Bureau.
2002: Faculty Member, Civil Eng. Dept., Faculty of Eng., Al-Fateh University.
1999: Lecturer Assistant, Civil Eng. Dept., Faculty of Eng., Al-Fateh University.
1998: Supervising Engineer at Al-Taaluf Al-Hur Construction Company.
1997: Engineer at the Libyan Army Administration.

Professional Memberships:

2009 AISC Student membership.
2008 ACI Student membership.
2002 Faculty Union Membership, Al-Fateh University.
1999 Engineers' Scientific Association – Tripoli\Libya.
1996 Engineers' Union Membership - Tripoli\Libya.

Name: Mostafa Farhat Ghashgesh Date of Degree: July, 2012

Institution: Oklahoma State University Location: Stillwater, Oklahoma

Title of Study: INVESTIGATIONS OF A PRECAST BRIDGE DECK SYSTEM

Pages in Study: 244 Candidate for the Degree of Doctor of Philosophy

Major Field: Civil Engineering

Scope and Method of Study:

Improved methods of bridge deck construction are greatly needed. Bridge decks are often the first element to require repair or replacement because of its direct exposure to the elements and tire wear. This dissertation presents a new precast overhang system that allows for significant improvements in construction speed, economy, and safety while meeting the AASHTO requirements and providing a serviceable structure. Welded rebar mats were also investigated to replace tied reinforcing bars with partial depth panels to improve the economy, constructability, and construction speed of bridge decks. Bridge decks have been constructed and tested that have used tied reinforcing and welded rebar mats. A self-written non-linear finite element program was created to model the tested specimens and provide an alternative, economic, and time-saving tool. Strut-and-tie modeling as well as design provisions of three design codes were also used to predict failure loads.

Findings and Conclusions:

Satisfactory results were obtained, which indicate that the system will allow a support beam to be removed in certain circumstances. The improved ability of the wire mat to help resist cracking could allow an owner either greater construction tolerances for the reinforcement placement or improved crack control and hence long term durability. The proposed FE program has proven successful at modeling the performance of concrete bridge decks with interior and overhang loading. For these specimens it was found that a shear reduction factor $\beta$ of 0.20 showed the best correlation with the experimental data. Additionally, it is found that the STM is the closest, in estimating failure loads and predicting the failure sequence and mode as well. FIP design recommendation was found the closest to experiments. Furthermore, it satisfactorily estimated the failure modes experimentally observed in all specimens.

ADVISER'S APPROVAL: Dr. M. Tyler Ley